The Non-Destructive Analysis of Lithium-Ion Battery Degradation

Robert Burrell

This thesis is submitted for the degree of

Doctor of Philosophy

January 2022

Department of Chemistry

In Dedication to my Parents.

Declaration

This thesis has not been submitted in support of an application for another degree at this or any other university. It is the result of my own work and includes nothing that is the outcome of work done in collaboration except where specifically indicated. Many of the ideas in this thesis were the product of discussion with my supervisor, Professor Harry Ernst Hoster.

Excerpts of this thesis have been published in the following academic publications.

1. R. Burrell, A. Zulke, P. Keil and H. Hoster, *Journal of The Electrochemical Society*, 2020, 167, 130544.
2. A. Zülke, Y. Li, P. Keil, R. Burrell, S. Belaisch, M. Nagarathinam, M. Mercer and H. Hoster, *Batteries & Supercaps*, 2021, 4, 849-849.

Abstract

This thesis investigates the electrochemical response and degradation of lithium-ion cells under combinations of calendar, cycle and compression conditions. Since the operating conditions of lithium-ion batteries are varied and dynamic throughout their life, the ageing of cells needs to be examined under representative individual scenarios. The following scenarios were examined separately using several non-destructive analysis methods, which respectively provide new methodologies, ageing theories and perspectives on the ageing of lithium-ion cells.

Calendar ageing promoted a spoon-shaped dependence of state-of-charge (SoC) on capacity fade, which was linked to shuttle-based self-discharge. After calendar ageing, cells were cycled under aggressive or conservative conditions. A potential ageing path dependence was identified, where the outcome of cycling was influenced by previous calendar history.

Reversible capacity losses were found to interfere with measurements of the degradation rate of cells during a cycling study, where the reversible loss of lithium into anode overhang regions led to greater capacity fade. Storage periods at low SoC recovered, quantified and identified the origins of the reversible capacity, and an alternative visualisation tool was proposed to identify time-related artefacts that led to such losses.

To aid the design of a test-rig capable of applying uniform pressure, finite element analysis and experimental validation measurements were performed. Next, static measurements in the absence of cycling were performed to disentangle the effects of pressure on lithium-ion pouch cells. Pressure was found to have an instant effect on capacity and pulse resistance. The largest increases in resistance were observed at very low pressure levels, which were found to be almost entirely reversible upon decompression.

These scenarios were then brought together to inform novel conclusions about the degradation and ageing behaviour of lithium-ion cells under dynamic conditions. Information gained from these studies provide the foundations for further examination of the effects of dynamic operational conditions.

Acknowledgements

Firstly, I thank my supervisor, Professor Harry Hoster for guiding me through my PhD and for providing me with many exciting and interesting opportunities over the past four years. I am immensely grateful for the knowledge, guidance and inspiration that he has given me throughout. It has been a pleasure to work under his supervision.

I would also like to thank Dr Peter Keil, who has taught me an enormous amount about the field. I am extremely appreciative of the approach and attitude towards research that he has instilled in me.

To the Hoster group at Lancaster University, who have always provided invaluable guidance and support throughout. My special thanks go to Dr Alana Zulke, Dr Mike Mercer, Dr Kenneth Nwanoro, Dr Mangayarkarasi Nagarathinam, Steve Wrigley, Dr Yi Li and Dr Violeta Gonzalez-Perez. I will never forget the memories shared over the past four years. It has been a pleasure to work with them all.

To the staff at the Lancaster University Chemistry Department, in particular, Professor Joe Sweeney, Dr Kathryn Toghill, Dr Abbie Trewin and Steve Holden for their support, help and encouragement over the past four years.

A special thanks goes to the friends I made in Lancaster, especially Dhruv, Shahin, Cindy and Sophie for all the amazing company, fun and memories throughout my PhD.

To my friends from home: Ben, Jamie, Lewis, Nick, Leon, Alex and Abed, who have always provided the laughs and the unwavering friendship, no matter the situation. A big thanks also to Imi for sharing this time with me and for always being supportive. She has continuously brought a real sense of fun, and I am enormously thankful for that.

To my Grandparents and family, who have always provided invaluable support and guidance. Their kindness, encouragement and advice has continuously given me inspiration throughout life and during my PhD.

Finally, to my parents, who have always been with me through the highs and lows of the past four years. I cannot express how much their support and advice has helped me progress throughout my life and during my PhD, and for that I am forever grateful.

Contents

List of Tables

List of Figures

List of Abbreviations and Acronyms

AC	Alternating Current
BoL	Beginning of Life
CC	Constant Current
CCCV	Constant Current Constant Voltage
CDA	Capacity Difference Analysis
CEP	Charging Endpoint
CT	Charge Transfer
CV	Constant Voltage
DC	Direct Current
DEP	Discharging Endpoint
DRT	Distribution of Relaxation Times
DVA	Differential Voltage Analysis
EIS	Electrochemical Impedance Spectroscopy
EoL	End of Life
EV	Electric Vehicle
FEA	Finite Element Analysis
GEIS	Galvanostatic Electrochemical Impedance Spectroscopy
GITT	Galvanostatic Intermittent Titration Technique
HLD	Homogeneity of Lithium Distribution
ICE	Internal Combustion Engine
LIB	Lithium-Ion Battery
LLI	Loss of Lithium Inventory
OCV	Open Circuit Voltage
SEI	Solid Electrolyte Interphase
SoC	State of Charge

List of Appendices

1 Introduction

1.1 Motivation

Over the past few decades, lithium-ion batteries (LIBs) have facilitated the expansion of the digital world in a way that far surpasses previous expectations. LIBs have become the energy storage device of choice in many consumer electronics because of their favourable properties such as a high energy density and adjustable form factor. Moreover, the current stance on the internal combustion engine (ICE) and the drive to reduce greenhouse emissions has led the automotive industry to look at alternative energy solutions, which has birthed the new age of electric vehicles (EVs)[1–4].

The original concepts of an energy storage device that functions like present day LIBs (reversible intercalation) were first conceived in the late 1970s[5]. This was further developed in the 1980s[6,7], but it wasn't until 1991 that Sony created a practical form of this technology. Since then, numerous breakthroughs and policy decisions[8] have propelled the industry into what it is today, where giga-factories produce vast quantities of high performance cells[9] and LIBs are at the core of our everyday life. Advancements in materials, usage strategies and battery modelling have enabled EVs to reach ranges in excess of 400 miles and last 10 or more years of daily use[10]. However, the price of LIBs must fall to be competitive with the ICE, as it currently remains the most expensive component in modern-day EVs[11]. A dependable and more substantial charging infrastructure, in addition to reducing fears of reliability and safety, must also be present to convince vehicle users to switch from the convenience and comfort of the ICE.

Aside from these factors, environmental harmony, lower production costs and higher energy densities are just some of the crucial matters that must be addressed moving forward. The latter of these is typically achieved through advancements in the materials of the anode, cathode and electrolyte. For example, graphite remains the anode material of choice for its dependability and stability, but doping of the active material with silicon (oxides) and other compounds is an exciting prospect for the future[12]. Moreover, high nickel content cathode materials have bred the next generation of high-energy cells with even greater outputs, leading them to achieve widespread penetration into the EV market[13]. Increasing demands of the outputs of LIB cells by both the manufacturers and the consumers is not without its downfalls, however. Greater volumes of lithium (de)intercalation at faster rates induces damaging stresses upon the battery components, both electrochemical and mechanical, that degrade the cells in new ways that had not been observed previously[12,14]. Even under non-operation conditions, the high electrochemical potentials that current cathode materials achieve creates internal environments that propagate reactions only detectable on minute scales and with precise examination of cell variables[13,15]. Therefore, in conjunction with research towards new materials, it is essential that the specific ageing behaviour and optimisation of new-age LIBs is examined and developed during both operation and storage conditions. Because the opportunity to examine cell post-mortem comes only at the very end of a cell's life, the ageing trends that emerge during operation must be analysed using non-destructive techniques. Knowledge gained during this process will undoubtedly benefit the operation, application and design of future batteries to reduce degradation and extend cell life.

1.2 Purpose

The lifetime of LIBs is often a highly dynamic affair, with periods of heavy usage intertwined with periods of open circuit storage and rest at varying states-of-charge (SoC). Experimentally, studies are typically segregated into what are known as calendar and cycle ageing studies, which examine the individual effects of each type of ageing. These types of studies remain fundamental in expanding our understanding of cell behaviour and have progressed the field enormously over the past decades. However, it is also important to examine the influence of extended calendar periods on subsequent use and operation of LIBs, as the life of a cell is naturally much more varied than this[16]. For

Robert Burrell - January 2022

example, long storage periods may occur when cells are shipped across the globe before operation and when EVs are parked, which is typically 90% of the time[13]. It is not currently well understood what influence these periods will have on the subsequent performance during extended use and whether cells will exhibit an ageing path dependence as a result of previous history[17].

Aside from the natural storage periods that arise throughout a cell's life, the intentional use of storage periods during cycling can yield important information about the reversible losses that occur during battery ageing[18,19]. Because such losses can influence the apparent degradation rate of LIBs, it is crucial to identify the ageing conditions in which these processes occur. With that, reversible and irreversible losses can then be separated and quantified, thus leading to more accurate battery state-of-health (SoH) and lifetime predictions.

The dynamic environment surrounding LIBs not only concerns their usage patterns, but also the external pressures present throughout their life. The drive to reduce weight in many applications forces manufacturers to pack more cells into tighter spaces, often with a reduced structural stability of the casing that encloses the battery components. Because LIBs are composed of multiple components, each with their individual compressibilities, the effects of external forces are complex and varied[20]. This is reflected in the literature, which presents a multitude of pressure application methods and ageing outcomes, both positive and negative, of the effect of pressure on LIBs[21]. Greater understanding of the underlying effects are therefore essential, and to achieve this, the problem must be approached systematically. A lack of a standardised pressure rig design may naturally lead to inconsistencies in the experimental outcomes between studies due to pressure inhomogeneities. It is therefore imperative that this issue is addressed before progressing to electrochemical testing.

As previously mentioned, the external pressures LIBs experience often vary substantially over time. It is therefore important to observe the reversibility of the measured electrochemical effects of pressure upon its release, which requires measurements that are performed in a static environment in the absence of cycles. Cycling is an important and vital part of the electrochemical testing of LIBs, but the complex interplay of processes may obscure the underlying effects of pressure. Simple, static electrochemical measurements may shed light on the more fundamental impacts of pressure on battery

performance. The findings from this may provide some foundations for use in the interpretation of data in further study.

1.3 Outline

This primary focus of this work is to experimentally investigate the degradation and electrochemical response of LIBs under various operating conditions. The ageing of lithium-ion cells in their respective conditions is therefore examined to gain a deeper understanding of the underlying processes and degradation mechanisms. Because the operating conditions of LIBs are varied and dynamic throughout their life, representative individual scenarios must be examined separately to identify and distil the fundamental electrochemical responses.

This work is divided into the following chapters, which is represented in Figure 1
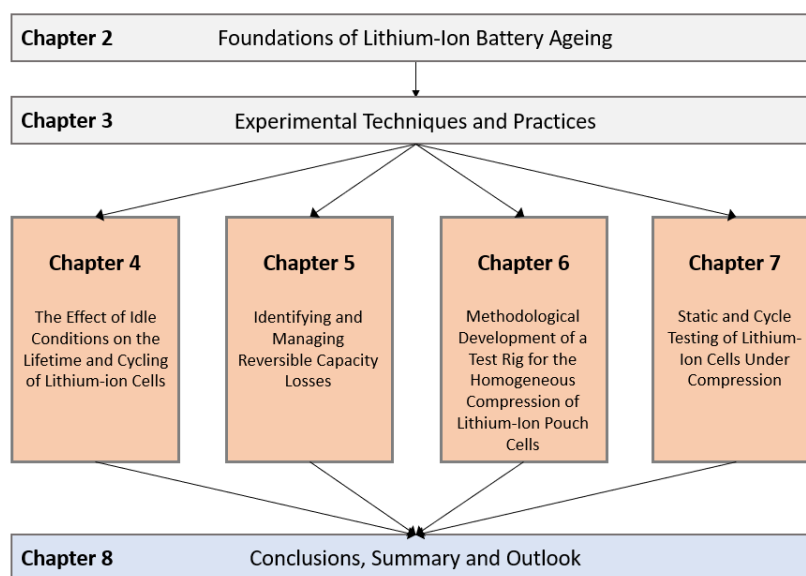
Figure 1. Flow diagram and thesis overview highlighting each chapter.

The following provides an overview of the chapters presented in this thesis.

Chapter 2: Foundations of Lithium-ion Battery Ageing

This chapter provides an introduction to the fundamental electrochemical concepts of lithium-ion LIBs, with a focus on battery ageing. The individual components of a cell, and the specific degradation that can arise for each, are described in detail based on reports in the literature. In addition, typical experimental usage patterns, such as cycle and calendar ageing, are presented and discussed, along with the unique ageing mechanisms that come with each. Finally, the definitions and ramifications of reversible capacity losses are introduced.

Chapter 3: Experimental Techniques and Practices

This chapter provides descriptions of the experimental methods and practices, along with details of the lithium-ion cells and equipment used throughout this thesis. The degradation monitoring and analysis techniques that enabled the examination and evaluation of data are also presented.

Chapter 4: The Effect of Idle Conditions on the Lifetime and Cycling of Lithium-Ion Cells

A long-term experiment containing both calendar and cycling measurements was performed on cylindrical commercial cells. Initial calendar ageing experiments were executed to separate and identify the degradation effects that occur in commercial lithium-ion cells during extended calendar storage periods. Cells were then cycled to examine the long-term effects that calendar storage periods have on cycling and to observe whether an ageing path dependence exists. These experiments employed a variety of techniques to track and observe degradation mechanisms, which ultimately informed new and important usage strategies for the long-term use of commercial lithium-ion cells.

Chapter 5: Identifying and Managing Reversible Capacity Losses

The primary focus of this chapter was to identify and manage reversible capacity losses that can occur during electrochemical cycling. Cells were operated in restricted voltage

windows and the reversible capacity losses were tracked through short-term storage periods at defined SoC. This study employed a number of analysis techniques to monitor irreversible and reversible degradation, whilst proposing novel methods for the tracking of battery ageing.

Chapter 6: Methodological Development of a Test Rig for the Homogeneous Compression of Lithium-Ion Cells

An analysis and appraisal of pressure test rig designs from the literature was carried out to test their effectiveness at applying uniform pressure. The key objective from this was to design a test rig capable of providing a homogeneous pressure distribution to lithium-ion pouch cells of diameters larger than 3 cm, which had not yet been reported in the literature. Existing designs were evaluated using finite element analysis (FEA) simulations, which were subsequently experimentally validated. The custom rig design from this study was to be used for all subsequent experiments involving the application of pressure to lithium-ion cells.

Chapter 7: The Reversible Compression Testing of Lithium-Ion Cells

To examine the effect of pressure on LIB pouch cells, multiple compression tests were performed. Static compression testing, in the absence of cycles, was performed to observe the instantaneous and direct effects of pressure on the performance of LIBs. In addition, the reversibility of the measured changes after decompression of cells was examined and the timescales of the reversibility was reported. The second half of the study explored the effect of pressure on the extended cycling performance of cells at three pressure levels, which provided a benchmark to assess the cells' response against those from the literature.

Chapter 8: Summary, Conclusion and Outlook

A short summary and conclusions of the results, including a projection of future work to be carried out, which builds upon the findings presented in this thesis.

2 Foundations of Lithium-Ion Battery Ageing

In this section, an overview of lithium-ion battery (LIB) composition and ageing is presented. Because LIBs suffer from capacity loss and increasing internal resistance during operation and storage, it is important to outline the degradation mechanisms by which ageing occurs.

In addition to battery ageing mechanisms, the fundamentals of battery testing routines such as cycle and calendar ageing are also discussed. These concepts will provide the foundations for battery testing throughout this thesis.

2.1 Lithium-ion Battery Composition and Operation

Figure 2 displays the key components of a LIB along with the fundamental electron and Li^+ movement during charge and discharge. LIBs are generally comprised of a negative and positive electrode, termed the anode and cathode, respectively, with a separator sandwiched between them.

The anode is typically comprised of a carbon-based active material adhered to a copper current collector[22]. Graphite is characteristically used as the active material host structure in many LIBs due to its low lithiation potential (0.2 V vs Li/Li^+), its developed stability and favourable gravimetric energy density (372 mAh g^{-1}). More recent efforts have turned to the development of graphite-silicon (oxide) composites due to their vastly enhanced energy density, though their implementation is not without significant hurdles[1,23]. Opposing the anode is typically an aluminium foil coated with a transition metal oxide active material, such as lithium iron phosphate (LFP) or lithium manganese oxide (LMO). More recently, high nickel content materials such as nickel manganese cobalt (NMC) and nickel cobalt aluminium (NCA) are favoured in electric vehicles (EVs) due to the higher energy density densities that can be achieved[15,24,25]. Separating the two electrodes is the

polymer separator, which prevents the anode and cathode from touching, but permits ionic transport between the two[26]. The battery is then filled with an electrolyte consisting of organic solvents, a conductive salt and various additives for improving battery performance[27].

In the discharged state of a cell, almost all lithium is intercalated in the cathode active material. During charging, an external current is supplied to the system and the lithium is oxidised at the cathode. The lithium then migrates through the electrolyte and separator and intercalates between the graphite planes at the anode where it is reduced. During discharge, the reverse of this process occurs[28].
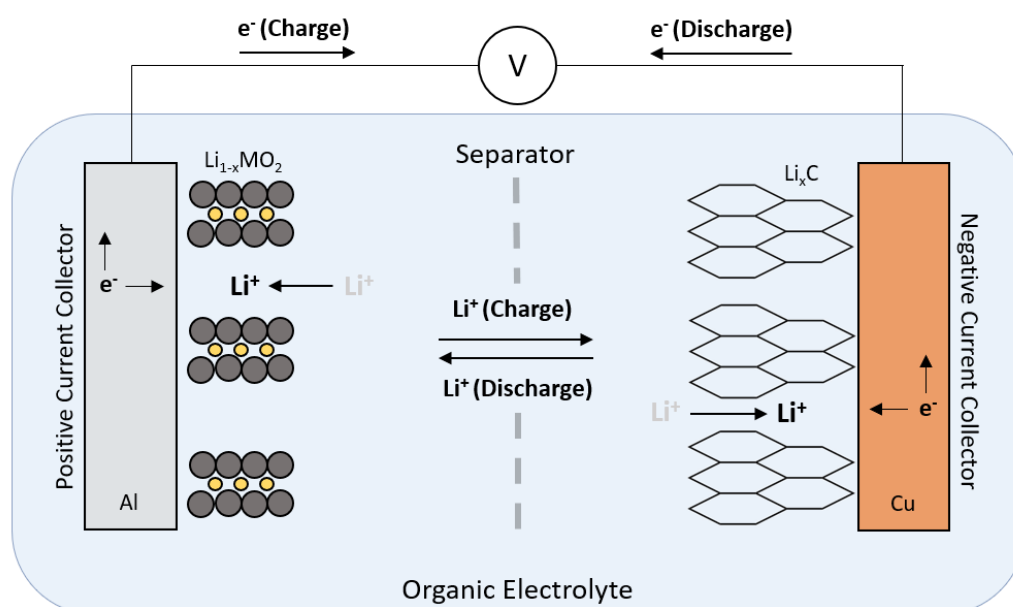
Figure 2. Key components of a lithium-ion battery with annotations of the flux of electrons and Li+ ions during charge and discharge.

2.2 Battery Component Ageing and Degradation

Throughout their operation and storage, the constituents of LIBs suffer degradation through irreversible side reactions. Environmental and operational conditions can aggravate such reactions, leading to effects such as capacity fade and a rise in internal resistances. This section will detail the various locations and processes of degradation within LIBs. The cells used throughout the experimental testing in this thesis possessed

graphite/graphite-silicon oxide anodes and NMC/NCA cathodes, and thus will be the focus of this section.

2.2.1 Anode

Graphite has been largely been adopted at the primary active material for the anodes of LIBs due to its favourable performance[1]. However, the growth of passivation films, mechanical stress and the deposition of metallic lithium are ongoing issues[14,29]. Moreover, the addition of silicon oxides can enhance the performance of LIBs, but at the expense of exacerbated side reactions[30].

2.2.1.1 Graphite

Growth of Passivation Films

Arguably the most regular and ongoing form of degradation at the anode is the growth of passivation films on the surface of the graphite active material, commonly known as the solid electrolyte interphase (SEI). The SEI is formed from the irreversible electrochemical decomposition of the electrolyte at the electrode surface[31]. This reaction consumes lithium, in competition to the electrochemical intercalation of lithium and arises due to the thermodynamic instability of the electrolyte at the operation potentials[13,32]. The reaction products form a passivating layer that is impenetrable to electrolyte molecules and is electrically insulating, but permeable to lithium ions. Because of this, further electrolyte reduction and lithium consumption is reduced as the SEI thickens; a process that has been reported to have a linear dependence with the square root of time[33]. Nevertheless, lithium is continuously consumed by SEI growth which results in capacity fade, whilst electrolyte decomposition reduces ionic conductivity and increases internal resistances. Moreover, this is exacerbated by the ongoing volume fluctuations and mechanical stresses that expose new surface of the active material to the electrolyte[14].

The composition of the reaction products has been shown to vary substantially and depends largely on the additives in the electrolyte[34,35]. An ideal SEI should contain insoluble and stable inorganic compounds such as Li_2CO_3, however, metastable organic

compounds such as ROLi and $ROCO_2Li$ are also typically produced[36,37]. Species produced during reactions at the cathode can also influence the composition of the SEI at the anode and will be discussed in a subsequent section.

In more extreme cases, the copper foil current collector can suffer oxidation-dissolution reactions due to high electrode potentials (~3.5 V vs Li/Li$^+$) during over-discharge[38]. Poor adhesion of the active material to the current collector can then contribute to substantial capacity fade through loss of active material. Moreover, the dissolved copper species can then deposit onto electrode surfaces which blocks intercalation sites and further reduces capacity[39].

Mechanical Degradation of the Active Material

Graphitic active materials also suffer degradation due to the mechanical stress exerted during intercalation/deintercalation. The intercalation of lithium in between the graphite planes can result in an expansion of the graphite layers by up to 10%[40]. The repeated motion of this expansion/contraction during electrochemical cycling may ultimately lead to the propagation of micro-cracks along grain boundaries of the polycrystalline graphite[41]. The extent of cracking within the active material is related to the current density (cycling rate)[41]. In addition, solvent co-intercalation, gas evolution and electrolyte reduction with the graphite exacerbate particle cracking and can lead to a rapid deterioration of the electrode[42]. Moreover, extensive cracking can lead to the irreversible expansion of the graphite particles during cycling, which increases the total volume of the active material. In constrained LIB geometries, such as in cylindrical cells, this increased volume will amplify the pressures within the electrode stack. Significant amounts of particle cracking may also lead to the electrical isolation of the particle if it detaches from the surrounding particles, which reduces the available capacity of the anode.

The expansion/contraction and cracking of the active material may also fracture the SEI structure and expose new surfaces of the graphite to the electrolyte[43]. New SEI is formed at the expense of irreversible cyclable lithium loss, which reduces the cell's capacity[44]. At the end of extended cycling, particularly after high cycling rates, the SEI will be substantially thicker and significantly contribute to both capacity fade and increases in internal resistance.

Lithium Plating

Lithium plating refers to the deposition of metallic lithium on the surface of the anode and can cause a sudden onset of non-linear ageing[45]. It is formed during the reduction of lithium ions at the surface of the graphite; a reaction that is not naturally competing with lithium-ion insertion as the intercalation potential is typically higher than that of deposition[29]. During charging, a deviation from equilibrium, known as polarisation, can drive the anode potential below 0.0 V Vs. Li/Li$^+$, at which point lithium deposition is thermodynamically feasible[29,46]. This polarisation can arise due to factors such as ohmic drop and limitations with charge transfer and solid-state diffusion, which is demonstrated in Figure 3. For instance, such barriers will require higher Li$^+$ local concentrations in the electrolyte to achieve a given galvanostatic current. The same increased Li$^+$ concentration will then also be in contact with less passivated electrode areas, where it will allow for Li metal deposition (Nernst equation). The onset and rate of lithium plating is therefore dependent on environmental and operational factors; low temperatures, high charging currents and high SoCs all increase the rate of lithium metal deposition. Moreover, a low anode/cathode ratio and manufacturing defects can also influence the propensity for lithium plating[47–49].

Deposited lithium on the surface of the anode can also reintercalate back into the host material, if electrical connection remains[50]. Plated lithium can be observed as a voltage plateau under open circuit conditions, which occurs due to the coexistence of graphite (0.8 V Vs. Li/Li$^+$) and lithium metal (0 V Vs Li/Li$^+$), however this may disappear after a length of time due to reintercalation[51]. Deposited metallic lithium may also react with the electrolyte, which reduces the cyclable lithium content and thus the capacity.
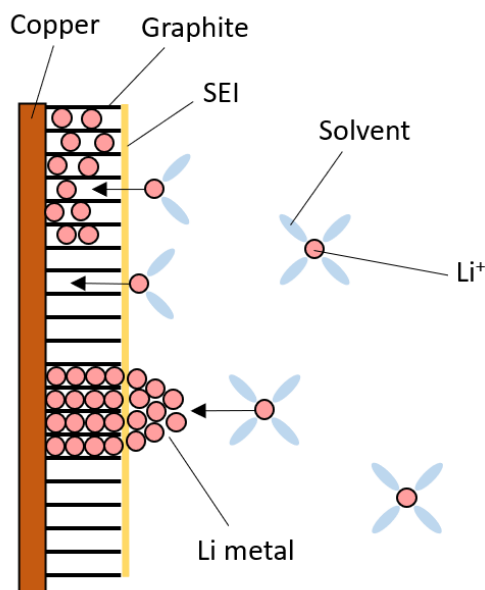
Figure 3. Diagram displaying the solid-sate diffusion limitations that can lead to lithium plating. Less lithiated regions of the graphite lead to intercalation of lithium into the host material.

2.2.1.2 Silicon Oxide

Silicon and silicon oxides have been identified as promising candidates for anode materials in future LIBs and are typically implemented as a composite with graphite (typically less than 10 w.t.%). The attraction of silicon largely arises due to its substantially higher theoretical capacity (3578 mAh g^{-1}) when compared with graphite (372 mAh g^{-1})[1]. Along with the aforementioned degradation mechanisms of graphite, silicon suffers substantial volume fluctuations (~300%) upon lithiation/delithiation[52–55]. These volume swings pulverise both the silicon particles and the electrode as a whole, which dramatically breakdown the SEI layer to cause a rapid increase in SEI growth and lithium loss[12]. This is demonstrated in Figure 4: expansion/contraction of the Si upon lithiation/delithiation produces cracks in the SEI layer that expose new electrode surfaces to the electrolyte.
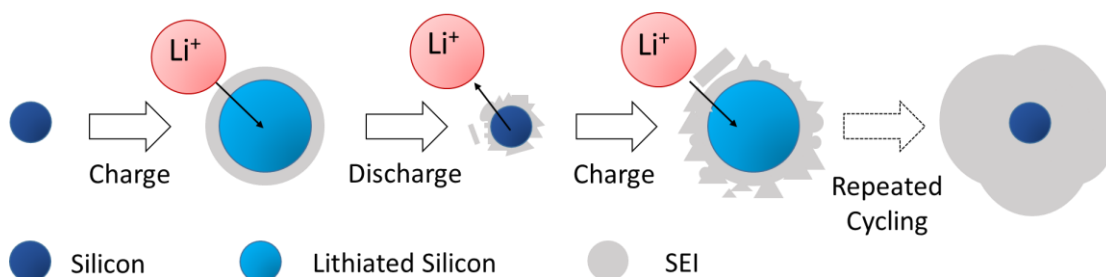
Figure 4. Schematic highlighting the effect of the lithiation and delithiation of Si on the SEI layer. Repeated cycling leads to greater breakdown and reformation of the SEI.

Silicon oxide species (SiO_x) suffer reduced volume fluctuations (160%) compared to elemental silicon (300%) but the mechanism still remains a significant issue compared to graphite[30]. Silicon oxides also bear a low initial coulombic efficiency due to the formation of irreversible lithium silicates upon the first lithiation, which requires 608 mAh g^{-1}.

$$4SiO + 4Li^+ + 4e^- \rightarrow 3Si + Li_4SiO_4 \tag{1}$$

$$Si + xLi^+ + xe^- \leftrightarrow Li_xSi \tag{2}$$

The lithium silicates then remain inactive during the subsequent delithiation, however the remaining Si is free to reversibly alloy with lithium[1] (equation 2). It is the higher density of Li_4SiO_4 compared to $Li_{3.75}Si$ that effectively limits the volume fluctuations of silicon oxides. Moreover, silicon oxides naturally have a low electrical conductivity which reduces the electrochemical activity of the active material[30].

The polymer binders used in silicon-containing graphitic anodes typically contain lithiated carboxylates that are introduced through aqueous processing. This introduces a trace water content into the system that hydrolyses $LiPF_6$ present in the electrolyte to produce HF acid[56,57]. Although having a relatively benign effect on graphite, the HF can vigorously react with Si and SiO_2 to severely hamper LIB performance.

2.2.2 Cathode

Cathode active materials suffer degradation throughout the life of LIBs as a result of various environmental and operational conditions. The gained improvements in reversible

capacity by using nickel-rich layered materials is offset by the degradation of active material. This section presents an overview of cathode degradation within lithium-ion cells, with a particular focus on NCA and NMC, which are used throughout this thesis.

Transition Metal Dissolution

Layered transition metal oxides can suffer dissolution of the constituent metals, leading to a decline in performance of LIBs. In particular, the manganese present in cathode active materials is particularly prone to dissolution[58–60], however, cobalt and nickel have also been reported[61]. Dissolution is aggravated by high cathode potentials and elevated temperatures, which can ultimately lead to structural instability of the host material.

Metal species dissolved at the cathode can migrate through the electrolyte and react at the anode. Mn and Ni have been previously observed as a contaminant in the SEI, further aggravating degradation of the passivating layer[59,61]. In addition, the dissolved metal species may occupy vacancies in the cathode host structure, leading to a restriction of the Li diffusion pathways[62].

Structural Degradation

Battery ageing can lead to a degradation in the mechanical stability of the host structure, which results in capacity and power fade within the cell. In NMC cathodes, a phase transformation from a rhombohedral to a spinel structure can occur at the surface of the particles. With more extreme cut-off voltages, the formation of rock salt phases can increase the charge transfer resistance of the material[63]. Doping nickel-cobalt oxides by partially substituting Ni by aluminium has shown to increase the stability of the host structure by reducing lithium nickel disordering, however, the inactivity of Al^{3+} reduces the reversible capacity [64].

NCA cathode materials suffer from the formation of an NiO-like layer with a rock salt structure on the surface of the primary particles[65]. NiO possesses a poor conductivity to both lithium ions and electrons and thus forms a resistance layer that increases charge transfer resistances[24]. Restricting the depth-of-discharge (DoD) during cycling has shown to significantly improve stability and performance, even at elevated temperatures of

$60^{\circ}C$[65]. NCA undergoes irreversible phase transformations above 55% delithiation that leads to a distortion of the lattice structure and irreversible capacity fade[24].

Volume changes during intercalation/deintercalation, particularly at high and low SoC, introduce mechanical stresses into the bulk active NCA material. Repeated cycling introduces micro-cracks at the inter-surface between primary particles, leading to crack propagation and the formation of secondary particles[65,66]. Pulverisation of the active material can lead to a loss of electrical contact and particle isolation of the active material which aggravates capacity fade and impedance increase[67].

The release of singlet oxygen has been detected in layered transition metal oxide cathode materials at SoCs above 80%[68]. The highly reactive singlet oxygen has been proposed to readily react with the electrolyte to form CO and CO_2 species. Newly formed CO_2 at the cathode can then be reduced at the anode in a shuttle mechanism that can subsequently induce a reversible self-discharge[68,69].

2.2.3 Electrolyte

The degradation of the electrolyte is highly dependent on the additives incorporated during the manufacturing process[70]. As mentioned in the sections prior, decomposition reactions frequently occur at the anode/cathode surface and in the bulk electrolyte. Decomposition of the conductive salt ($LiPF_6$) as a result of water impurities has been detected by the presence of DFP and POF_3 in tested samples, reducing the ionic conductivity of the electrolyte and increasing the ohmic resistance of the cell[71,72].

The primary solvent decomposition reaction is the polymerisation of ethylene carbonate (EC) at the anode surface during the formation of the SEI[71,73]. The development of this reaction with electrolyte additives, particularly in the initial few cycles, is highly influential on the subsequent performance of the LIB. The oxidation of electrolyte components can also be observed at the cathode. For example, CO_2 gas evolution, particularly in the presence of $LiCO_3$, is aggravated at high temperatures and SoC[74]. The CO_2 can result in the drying-out of local electrode regions[75] and play a role in self-discharge shuttle mechanisms that promote a reinsertion of lithium back into the cathode[13].

2.2.4 Separator

The separator is crucial in maintaining function of LIBs; however, it is not immune from degradation. Separator membranes subjected to mechanical loads can succumb to pore deformation that limits lithium diffusion pathways and increases cell impedance[76], even below the polymer's melting point[77]. Deformation has been found to be highly dependent on loading direction, where the mechanical properties in the extrusion (longitudinal) direction are superior to the lateral (transverse) direction[77].

The products of decomposition reactions of $LiPF_6$ have been shown to non-uniformly deposit on the surface of the separator, leading to increases in local ionic impedance[42,78]. Non-uniform blocking of the pores can lead to non-uniform current densities, and ultimately, lithium plating and the formation of dendrites[79]. If dendritic growth continues, the separator may be penetrated, and a short circuit may occur. If cell temperatures reach values high enough, intended separator deformation may occur (shutdown) and significantly hinder ionic transport through the membrane[79].

2.3 Experimental Battery Ageing

Experimental ageing tests on LIBs are typically divided into two key categories: cycle ageing and calendar ageing. The former largely consists of the application of a current load and cyclical repetitions of charges and discharges, whilst the latter consists of storing the cells at defined SoCs and temperatures[80,81]. This section will describe the fundamental designs of each and detail the key conditions that influence specific battery ageing.

2.3.1 Cycle Ageing

Cycle ageing studies involve the operation of LIBs that include repeated charge/discharge procedures[16,51,80]. The controlled parameters are often the charge/discharge currents, the charge/discharge cut-off voltages, depth-of-discharge (DoD), and the operation temperature[82,83]. Repeated cycling is demonstrated in Figure 5, where blocks of cycles are typically sandwiched between reference performance tests (check-ups) that periodically measure the battery's performance, however, check-ups are not always used.

Whereas the voltage limits and charge/discharge currents are allowed to vary for each test condition during cycling, all cells are typically subjected to identical check-up routines for equal comparison.
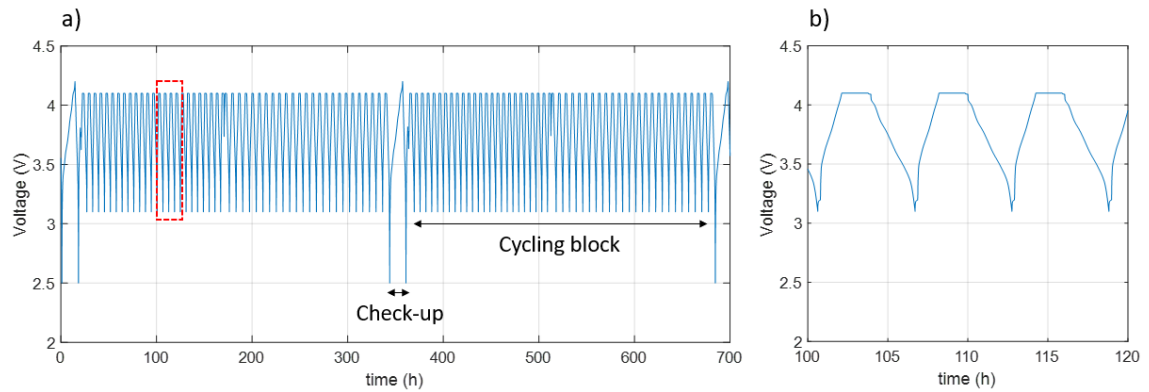
Figure 5. (a) Voltage Vs. time during a cycle ageing study that displays cycling blocks sandwiched between check-up routines. (b) expansion of the red square in a) that highlights individual cycles.

With respect to battery ageing, high charge/discharge currents, high average voltage, high/low temperatures, and large voltage windows are all expected to accelerate cell degradation[49,84,85]. In conjunction with lithium transport limitations, high charging currents can lead to lithium plating, electrolyte decomposition and SEI breakdown to result in rapid capacity fade and resistance rise. If large quantities of deposited lithium react with the electrolyte, then non-linear capacity fade may ensue[86]. A high average cell voltage corresponds to higher cathode and lower anode potentials, and promotes a greater rate of side reactions within the cell. Moreover, high temperatures also improve the kinetics of such reactions and increase the rate of capacity fade.

2.3.2 Calendar Ageing

Calendar ageing is the degradation of LIBs under non-operating conditions, typically in an open circuit. Cells primarily degrade through electrolyte oxidation/reduction and the formation of surface films at either electrode, which are aggravated by high storage temperatures and SoCs[13,74,87]. The approximate rates of such reactions are dependent on

the specific chemistry of the battery[88]. Surface film formation, particularly at the anode, dominates the total loss of cyclable lithium and has shown growth with a square root of time dependence. Capacity fade is typically highest in the initial months, followed by a stagnation in the rate of capacity decline[13].

To periodically measure battery ageing, check-up procedures are used at set time intervals, as demonstrated in Figure 6. Moreover, additional methods of investigation are often used, such as electrochemical impedance spectroscopy (EIS)[89].

Calendar and cycle ageing are not mutually exclusive; calendar ageing occurs at all times during a LIB's life, even during operational periods. Disentangling the processes and damage that occurs due to one or the other is a significant challenge, although their relative contributions are said to add in a linear fashion[32,90]. Furthermore, a path dependence of previous ageing history on the subsequent outcome of ageing tests has been established, however, further exploration of the multitude of outcomes and dependencies needs to be pursued[17,91].
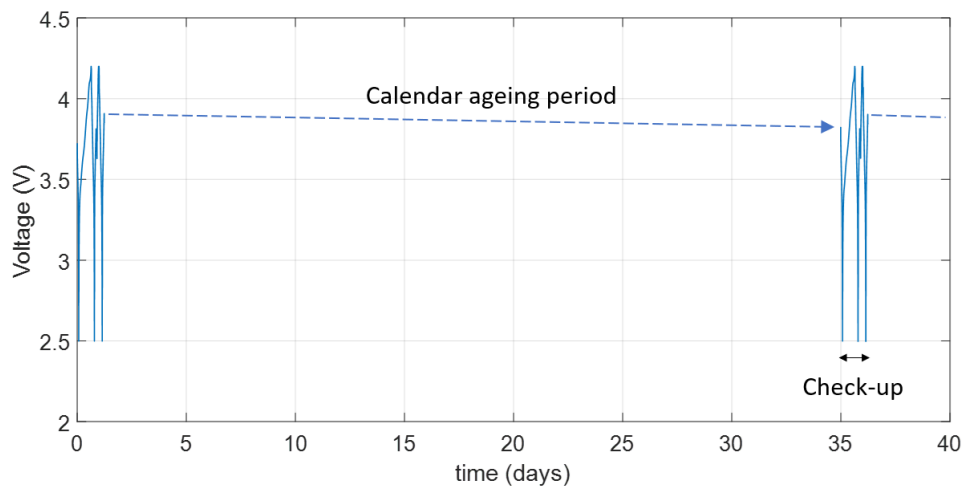
Figure 6. Voltage Vs. time during a calendar ageing study that displays OCV periods sandwiched between check-up routines. Dotted arrows resemble the voltage trace during calendar storage.

2.3.3 Reversible Capacity Effects

Not all capacity loss within LIBs is irreversible, some exhibit reversible losses that may influence experimental ageing rates[19,92,93]. Reversible capacity loss is capacity (lithium) that is inactive in the short term but can be recovered under specific conditions. Its origins can be ascribed to multiple processes: anode overhang, inhomogeneous lithium distribution, formation of covering layers on the anode's surface, temperature gradients and pressure gradients[19]. Under certain operational and environmental circumstances, some lithium may not be immediately accessible during charge and discharge.

The anode overhang regions are the passive regions that do not have a direct cathode counterpart, as the anode is oversized compared to the cathode to prevent lithium plating at the edges[94]. These regions can only take part in charge/discharge very slowly, therefore they can act as a lithium sink or lithium source when lithium diffuses into or out of these regions, respectively. Lithium that diffuses to these regions reduces the cyclable lithium content, and the discharge capacity is reduced. However, under certain storage conditions, this lithium can be recovered to increase the cyclable lithium content and thus increase the discharge capacity[18]. For inhomogeneous lithium distributions, localised regions of highly delithiated states may prematurely trigger the discharging cut-off voltage to give a lower discharge capacity[95].

2.3.4 Effects of Compression on Lithium-ion Cells

LIBs frequently experience pressures throughout all areas of their life, from calendar pressures in manufacture and processing, to stack pressure in battery packs. Previous work has demonstrated the effects of compressive loads on LIB performance, however the inherently complex nature of mechanical and electrochemical interactions has led to contradictory and ambiguous results across the literature[2,21,76,96–98]. Low levels of external compression has shown to reduce capacity fade by minimising electrode layer delamination that can cause a separation of the active material from the current collectors from the formation of gas by-products. Moreover, externally applied pressure has increased the capacity of aged cells by up to 15%, but without any significant effect on

fresh cells[98]. Similarly, a study that applied a range of pressures (0.66 – 1.98 MPa) to single-layer pouch cells observed an optimum pressure of 1.32 MPa that the extended cycle life by limiting the reduction of cyclable lithium[21]. On the other hand, low level pressures in a prismatic cells have been found to increase the rate of capacity fade compared to cylindrical cells with identical chemistry and materials[99]. The lower stack pressures permitted an increased swelling of the anode active material which reduced ion access and hindered electrochemical kinetics during cycling. Electrochemical impedance spectroscopy (EIS) has also been employed to couple electrochemical and mechanical effects. Pore deformation of the separator was found to reduce the rates of electrochemical reactions due to impeded kinetic and mass transport processes in compressed pouch cells[76].

It is evident that multiple discrepancies exist in the literature. No single outcome has been pinned to the effect of pressure on the ageing of LIBs. Moreover, another inconsistency between studies is the test rig design and method of pressure application. No standardised set-up has been described for this avenue of research, which is an inherent issue when comparing studies.

2.4 Conclusions

To summarise, studies presented in the literature have extensively studied the electrochemical processes that occur during battery degradation. Experimental ageing studies presented in the literature are typically divided into calendar and cycle ageing but are often performed separately or in parallel. In reality, cells are typically stored for extended periods of time before operation, such as storage in a warehouse or during shipping. Therefore, it is important to examine the effects of extended storage at different SoCs on the subsequent cycling of cells. From this an apparent ageing path dependence may be identified, where is it has been suggested that cells possess a predisposition for ageing according to their previous history. This path dependence has been identified in the literature; however, it requires further exploration.

Another interesting area of research is the study of both irreversible and reversible losses. The literature presents a handful of studies which observe and quantify this behaviour, with reversible capacity losses being particularly dominated by the effects of the anode

overhang. It has been established that these passive overhang regions can act as a lithium sink during operation, which reduces the observed capacity during operation. To further identify the impact that these regions have on the outcome of cycling experiments, additional studies must be performed. To what extent can these regions influence the outcome of cycling, and what methods can we use to detect the effects?

As is evident from the presented literature on the compression of LIBs, no conclusive effect of pressure on ageing has been identified, and many studies contradict previous works. In addition, the test rig used to apply pressure can vary substantially between studies, both with design and method of pressure application. Two key areas of exploration are identified. Firstly, it is crucial that a test rig capable of providing a uniform pressure distribution is created and that a standardised approach to pressure application is defined. Secondly, the effect of pressure on both static electrochemical testing and cycle ageing needs to be observed, where static testing is defined as testing in the absence of cycles. The primary focus of studies presented in the literature is typically on the cycle ageing of cells, however it may be beneficial to distil the more direct effects of pressure on both capacity and resistance. By studying the fundamental and more instantaneous effects of pressure on cell parameters through static testing, a better understanding of its effects may be achieved.

To approach the aforementioned opportunities, experimental ageing studies combining both cycle ageing and calendar (storage) ageing are presented in this thesis. Initially to aid identification of an ageing path dependence, then to explore the irreversible and reversible capacity losses. In addition, a pressure test rig capable of applying uniform pressure is designed using key successful elements of design rigs from the literature. The product of this is then to be used for the electrochemical testing of LIBs under compression during both static and extended cycling tests.

3 Experimental Techniques and Practices

The underlying aims of the studies presented in this thesis are to identify and track the key degradation mechanisms occurring as a result of a different operating conditions. To achieve this, non-invasive electrochemical testing is performed to obtain key cell parameters throughout ageing. Well-established techniques, such as capacity measurements, current step response analysis and differential voltage analysis (DVA), current step response analysis and electrochemical impedance spectroscopy (EIS) are considered reliable and robust. Using these techniques effectively requires a detailed understanding of their fundamental principles. This section will provide detail of the key understanding behind the techniques, which is then used in the subsequent chapters to interpret the data presented in this thesis. In addition, descriptions of the tested LIBs and experimental practices are presented, which form the foundation for all subsequent experimental ageing studies.

3.1 General Experimental Information

3.1.1 The Lithium-ion Cells Studied

3.1.1.1 Samsung 35E3

The lithium-ion cell used in Chapter 4 and Chapter 5 in this thesis was an 18650 commercially available cell from Samsung, with product number INR18650-35E3. This high-energy cell is comprised of an NCA cathode and a graphite-silicon composite anode and possesses a standard discharge capacity of 3.35 Ah. Due to consistently achieving 3.40 Ah during initial testing, 3.4 Ah was used as the value to describe the discharge capacity of these cells. Additional information including the key cell parameters can be found in Table 1.

Table 1. Key information and parameters of the Samsung 35E3 cell

Manufacturer	Samsung
Product number	INR18650-35E3
Cathode chemistry	NCA
Anode chemistry	Gr-Si (2 w.t.% Si)
Standard (rated) discharge capacity	3.35 Ah
Charging cut-off voltage	4.2 V
Nominal voltage	3.6 V
Discharging cut-off voltage	2.5 V
Max. charging current	2.0 A
Max. discharging current	8.0 A (continuous), 13.0 A (non-continuous)
Initial internal impedance	35 mΩ (+/- 0.32%)

Due to Samsung being a highly reputable and sophisticated manufacturer of lithium-ion cells, a high reproducibility in output is expected from cells of the same batch. However, it is still imperative to carry out initial batch screening tests to determine deviations and outliers of the mean capacity. Figure 7 displays the absolute discharge capacities and distribution of capacities calculated from a constant current (CC) discharge for 178 cells of the same batch. The mean discharge capacity for all 178 cells was calculated to be 3.40 Ah, with a standard deviation of 0.011 Ah, which equates to 0.32% of the total capacity. Furthermore, a narrow distribution of capacity is seen with these cells in Figure 7b; only 2/3 cells show a poor capacity within the batch. Without these outliers, the standard deviation would drop to ~0.2% of the total capacity. The standard deviation in resistance calculated from direct current (DC) pulse measurements was found to be 0.32% of the total resistance.
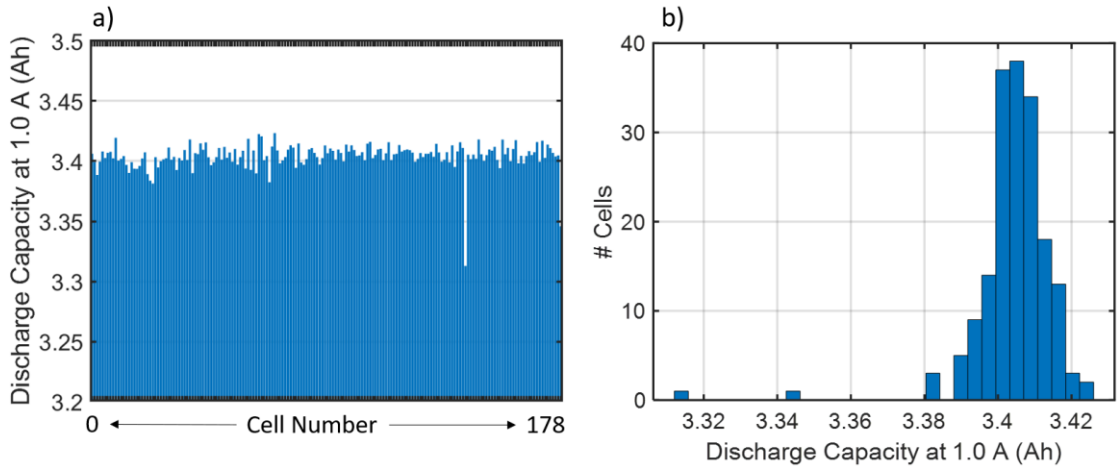
Figure 7. (a) Absolute discharge capacities and (b) distribution of discharge capacities for 178 Samsung 35E3 cells of the same batch.

3.1.1.2 LiFun 2051A0

In chapter 7, the tested cell was a LiFun 2051A0 pouch cell, with a graphite anode chemistry and a nickel-manganese-cobalt ($LiNi_{0.8}Mn_{0.1}Co_{0.1}O_2$) cathode chemistry, as provided by the manufacturer. Additional information on the LiFun cell can be found in Table 2.

Table 2. Key information and parameters of the LiFun 2051A0 cell.

Manufacturer	LiFun
Product number	2051A0
Cathode chemistry	NMC811
Anode chemistry	Gr
Standard (rated) discharge capacity	0.15 Ah
Charging cut-off voltage	4.2 V
Nominal voltage	3.8 V
Discharging cut-off voltage	3.0 V
Max. charging current	Not specified
Max. discharging current	Not specified

Initial internal impedance	411 mΩ (+/- 5.43%)

The rated capacity is >0.15 Ah, however 0.135 Ah was found to be the measured capacity during batch testing, which is presented in Figure 8. The standard deviation for the capacity of the LiFun cells was found to be 0.0015 Ah (=1.13% of total capacity). All C-rate values in this this thesis were calculated relative to 0.135 Ah. The standard deviation for resistance was found to be 5.43% of the total resistance with outliers removed. The voltage limits are defined as 4.2 V – 3.0 V and were not exceeded during testing. No current safety limits were provided by the manufacturer, however current rates were kept within 1.5C.
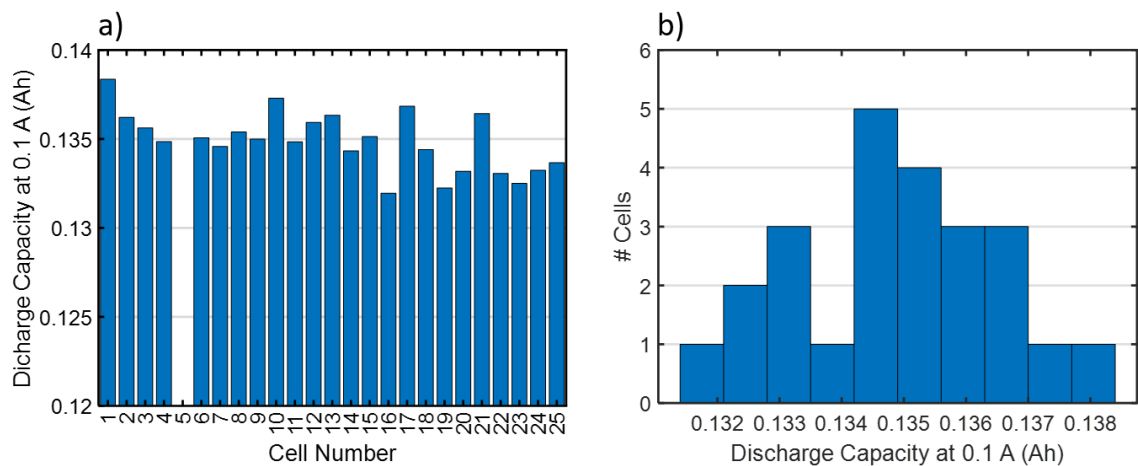
Figure 8. (a) Absolute discharge capacities and (b) distribution of discharge capacities for 25 LiFun 2051A0 cells of the same batch. Cell 5 displayed a capacity of 0.00 Ah.

3.1.2 Equipment Used

Two battery testers were used to obtain the data presented in the subsequent chapters. All electrochemical cycling and static testing of the lithium-ion cells was carried out on Basytec CTS battery test systems with multiple ±5 A/6 V channels. Electrochemical impedance spectroscopy (EIS) and galvanostatic intermittent titration technique (GITT) measurements were carried out on a Biologic BCS 815 system.

All cell testing was conducted in thermal chambers to ensure a stable thermal environment during ageing, as fluctuations in temperature can create large differences in measurable output. Memmert IPP260 Plus, Espec PU-2J, Binder MK240 and Novonix Peltier Cooled Thermal Chambers with accuracies of 0.1°C, 0.3°C, 0.5°C, 0.5°C respectively, were used. All cycle-aged cells in the same experimental dataset were tested in the same thermal chamber at the same time, i.e., cells of the same study were not aged in separate thermal chambers at the same time. This ensured that all cells experienced the same thermal environment throughout their life and thus reduced temperature-induced variations.

3.1.3 Half-Cell Fabrication

Prior to opening, each 18650 cell was fully discharged to 2.5 V with a CV hold of 10 h. Anode and cathode material was punched out to give 19 mm (diameter) discs in and assembled with 16 mm (diameter) lithium metal disks from Xiamen Tob New Energy Technology. The electrolyte used was 1.0 M $LiPF_6$ in 50/50 (v/v) ethylene carbonate and dimethyl carbonate from Sigma Aldrich and glass fibre from Whatman (grade GF/F) was used as a separator. Coin cells were rested for 24 hours for sufficient wetting of the active materials before three C/25 cycles on a Biologic BCS 815 system at 25°C in an Espec PU2J thermal chamber. All half-cell fabrication was carried out by Dr. Mangayarkarasi Nagarathinam.

3.2 Experimental Procedures and Definitions

This section provides an overview of the key experimental procedures and definitions that are core to the studies presented in this thesis.

3.2.1 Check-up Routine

In battery ageing studies, periodic reference performance tests ('check-ups') under identical conditions are vital for the comparison of cells with different ageing protocols. Using an identical check-up routine for cells within the same ageing study allows for a more direct comparison between cells, as they are scrutinised under the same voltage

limits, applied currents and charge/discharge steps. Two similar forms of check-up were used in this thesis, which are depicted in Figure 9 below. Although the current and voltage values may differ depending on the different types of cells used, the main structure remained the same over all experiments. The values given in Figure 9 and the description that follow are for the Samsung 35E3, however the LiFun cells used an identical check-up routine to Figure 9b, but with different operational parameters. The shaded regions indicate the various stages of the check-up which highlight the different electrical tests conducted. Figure 9a shows the first version of the check-up, which is split into 3 key stages. Stage I is a 0.25 A (low current) charge for DVA, stage II is a 1.0 A constant current (CC) discharge for discharge capacity measurements and stage III contains 3.0 A discharge pulses for resistance measurements. Version 2 of the check-up, shown in Figure 9b, differs only with an addition of an extra stage. Stage III is now a low current (0.15 A) discharge step for DVA and capacity difference analysis (CDA), whilst stage IV contains the 3.0 A discharge pulses for resistance measurements (identical to stage III Figure 9a). All check-ups throughout this thesis were performed at 25°C.
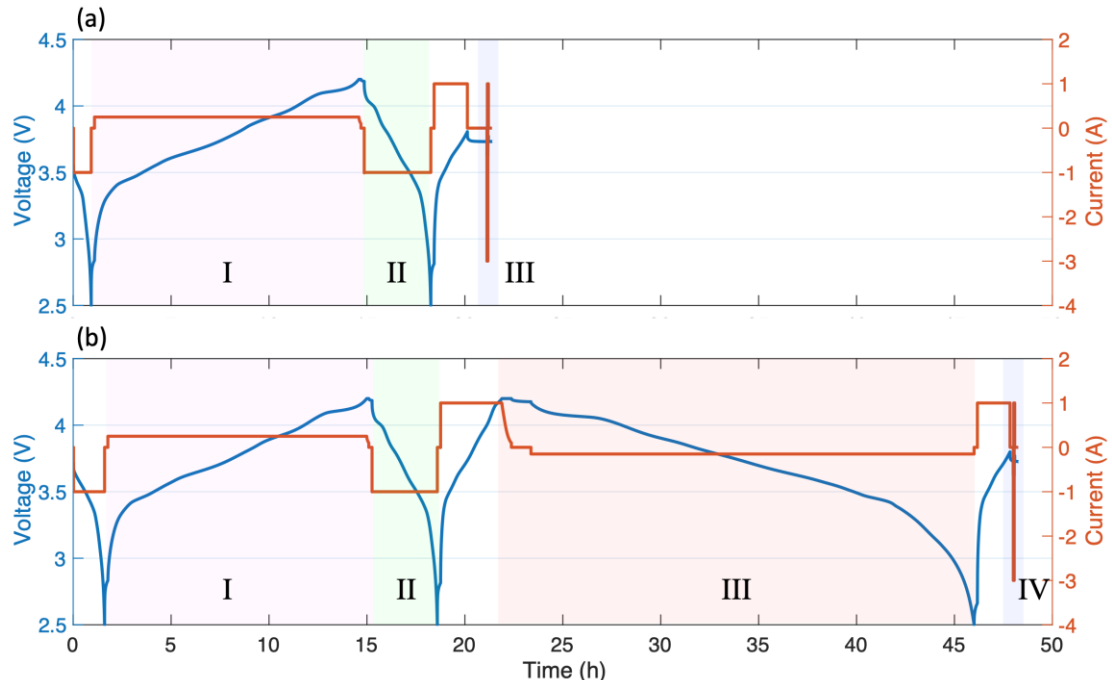
Figure 9. Voltage and current traces during the check-up procedure showing (a) version 1 with the 3 stages and (b) version 2 with the addition of a low current discharge.

3.2.2 Charging and Discharging

Constant current (CC) charging and discharging is a simple and common method used to either charge or discharge a lithium-ion battery. The rate at which a cell is CC charged or discharged is typically quoted as the C-rate, which is the capacity of the battery (in Ah) divided by the applied CC current (in A).

LIBs have predefined terminal voltage limits, which are the maximum and minimum voltage that should be measured at the terminals. These are termed the charging cut-off voltage and the discharging cut-off voltage, which are 4.2 V and 2.5 V, respectively, for the Samsung 35E3 cell. Here, the terminal voltage is the difference between the individual electrode potentials (+ an IR component with an applied current), where each electrode potential is a function of the lithiation degree of a given electrode. These limits must not be exceeded during charging/discharging to prevent unwanted degradation and to ensure the safe operation of the battery.

Figure 10 displays the voltage profile for the anode, cathode and full-cell during the charge of the Samsung 35E3 cell from 2.5 V to 4.2 V. At these maximum voltage limits, it evident that the theoretical maximum degree of (de)lithiation has not been reached for either electrode. The individual electrodes are kept within permissible degrees of lithiation to prevent unwanted side reactions that can occur if these limits are breached. For example, if the full-cell charging cut-off voltage is exceeded, then the anode potential may dip below 0.0 V vs. Li/Li^+, which can cause lithium plating[29].

The voltage limits governing the full-cell charging and discharging cut-off voltages therefore stem from the individual electrode potentials at the end of charge and discharge. The value of the charging cut-off voltage is prescribed by the rising potential of the cathode, which prevents further delithiation of the cathode and reduces degradation to the lattice structure[100]. This is observed in Figure 10 when approaching 100% SoC. At the other end towards 0% SoC in Figure 10, the full-cell discharging cut-off voltage is defined by the steeply rising anode potential, as further delithiation of the anode can lead to dissolution of the copper current collector[101].
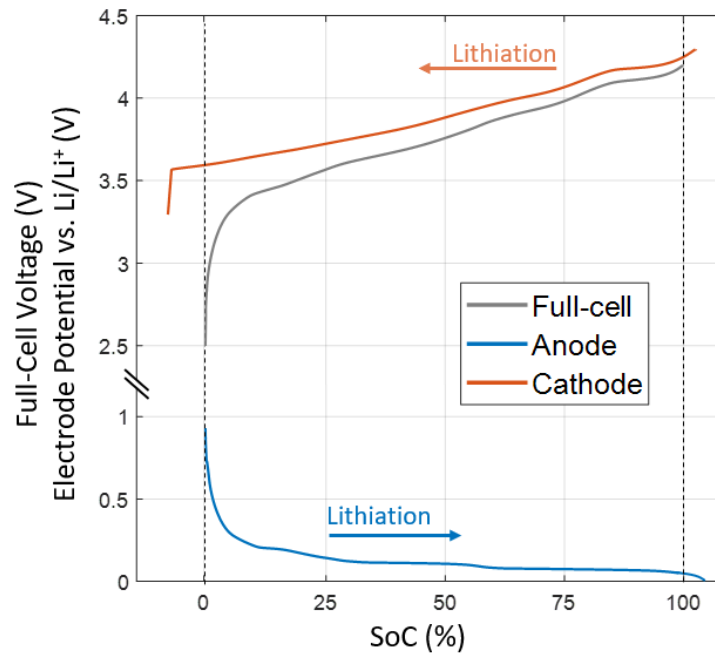
Figure 10. Voltage profile of the full-cell, anode and cathode of a Samsung 35E3 18650 during a charging sequence. The SoC x-axis is in reference to the full cell, from which the degrees of lithiation of both electrodes can be observed.

The voltage measured at the terminals of the full-cell is not solely based on the difference between the two electrode potentials, it has an additional IR component calculated by ohms law:

$$V = I \times R \tag{3}$$

Therefore, the measured terminal voltage is as follows[102]:

$$v(t) = OCV\big(z(t)\big) - I(t)R_0 \tag{4}$$

Where v is the terminal resistance, (t) denotes continuous time, OCV is the open circuit voltage, z denotes state-of-charge (SoC), I is applied current and R_0 is the series (ohmic) resistance. Thus, the terminal voltage is comprised of the open circuit voltage (as a function of SoC) and the applied current multiplied by the internal resistance of the cell.

The current remains constant during CC charging/discharging; hence the internal resistance has a strong influence on the measured voltage of the cell. Because the resistance can be influenced by changes in environmental temperature, it is imperative to carry out battery testing at a controlled, constant temperature. Reductions in temperature

cause increases in the resistance due to the kinetic hinderance of processes such as (de)intercalation, which is demonstrated in Figure 11a. This can augment the ohmic drop contribution to the measured voltage, which is demonstrated during the discharge sequence in Figure 11b. The result is an apparent downward shift (red vertical arrow) of the entire voltage curve to produce a lower average voltage value. What this means is that, at the end of discharge, the discharging cut-off voltage is reached sooner and less capacity can be extracted (red horizontal arrow).
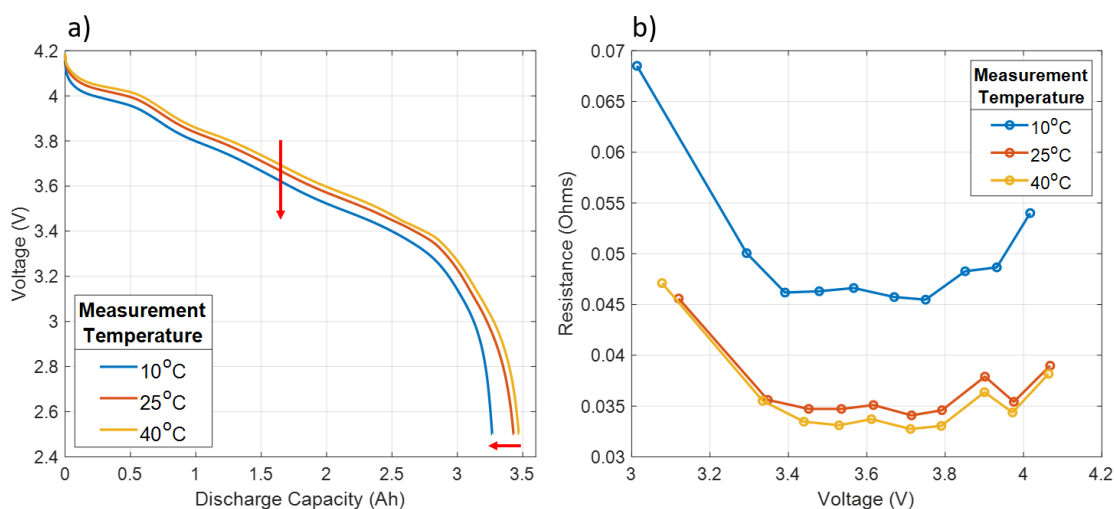
Figure 11. (a) discharge capacity plots demonstrating the effect of lower temperatures on discharge capacity and average voltage. (b) The internal resistance as a function of cell voltage at different temperatures.

During charge/discharge, an additional constant voltage (CV) step can be introduced after the CC step to give what is known as constant current constant voltage (CCCV) charging. A simple graphical representation of this is presented in Figure 12. After a CC step, concentration gradients of lithium within the cells are present, thus if the charge or discharge step terminates here, the voltage relaxes to a point below/above the desired voltage and the cell is not fully charged/discharged. The CV step after a CC charge/discharge maintains the target cell voltage, whilst the current is permitted to fall to a predetermined current cut-off value, typically 1/10th the applied current. This CV step promotes the dispersion of the lithium concentration gradients and the desired SoC can be more accurately achieved.
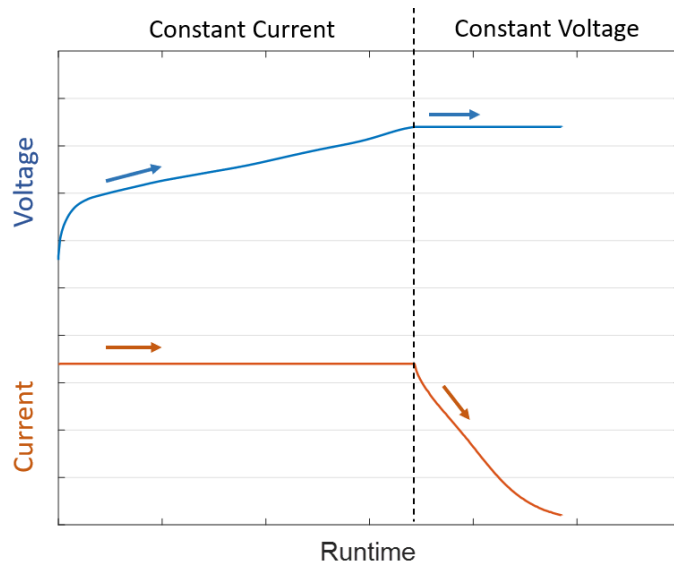
Figure 12. Graphical representation of a CCCV charging sequence. The dashed line represents the point at which the sequence switches from CC to CV.

A CCCV charging scheme and a CC discharging scheme was used throughout all cycling presented in this thesis. An open circuit voltage (OCV) rest periods were employed at the end of each charge/discharge sequence, with a duration of 10 minutes unless otherwise stated. During check-up procedures, CCCV charging and CC discharging was used throughout and all discharge capacity values were calculated after a CC discharge.

3.3 Current Step Response for Resistance Calculation

The time required to set-up and run electrochemical impedance spectroscopy (EIS) measurements throughout cycling studies means its implementation is not always practical. The calculation of the internal resistance by use of a current step response is a rapid and simple method for obtaining resistance values during cycling studies as the cells do not need to be disconnected from the battery test systems.

A battery's voltage response to a step in the applied current can be used to calculate DC resistance. Since lithium-ion batteries exhibit multiple time constants for the various processes that occur within a cell, the current step duration can strongly influence the calculated resistance values[103,104]. Increasing the length of the step will incorporate additional time constants into the total resistance value, which increases the calculated

resistance. This means separation of the contributions towards the total resistance is difficult, unlike in EIS, which is a favoured method for separation.

Based on previous reports employing discharge pulses to determine internal resistance[105–107], 10 s DC discharge pulses were used during all check-ups presented in this thesis. Additional pulse lengths were used for specific purposes in experimental investigations, but are stated at the point of use. A pulse of this length will likely contain ohmic, SEI transport, charge transfer and partial diffusion resistance contributions[104]. Unless otherwise stated, 1C discharge pulses were used through this thesis, which provides a sufficient response from the cell without inducing degradation or significant heating.

Figure 13a and Figure 13b displays the current and voltage profiles, respectively, during a 10 s discharge pulse. Using the current and voltage values obtained from the last datapoints before the discharge pulse and the last datapoints during the discharge pulse, the DC internal resistance, R_{DC}, can be calculated as follows:

$$R_{DC} = \frac{V_{10\,s} - V_{0\,s}}{I_{10\,s} - I_{0\,s}} \qquad (5)$$

The values for I_0 and V_0 are always taken as the final data points at the end of the rest period (no applied current) before the discharge pulse (applied current). This aims to minimise the error introduced by the sampling rate, as a variation in I_0 and V_0 may be present if the values are taken as the first data points in the discharge pulse sequence.
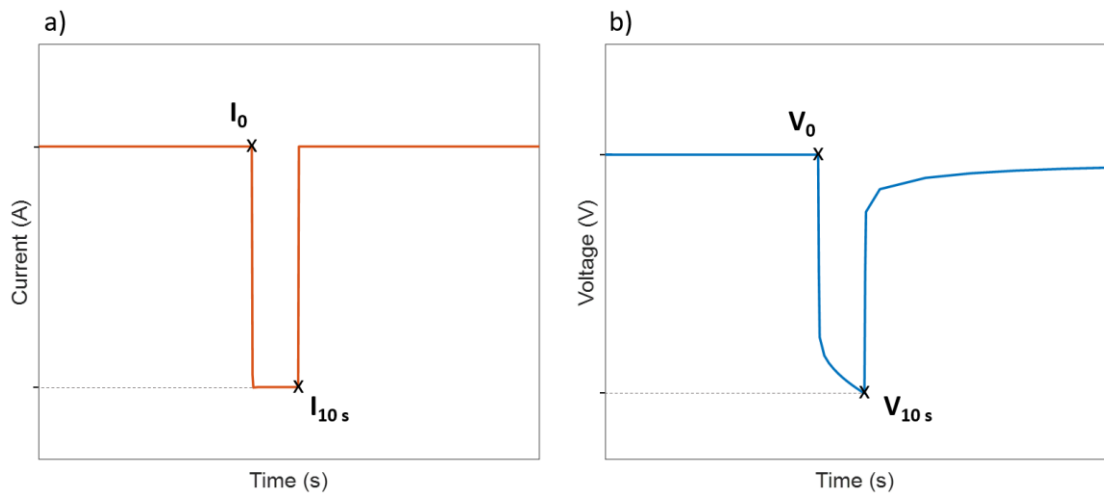
Figure 13. (a) Current and (b) voltage trace during a 10 second discharge pulse for internal resistance calculation.

The pulse resistance method is not without its limitations and inaccuracies, however. In addition to its inability to resolve different time constants, it is also highly sensitive to environmental conditions, such as temperature and SoC. To minimise such influence, temperature was thus kept constant throughout each experimental ageing study and discharge pulses were performed at 50% SoC during check-ups. Accurate SoC values were calculated during each check-up by determining the total remaining capacity of the cell in the previous full discharging step. This ensures that ageing-based capacity drifts are mitigated and that the DC resistance measurements are recorded under identical conditions through each ageing study. The current step response method can then provide a sufficient indication of the evolution of internal resistance.

3.4 Galvanostatic Intermittent Titration Technique (GITT)

GITT is an electrochemical analysis technique that is used to calculate the diffusion coefficients of anode and cathode active materials. Starting from a fully charged or discharged state, the half-cells are subjected to a series of discharge/charge pulses with a prescribed relaxation time under OCV conditions in between each pulse. The relaxation time must be sufficient enough for the lithium concentration gradients within the cell to disperse and for the cell to reach towards an equilibrium state. This state is known as the OCV. Due to a range of pulse currents, pulse lengths and relaxation times being used in the GITT measurements in this thesis, the specific parameters for each experimental test will be described at the point of mention.

All diffusion coefficients presented in this thesis were calculated using Sand's approach[108,109]. Using the Sand's equation, the time-related evolution of lithium concentration at the particle surface can be described by

$$C_{surf} = c_0 + 2\frac{I}{SF\sqrt{D_s\pi}}\sqrt{t} \tag{6}$$

where c_{surf} is the particle surface concentration, c_0 is the initial (rest) concentration, I is the applied current, S is the surface area of the electrode-electrolyte interface, F is

Faraday's constant D_s is the diffusion coefficient and t is time since the beginning of the applied current pulse. In GITT, the voltage is measured instead of the direct measurement of the concentration, and given that the variation the particle surface concentration is small, the voltage can be linearised to give

$$V = U(c_0) + (c_{surf} - c_0)U'(c_0) - R_{IR}I \tag{7}$$

where U is the OCV as a function of concentration, U' is its derivative and R_{IR} is the cell's internal resistance. Combining equation (6) and (7) gives

$$V = U(c_0) - R_{IR}I + 2\frac{U'(c_0)I}{SF\sqrt{D_s\pi}}\sqrt{t} \tag{8}$$

thus, the voltage evolves as $\sqrt{t}$. To calculate the diffusion coefficient, the coefficient in front of $\sqrt{t}$ is fitted for each pulse and the fitted value is termed m_{fit}. The diffusion coefficient can then be calculated as

$$D_s = \frac{4}{\pi}\left(\frac{I}{FS}\frac{U'(c_0)}{m_{fit}}\right)^2 \tag{9}$$

All diffusion coefficient calculations were performed on a MATLAB package provided by Dr Ferran Brosa Planella[109].

3.5 Charge and Discharge Endpoint Tracking (Coulomb Tracking)

The loss of lithium can be observed during calendar ageing by the use of the coulomb tracking method[81]. This examines the slippage of the charging and discharging endpoint from the periodic check-ups during ageing. This method has the advantage of being able to track the endpoints, but without the need to keep the cells connected to a battery test system.

First, all measurement data is ordered chronologically. Because during OCV storage no charge flows into or out of the cell, the change in charge balance always remains zero between measurements. However, the current integration may be susceptible to drifts due to small offset errors in the current measurement when the cells are not connected to a

battery test system during long-term storage, which is observed in Figure 14b. To overcome this, a continuous Ah balance is generated, which uses the last Ah value from a given measurement as an offset for the subsequent measurement, which is demonstrated in Figure 14c. The continuous Ah balance is then used to track the slippage of charging and discharging endpoints. Tracking of the endpoints of a specific charge (charging endpoint – CEP) and discharge (discharging endpoint – DEP) sequence throughout ageing can provide an insight into the side reactions occurring at either electrode[81,110].
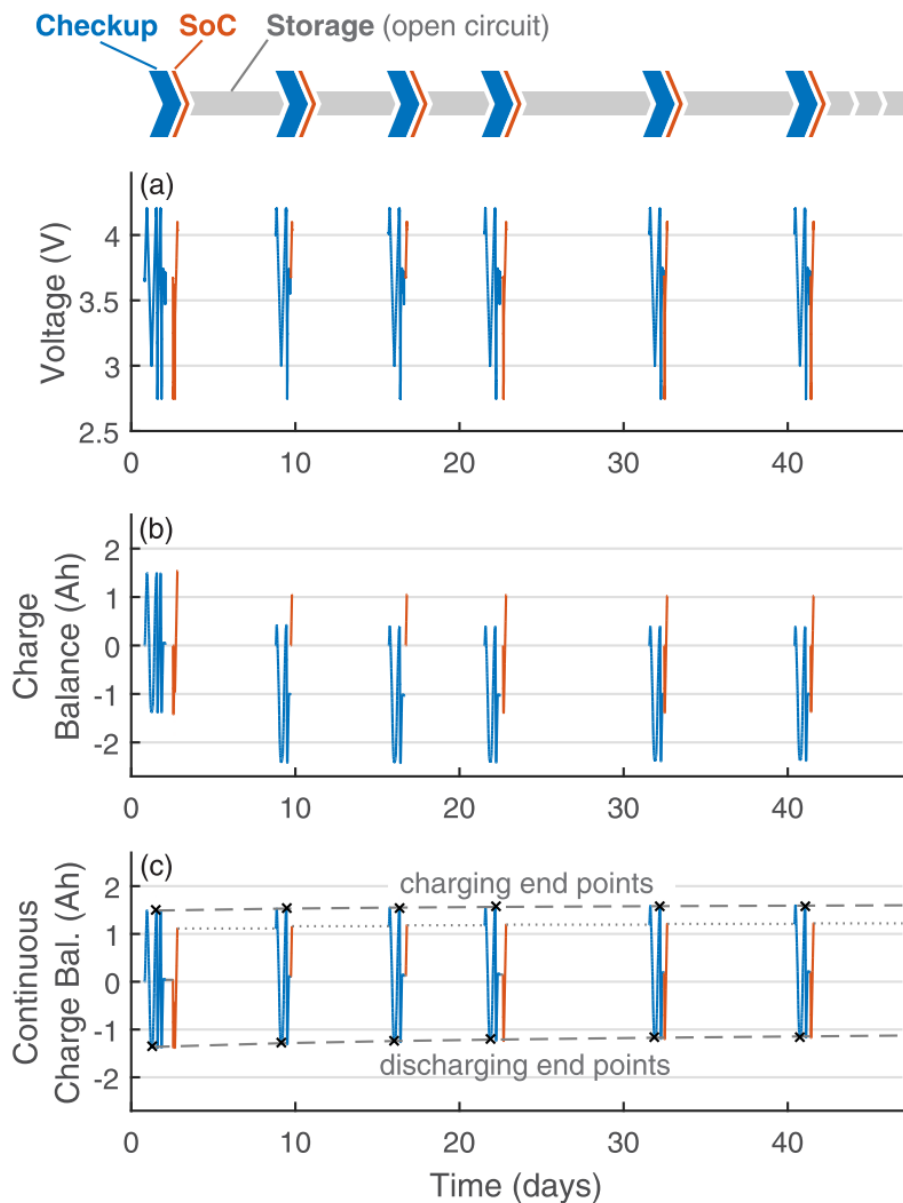
Figure 14. Graphical representation of the coulomb tracking method. (a) Repetitive check-up test sequence, which brings cells to a specific SoC, (b) charge balances of the individual check-up measurements, (c) continuous charge balance

after post-processing, where final ampere-hour value of each check-up measurement is used as an offset for the subsequent test measurement[81].

Side reactions that occur at the anode are generally attributed to SEI growth and electrolyte reduction, whilst side reactions at the cathode are generally related to electrolyte oxidation and transition metal dissolution. This changes the lithiation degree of each electrode during storage, which causes an internal shift in the anode/cathode half-cell curve. This shift is then observed as a change of the charge/discharge endpoint.

Interpretation of endpoint plots can be explained through examination of Figure 15 below, which is an extract from a publication by Zulke et al. Here, the charging endpoints (CEP) and discharging endpoints (DEP) are plotted over time for cells calendar aged at multiple SoCs and temperatures. Here, $C_{eff} = CEP - DEP$. With no side reactions or self-discharge, the CEP and DEP would remain unchanged. A self-discharge in the absence of capacity fade would mean a cell delivers fewer electrons during a given discharge than were moved from cathode to anode during charging. This would result in the CEP and DEP moving in a positive direction, but whilst maintaining the same distance. Electrochemical side reactions occurring at the anode cause a certain amount of Li^+ to become irreversibly added to the continuously growing SEI layer, instead of being reversibly intercalated into the anode. In this case, the discharging procedure would finish sooner than would be expected, based on the amount of charge consumed during charging. Thus, the CEP and DEP can be used to provide information occurring at either electrode. This is demonstrated in Figure 15, where steeply rising CEPs and DEPs, particularly at higher SoCs and temperatures, indicate a greater rate of self-discharge within the cell. Moreover, DEPs are expected to increase at a greater rate due to the increased loss of Li due to SEI growth[13].
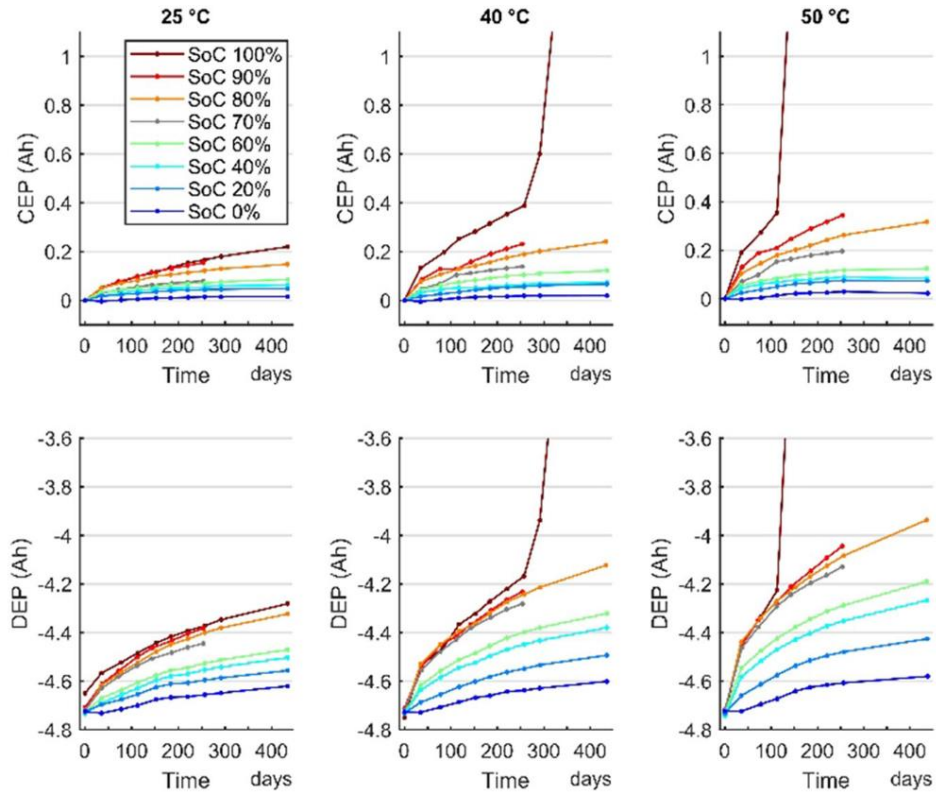
Figure 15. Endpoint slippages for charging (CEP - top row) and discharging (DEP - bottom row) as a function of storage SoC and at three different temperatures[13].

3.6 Coulombic Efficiency

Coulombic efficiency (CE) is defined as the ratio of charge extracted from the anode during delithiation divided by the charge transferred to the anode during lithiaton. Through accurately tracking the charging and discharging endpoint capacities during cycling, the consumption of Li can be measured[35,44,111]. CE is calculated by dividing the capacity extracted during discharge by the capacity extracted during the preceding charge

$$CE = \frac{Q_{discharge}}{Q_{charge}} \tag{10}$$

where $Q_{discharge}$ is the discharge capacity and Q_{charge} is the preceding charge capacity[44]. Therefore, a CE close to 1 indicates that less lithium is consumed for a given cycle, as the amount of charge (lithium) put into the anode through lithiation is almost entirely extracted during subsequent delithiation. The main cause for lithium consumption is said to be through solid electrolyte interphase (SEI) growth[35]. Because

the lithium, and thus the charge, consumed per cycle during routine cycling is extremely small, CE values of mass-produced cells are typically >0.999.

The CE can also exceed 1 under certain circumstances. Lithium diffusion from the anode overhang to the active region (and vice versa) can strongly influence the measured capacity during a given charge/discharge. In between periods of cycling, if a cell is stored at an SoC higher than the average cycling SoC, then there will likely be a net diffusion of lithium from the active anode region to the anode overhang region. When cycling is resumed, lithium will then diffuse back to the active region, which reduces the measured charge capacity and inflates the subsequent discharge capacity. According to equation (10), this will result in a CE>1. When a cell is stored at an SoC lower than the average cycling SoC, then the opposite occurs and the CE will be noticeably <1[93].

3.7 Electrochemical Impedance Spectroscopy

3.7.1 Theory

Electrochemical impedance spectroscopy (EIS) is an experimental method used to test not only the resistance of a battery, but the capacitive and inductive behaviour. Electrochemical processes within a cell possess a frequency dependence, which EIS exploits. For galvanostatic measurements, an alternating current (AC) excitation signal is applied to the electrochemical system and the phase shift and amplitude of the voltage is measured[112–115]. For potentiostatic measurements, an alternating potential signal is applied and the resulting current response is measured. The impedance is a frequency-dependant complex number, Z, which is calculated by observing the voltage-current ratio and their phase angle shift, Φ. The complex impedance

$$Z(\omega) = \frac{V(\omega)}{I(\omega)} \cdot e^{j\phi(\omega)} = Z'(\omega) + jZ''(\omega) \tag{11}$$

is derived where ω is the angular frequency ($\omega = 2\pi \cdot f$) of the excitation, Z' is the real part of the complex impedance, Z'' is the imaginary part of the complex impedance and $j = \sqrt{-1}$.

During galvanostatic EIS (GEIS) measurements, a range of excitation frequencies are often explored in a frequency sweep. A typical excitation frequency range for lithium-ion batteries is from multiple kHz down to mHz[116,117], thus the frequency range adopted in this thesis is between 5 kHz to 10 mHz. The impedance of a cell is highly dependent on SoC, so a single GEIS sweep only provides a snapshot of impedance in the available capacity window. To explore the evolution of impedance over the entire SoC window, GEIS sweeps need to be performed at multiple SoCs. This process is time consuming, particularly in the low frequency range.

Figure 16a displays an example Nyquist plot for a GEIS sweep of the Samsung 35E3 cell, highlighting the key contributions to the overall spectrum. Figure 16b displays the electrochemical processes that are commonly assumed to dominate the response at certain estimated frequency regions. The upper part of the EIS spectrum in Figure 16a represents the capacitive behaviour of the cell and is comprised of 3 key electrochemical processes. At low frequencies, a sloping line represents the impediment in mass transport associated with diffusion[103,113]. In the Hz region in the upper part of the spectrum, two semicircles overlap which renders them indistinguishable from one another. These represent the limitations with charge transfer and passivation layers associated with both electrodes[82,117].

The lower part of the spectrum is indicative of the inductive behaviour of the cell. The spiral windings of the jelly roll in the 18650 cell introduce increased inductance when compared to the stacked geometries of pouch and prismatic cells[116,118]. As the jelly roll structure remains largely intact with ageing, the inductive tail only displays minor changes throughout cell life.

The cell behaves like an ohmic resistor when the phase shifts from the capacitive and inductive contributions cancel each other out, which is the point at which the imaginary part of the impedance is zero (intercept). This occurs very close to 1 kHz for this cell and is comprised of resistance contributions from the current collectors, active masses, the contact resistance between them and electrolyte resistance[103].
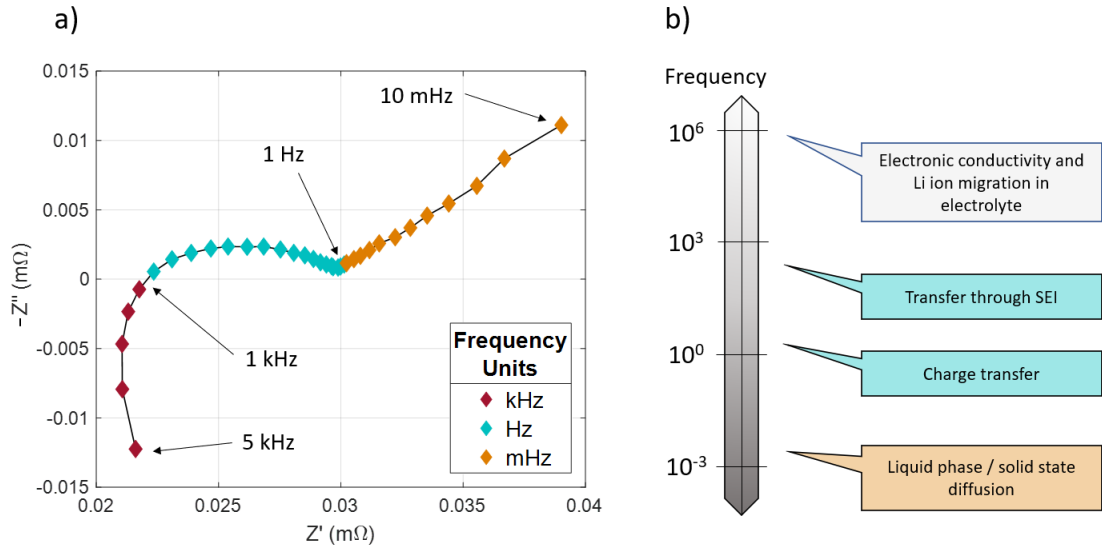
Figure 16. (a) Example Nyquist plot of the Samsung 35E3 cell for a GEIS sweep from 10 mHz to 5 kHz at 50% SoC and 25⁰C with highlighted frequency units, (b) electrochemical processes and their estimated excitation frequency.

3.7.2 Distribution of Relaxation Times

The distribution of relaxation times (DRT) is a method used to deconvolute an impedance spectrum and resolve the time constants associated with the electrochemical processes and is plotted in Figure 17b[116,117,119].
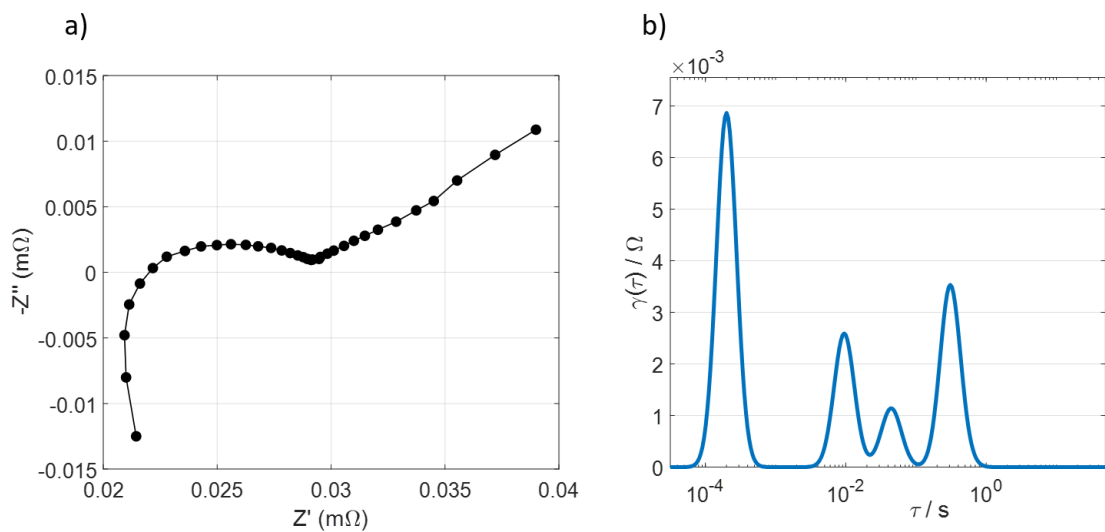
Figure 17. (a) Example Nyquist plot of the Samsung 35E3 cell for a GEIS sweep from 10 mHz to 5 kHz at 50% SoC and 25⁰C, (b) corresponding DRT plot. that separates the time constants.

It uses the assumption that all impedance components can be described by an infinite number of RC elements[117]. A DRT for two ideal processes can be represented by equation (12).

$$Z_{complete} = Z_{RC1} + Z_{RC2} = \frac{R_1}{1+j\omega R_1 C_1} + \frac{R_2}{1+j\omega R_2 C_2} = \frac{R_1}{1+j\omega\tau_1} + \frac{R_2}{1+j\omega\tau_2} \qquad (12)$$

Here, R is the polarisation and τ is the time constant of the corresponding process. τ represents the relaxation frequency or relaxation time of the physical process and is equal to $\tau_i = R_i C_i = 1/2\pi f_i$. In reality, the complex composition of lithium-ion batteries means they possess a distribution of time constants, thus the relation between impedance and DRT can be expressed as

$$Z(\omega) = R_0 + Z_{pol}(\omega) = R_0 + R_{pol}.\int_0^\infty \frac{g(\tau)}{1+j\omega\tau} d\tau \qquad (13)$$

where $(g(\tau)/1+j\omega\tau)d\tau$ provides the fraction of the overall polarisation with the relaxation times between τ and $\tau + d\tau$. R_0 and R_{pol} are the ohmic resistance and polarisation, respectively[117]. With a numerical calculation of DRT, a finite number of RC must be specified, hence the equation becomes

$$Z_{pol} = \sum_{k=1}^{N} \frac{R_k}{1+j\omega\tau_k} \qquad (14)$$

to give the overall polarisation resistance. An inherent issue with using DRT is extracting $g(\tau)$ from equation (14), which is a complex mathematical problem. Therefore, all DRT plots in this thesis were created through the use of a Matlab package, DRTtools[120]. Nevertheless, the time constants for each dominant process can be observed in a DRT plot. This is demonstrated in Figure 17b, which exposes the individual processes that would otherwise be difficult to distinguish in Figure 17a. The processes governing the overlapping semicircles observed in both Figure 17a are now revealed in the DRT plot in Figure 17b. Each peak represents a different time constant present in the EIS spectra. The inductive behaviours of the cell are neglected in this DRT calculation.

3.8 Differential Voltage Analysis

The voltage change with respect to capacity during charge or discharge is formed from the superposition of the individual voltage curves from the anode and cathode. Observing the rate of change of the voltage with respect to incremental increases in capacity can reveal important information about the ageing processes during battery testing and is termed differential voltage analysis (DVA). This non-destructive tool can track changes occurring at the anode, cathode and interactions between the two. The fundamentals and application of DVA will be explained in detail in the following section.

3.8.1 Theory

DVA is a non-invasive and non-destructive analysis technique used to track key degradation mechanisms during battery ageing. The derivative dV/dQ is calculated from the differentiation of a voltage curve from either a CC charge or discharge sequence and is then plotted against capacity[81,121]. A low current during charge/discharge is required in order to obtain sufficient resolution of the peaks in the DVA profile[121]. A low current charging sequence and the corresponding differential voltage plot can be found in Figure 9a and Figure 9b, respectively.

As the full-cell voltage profile is comprised of the superposition of the voltage curves from the anode and the cathode, DVA can be used to track changes relating to the anode, cathode and electrode balancing, without inserting a reference electrode[81]. The characteristic peaks in a DVA curve represent phase transitions occurring at either electrode, thus monitoring their position and shape can provide information relating to the corresponding electrode[121]. The electrodes inside a battery can be viewed as a series connection and that identical current flows through both electrodes. Therefore, the dV/dQ of the full-cull shows a linear superposition of the derivatives of the anode and cathode half-cell potentials[32,121]. As the voltage of the full-cell can be written as

$$V_{cell} = V_{cathode} - V_{anode} \tag{15}$$

the (dV/dQ)$_{cell}$ can be written as

$$\left(\frac{dV}{dQ}\right)_{cell} = \left(\frac{dV}{dQ}\right)_{cathode} - \left(\frac{dV}{dQ}\right)_{anode} \tag{16}$$

By contrast, the dQ/dV, another non-invasive degradation tool[122,123], is represented as the reciprocal of the above derivative:

$$\left(\frac{dQ}{dV}\right)_{cell} = \frac{1}{\left(\frac{dV}{dQ}\right)_{cathode} - \left(\frac{dV}{dQ}\right)_{anode}} \tag{17}$$

In a dQ/dV curve, the peaks represent phase equilibria, as opposed to the phase transitions in a dV/dQ curve. A disadvantage of this technique is that dV can be zero around flat voltage regions during a charge/discharge sequence (e.g. phase equilibria). Division of dQ by zero therefore inhibits computation of the derivative for this time step[121].

3.8.2 Degradation Monitoring

To demonstrate the reconstruction of the full-cell voltage behaviour from the individual electrode's half-cell voltages, Figure 18a displays how the voltage profile for the Samsung 35E 18650 cell is comprised of the difference between the anode and cathode half-cell curves. Figure 18b shows the derivatives of the curves in Figure 18a.
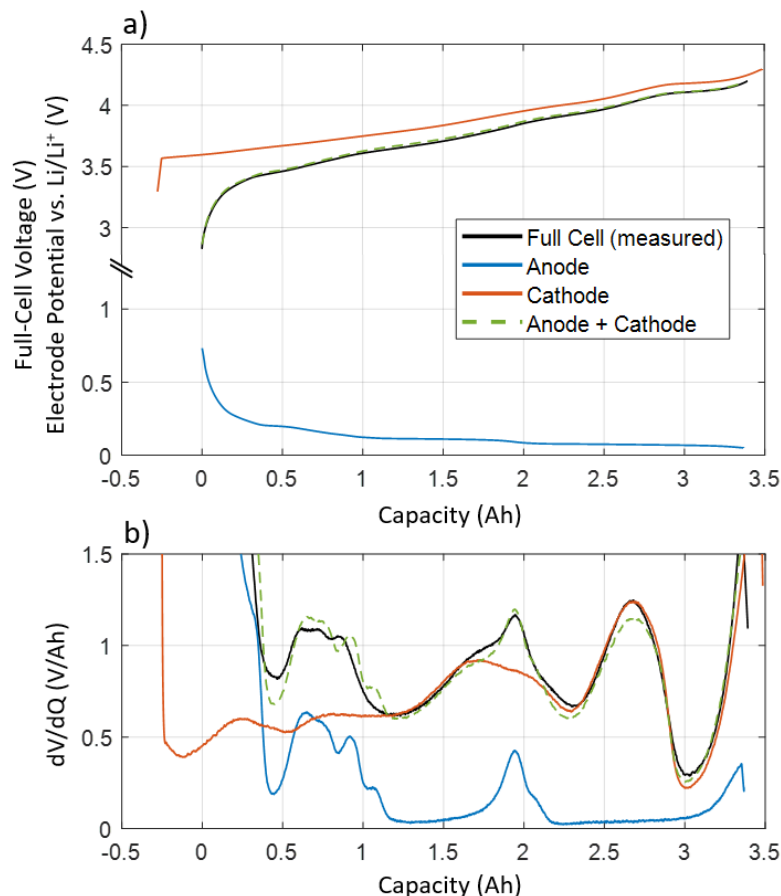
Figure 18. Recreated full-cell voltage profile and corresponding derivatives of the Samsung 35E 18650 cell using half-cell data. (a) Voltage profile during a low current charging sequence; (b) corresponding derivatives.

From observing Figure 18a and Figure 18b, the phase transitions occurring at either electrode can be identified as the peaks in the full-cell DVA profile. DVA can therefore be used to track the changes at either electrode by monitoring these features with ageing.

The discharging cut-off voltage at 0% SoC for the full-cell is determined by the rising anode potential when it is almost completely delithiated, which is reflected in the shape of the voltage profile of the full-cell. The charging cut-off voltage at 100% SoC for the full-cell is not defined by saturated lithiation of the anode, as the anode is typically oversized and the voltage profile fairly constant in the high SoC region. Instead, it is determined by the rising cathode potential with its approach to the maximum degree of delithiation of around 55%, which is enforced to avoid significant deformation of the lattice[100]. These two features define the discharging and charging endpoint, respectively,

and are identified in the full-cell differential voltage curve as the steep slopes at either end of the profile in Figure 18b.

Figure 19 displays a dV/dQ curve annotated with various peak and region markers. Peaks labelled (A_{1-3}) correspond to features of the anode and peaks labelled ($C_{1,2}$) correspond to features of the cathode. Using the assignment of these peaks, regions Q1, Q2 and Q3 can be identified, which are then used for the determination of ageing contributions from the anode, cathode and electrode balancing.
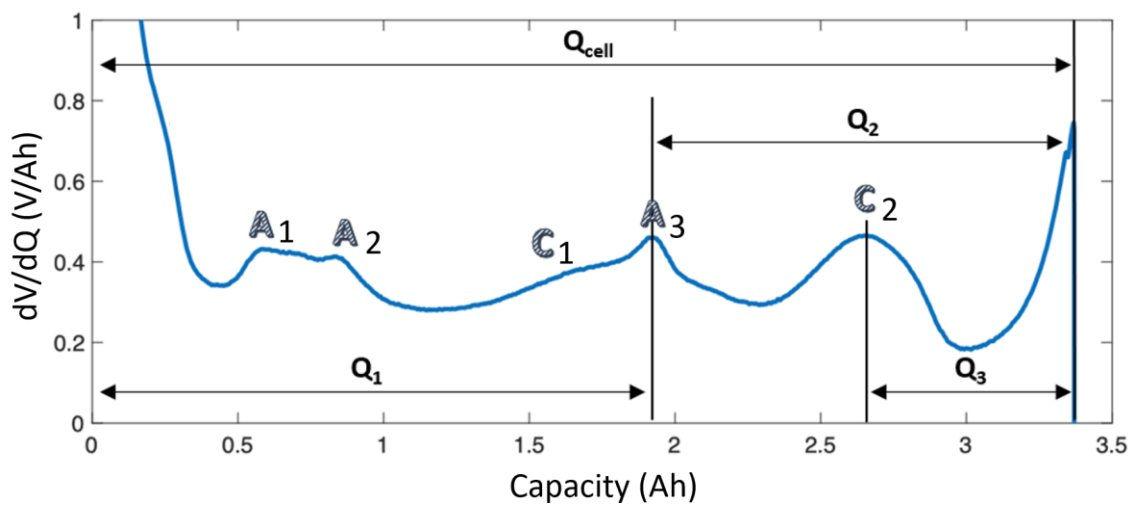
Figure 19. dV/dQ curve with the assignment of anode (A) and cathode (C) peaks. The definition of capacity regions Q1, Q2 and Q3 allow for the determination of degradation mechanisms occurring during ageing.

Q_{cell} represents the total capacity of the cell. The Q1 region is defined by the distance between 0% SoC and the central graphite peak at approximately 1.9 Ah, which corresponds to when the anode is half lithiated (stage I – stage II)[14,81,124]. Q1 is proportional to the capacity of the anode. Likewise, Q3 reflects the charge passed between transitions in the cathode and is therefore proportional to the capacity of the cathode. A shrinkage in these regions would indicate a reduction in the storage capabilities of the corresponding electrode, such mechanisms include electrode particle cracking or corrosion of current collectors[125]. The Q2 region is defined by the distance between the central graphite peak and 100% SoC. As reported in the literature, a change in this region would indicate a shift of the internal half-cells curves against one another, which in turn changes the lithiation degree of the two electrodes[81,121]. The primary cause for a change

in electrode balancing is said to be an irreversible loss of lithium that induces a slippage of the internal half-cell curves that alters the lithiation degree of the electrodes[81,126].

Based on the above, it has been proposed that the Q2 region is therefore a suitable indicator for the loss of lithium (LLI) within the cell. However, Q_{cell} is likely the best proxy for the cyclable lithium inventory, as Q2 only reflects the lithium inventory change if the Q1 region is constant. As $Q_2 = Q_{cell} - Q_1$, it thus does not add value over evaluation Q_{cell} directly. This is demonstrated in Figure 20, which displays various correlation plots between the different regions over an entire dataset of calendar aged cells at 25ºC and 40ºC.
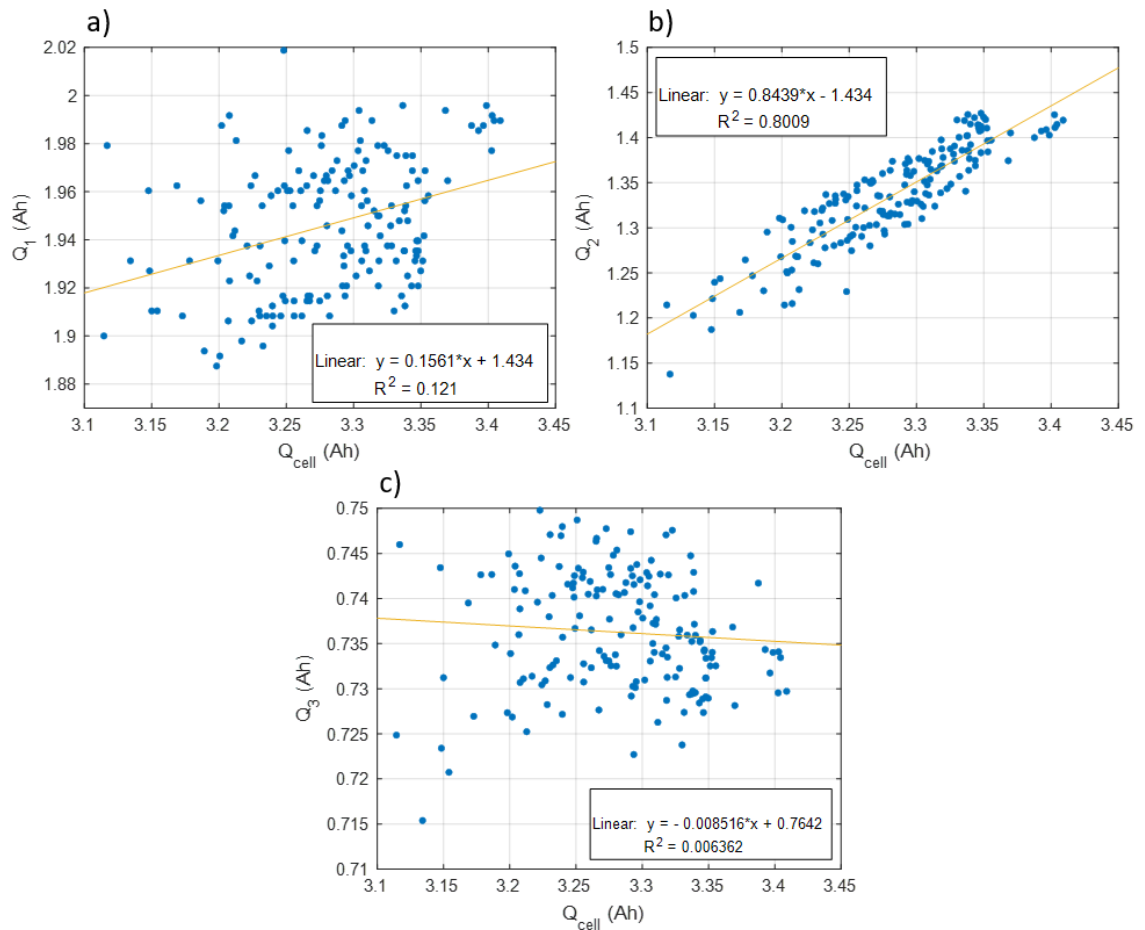
Figure 20. Correlation plots for entire calendar ageing dataset for (a) Q1, (b) Q2 and (c) Q3 vs. Qcell.

A substantially low correlation is observed for both Q1 (Figure 20a) and Q3 (Figure 20c), whereas a strong correlation is observed for Q2 vs. Q_{cell} (Figure 20b). This indicates that Q2 provides no further information than Q_{cell} for capacity loss. Because Q2 evaluation is dependent on Q1 and Q3 being constant, Q_{cell} is suggested as a more robust measure of cyclable lithium inventory. Throughout this thesis it is suggested that Q_{cell} would thus be a better indicator for the cyclable lithium inventory, as changes in the Q1 and Q3 regions would only impact Q_{cell} if the anode or cathode capacity became the limiting parameter to stop charge or discharge, respectively.

An alternative approach to measuring changes to the storage capabilities of the electrodes and the cyclable lithium inventory could be to perform OCV curve fitting using the 'Alawa' Toolbox[127], however this method was not performed in this thesis.

Slight banding is observed above and below the line of best fit in Figure 20b. To explain this occurrence, Figure 21 displays the Q2 and Q1 capacities vs. the Q_{cell} capacities for only the cells aged at 25ºC. Only half the dataset from Figure 20 is plotted for clarity and to show the separation of certain storage conditions/cells.

Figure 21a clearly displays a separation of Q2 values between the storage conditions. Cells aged with a storage SoC of >=80% show higher Q2 values than those aged with a storage SoC <80%, with an apparent separation between the two. When observing Figure 21b, these cells aged at an SoC >=80% display consistently lower Q1 values compared to the lower SoCs. Because $Q_2 = Q_{cell} - Q_1$, the Q2 values for SoCs >=80% are augmented by the lower Q1 values. For further confirmation of the Q1 changes, please see the evolution of the central graphite peak markers in Figure 31, which displays a Q1 shrinkage for SoCs <80% and an enlargement for SoC >=80%.

It is also interesting to note from a degradation perspective that SoCs >=80% promote a comparatively greater reduction in the storage capabilities of the anode.
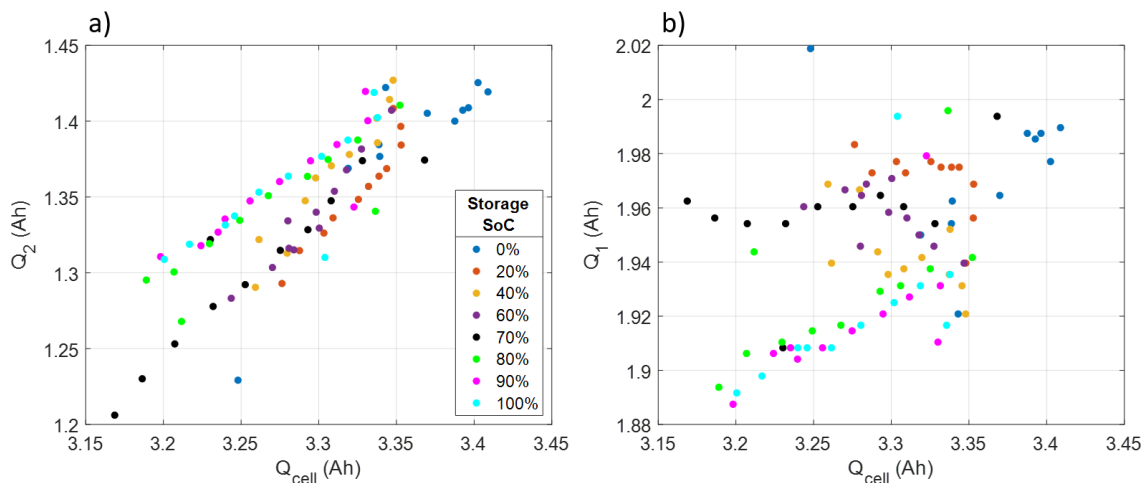
Figure 21. Correlation plots for 25ºC calendar ageing data for (a) Q2 and (b) Q1 vs. Q_cell.

Periodic examination of the DVA curves throughout the life of a cell can reveal the dominant ageing mechanisms through time. In addition to the changes in magnitude of the three capacity regions, the shape of the characteristic peaks can also change. The flattening and suppression of peak height has been linked to the degree of homogeneity of lithium distribution[128] (HLD), which has shown to have detrimental effects on battery health[95,129]. A lower HLD indicates a broader SoC distribution across an electrode, where there can be pockets of concentrated lithium and other regions that are less lithiated. During a given charge or discharge sequence, a particular electrode transition can therefore occur at different times across the electrode, as illustrated by the voltage profile during the stage 2 – stage 1 transition in Figure 22. The capacity location for a transition will then be represented as an average over the entire electrode at which the transition takes place. In the case of a high HLD and thus a narrow SoC distribution (a), this step transition, and therefore the corresponding DVA peak, remains sharp as the transition occurs at a similar point in time across the electrode. In the case of a low HLD with a broad SoC distribution (b), this step is smeared over a larger capacity range due to its occurrence over a larger time period across the electrode. The resulting voltage and DVA profile becomes flatter and broader. In an extreme case, the considerable flattening of the DVA peak renders its identification a challenge.
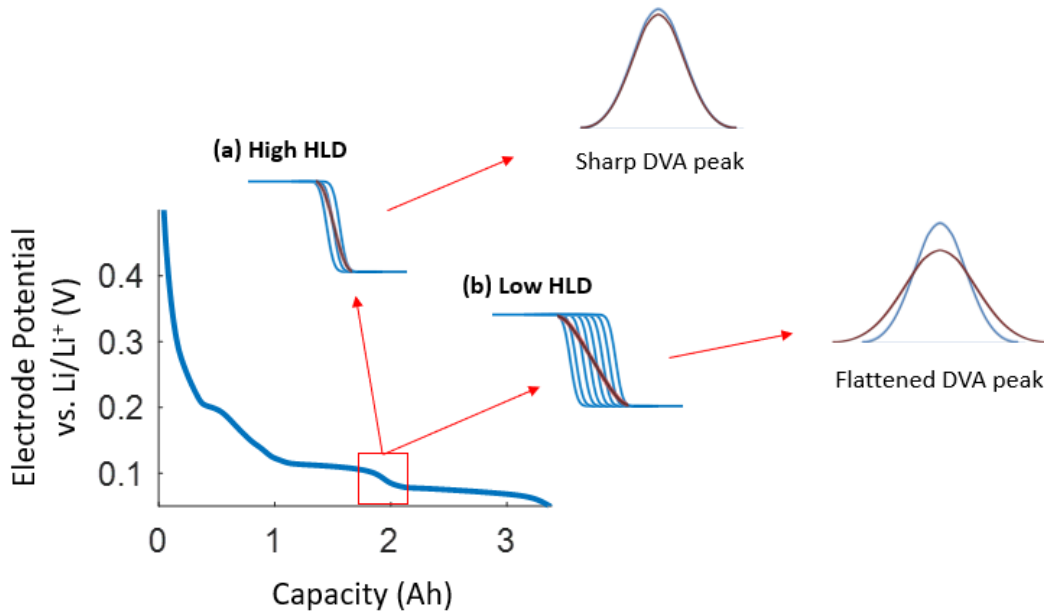
Figure 22. Discharge voltage profile for graphite vs. Li/Li+ highlighting the stage2-stage 1 transition (50% graphite lithiation) with the red rectangle. The transition is shown in terms of the voltage profile and the resulting DVA curve peak. (a) The case of a high homogeneity of lithium distribution resulting in a narrow SoC distribution and thus a sharp transition. (b) the case of a low homogeneity of lithium distribution resulting in a broad SoC distribution and a flatter transition. Smearing of the transition produces a DVA peak that is flatter in shape.

4 The Effects of Idle Conditions on the Lifetime and Cycling of Lithium-Ion Cells

4.1 Introduction

Electric vehicles (EVs) may spend up to 90% of their lifetime parked, during which the lithium-ion batteries (LIBs) remain in an idle state[130]. Before their use in a particular application, LIBs may spend months in storage or in transit accumulating time spent under non-operational conditions. Such conditions are known as calendar ageing conditions, which are typically performed experimentally in the absence of a load[32,89]. However, even during operation, LIBs are subjected to the effects of calendar ageing, as time-averaged state-of-charge (SoC) can often play a significant role in the outcome of an experimental ageing study[19]. Because of this, it is imperative to carry out the experimental testing of cells not just solely the effects of calendar ageing, but also its effect on the subsequent operation of cells. This combination of ageing criteria may lead to certain ageing path dependencies that are of high importance for more accurate lifetime estimations.

Experimental ageing studies are typically separated into calendar ageing and cycle ageing, where in the former the cells are tested in the absence of a current load and in the latter the presence of a current load and cyclical loading. For calendar ageing, it has been extensively demonstrated that battery degradation is highly dependent on storage state-of-charge (SoC) and temperature, where parasitic side reactions occurring at either the

anode or cathode dominate the ageing outcome[13,105,106,131,132]. For the anode, higher storage SoCs lead to lower anode potentials where electrolyte reduction and SEI growth have been identified as a key source for loss of lithium inventory[87,105,131,133]. Electrolyte oxidation, transition metal dissolution and loss of active material due to high half-cell potentials have all been reported to occur at the cathode during calendar ageing[81,89,131,134]. It is generally stated that higher storage SoCs, and thus higher cathode potentials, result in more rapid degradation of LIBs. However, recent reports have verified the existence of a spoon shape dependency of storage SoC on capacity fade in which capacity fade is highest around 80% SoC and decreases towards 100% SoC[13,15]. It was conveyed that more positive/negative cathode/anode potentials increase the rate of shuttle mechanisms leading to a greater reversible self-discharge, respectively. Such processes reduced the Li^+ current available for SEI formation, resulting in less irreversible capacity fade at higher storage SoCs.

Cycle ageing studies frequently report the negative impact of high charge/discharge currents, larger depth-of-discharge (DoD) and temperature extremes on LIBs. High charging currents, especially coupled with low operation temperatures, may drive the anode potential below 0.0 V Vs. Li/Li^+ leading to Li metal deposition at the surface of the anode[29,135]. Deposited Li can further react with the electrolyte to result in a feedback loop that promotes a non-linear and rapid capacity decline[45,136]. Higher/lower charge/discharge cut-off voltages have shown to increase the rate of oxidation/reduction reactions, respectively, in addition to increased SEI growth and repair[65,69]. However, cycling studies rarely state the previous storage conditions of examined LIBs or its effect on cycling outcome, despite battery ageing displaying a distinct dependency on such conditions. Cycling and ageing studies are commonly treated as independent, even though calendar storage effects influence battery state-of-health (SoH) throughout their entire useful life. Efforts into combined cycling and calendar measurements have suggested a degradation path dependency, which renders the summation of cyclic and calendar ageing as potentially inaccurate[17]. Moreover, a combined calendar and cycling study of NCA/graphite cells directly examined path dependency and environmental conditions and revealed a degradation path dependency at higher C-rates, but not at lower C-rates. Longer continuous cycling durations in between calendar periods were found to negatively affect battery SoH[91]. Finally, the frequency of cycling was found to be an important factor in path dependent LIB ageing[137]. These studies all demonstrate a strong case for path dependency during combined calendar and cycle testing, however, the

influence of extended calendar periods on the outcome of subsequent continuous cycling has not been discussed. Considering LIBs are stored for significant lengths of time at various SoCs before electrochemical testing and operation, it is of high importance to understand such conditions.

This chapter fundamentally explores cell ageing behaviour and whether an ageing path dependence is exhibited throughout their operational life. Initially, cells are calendar aged at multiple SoCs and temperatures for extended periods of time to observe their response to specific storage conditions. After this period, cells are stored at a low SoC to observe any relaxation behaviour and to quantify any reversible phenomena. Finally, the cells are subjected to one of two cycling conditions: 'aggressive' or 'soft'. It is in this final stage where the previous extended storage history may influence the ageing outcome during cycling and produce an ageing path dependence.

4.2 Experimental Design

Two ageing studies were performed in succession to primarily explore if cells display a path dependence to degradation. Initially, cells were calendar aged at defined storage SoCs and temperatures to obtain the cells' response to storage conditions for extended periods of time. Next, 1 month of relaxation at a low SoC was applied to all cells to observe reversible ageing effects and to recover reversible capacity losses. Finally, cells were subjected to one of two cycling conditions to identify if a cell's previous storage history can influence the ageing outcome during cycling.

4.2.1 Lithium-ion Battery Studied and Equipment Used

The cell used in this study was a high-energy 18650 commercially available cylindrical cell manufactured by Samsung. The cathode chemistry was lithium nickel-cobalt-aluminium ($LiN_{0.8}Co_{0.15}Al_{0.05}$) and the anode chemistry was a graphite/silicon oxide (SiO_x) blend. All cells in this study were obtained from the same batch to minimise variations in performance. With the model name INR18650-35E, the cell has a rated capacity of 3.35 Ah with the voltage limits of 4.2 V -2.5 V and a nominal voltage of 3.6

V. A more detailed description of the cell can be found in Table 1. The cell was operated within the safety limits specified by the manufacturer at all times.

During ageing in both cycle and calendar portions of this study, cells were kept in Memmert IPP260 Plus and Espec PU-2J thermal chambers to ensure identical environmental conditions. Electrochemical testing was carried out on Basytec CTS battery cyclers for check-ups and cycles, whilst electrochemical impedance spectroscopy (EIS) was carried out on a Biologic BCS 815 system. Battery Dynamics 3-pin cell holders were used for all testing on both systems.

4.2.2 Experimental Ageing Procedure

4.2.2.1 Calendar Ageing

In this portion of the study, cells were stored at eight different SoCs between 0% and 100%. At each SoC level, two temperatures were examined, 25ºC and 40ºC, to give 16 different test conditions which are presented in Table 3.

Table 3. Calendar ageing test matrix.

Temperature (ºC)	Storage SoC (%)							
25	0	20	40	60	70	80	90	100
40	0	20	40	60	70	80	90	100

Here, SoC is defined as the charge stored with respect to the total measured capacity of the cell

$$SoC = Q_{stored} / C_{measured} \tag{18}$$

Target SoCs were chosen to obtain both an even spread of the entire SoC range plus additional SoC resolution at higher voltages. Figure 23 displays the positions of the chosen storage SoCs on the voltage profile for the cell.
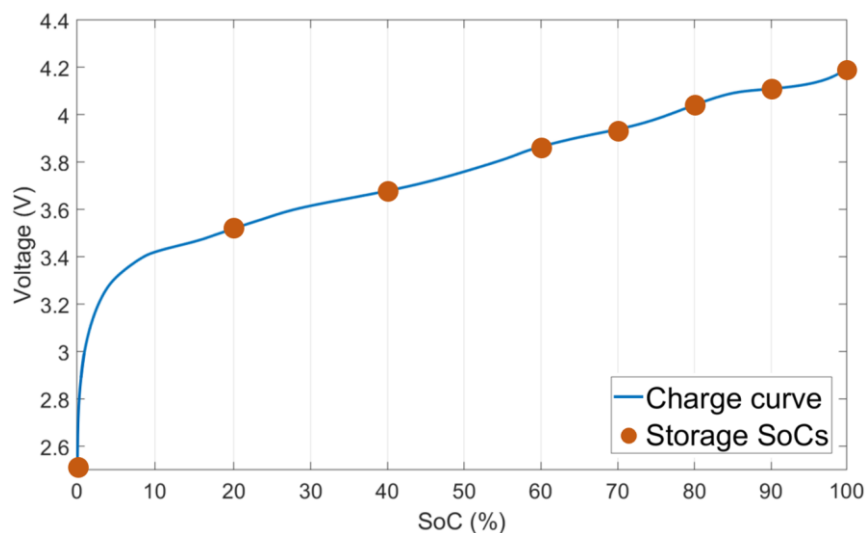
Figure 23. Charge curve with the eight storage SoCs identified on the voltage curve.

Throughout the entire testing period, the cells were stored at the eight different SoCs in two thermal chambers for the two ageing temperatures: 25⁰C and 40⁰C. To track degradation throughout cell lifetime, check-up procedures were used before testing and at intervals throughout calendar ageing. All check-ups were performed at 25⁰C, regardless of individual ageing condition. The voltage and current profile during these check-up measurements are presented in Figure 24. This procedure is largely similar to the check-up presented in Figure 9a (section 3.2.1, page 26) and is comprised of a 0.25 A CC charging step for DVA, a -1.0 A discharge for capacity measurements and two -3.0 A 10 s discharge pulses for DC resistance determination. Additional steps to achieve the desired storage SoC are inserted at the end of the check-up after the discharge pulses. Storage SoCs were all determined using a 1.0 A charging sequence after a full CC discharge from 4.2 V to 2.5 V. This discharge step was used to calculate total remaining capacity of the cell periodically during ageing. This value was then used to calculate subsequent storage SoCs, which minimised storage SoC drifts throughout cell life. For achieving 0% SoC, the check-up test was terminated after the CC discharge to 2.5 V. To achieve 100% SoC, the check-up test was terminated after the CC charge to 4.2 V.
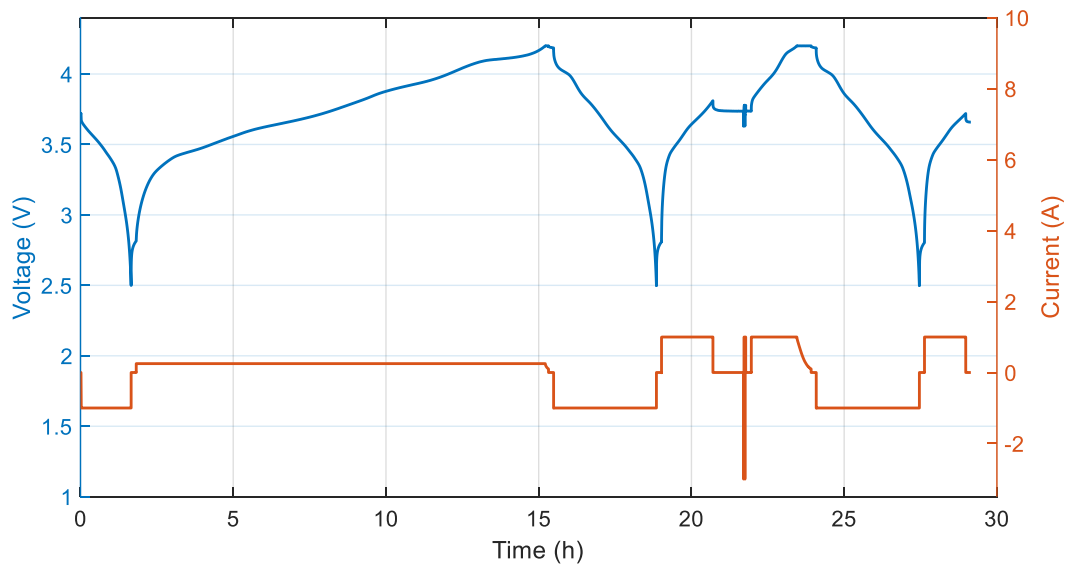
Figure 24. Measured voltage and applied current profiles during for an example check-up. Final step displays a CC charge to 30% SoC based on the calculation from the previous CC discharge.

In conjunction with check-up procedures, EIS was performed for detailed analysis of the resistance spectra. EIS testing was executed before each check-up to ensure that the final part of testing before calendar storage was the target SoC acquisition. All EIS measurements were performed at 25⁰C and at 50% SoC from 10 mHz to 5 kHz with an excitation current amplitude of 40 mA and after a rest of 1 h once reaching 50% SoC.

4.2.2.2 Relaxation Periods

After 19 months of calendar ageing at various SoCs and temperatures, all cells were entered into an identical relaxation period of 1 month. Cells were CCCV discharged with a discharge current of -1.0 A to 2.8 V with a CV termination criteria of 10 h. A cut-off voltage of 2.8 V was chosen to achieve a near 0% SoC but to minimise any excessive cell damage. A relaxation of the voltage after the CV step produced storage voltages between 2.91 V and 3.12 V, which corresponds to storage SoCs of 0.5%-1.5% for all cells. Cells were then stored at these low SoCs at 25⁰C for 1 month. EIS and check-up procedures were performed before and after the relaxation period at 25⁰C.

4.2.2.3 Cycle Ageing

In the final section of this study, all cells were subjected to one of two cycling routines, termed aggressive and soft cycling. The split between the two cycling conditions for different calendar ageing SoCs are tabulated in Table 4 and the cycling parameters are tabulated in Table 5. All cells that were previously calendar aged at a particular SoC were cycled according to the designation in Table 4. For example, both cells that were calendar aged at 70% SoC (one at 25°C and one at 40°C) were cycled under the aggressive cycling conditions. All cycles and check-ups for both conditions were performed at 25°C in thermal chambers to ensure identical environmental conditions. The check-up used periodically throughout the cycling routines was the updated check-up procedure, as presented in Figure 9b (section 3.2.1, page 26). It is comprised of a 0.25 A CC charging step for DVA, a -1.0 A discharge for capacity measurements, a 0.15 A CC discharge for DVA and CDA and two -3.0 A 10 s discharge pulses for DC resistance determination.

Table 4. Test matrix for designation of cells to either aggressive or soft cycling conditions

Cycling Condition	Previous calendar storage SoC (%)			
Aggressive	0	70	90	100
Soft	20	40	60	80

Table 5. Cycling parameters for aggressive and soft cycling conditions.

Cycling Parameter	Aggressive	Soft
Charge/discharge current (A)	+1.7/-1.7	+1.0/-1.0
C-rate	0.50 C	0.29 C
Charge/discharge cut-off voltage (V)	4.2/2.5	4.2/3.4
Temperature (°C)	25	25

4.3 Results and Discussion

4.3.1 Effect of Calendar Storage Periods

Calendar periods are presented vs. storage time, whereas subsequent cycling periods are presented vs. duty cycles.

4.3.1.1 Capacity Fade Over 19 Months

Relative capacity values are a common indicator for the state of health (SoH) of LIBs and indicate the approximate range for aged electric vehicle (EV) batteries. This section examines the relative capacities of cells stored under different conditions to elucidate the most detrimental conditions for battery health.

Figure 25 displays line graphs for all cells in the calendar study to observe relative capacity loss rates. Relative capacity obtained from check-ups are plotted over 19 months, where the start point reference (100%) is the capacity measured before ageing. Certain outliers have been removed to aid viewing. Brief issues with the thermal chambers during a small number of check-ups, particularly for cells stored at 40⁰C, meant that the cell temperatures varied during the measurement. However, these temperature changes were only brief and were not expected to alter the outcome of the experiment due to their short duration. For consistency, both plots in Figure 25 had the same data points removed. To preserve transparency with the data set, Figure 25 is presented in the appendix with the inclusion of all test data points.

Comparing all storage SoCs in Figure 25a and Figure 25b, cells show faster capacity fade over 19 months when stored at 40⁰C instead of 25⁰C. Capacity loss for cells stored at 25⁰C and 40⁰C is between 1-5% and 2-7%, respectively. Cells with a lower storage SoC generally show less capacity fade over 19 months, however the exact relative capacity-SoC trend will be explained in a subsequent subsection.

For cells stored at <=20% SoC, increases in capacity are observed in the early months, with a maximum of 0.8% capacity increase for cells stored at 0% SoC. This occurrence

can be explained by the diffusion of lithium to and from the passive anode overhang regions in commercial cells which are the perimeter portions of the anode active material that do not have a direct cathode counterpart[93,138]. The anode is typically oversized compared to the cathode to reduce lithium plating at the edges of the anode during charging. This provides additional space that lithium can diffuse into or out of and thus they act as a lithium sink or a lithium source, respectively[19] (see section 2.3.3). In the case of these data, when cells are stored at low SoC a concentration gradient between the more highly lithiated overhang and the more lithium-depleted active portion of the anode will drive lithium diffusion into the active region. This then boosts the cyclable lithium content, which shows as an increase in relative capacity.

Apart from storage at low SoC, capacity fade follows a characteristic trend in which capacity loss is greatest in initial months, but then settles at a lower loss rate. This has been reported as an approximate square root of time dependency of the capacity fade[13,106]. Here, the initial losses are greater when storing the cells at a higher temperature, where almost half the total capacity loss over the 19 months is lost in the first 3 months of storage (70% SoC at 40°C). However, very little capacity loss is observed when storing the cells at 0% SoC for 19 months at either temperature, but particularly at 25°C (~1%).
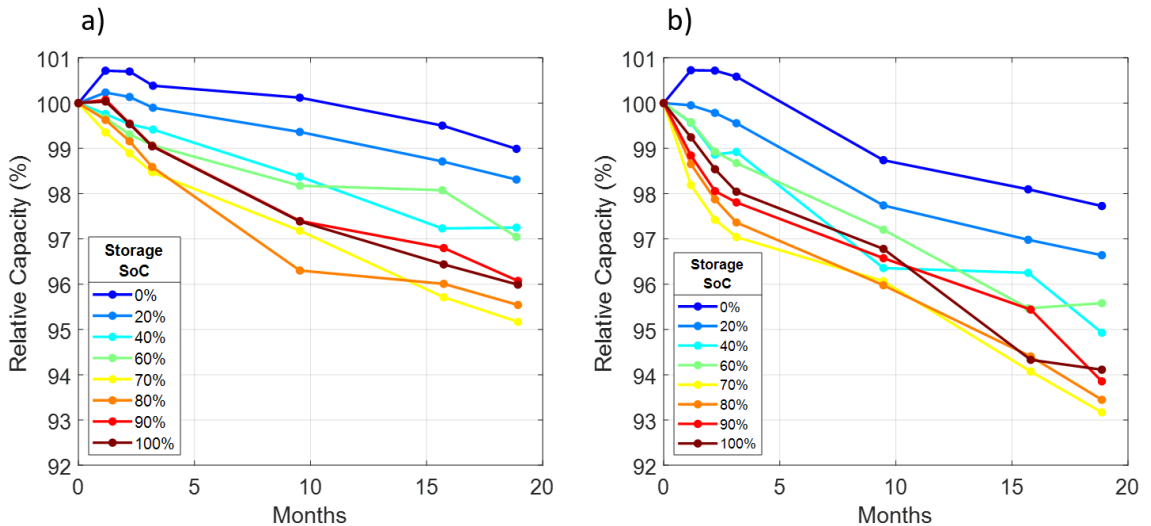
Figure 25. Relative capacity vs. storage months for cells stored at different SoCs at (a) 25°C and (b) 40°C.

Figure 26 displays the relative capacity vs. SoC trend after storage for 19 months at 25°C and 40°C. For each storage SoC, storing the cells at a higher temperature resulted in

greater capacity fade, likely a result of the increased rate of side reactions, such as SEI formation. A consistent trend exists for both temperatures: a 'spoon shape' is observed for the relative capacity, as reported previously[13,15]. Capacity fade predominantly increases for storage SoCs 0% through to 60% but decreases from 70% to 100%. Typically, capacity fade has been reported to increase through the SoC range from 0-100%, which has been attributed to a higher rate of side reactions. These reactions, such as SEI growth at the anode and oxidation reactions at the cathode, reduce the inventory of cyclable lithium[81,105,131,139].
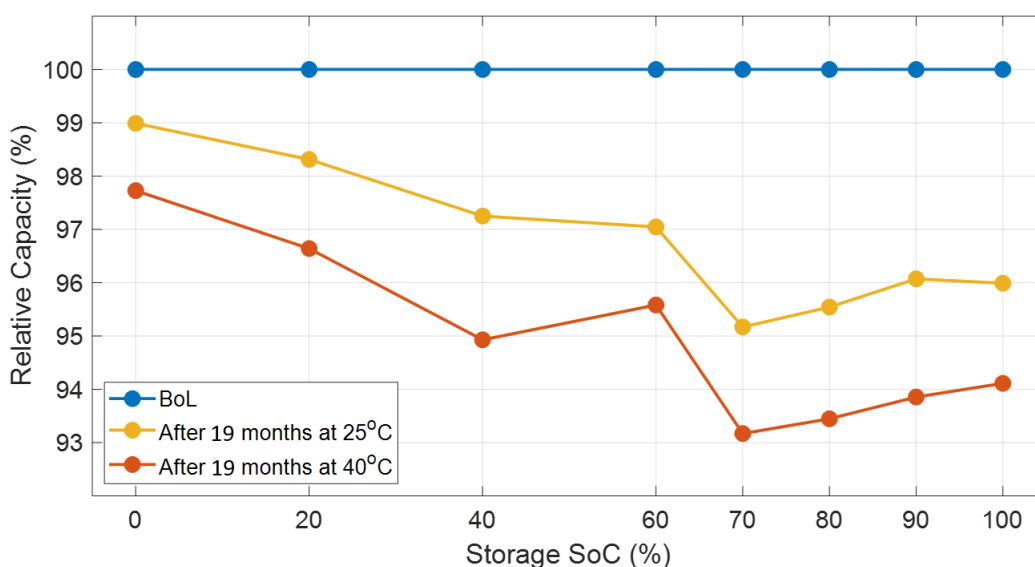
Figure 26. Relative capacity vs. storage SoC at 25ºC and 40ºC over 19 months.

A hypothesis first developed by Zulke et al., the 'spoon shape' has been suggested to be indicative of a higher rate of side reactions at the anode and cathode that can *reduce* irreversible capacity loss through a reversible self-discharge[13]. The cell in question was a high-energy NCA/graphite-silicon cell akin to the one used in this study. This hypothesis proposes that shuttle mechanisms ensue during OCV conditions at high storage SoC, as the relative half-cell potentials at the anode/cathode are more negative/positive, respectively. It is proposed that two CO_2 molecules are reduced at the anode to produce an oxalate ion, which can then diffuse to the cathode to become re-oxidised back into CO_2. Because electrons can only be consumed/provided at the electrodes when accompanied by the intercalation/deintercalation of Li^+, respectively, this shuttle

effectively transports two electrons from anode to cathode and promotes the reinsertion of lithium back into the cathode[13]. This Li^+ current is removed from the (shared) Li^+ current used during irreversible SEI formation.

This reaction model is illustrated in figure 27, which shows a mass-flow Sankey-style diagram. Line and arrow thickness in the centre portion represent the relative rates of reactions. Currents associated with shuttle mechanisms are matched with equal Li^+ currents to satisfy electroneutrality in the electrolyte and also to supply and consume electrons at the anode and cathode, respectively. A parallel Li^+ current feeds into ongoing SEI formation at the anode.

The behaviour described above is driven by the relative potentials of anode and cathode: the rate of self-discharge is driven by the cathode potential and the Li^+ supply is driven by the anode potential. At increasing SoCs > 60% the cathode potential increases, whilst the anode potential remains approximately in a plateau region. This plateau causes a stagnation in the total Li^+ current (shared between self-discharge and SEI formation), however the increasing storage SoC increases the cathode potential, which increases the rate of shuttle-based self-discharge (Figure 27d). In effect, this reduces the available Li^+ current for SEI formation, which reduces the irreversible capacity fade. At 80% SoC in Figure 27c, the lower cathode potential results in a slower rate of shuttle-based self-discharge, meaning there is a greater proportion of Li^+ current for SEI formation, which results in greater irreversible capacity fade. This phenomenon is the proposed mechanism behind the spoon-shaped dependency of capacity fade on storage SoC.
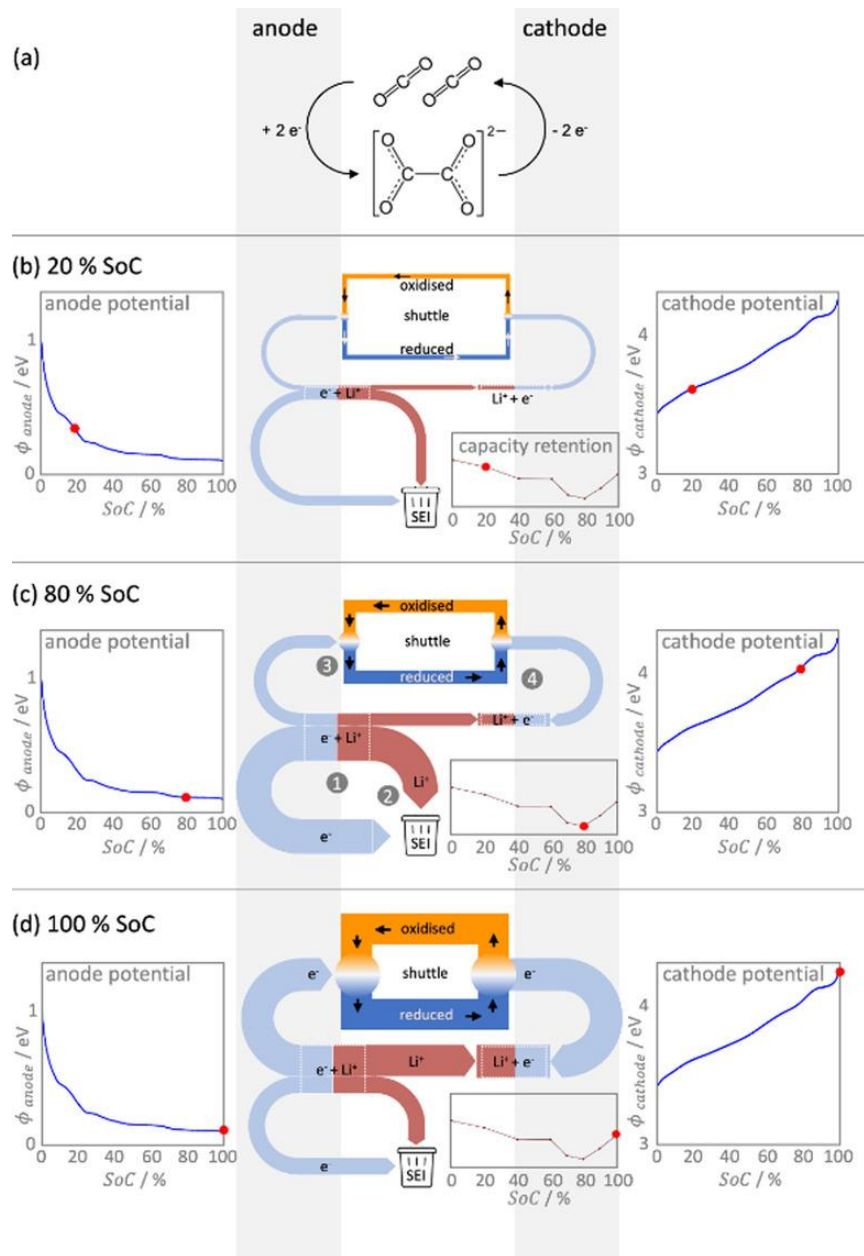
Figure 27. (a) Illustration of the CO_2-based shuttle mechanism of self-discharge, (b)-(d) mass flow model of reversible self-discharge rates along with irreversible SEI formation and a corrosion-type electron transfer at three different storage SoCs. Left and right columns display the anode and cathode potentials vs. SoC, respectively. The centre insert displays the relative capacity as a function of storage SoC[13].

An approximate plateau can be seen for cells stored at 60% SoC, which corresponds with the phase transition of the graphite when it is half lithiated and has been reported previously[131]. The location of central graphite peak at $Li_{0.5}C_6$ in the DVA curve of a fresh cell (see section 3.8.2 for DVA example) was found to occur at ~57% SoC of the full cell, meaning that, if the anode were to be fully lithiated, the full-cell would be approximately

at 114% SoC. Therefore, the anode is only 88% lithiated when the full-cell is at 100% SoC and thus the anode is approximately 14% oversized.

4.3.1.2 Endpoint Slippages Indicate Electrode Side Reactions

The charging and discharging endpoints (CEP and DEP, respectively) are presented in Figure 28. For information on the endpoints and their calculation, see section 3.5 (page 34). Because of missing data in the data set, the endpoints were calculated using the coulomb tracking[81] technique with Ah-balance adjustments. Additional offsets were calculated if the ah-balance exhibited jumps of more than a prescribed Ah value and were subsequently brought in line with the continuous Ah-balance. Inconsistencies observed in the CEP and DEP can be explained by this pre-processing adjustment, however the general trends remain true and are to be interpreted.

Figure 28a and Figure 28b show the evolution of CEPs for cells calendar aged at 25ºC and 40ºC at 8 SoCs. Although the inconsistencies mentioned above are present, the higher storage SoCs generally produce greater slippage of the CEP. CEP slippage is a symptom of increased side reactions at the cathode, such as transition metal dissolution and electrolyte oxidation[43,140]. Such reactions can promote a reinsertion of lithium back into the cathode that is observed as a potential decrease and a shift of the cathode half-cell. If this slippage is greater than slippage of the DEP, then the available capacity window and the utilisation of both electrodes can increase[32,81].

The slippage of the DEPs are depicted in Figure 28c and Figure 28d. Again, the finer trends cannot be identified due to the data inconsistencies, but the general trends will be interpreted and discussed here. Greater slippages of the DEPs are observed with an increase in storage SoC, indicating aggravated side reactions that consume lithium at the anode, such as SEI growth and electrolyte reduction[81,105,141]. In addition, coupled side reactions, where oxidation products produced at the either electrode migrate to the opposing electrode, may increase endpoint slippages[13,15,44]. For these data, it seems likely that more positive/negative cathode/anode potentials at high SoC yields a greater rate of side reactions, respectively, which increases the CEP and DEP slippages.
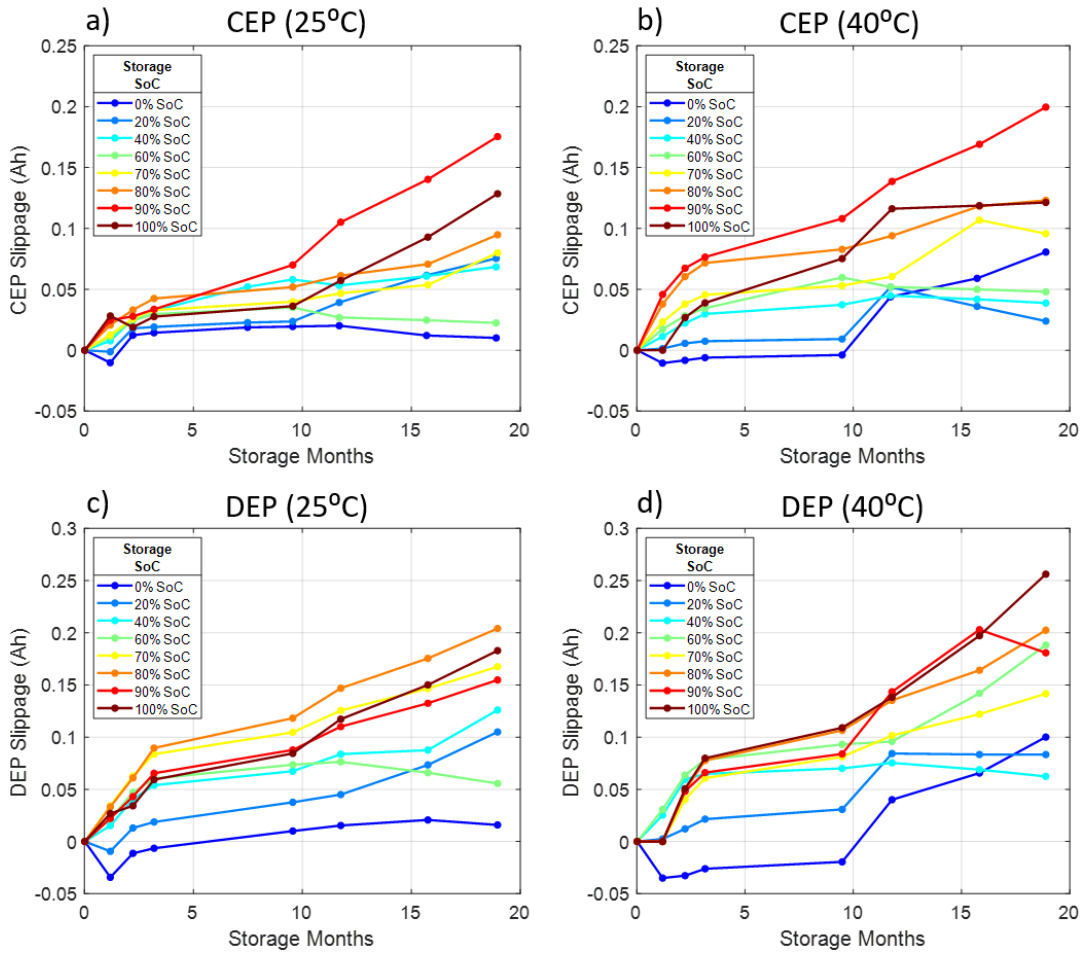
Figure 28. Endpoint slippages as a function of storage SoC over 19 months for both the charge (a and b) and discharge (c and d) at 25ºC (a and c) and 40ºC (b and d).

4.3.1.3 Resistance Over 19 Months

Battery ageing during non-operation periods can affect the battery resistance in addition to the capacity[87,105], therefore pulse resistance measurements and EIS data are interpreted in this section. DC pulses were performed in the check-up for a duration of 10 s and at 50% SoC and 25ºC. Impedance spectra were obtained at multiple SoCs, however only an EIS sweep at 50% SoC is discussed in this section. In support of the Nyquist plots, DRT plots are also examined.

4.3.1.3.1 DC Discharge Pulse Measurements

The DC resistance for cells stored at 2 different temperatures are displayed in Figure 29a and Figure 29b. Using a DC discharge pulse for the calculation of cell resistance is an

established method due to its ease of implementation and fast acquisition[104]. The calculated resistance values are comprised of contributions from multiple origins, which are ultimately affected by pulse duration. In addition, the calculated resistance value will also be affected by the error associated with the voltage measurement. The voltage resolution of the BaSyTec CTS battery test system is 0.3 mV. The approximate voltage change during a -3.0 A 10 s discharge pulse at 50% SoC for a fresh cell is 0.1089 V, meaning one might expect an error of ±0.28% associated with the voltage measurement in these tests, which is deemed small in comparison to the observed changes in Figure 29. Moreover, the data acquisition sampling rate may influence the outcome of the voltage measurement, which is set to 1 Hz for discharge pulses. However, for the reasons mentioned in section 3.3, and that all tests are performed consistently, the influence that this has on the outcome of these tests is expected to be small. For these reasons, DC pulse resistance measurement remains a useful tool for an insight into cell internal resistance. All discharge pulses were performed at 50% SoC for a duration of 10 s and 25°C for consistency.

In both Figure 29a and Figure 29b, all cells show little increase in resistance after 2 months of ageing, and in some cases, show a decrease in resistance. This is perhaps due to maturation of the SEI and/or redistribution of lithium with the active materials, which may reduce the deintercalation path for lithium in the anode[142]. After 9 months of ageing at 25°C, very little gains in resistance are observed throughout the SoC range, with a maximum of 2% seen for the cells stored at 90% and 100% SoC. Larger increases in resistance are seen for cells stored at 40°C after 9 months, particularly again for SoCs >=90%, which show 4-5% increase in relative resistance. After 19 months, further amplification of the resistance is observed at both temperatures to give maximum values of 7% and 14% over a fresh cell at 25°C and 40°C, respectively. In all SoC cases, higher temperatures increase the rate of resistance growth over 19 months, which has been regularly reported in previous studies[87,105,131]. Higher temperatures improve the kinetics of the side reactions taking place within the cell, whether it be electrolyte reduction and SEI formation at the anode or electrolyte oxidation at the cathode.

Interestingly, cells stored at 70% SoC do not show significant gains in resistance over cells stored at <70%, even though this condition displays the largest reduction in relative capacity. Moreover, a substantial increase in resistance and temperature dependency is observed for cells stored above 70% SoC and an approximately inverse relationship is

established compared to what is expected with the relative capacity in Figure 26. I.e., the increase in resistance from 70-100% is met with decreasing capacity fade in that order. Higher SoCs correlate with more delithiation of the cathode and thus more positive potentials. These higher potentials encourage the dissolution of transition metals and the electrochemical oxidation of electrolyte at the cathode[69]. These processes would naturally lead to higher DC resistance values due to a reduction in conductivity[143]. Furthermore, the electrons ejected from these reactions may swiftly be consumed by Li^+ in the electrolyte at the cathode, resulting in a reinsertion of lithium back into the cathode to satisfy charge neutrality[13]. This reaction model, whereby electrons ejected during oxidation reactions at the cathode are consumed by Li^+ and promote a reinsertion of lithium back into the cathode, is discussed previously in section 4.3.1.1, which uses a Sankey-style diagram to explain the competing reactions during these processes (Figure 27). In addition, lower potentials at the anode at high SoC promote reduction reactions such as SEI growth which thicken passivation films at the surface of the anode.

From these data, it is recommended that the cells are stored at SoCs below 40% in order to reduce unwanted degradation. Cells in this SoC range are less susceptible to capacity fade and DC resistance increase after extended storage periods.
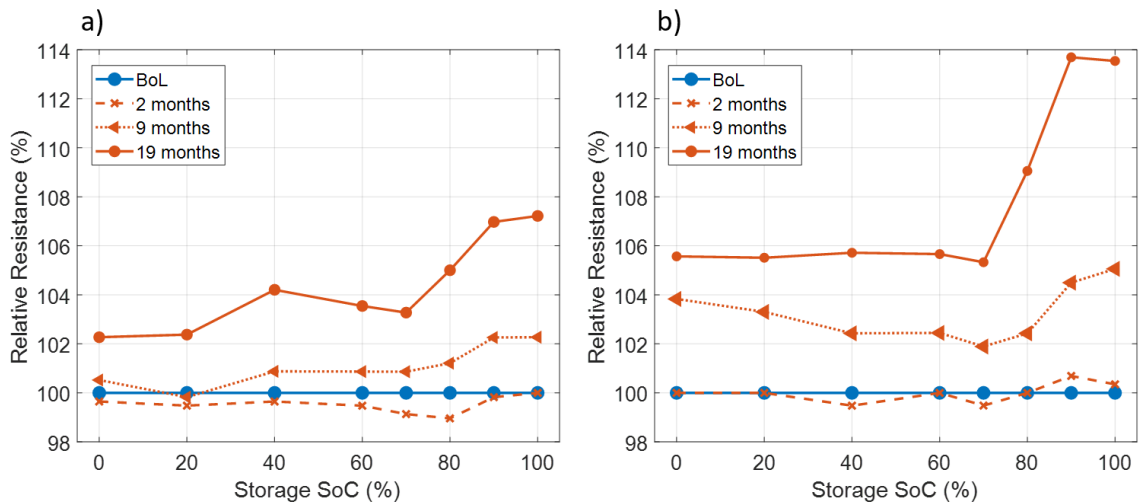
Figure 29. DC resistance plots as a function of storage SoC at (a) 25ºC and (b) 40ºC.

4.3.1.3.2 EIS Insights

To gain separation of the resistance contributions during cell ageing, EIS was performed at 50% SoC and 25°C. The resulting Nyquist plots for cells aged at 25°C and 40°C are presented in Figure 30a Figure 30b, respectively, whilst the corresponding Distribution of Relaxation Times (DRT) for selected cells aged at 25°C and 40°C are plotted in Figure 30c and Figure 30d, respectively. For more information on the theory of DRT, please see section 3.7.2.

Figure 30a and Figure 30b display the EIS spectra for cells aged at various SoCs for 19 months at 25°C and 40°C, respectively. A right shift of the curves at the point of interception with the x-axis is observed for all cells, which indicates increasing ohmic resistance contributions during storage. An approximate trend is observed: increasing ohmic resistances with increasing storage SoC and temperature. Storage at high SoC and temperatures may promote electrolyte oxidation reactions which reduce electrolyte conductivity and increase ohmic resistance[144,145]. Storage of cells at 0% SoC has a noticeably small impact on the EIS spectra after 19 months of ageing, particularly when stored at 25°C.

The right shift of the entire spectrum is accompanied by an enlargement of the semicircles in the 1-1000 Hz region, particularly for cells stored at higher temperatures. This region is suggested to reflect changes associated with migration of Li^+ through the SEI and charge transfer (CT) reactions[117,146,147]. Separation of these processes is challenging with only observation of the Nyquist plots; hence the DRT are plotted for selected cells stored at 25°C and 40°C for 18 months in Figure 30c and Figure 30d, respectively. Peak and peak labels highlight the various identifiable peaks and regions of the time constants axis: peak 1 can be observed to track changes with the SEI, region 2 for observation of the CT reactions at either electrode and peak 3 for diffusion-related changes[116,146–148].

The little change observed in the EIS spectra for cells stored at 0% SoC is confirmed with the plots of the DRT. Only minimal changes in the DRT profile appear after storage at 0% SoC and 40°C. However, there is increased augmentation of peak 1 for higher SoCs and temperature. Because this peak is suggested to correspond to Li^+ migration through the SEI, storage at higher SoCs and temperature may increase the growth rate of the SEI, which restricts the passage of Li^+. This presumption is consistent with previous calendar ageing reports[105,131,147,149]. Moreover, a shift of the peak to lower frequencies is observed

for cells stored at 100% SoC, indicating a reduction in the rate of this process. Region 2 highlights the CT processes at either electrode, however, separation of peaks according to each electrode remains a challenge. Nevertheless, moderate deviations of the DRT profile in region 2 are observed with respect to the peak at approximately 50-100 Hz. Higher storage SoCs and temperatures result in a shift to higher frequencies and increases in resistance for this CT process. The remaining peaks in region 2 appear largely unaffected by storage at any SoC or temperature. Previous studies have reported the increase of CT resistance at the interface between electrolyte and cathode electrolyte interphase (CEI) as a dominant factor in impedance rise, particularly at higher storage SoC[134,150]. This explanation could fit the changes observed in this peak: higher storage SoCs increase the electrochemical potential at the cathode, improve the kinetics of side reactions occurring there and ultimately alter the properties of the CEI.

Peak 3 is suggested to correspond to the process of diffusion within the cell, which is comprised of both electrolyte and solid-phase diffusion[146]. Storage at 25ºC increases the diffusion resistance more than storage at 40ºC. This observation may be due to reduced lithium mobility in a number of areas: in the electrolyte, within the porous electrodes, within the active masses and through the SEI[103]. Greatest enlargement in diffusional resistance is seen for the cell stored at 70% SoC and 25ºC, which displays around 10% increase in peak height. This is compared to around 5% increase when stored at 70% SoC and 40ºC.
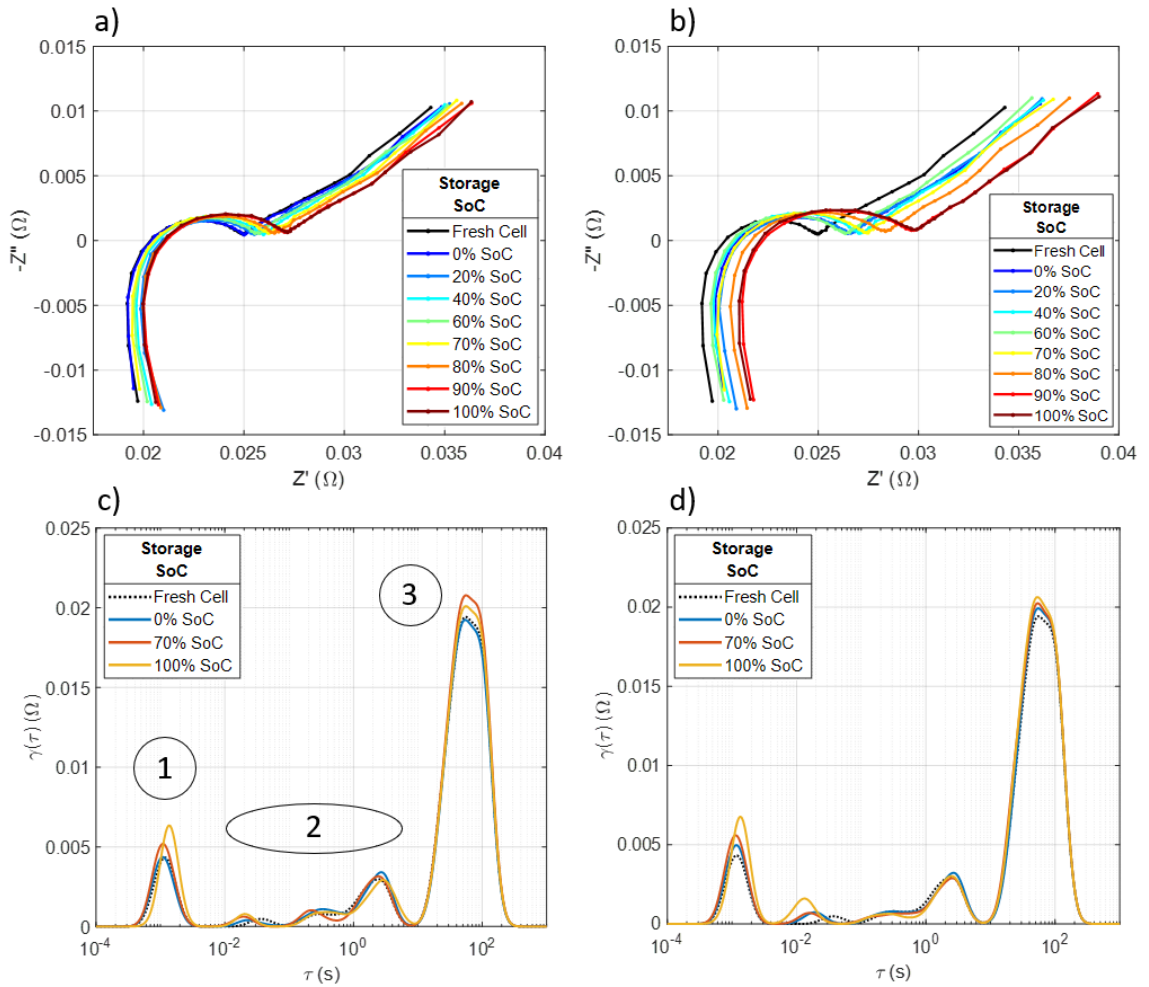
Figure 30. Nyquist plots of cells stored at various SoCs for 19 months at (a) 25ºC and (b)40ºC and corresponding DRT plots for selected SoCs at (a) 25ºC and (b) 40ºC.

4.3.1.4 Differential Voltage Analysis - DVA

DVA was performed to identify the origins of capacity fade during calendar ageing periods. Depicted in Figure 31 are the DVA curves for cells aged at 25ºC and various SoCs over 19 months. Please see section 3.8 for detailed information on DVA and the indicators for degradation tracking. The central graphite peak, highlighted by the circles and observed at around 1.9 Ah, is essentially immobile in its position on the horizontal SoC axis, despite significant reductions in relative capacity. This indicates little change in the storage capacity of the anode over the ageing months. For storage SoCs 0-60%, the height of the central graphite peak displays little change, however for storage SoCs above 60%, peak height reductions are observed. This reduction is highest for 70% but reduces towards 100% SoC, which shows little change in peak height.

Inhomogeneous lithium distribution in the graphite anode, as quantified via a lower Homogeneity of Lithium Distribution (HLD), is a likely cause of this behaviour[95]. In this picture, lithium accumulates/depletes in regions with higher/lower current densities that arise from spatially varying passivation layer growth. This creates a higher spatial variation of SoC across the electrode and, in turn, flatter voltage transitions, which are observed as flatter, broader DVA peaks (see section 3.8.2). However, with this data it is likely that there is a reduction of HLD in combination with changes in the cyclable lithium inventory.

Loss of lithium inventory over time causes apparent shifts of the anode and cathode contributions to the overall DVA curves: anode and cathode related peaks appear to move left and right, respectively, towards higher and lower SoC, respectively. This is most visible by the apparent shift to the left of the broad, central peak relating to the cathode that is overlayed with the central graphite peak and is identified by a cross in each figure panel. This effectively causes a separation of the two peaks so that now the central graphite peak lies at a position on the edge of the central cathode peak. Because the DVA curve is the summation of the two half-cell DVA curves, the total height for the central graphite peak will ultimately be smaller. This is supported by observing the peak sharpness: if a large reduction in HLD at the graphite had occurred, then a significantly flatter peak would be produced. Here, peak sharpness is largely maintained for most cells, apart from 70% and 80% SoC. Moreover, the valley belonging to the anode at 0.5 Ah shows little change, suggesting the reduction in peak height is predominantly caused by a loss of cyclable lithium and a changing in the balancing of the two electrodes in conjunction with small reductions in HLD.
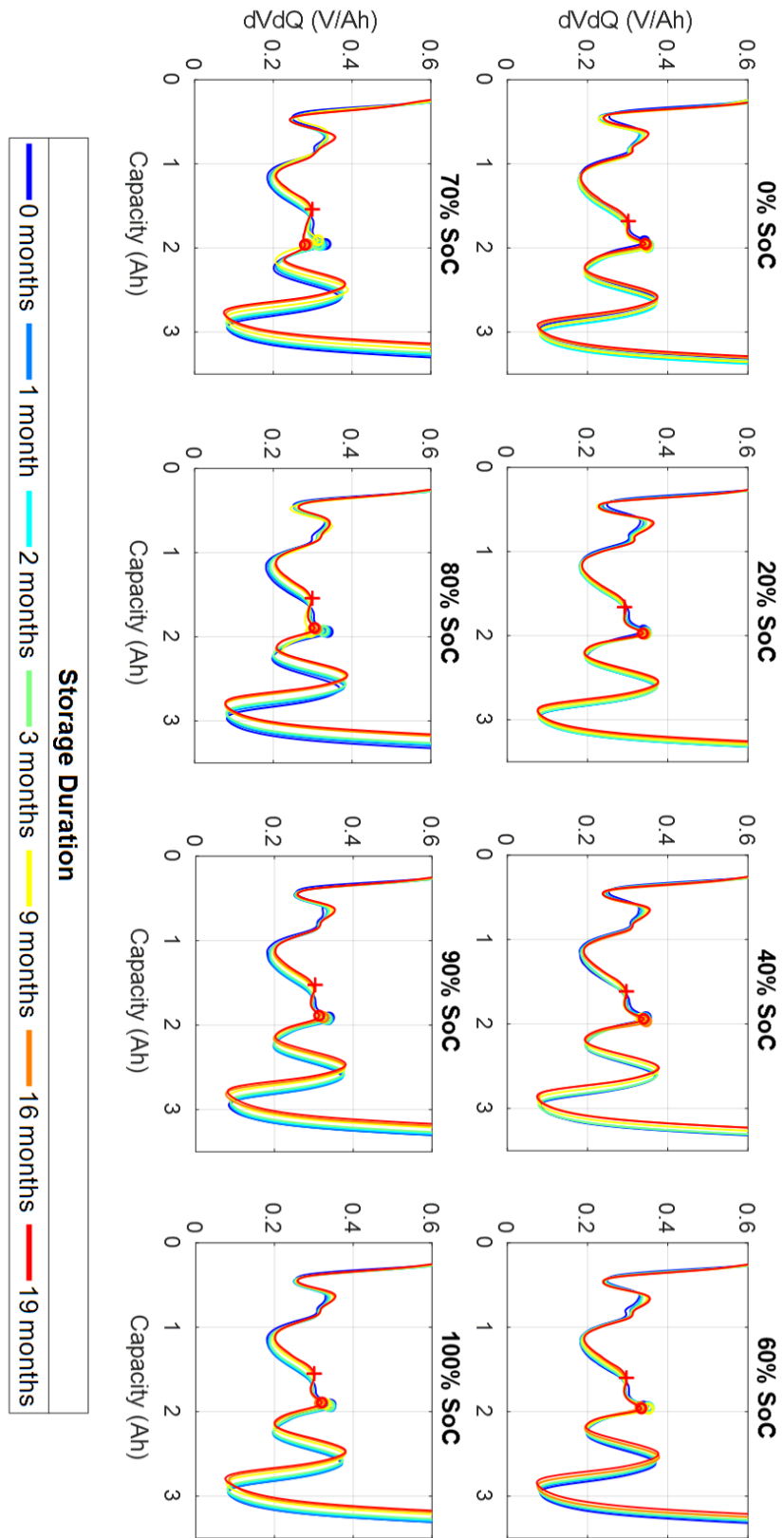
Figure 31. Differential voltage curves for cells stored at 25ºC and multiple SoCs over 19 months. The circle markers highlight the position of the central graphite peak at each time interval. The cross markers indicate the final position of the broad cathode peak.

Robert Burrell - January 2022

To facilitate the identification of degradation modes, the degradation indicators Q1, Q2 and Q3 can be examined in terms of their absolute capacities, as described in section 3.8.2. However, as also discussed in section 3.8.2, Q2 capacities are not necessarily a reliable indicator for the cyclable lithium inventory and that Q_{cell} is a more robust measure. Here, Q2 will be displayed for reference, but will not be interpreted as a measure for cyclable lithium inventory. Figure 32 exhibits the capacity values for each Q region taken from the DVA curves of cells after 19 months of calendar storage. Values are displayed alongside those for a fresh cell, which are taken as an average over all cells in the investigation before storage.
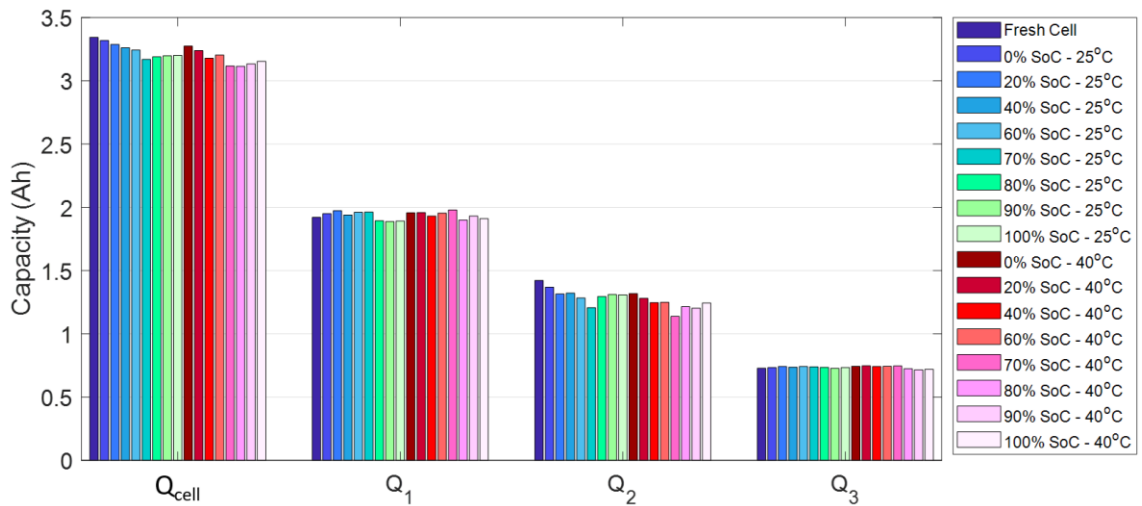
Figure 32. The capacities for Q_{cell}, Q1, Q2 and Q3 regions after 19 months of calendar ageing at multiple SoCs.

The overall capacity Q_{cell} after 19 months forms a spoon-shaped trend with respect to SoC at both temperatures and higher temperature increases capacity fade at each given SoC. Q1, which is linked to the anode capacity, shows only minor changes over 19 months for both temperatures. In the lower SoC region, Q1 values remain approximately equal to or even slightly exceed those of fresh cells. For 80%, 90% and 100%, only a slight drop in Q1 capacity is seen at both temperatures, which corresponds with a substantial increase in resistance for these cells.

Q2 capacities substantially decrease after 19 months at all SoCs. An approximate spoon-shaped trend exists at both temperatures, similar to the trend observed in the overall

capacity Q_{cell}. Q3, which reflects the cathode capacity, shows the least change amongst all regions. No discernible increase or decrease of the capacities can be seen at any SoC or temperature, indicating negligible changes to the cathode storage capabilities after 19 months of calendar ageing.

At the bottom line, the largely parallel behaviour of Q_{cell} and Q2 in Figure 32 points to a loss of lithium inventory as the main cause of capacity fade. In analogy to the arguments proposed by Zulke et al.[13], we attribute the decreasing capacity fade rates between 80 % and 100 % storage SoC to increasing rates of reversible self-discharge (e.g. via shuttle mechanisms) that alleviate the irreversible loss of lithium into passivation film growth.

4.3.2 Effect of Relaxation Periods

Relaxation periods were employed immediately after calendar ageing for 19 months to explore the cells' response to conditions different to their experimental ageing environments. Cells may typically undergo relaxation periods in between periods of use, for example when an EV is at rest. Here, relaxation periods are defined by the storage of cells at near-0% SoC and 25ºC. Since applying a CV discharge at 0% SoC was found to be detrimental to battery health, a CV discharge at 2.8 V with a termination criterion of 10 hours was used to minimise degradation whilst maintaining a low SoC.

4.3.2.1 State-of-Charge Dependency on Capacity Recovery

The relative capacity vs. SoC trends before and after low SoC storage at 25ºC and 40ºC are presented in Figure 33a and Figure 33b, respectively. Discharge capacity values are calculated from 1.0 A discharges during check-ups. After storage at low SoC for 1 month, the spoon shape remains prominent at both temperatures, however the severity of the trend has been reduced slightly, indicating the mechanisms mentioned previously still dominate the overall capacity trend. The capacity-SoC trend exists as a flatter curve after the relaxation period, i.e. greater capacity recovery is observed for higher calendar storage SoCs. For example, little-to-no recovery in capacity is seen for cells previously stored at 0% SoC, yet cells stored at 100% recover up to 2%.
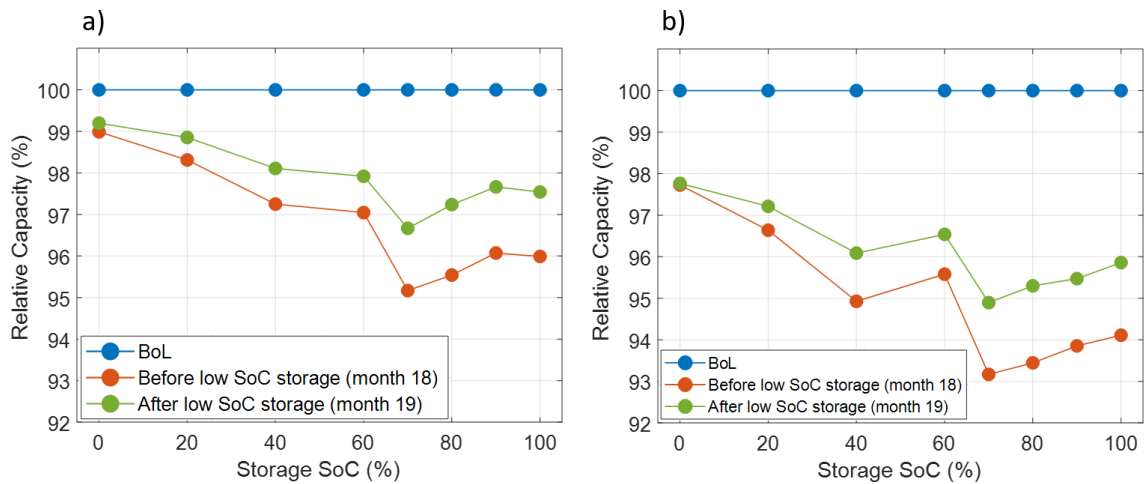
Figure 33. Relative capacity vs. storage SoC before and after low SoC storage for cells aged at (a) 25ºC and (b) 40ºC. Capacity values were obtained during check-up measurements at 25ºC.

Recoveries in capacity observed during low SoC storage are largely a result of lithium diffusion from the passive overhang regions into the active regions, which boost the content of cyclable lithium, and subsequently, the discharge capacity. Please see section 2.3.3 for information on anode overhang. Calendar storage at higher SoCs will create a stronger concentration gradient between the active region and the overhang region, which drives the diffusion of greater quantities of lithium into the overhang regions ('overhang lithium'). During low SoC storage, increasing amounts of returning overhang lithium show as greater capacity recoveries[18].

Looking deeper at the trend, three approximate regions exist in terms of capacity recovered: 0-20%, 40-60% and 70-100%. Similar capacity recoveries are observed for cells in each region, but each region displays different recoveries. For example, 70-100% all show approximately 2% recovery, but 40-60% shows approximately 1% recovery. These regions roughly coincide with the plateau regions of the anode half-cell potential: cells showing a similar recovery in the 70-100% region are all located along the stage I plateau of the graphite, a particularly flat region of the voltage profile[151]. Capacity recovery during low-SoC storage is a proxy for the amount of overhang lithium. The recovered capacity shows plateaux that match those of the anode half-cell potentials. This indicates that the local electrochemical potential is the driving force for lateral lithium exodus into the overhang area. If, in contrast, the local lithium concentration in graphite

was the main driving force, the amount of overhang lithium would simply follow SoC. This observation is in line with the observation of sluggish equilibrations of lateral SoC inhomogeneities in electrodes in voltage plateaux regions: Concentration gradients in such regions result in smaller spatial variances of electrochemical potential[19,152].

Likewise, capacity gains from recovering a given amount of overhang lithium are determined by the anode potential rather than the SoC. Flat potential regions will thus exhibit similar capacity recoveries, whereas the steep potential profile at low SoC causes the dissimilarities in recoveries. Moreover, the SoC during relaxation and calendar ageing at 0% SoC are very similar, thus lithium lost to the overhang regions for these cells is expected to be miniscule.

4.3.2.2 The Limited Effect of Relaxation on Resistance

Shown in Figure 34a and Figure 34b are the relative DC resistances vs. storage SoC plots for cells aged at 25⁰C and 40⁰C before and after low SoC storage, respectively. After low SoC storage, the resistance trend across the SoC range largely remains the same. Less than 1% change is observed in most cases, with a maximum of 1.5% seen for the cell previously stored at 70% SoC and 40⁰C. No discernible effects can be deduced with respect to the DC resistance when subjecting these cells to relaxation periods at low storage SoC. Moreover, no differences between cells previously aged at different temperatures exist. This lack of alteration occurs concurrently with a recovery in capacity during the same period. Therefore, the processes that contribute to the recovery in capacity do not appear to trigger a change in the DC resistance. If these processes are hypothesised to be lithium diffusion and redistribution, then the lithium mobility has shown to have no effect on resistance in this instance.
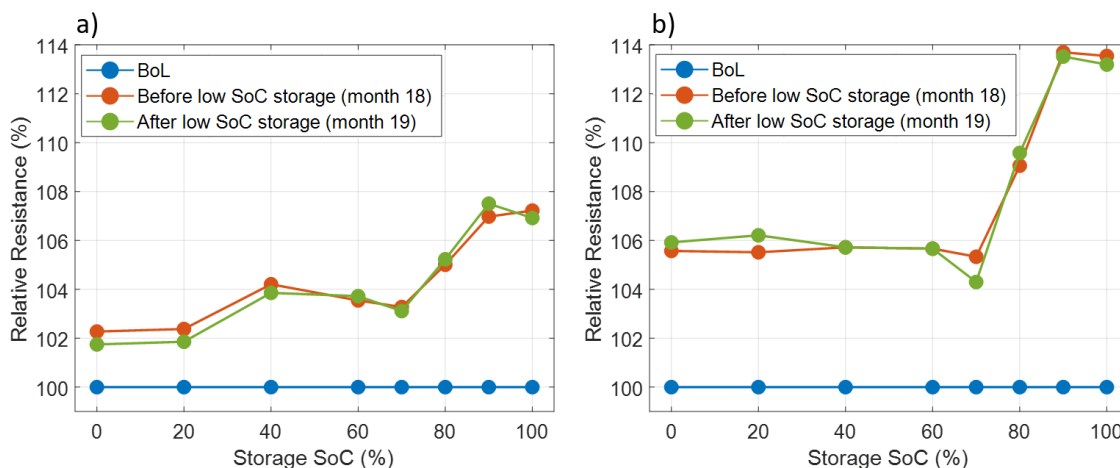
Figure 34. Relative resistance vs. storage SoC before and after low SoC storage for cells aged at (a) 25⁰C and (b) 40⁰C. Resistance values were obtained during check-up measurements at 25⁰C.

To separate out the relative contributions to the overall resistance, EIS was performed before and after relaxation periods. Figure 35a and Figure 35b display the Nyquist plots for cells calendar aged for 19 months at 25°C and at 70% and 100% SoC, respectively, and after 1 month of low SoC storage. Figure 35c and Figure 35d display the corresponding DRT. Observing the point at which the plots in figure Figure 35a and Figure 35b intercept the x-axis reveals changes in the ohmic resistance of the cell. 1 month of storage at low SoC produces little change in the ohmic resistance of either cell, indicating little change in the electrolyte composition and/or current collectors. Slight variations of the two semi circles and diffusion tail are seen during the relaxation period; thus, the DRT are plotted to examine this further in Figure 35c and Figure 35d. The highest frequency peak (lowest time constant) is suggested to correspond to the properties of the SEI, which show a small change after storage at low SoC. For both cells, a slight reduction in the resistance of this process is seen, which is related to Li^+ migration through the SEI[116,153,154]. The central region of the DRT plot ($10^{-2} – 10^1$ s) is suggested to relate to the charge transfer at either electrode and reveals very little alteration in the resistance or frequencies associated with these processes after storage. The peak with the lowest frequency is suggested to correspond to the solid and liquid phase diffusion of lithium and shows differing results depending on the previous storage SoC. The cell calendar aged at 70% SoC produces an increase in the resistance after low SoC storage, whereas the cell calendar aged at 100% SoC produces a decrease. This result does not correlate with any substantial differences observed during the ageing of these cells and thus requires further investigation in future studies.
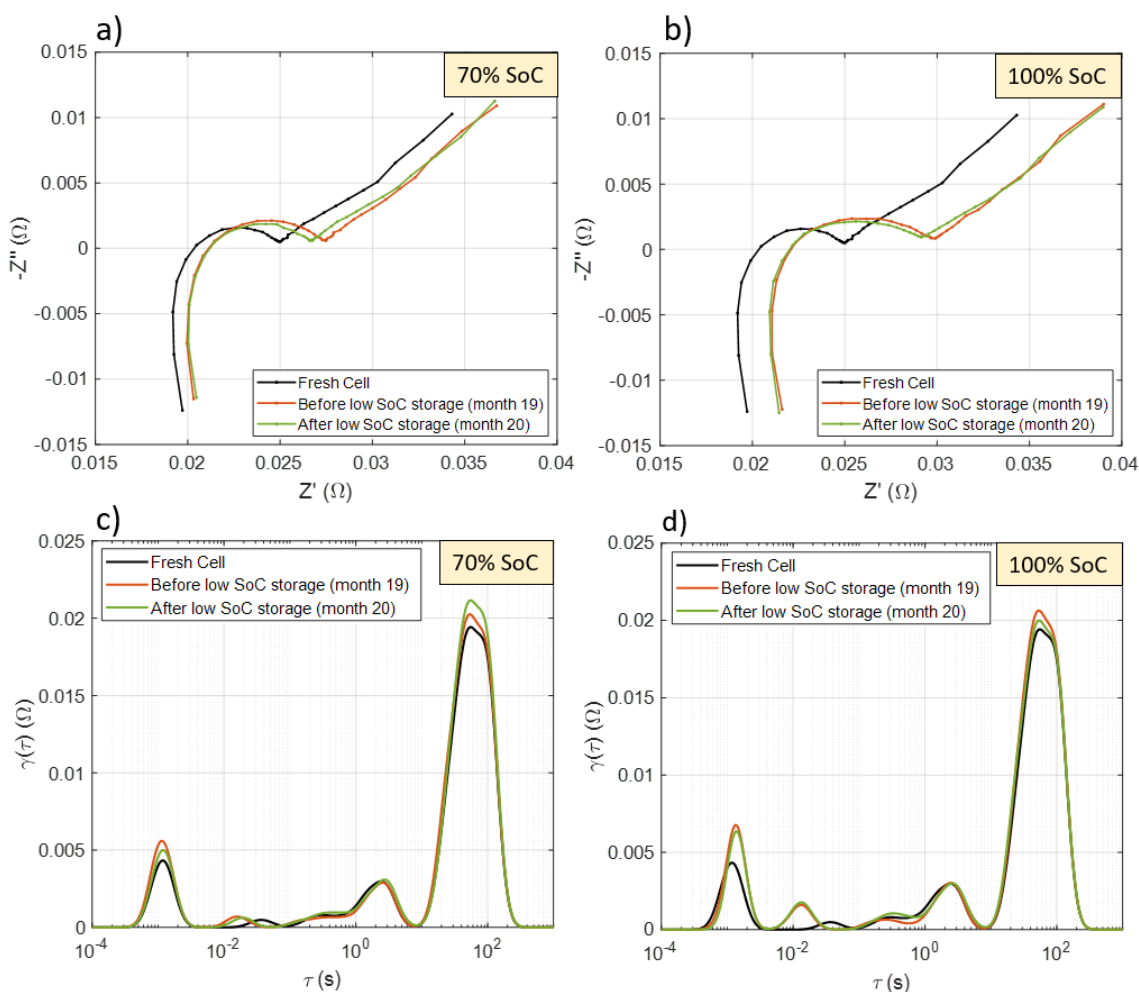
Figure 35. Nyquist and DRT plots for selected cells before and after low SoC storage at 25⁰C. (a) and (b) calendar aged at 70% SoC for 18 months, (b) and (d) calendar aged at 100% SoC for 18 months.

4.3.2.3 The Observable Influence of Relaxation on DVA Features

The evolution of the DVA spectra before and after low SoC storage are displayed in Figure 36 for cells previously aged at 25⁰C. For all cells, the recoveries in capacity observed in Figure 33 are visible in the DVA plots, which manifests itself as a stretching of the DVA curve along the capacity axis. For storage SoCs of 60% and below in Figure 36, very little change in the DVA profile is seen across the entire curve, apart from the stretch mentioned previously. These cells exhibited only small changes in the DVA curve during initial calendar ageing, which is reflected by little-to-no change in Figure 36. From 70% to 100% SoC, larger variations in the profiles can be seen, particularly in the Q1 region. Firstly, the central graphite peak located at 1.9 Ah shifts to the right after low SoC

storage, indicating an increase in the storage capabilities of the anode. This is paired with a marked increase in the sharpness of the peak, which is representative of an increase in HLD of the graphite[92,129]. Low SoC storage promotes lithium mobility within the active material and reduces the SoC range across the graphite to produce a sharper voltage step transition.
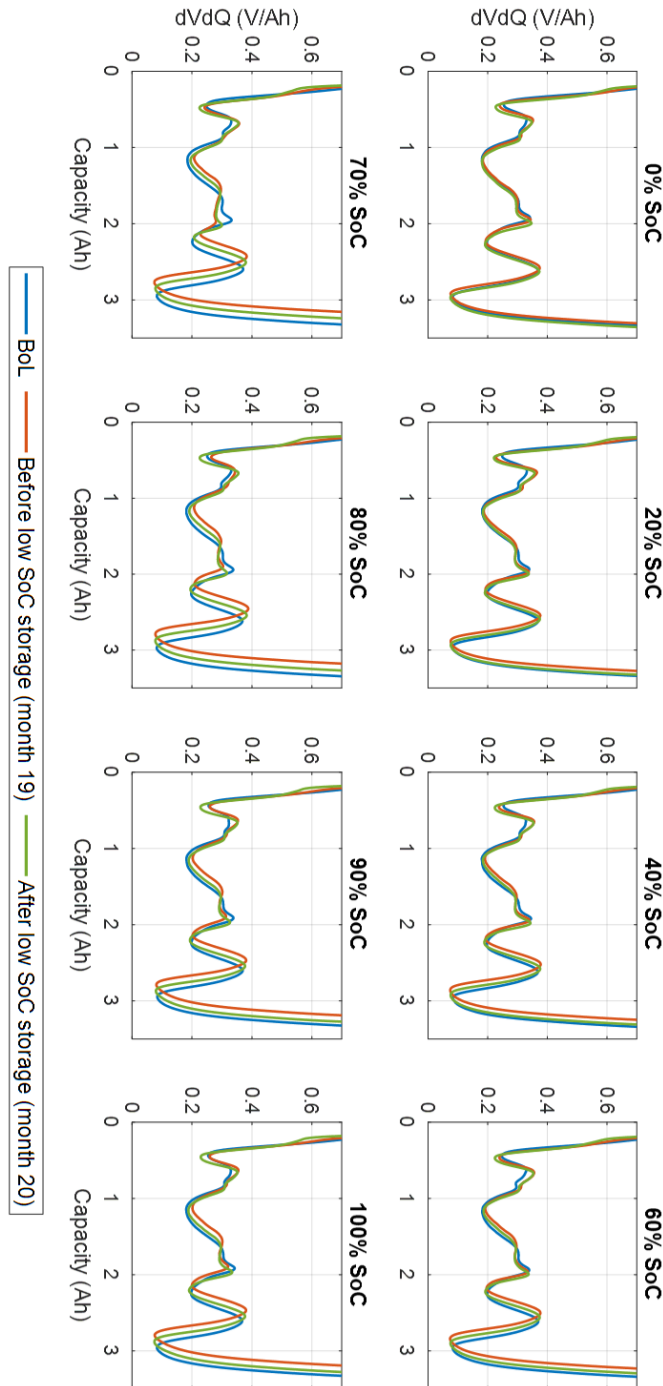
Figure 36. Differential voltage curves for cells calendar aged at 25⁰C and multiple SoCs before and after low-SoC storage.

The relative capacity vs. SoC trends before and after relaxation for each Q region are presented in Figure 37. The BoL values at 100% relative capacity are specific to each specified Q region for a fresh cell. Figure 37a displays the relative capacities for the entire capacity region during the charging sequence for DVA. Unlike in Figure 33a, very little capacity is recovered after low SoC storage for 1 month and no SoC dependency is observed. There are a number of differences which can contribute to the observed difference. Firstly, the DVA plots and Q regions here are extracted from a charging sequence, whereas the total capacities presented in Figure 33a are extracted from a discharging sequence. Additionally, the charging sequence for calculation of the DVA curves is only a CC charge and thus Q_{cell} does not represent the total capacity needed to charge the cell to 100% SoC, whereas the capacities seen in Figure 33a are extracted after a CCCV charge to 100% SoC. Lastly, DVA requires a slow charging sequence (0.25 A) to achieve sufficient resolution of the peaks, which contrasts with the moderate discharge current (1.0 A) used for the discharge capacities in Figure 33.

The largest recovery in capacity across the SoC range is associated with the cathode in the Q3 region, as seen in Figure 37d. The capacities for the Q3 region recover to near-100% for all SoCs, aside from 70% and 80%. This reiterates that storage at these SoCs and temperature produce such little degradation of the cathode and that capacity lost from the Q3 region during calendar ageing can largely be recovered with a low SoC relaxation period of just 1 month. The Q1 and Q2 regions in Figure 37b and Figure 37c, respectively, show only very small changes in capacity (<0.3%) after 1 month of low SoC storage. Most cells show an increase in relative capacity, particularly at SoCs <80%.

The low current charge used for DVA (duration: 13.5 Hours) likely provides sufficient time for some lateral redistribution of lithium within the anode, thus any recoveries arising from this effect will likely be minimal. By contrast, the moderate current discharge used for the calculation of values in Figure 33a is unlikely to provide sufficient time for lateral redistribution. However, because the low SoC storage may have reduced the variation in SoC distribution in the anode, greater capacities could be recovered due to the discharging cut-off voltage being reached later in time[155].
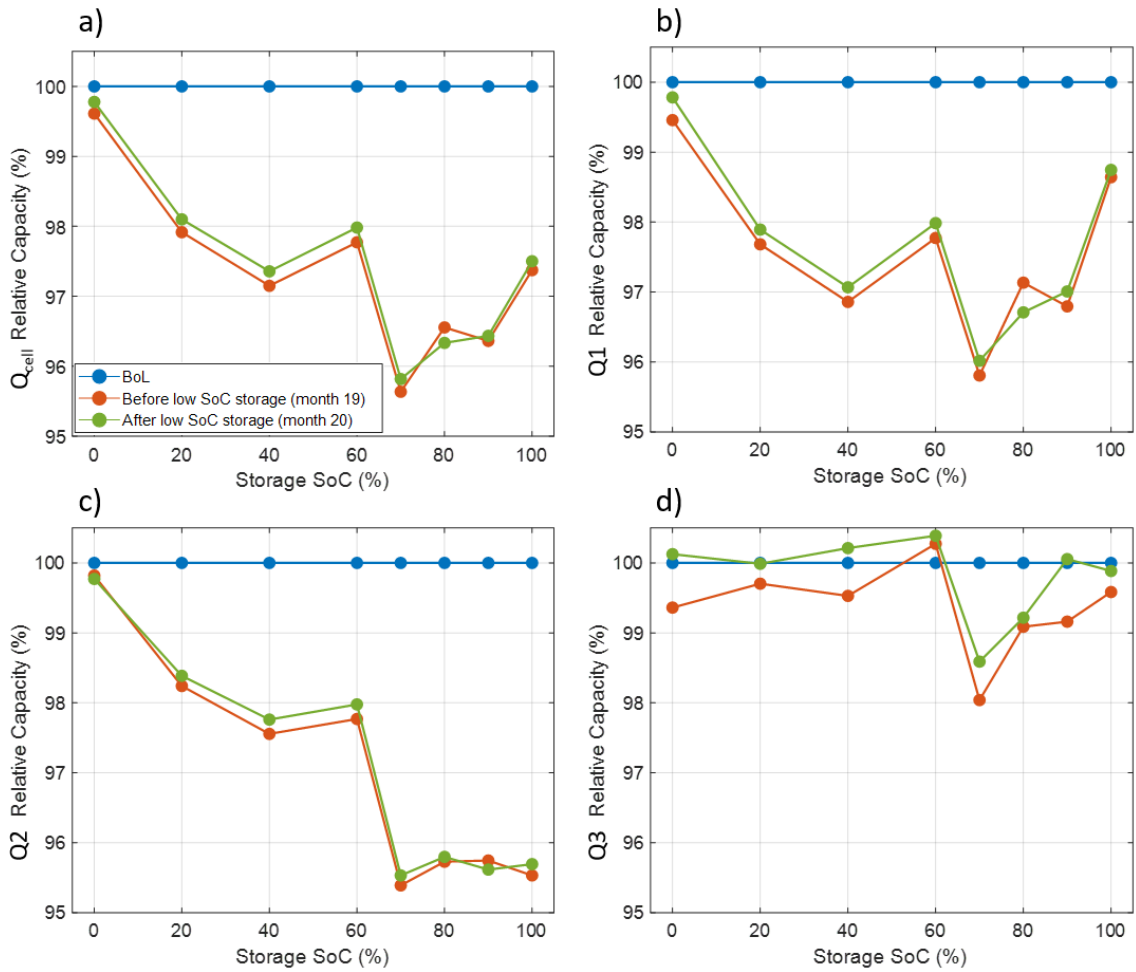
Figure 37. Relative capacity as a function of SoC before and after low SoC storage for the different Q regions obtained from DVA for cells stored at 25ºC. (a) Q_{tot}, (b) Q1, (c) Q2 and (d) Q3.

4.3.3 Cycling after Calendar Ageing

After calendar ageing and relaxation periods, all cells were subjected to one of two cycling conditions: aggressive or soft cycling. Cycling parameters for both conditions are detailed in Table 4 and Table 5 at the beginning of this chapter. In this section, previous cell history will be evaluated for its influence on the subsequent ageing under each cycling condition. All plots present duty cycles for a given condition.

4.3.3.1 Relative Capacity

Figure 38 displays the relative capacity for cells cycled under two cycling protocol conditions at 25⁰C, where the capacities at 0 cycles are a continuation of the capacities after low SoC storage. The rate of capacity fade is greater for cells under aggressive conditions in all cases and is exacerbated by elevated temperatures during previous calendar storage. Moreover, the non-linear ageing is reached sooner, and the non-linear decline in capacity is more rapid for cells that were previously calendar aged at 40⁰C with the exception of the 70% SoC cells, which show similar points of decline. Calendar ageing at elevated temperatures likely produces a thicker, more restrictive SEI due to the increased production of reaction products at the graphite-electrolyte interface[105,139]. This then further restricts Li^+ diffusion through the SEI during the charging process, which leads to lithium plating, and subsequently, non-linear ageing[45,136]. Non-linear ageing begins to occur at approximately 85-90% relative capacity for all cells cycling under the aggressive conditions.
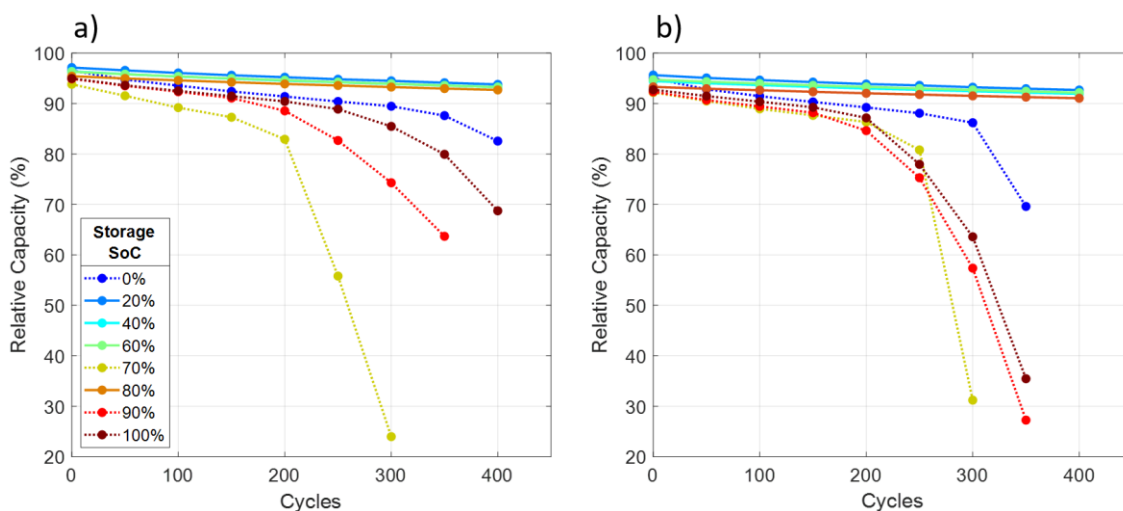
Figure 38.Relative capacities for cells cycled after calendar storage at various SoCs and at (a) 25⁰C and (b) 40⁰C. Cells with a previous calendar storage SoC of 20, 40, 60 and 80 % were cycled under soft cycling conditions (+/- 1.0 A, 4.2 V/3.4 V), and cells with and SoC of 0, 70, 90 and 100 % were cycled under aggressive conditions (+/- 1.7 A, 4.2 V/2.5 V). Al cycling was performed at 25ºC.

When observing a given SoC for the aggressive cycling condition, an approximate trend is apparent: the onset of non-linear ageing is in accordance with the capacity fade

observed during calendar ageing. For example, the 70% SoC cell showed the greatest loss in capacity during calendar ageing and showed the most rapid non-linear decline in capacity during cycling. This demonstrates two points. Firstly, that capacity fade during calendar ageing provides an approximate indication of current SoH of a cell before non-linear ageing. Secondly, it supports the proposed mechanism for the spoon-shaped trend during calendar ageing. If storage at SoCs >70% reduces the available Li^+ current for irreversible SEI formation, then one may expect these cells to have a thinner, less restrictive SEI and thus be less susceptible to Li plating. In this study, storage at high SoCs appears to have a relatively benign effect on cell capacity during both calendar and cycle ageing when compared with storage at 70% SoC.

All cells cycling under soft conditions (previous storage SoC = 20, 40, 60 and 80 %) in Figure 38 produce very little capacity fade over 400 cycles, with no indication of non-linear ageing. Less than 5% capacity fade is observed over 400 cycles, which demonstrates the high cycle life that can be achieved under these conditions for this cell. In addition, the variation in capacity fade between the different cells is far less under soft cycling than under aggressive cycling and the capacities narrowly converge to a difference of ~3% after 400 cycles. The trend in relative capacity for the SoCs remains unchanged throughout cycling, which is approximately an increase in capacity fade with previous storage SoC. Conservative cycling routines appear to draw no additional ageing as a result of previous history and that the soft cycling parameters do not induce any path dependence when solely observing relative capacity.

4.3.3.2 Relative Resistance

The evolution of relative resistance during cycling is presented in Figure 39 for cells previously calendar aged at various SoCs and at 25ºC and 40ºC. Aggressive cycling conditions promote faster resistance increase than soft cycling conditions in all cases. Moreover, non-linear resistance increase is seen for all aggressively cycled cells, a trend that mirrors the non-linear capacity fade in Figure 38. Cells enter non-linear resistance increase in the order that is seen for capacity: 70, 90, 100 and finally 0% SoC. This is evidence of a positive feedback loop during non-linear ageing. More aggressive charge and discharge currents will increase the rate of degradation processes, such as the breakdown and reformation of the SEI, which promotes resistance increase by restricting

the diffusion of Li through the passivating layer[125]. A higher cell resistance will then create a larger voltage drop that may push the anode potential below 0 V during charging, at which point Li plating becomes thermodynamically feasible[29]. Plated Li can then react with the electrolyte to promote further SEI growth, which consumes lithium and degrades ionic kinetics, leading to more lithium plating[136]. Using this rationale, one might expect to observe a sooner onset of non-linear ageing for cells that start cycling with a higher resistance, however this is not the case. Between 70% to 100% storage SoC, cells show an increase in resistance after calendar ageing at higher SoCs: a maximum difference of approximately 8% (see Figure 29). During subsequent cycling, cells stored at higher SoCs throughout calendar ageing enter non-linear ageing later than those stored at lower SoCs. An explanation for this may lie in the processes underpinning calendar storage at high SoCs. The more extreme anode/cathode potential at 100% SoC compared to 70% SoC may contribute to amplified rates of side reactions occurring at either electrode. At the anode, these reactions could consume a larger share of the Li^+ current that would otherwise be utilised in SEI formation, thus reducing the irreversible lithium losses and reducing the thickness of the SEI. However, the reactions occurring at the anode and cathode likely consume greater quantities of electrolyte, which reduces the ionic conductivity and consequently increases the resistance[81]. The cell stored at 100% SoC now has a thinner, less restrictive SEI, but a decreased ionic conductivity that contributes significantly to the DC resistance observed. When cycled, this cell is then less susceptible to lithium plating than the cell stored at 70% SoC, which has a thicker SEI.

All cells cycled under soft cycling conditions show very little increase in DC resistance over 400 cycles and the trend between the various SoCs remains the same throughout, regardless of the previous calendar ageing temperature. The cell stored at 0% and 80% SoC during calendar ageing show the least and most resistance increase before and after the cycling period, respectively. Nevertheless, only a maximum of ~6% relative resistance increase is observed over 400 cycles at either temperature. This demonstrates that raising the discharging cut-off voltage to 3.4 V and reducing the charge/discharge current to 1.0 A significantly improves the cycle life of these cells, irrespective of the previous storage conditions. It is therefore recommended that these cells are cycled with conservative operation conditions if the cells have been stored for extended periods of time in order to extend cycle life.
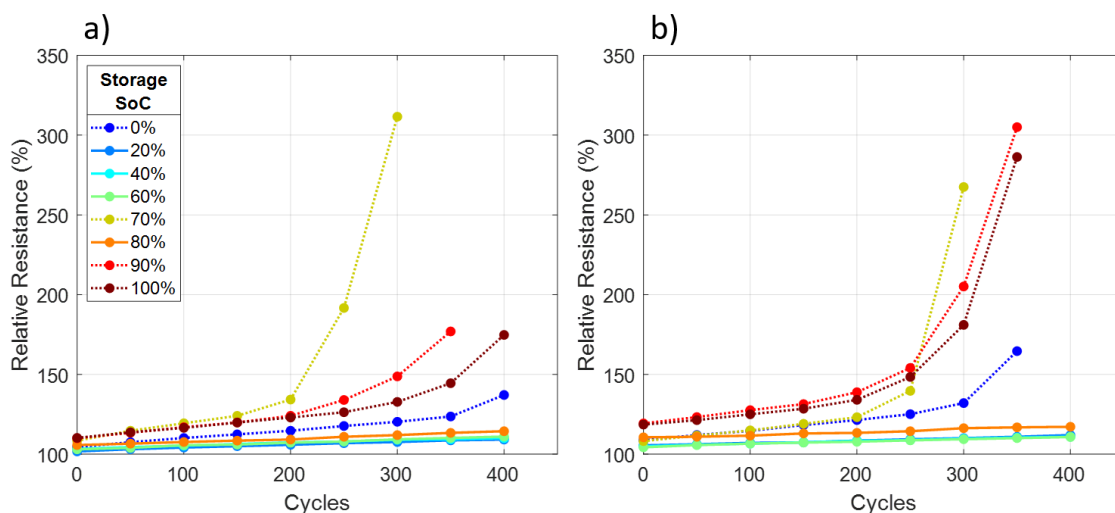
Figure 39. Relative resistances for cells cycled after calendar storage at various SoCs and at (a) 25ºC and (b) 40ºC. Cells with a previous calendar storage SoC of 20, 40, 60 and 80 % were cycled under soft cycling conditions (+/- 1.0 A, 4.2 V/3.4 V), and cells with an SoC of 0, 70, 90 and 100 % SoC were cycled under aggressive conditions (+/- 1.7 A, 4.2 V/2.5 V). All cycling was carried out at 25ºC.

4.3.3.3 Differential Voltage Analysis

The evolution of the DVA plots for aggressively cycled cells is presented in Figure 40. Final DVA plots have been removed in some cases to preserve clarity. Light pink curves represent the cell in a completely fresh state before calendar or cycle ageing.

All cells show similar trends throughout cycling, albeit at different rates. Cells previously stored at 0% SoC display the greatest preservation of DVA shape throughout cycling, however they also show very little change between the fresh cell and the end of calendar ageing for 20 months. Most notable changes are observed in the Q1 region, where the central graphite peak shifts to lower capacities and shows a reduction in sharpness to the point where it is no longer visible. The former indicates a reduction in the storage capabilities of the anode and the latter a decrease in the homogeneity of lithium distribution (HLD)[95]. In addition, the Q3 region exhibits a reduction in capacity, which is demonstrated by the increase in the cathode peak height and highlighted by the red arrow for the 0% SoC cell at 40ºC. This is indicative of a decrease of the Q3 region and a reduction of the cathode's storage capabilities. The cells stored at 70% SoC show the most rapid reduction in the central graphite peak height, which completely disappears after just 100 cycles at both temperatures. However, these cells began cycling with an

already reduced peak sharpness, which highlights the detrimental effect of storing these cells at 70% SoC on both initial ageing and cycling.
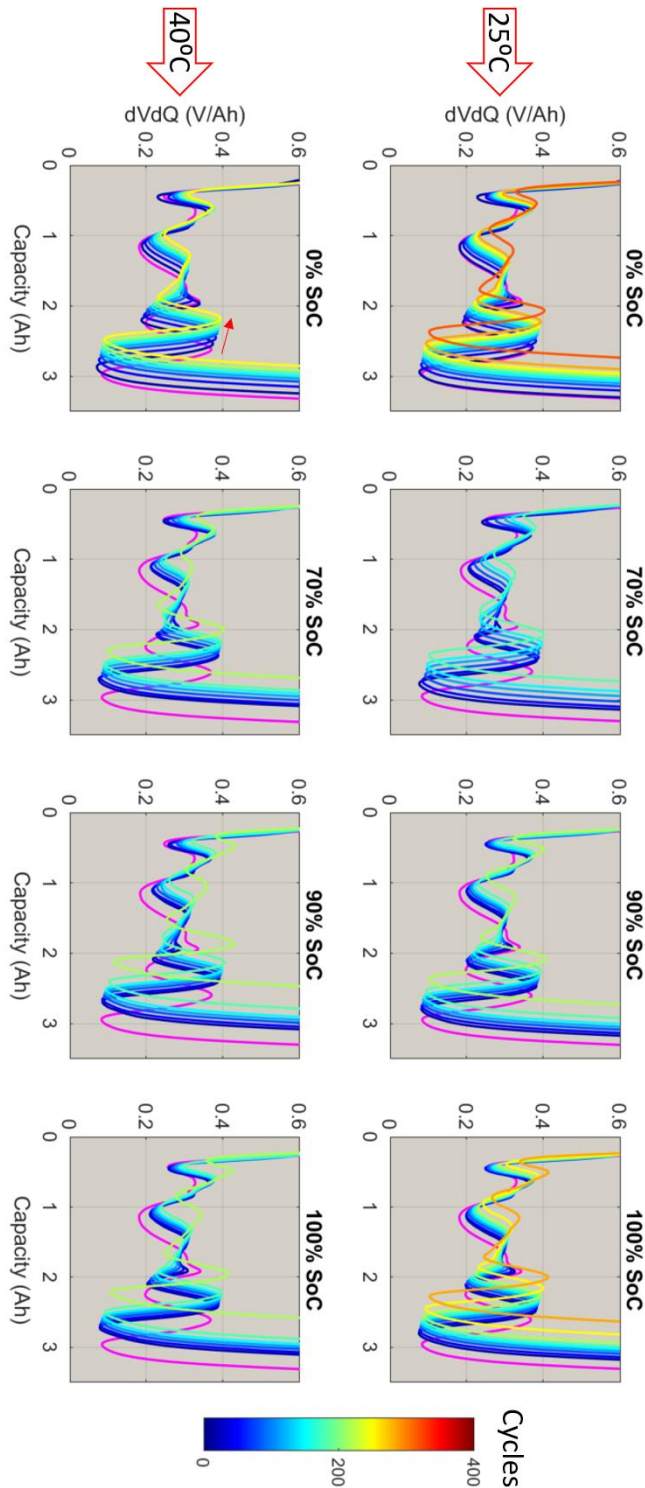
Figure 40. DVA plots for all cells subjected to aggressive cycling conditions. Graph labels represent previous storage SoCs during calendar ageing. Top row: cells calendar aged at 25⁰C, bottom row: cells calendar aged at 40⁰C. The pink curve is the DVA profile of a fresh cell.

During non-linear ageing, two things are most prominent: collapse of the Q1 region and also significant reductions of the Q2 and Q_{cell} regions. This is best demonstrated for the cell stored at 90% SoC and 40ºC. Both of these effects occurring in conjunction with one another is indicative of the likely processes occurring during non-linear ageing and the presence of a feedback loop. As the Q1 capacities diminish during linear ageing, the SEI at the anode approaches a critical point in which the pore diameter is reduced to an extent that substantially limits the flux of Li^+ through it. This causes more rapid reductions in the Q1 capacities as the anode cannot be charged to the same extent. Because the same amount of charge is still trying to be passed through the anode, lithium plating likely proceeds. Due to the now slow rate of diffusion through the SEI, Li^+ is now compounded at the surface of the anode as Li metal; a process which rapidly consumes lithium and reduces the cyclable lithium content. Further, this plated Li can react with the electrolyte to contribute to capacity loss[29]. This would then significantly alter the cyclable lithium content, which could then cause the rapid decline in the Q_{cell} region observed in Figure 40. Increasing the temperature during calendar storage from 25ºC to 40ºC does not seem to have any noticeable effect on the evolution of the DVAs during aggressive cycling, as the trends remain similar between the two temperatures.

Figure 41 displays the progression of DVA profiles for cells subjected to soft cycling conditions over 400 cycles, where the pink curves represent each cell in a fresh condition before calendar or cycle ageing.

Greater DVA shape preservation is observed for all cells during soft cycling when compared to aggressive cycling, particularly in the Q1 region. Cycling under these conditions preserves a more uniform lithium distribution within the anode, perhaps due to lower localised current densities from using more conservative charge/discharge currents and voltage limits. In addition, the location of the central graphite peak remains largely unchanged with respect to capacity for all conditions, thus the Q1 region retains almost all its initial capacity and the anode displays only minor changes with its storage capabilities. Moreover, the Q3 capacities exhibit only minor reductions for all cells, indicating very little change with respect to the cathode's storage capabilities during cycling. The majority of capacity loss for all cells arises in the Q_{cell} (and Q2) region, which suggests that a loss of cyclable lithium is the key cause of capacity fade for all cells subjected to soft cycling conditions[126]. In terms of the influence of previous history on

cycle ageing, no prominent trend is detected between storage SoC/temperature and alteration of DVA shape and Q region capacities during cycling.
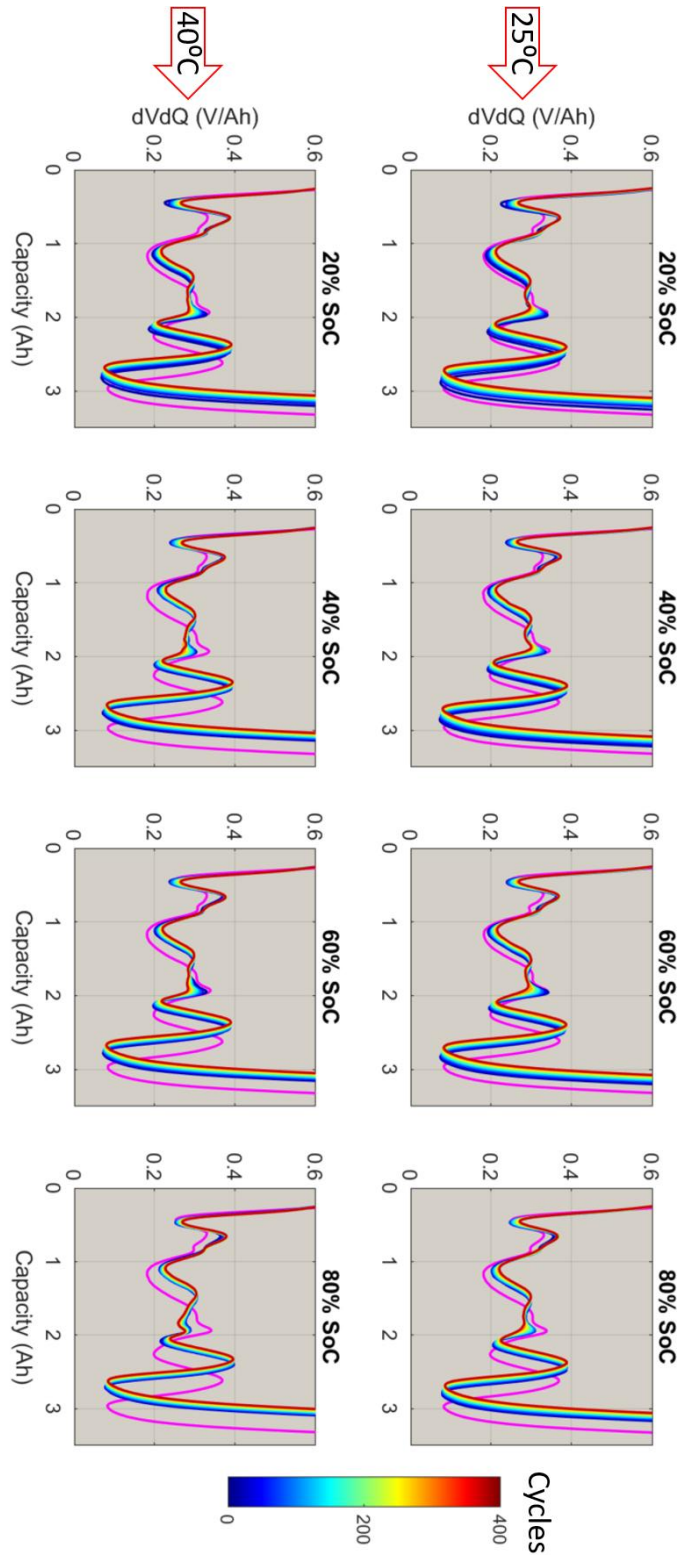
Figure 41. DVA plots for all cells subjected to soft cycling conditions. Graph labels represent previous storage SoCs during calendar ageing. Top row: cells calendar aged at 25⁰C, bottom row: cells calendar aged at 40⁰C. The pink curve is the DVA profile of the fresh cell before calendar ageing.

Larger differences between the cells are established by the end of the calendar ageing period than throughout the cycling period. For example, the cell calendar aged at 80% SoC and 40ºC exhibits substantial changes of the central graphite peak between a fresh cell and 0 cycles, but only minor changes during the cycling period. This could be evidence of a proposed path dependence whereby the ageing mechanisms during the calendar period inflict an irreversible change of the DVA profile, and thus the cell's chemical characteristics. Once this irreversible alteration has been made, the cell continues to age according to the path defined during the calendar periods and does not relax to form a shape similar to other cells. I.e., after 400 cycles, the ageing of the cells does not converge to a similar shape that would otherwise indicate that any previous history has been nullified. Although the overall ageing mechanisms are similar for all cells, the subtleties with respect to the DVA profiles remain individual throughout cycling.

4.4 Conclusions

Spoon Shape Capacity-SoC Trend

Calendar ageing of cells at eight SoCs and two temperatures revealed an approximate spoon shape in the relative capacity vs. SoC trend, where 70% SoC storage was most detrimental and increasing towards 100% SoC produced less capacity fade. DVA revealed that this trend was dominated by the Q_{cell} (and to some extent Q2) capacities and thus indicated a loss of cyclable lithium was the primary cause of capacity fade. Based on previous reports, it was proposed that higher cathode and lower anode potentials increased the rate of side reactions at both electrodes, respectively. The key driver for the spoon shape was initially proposed by Zulke et al.[13] and was further identified in this thesis. It was suggested to be an increased frequency of shuttle mechanisms that transport electrons from the anode to the cathode via oxalate ions. This induced a reversible self-discharge and removed Li^+ current from the ongoing SEI formation process, which reduced irreversible lithium loss at progressively higher SoCs. The availability of total shared Li^+ current for SEI formation, which was determined by the rate of shuttle-based

self-discharge, either limited or promoted irreversible capacity loss. These reaction mechanisms were illustrated by use of a Sankey-style mass flow diagram.

The Benefit of Employing Relaxation Periods

Relaxation periods, where cells were stored at near 0% SoC, were useful for recovering and quantifying reversible capacity losses. Reversible losses were mainly attributable to lithium diffusion to the passive anode overhang areas during storage, particularly at high SoC. Approximate SoC regions of similar capacity recovery were identified, which corresponded to the plateau regions on the anode half-cell potential. The spoon shaped capacity-SoC trend persisted throughout low SoC storage, which indicated the irreversible nature of the trend. A recovery in capacity was not matched with a significant increase or decrease in relative DC resistance for any SoC. If capacity recovery was mainly lithium redistribution within the anode, then these processes did not correspond to changes in DC resistance. Prominent peaks in the DVA spectra corresponding to the graphite increased in sharpness after low SoC storage, which was suggestive of increases in the HLD and a narrower SoC distribution across the anode.

Relative Capacity as an Indicator for Non-linear Ageing

Harsh cycling conditions of higher charge/discharge currents and more extreme voltage limits promoted non-linear ageing after as little as 200 cycles. Cells entered non-linear ageing in the order of greatest capacity fade during calendar ageing: 70%, 90%, 100% and finally 0% SoC. This contrasted with the DC resistance increase during calendar ageing, which showed 100% to have the greatest increases. DC resistance for 100% SoC was proposed to have greater contributions from electrolyte conductivity due to the increased rate of oxidation/reduction reactions at high SoC, whereas 70% was said to have a thicker SEI. A thicker SEI for cells stored at 70% SoC would promote lithium plating sooner during cycling, which may then react with electrolyte to produce a feedback loop that is characteristic of non-linear ageing. This supported the proposed spoon shape mechanism of reduced Li^+ current for SEI formation at storage SoCs >70% and demonstrated path dependent ageing for calendar aged cells.

Path Dependence During Cycling Under Conservative Conditions

A potential ageing path dependence was identified for cells cycled under soft cycling conditions. Capacity and resistance data highlighted little change in degradation rate amongst the cells and whose ageing trend persisted over 400 cycles. However, DVA revealed subtle differences in the shape of the voltage profiles. DVA profiles at the end of the calendar ageing periods differed between cells stored at different SoCs. These differences were preserved during cycle ageing, where cells appeared to continue ageing along their predefined path, which was exhibited as a retention of the DVA features specific to each cell. If no path dependence was established during calendar ageing, then one might expect the DVA profiles for different cells to converge to similar shapes during cycling. Such path dependencies were strongly shown for cells cycled at high C-rates (aggressive), but were somewhat less pronounced at low C-rates (soft) and may not play a significant role in the ageing under conservative ageing conditions.

5 The Identification and Management of Reversible Capacity Losses

5.1 Introduction

Cycle ageing studies of lithium-ion batteries (LIBs) performed under well-defined conditions are essential tools for assisting the development of cycle-life prediction models, which commonly report the irreversible capacity losses as a function of battery ageing time[85,105,156]. Such studies typically utilise fixed protocols but with varied parameters such as the voltage window, depth-of-discharge (DoD) and C-rate. These studies are often time consuming, leading to accelerated ageing tests with a minimal number of cycles. It is commonly known that time spent at certain voltages can draw smaller or larger contributions from reversible processes, however, reversible losses accumulated during cycling are seldom documented and examined. These reversible processes have largely been ascribed to the effects from the anode overhang[18,93,155,157] and inhomogeneities of lithium distribution within the active material[51,95,128,129,158], including the formation of a dense covering layer on the surface of the anode[52,155,159]. In addition, the effects of pressure gradients[86] and temperature gradients[160] have also been considered.

Perhaps the most influential factor to the reversible losses are the anode overhang areas, which correspond to the perimeter portions of the anode active material that do not have a direct cathode counterpart[92,161]. The anode overhang, sometimes referred to as the passive electrode, can act as a lithium sink or a lithium source depending on the extension of time spent by the cell at a certain voltage[162]. At higher cell voltages, the disparity in electrochemical potential between active anode and anode overhang creates a concentration gradient that drives lithium diffusion into these peripheral regions, which then becomes inaccessible in the short term. This flow of active lithium between the active

(active anode) and the passive electrode (anode overhang) is also known as the passive electrode effect[162]. Passive electrode effects are reversible because lithium ions tend to diffuse back to the active electrode if enough time is allowed once the opposite gradient situation is established, for instance when the cell is fully discharged. During the routine cycling of commercial LIBs, which usually contain an intentionally oversized anode to reduce lithium plating at the edges, this dynamic process may go unnoticed or be ascribed to irreversible capacity fade, as the time periods spent in certain voltage and SoC regions are not explicitly accounted for. From a methodological perspective, it is therefore important to consider the ageing conditions under which these reversible processes are most likely to occur in order to manage reversible capacity losses and to improve cycle-life predictions.

In practice, high-drain devices powered by LiBs are rarely charged to the maximum charging voltage specified by the manufacturer, mainly to increase operation safety and cycle life, but little is disclosed about how reducing the charging voltage can act on the reversible capacity fade observed. Recent studies have demonstrated that carrying out shallow cycling procedures about median state-of-charge (SoC) values resulted in an increased reversible capacity loss in the electrodes of an LiFePO$_4$/Graphite cell as a result of insufficient driving forces for the rehomogenisation of Li within the active material[152,163]. In this chapter, the effects of limiting the cycling voltage window on the irreversible and reversible ageing of cells is explored. Rest periods between blocks of continuous cycling are introduced to allow for the quantification of reversible capacity losses to the anode overhang; a method previously shown not only to quantify reversible losses but also to extend the lifetime of the cell[18,51,152]. By examining lithium mobility within the graphite active material, a mechanism for reversible capacity loss during cycling is proposed.

5.2 Experimental Strategy

A two-part experimental ageing study was performed to identify and manage reversible capacity losses during the cycling of LIBs. Initially, cells were cycled in restricted voltage windows that limited both the charging and discharging cut-off voltage. Subsequently, all cycled cells were entered into relaxation periods, where the cells were stored at defined SoCs to probe and quantify reversible capacity losses.

5.2.1 Lithium-ion Battery Studied and Equipment Used

All cells used in this study were high-energy 18650 cylindrical cells manufactured by Samsung with the model name INR18650-35E. The anode chemistry was a graphite/silicon oxide (SiO_x) blend and the cathode chemistry was lithium nickel-cobalt-aluminium ($LiN_{0.8}Co_{0.15}Al_{0.05}$). The cell has a rated capacity of 3.35 Ah with maximum voltage limits of 4.2 V – 2.5 V and a nominal voltage of 3.6 V. A more comprehensive list of cell parameters can be found in Table 1. Throughout experimental testing, the cell was operated within the manufacturer's safety limits at all times.

All cells were cycled on BaSyTec CTS battery cyclers at 25ºC in Memmert IP260 PP thermal chambers to ensure identical environmental conditions. Additional galvanostatic intermittent titration technique (GITT) measurements were carried out on a Biologic BCS 815 system in a Espec PU2J thermal chamber. Battery Dynamics 3-pin cell holders were used for all testing on both systems.

5.2.2 Experimental Ageing Procedure

5.2.2.1 Cycle Ageing

During cycling procedures, all cells were charged using +1.0 A (0.29 C) and +1.7 A (0.5 C) in alternating blocks of 48 cycles (i.e., 48 cycles at +1.0 A followed by 48 cycles +1.7 A). The discharging current used was -1.0 A in all cases. To investigate the effect of restricted voltage windows on battery ageing, two charging cut-off voltages and three discharging cut-off voltages were used to give a total of six different test conditions. These voltage windows, along with additional details on the cycling procedures can be found in Table 6. During cycling, constant current (CC) discharge and constant current constant voltage (CCCV) charging was used with a current cut-off of 0.1 A (0.029 C) during the CV phase.

Table 6. Protocol parameters used during cycle-ageing procedures.

Cell	Charge cut-off voltage/V	Discharge cut-off voltage/V	Charge current/A	Discharge current/A	SoC Range (%)	Mean SoC (%)
1	4.2	3.4	+1.0/+1.7	-1.0	8.7 – 100	54
2	4.2	3.1	+1.0/+1.7	-1.0	1.5 – 100	51
3	4.2	2.5	+1.0/+1.7	-1.0	0 – 100	50
4	4.1	3.4	+1.0/+1.7	-1.0	8.7 – 86.5	48
5	4.1	3.1	+1.0/+1.7	-1.0	1.5 – 86.5	44
6	4.1	2.5	+1.0/+1.7	-1.0	0 – 86.5	43

To evaluate performance during ageing, check-up procedures were performed before testing and after each 48-cycle block. All check-ups were performed at 25ºC in thermal chambers for identical environmental conditions. Throughout cycling, the check-up procedure was identical to that seen in Figure 9a (section 3.2.1, page 26) and consisted of a 0.25 A CC charging step for DVA, a -1.0 A discharge for capacity measurements and two 10 s discharge pulses of -3.0 A to determine DC resistances.

5.2.2.2 Relaxation Periods

After 528 cycles, all cells entered a two-phase relaxation procedure. In the first phase, cells were stored at 50% SoC for 12 weeks. In the second phase, cells were stored at 0% SoC for 12 weeks. After a storage interval of three weeks, an updated check-up procedure was used, which can be found in Figure 9b (section 3.2.1, page 26). To achieve the desired storage SoC of 50% an additional protocol was used after each check-up that consisted of a +1.0 A charging sequence after a full CC discharge from 4.2 V to 2.5 V. This discharge step was used to calculate total remaining capacity of the cell periodically during ageing, which was subsequently used for determining 50% SoC. To achieve 0% SoC, the check-up test was terminated after the CC discharge to 2.5 V. For the duration of both relaxation phases, the cells were stored at 25ºC. For clarity on the experimental procedure, a flow diagram is presented in Figure 42.
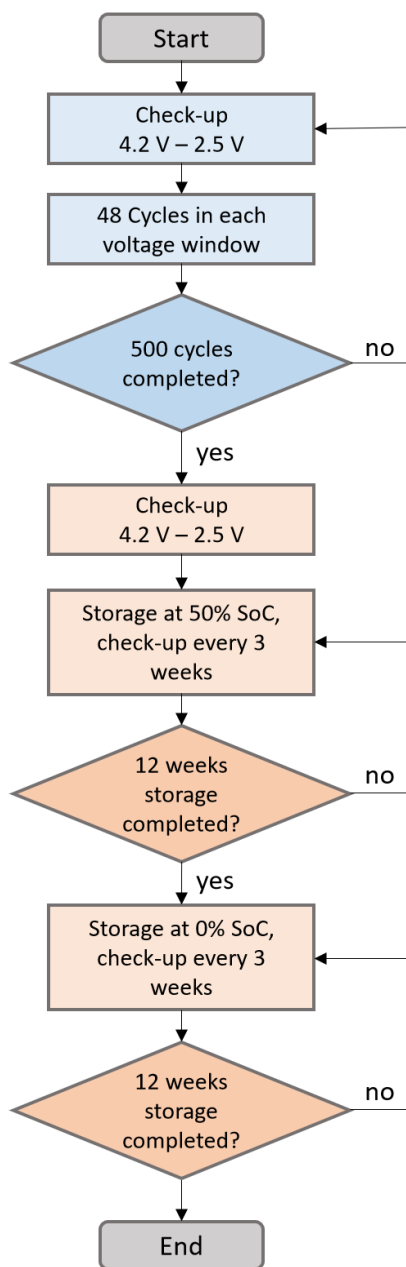
Figure 42. Flow diagram of the experimental procedure. Blue shading denotes the cycling periods and orange shading denotes storage periods. Voltage limits expressed in check-up box is applied during all check-ups.

5.2.2.3 Half-Cell Fabrication and Testing

Additional electrochemical testing required the fabrication of half-cells from harvested anode and cathode material of a disassembled full-cell, as reported previously[32]. The full details of coin cell fabrication can be found in section 3.1.3 (page 26).

Galvanostatic intermittent titration technique (GITT) was performed in order to obtain diffusion coefficients for the active materials. Anode half-cells were charged to 0.0 V Vs.

Robert Burrell - January 2022

Li/Li$^+$ and then subjected to 10-minute discharge pulses of 1.25 mA to 0.8 V Vs. Li/Li$^+$ with a relaxation of 45 minutes of relaxation in between each pulse followed by 10-minute charge pulses of 1.25 mA to 0.0 V Vs. Li/Li$^+$ with 45 minutes of relaxation. Cathode half cells were charged and discharged using 1.25 mA 10-minute pulses between 3.4 V and 4.3 V. The diffusion coefficients were calculated using Sand's approach[108].

5.3 Results and Discussion

In this study, the impact of multiple voltage windows on battery ageing during cycling was explored. Two charging cut-off voltages and three discharging cut-off voltages gave six different test conditions. Furthermore, calendar storage periods (see section 2.3.2, page 17) were employed immediately after cycling to quantify reversible capacity losses. A deeper examination of the unusual effect of lowering the charging cut-off voltage is presented, and a reversible capacity loss mechanism is proposed. In this section, the ageing data is plotted against duty cycle number for the ease of comparison of the different test conditions. Alternative plots versus full equivalent cycles can be found in the appendix highlighting that the conclusions remain valid.

5.3.1 Impact of Voltage Window During Cycling

Lithium-ion batteries within electronic devices are typically operated in restricted voltage limits in order to extend cell life. Therefore, this section describes the direct comparison of cycling within restricted voltage windows and its effect on capacity, resistance and differential voltage curves. Cells are cycled in six different voltage windows, comprised of 2 charging and three discharging cut-off voltages, with moderately fast charging currents for this Samsung 35E cell.

5.3.1.1 Relative Capacity and Capacity Utilisation – the Unusual Effect of a Higher Charging Voltage

The effect of cycling within restricted voltage windows on relative capacity is displayed in Figure 43, where all capacities displayed are obtained from a 1.0 A discharge during each check-up. After an initial drop in relative capacity, all cells display a near-linear capacity fade up to 528 cycles, albeit with varying slopes. A noticeably faster reduction in capacity is observed for cells discharged to lower cut-off voltages. This is particularly apparent for both cells discharged to 2.5 V, which show >2% greater reduction in capacity over 528 cycles. This effect is likely as a result of both higher intercalation related stresses in the nearly completely delithiated anode and volume fluctuations associated with the silicon oxide species[12,14]. Strong Li concentration gradients between surface and bulk graphite in the early stages of intercalation leads to an increase of Li_xC d-spacing at the surface of the graphite particles. Higher local stresses at the graphite edge sites can then result in the breakage of c-c bonds, thus exposing more graphite to the electrolyte, which results in greater (re)formation of the SEI[14]. In addition, large volume fluctuations of the SiO_x during (de)lithiation pulverises the particles, leading to isolation of active material and increased SEI formation as new surfaces are exposed to the electrolyte[12,30,54,164].

For the same charging cut-off voltage, lowering the discharging cut-off voltage from 3.4 V to 3.1 V induces ≤1% additional capacity fade over 528 cycles. Based on a reduction of the discharge capacity by ~15% when discharging to 3.4 V instead of 3.1 V, this would result in a substantial reduction in the total discharge throughput of the cell over 528 cycles, with little change in relative capacity. Furthermore, lowering the discharging cut-off voltage to 2.5 V from 3.1 V increases the discharge capacity by ~10%, however this is met with ~2.5% additional capacity fade. From a usage standpoint, it is therefore advisable to impose a discharging cut-off voltage of 3.1 V over 3.4 V or 2.5 V to maximise output whilst minimising the trade-off with battery ageing.

By raising the charging cut-off voltage from 4.1 V to 4.2 V, capacity fade was reduced by ~1% in all cases, regardless of the discharging cut-off voltage. Furthermore, this difference in relative capacity between cells with different charging cut-off voltages appears to be developed in the early stages of cycling and is subsequently maintained through to 528 cycles. This effect is observed with little change in its magnitude throughout cycling in most cases and is particularly apparent for the cells discharged to 2.5 V. Because the magnitude of the gap does not continue to increase further once it has

established, the capacity loss mechanism must be technically capped. If this effect were an accumulation of damage due to one or more ageing processes, then one would expect this difference between capacities for 4.1 V and 4.2 V to continue to enlarge during cycling.
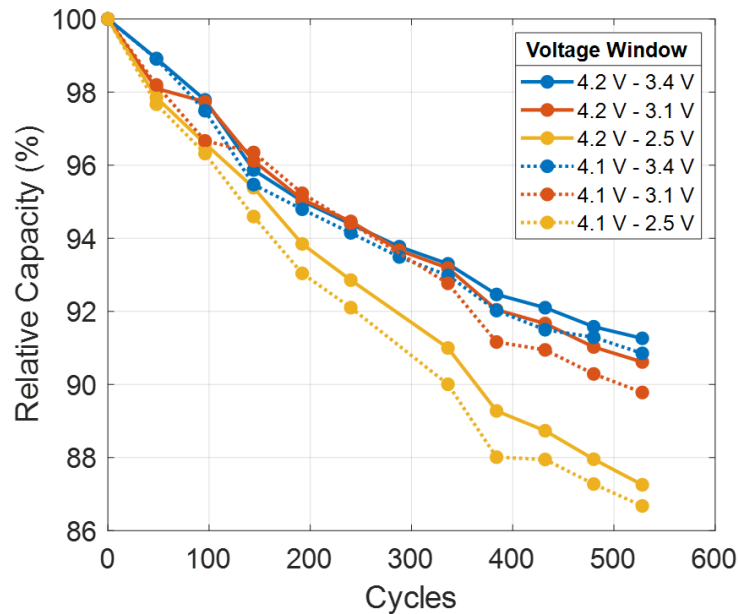
Figure 43. Relative capacity vs. cycles for all 6 different cycling voltage windows. Cycles are given as duty cycles and represent one charge and discharge sequence in a given voltage window.

5.3.1.2 Resistance Increases with Larger Voltage Windows

Figure 44 displays the relative DC resistance values for all 6 test conditions obtained from each check-up during cycling. Resistance values were calculated from the step response during a 10 s -3.0 A discharge pulse at 50% SoC. Over the first 50 cycles, all cells show either an initial decrease or very little change in internal resistance, despite the sharp decrease in capacity observed in Figure 43 From 50 cycles on, incremental increases in resistance are seen for all test conditions. The cells charged to 4.2 V show greater increases in resistance by up to 12.5% over their 4.1 V counterparts, which is the reverse outcome based on the capacity measurements in Figure 43.

The initial decrease in resistance could be due to the maturation of the SEI during the early stages of cycling and/or the redistribution of Li within the active materials. A

redistribution of Li, particularly within the graphite particles, could produce a concentration gradient within the particle that shortens the deintercalation path, ultimately reducing the resistance[158].

The observation that charging to 4.2 than 4.1 V increases resistance indicates two things: firstly, capacity fade is not simply inversely correlated with resistance, and that the technically capped capacity loss mechanism may not significantly contribute to resistance increase.

When examining the effect of different discharging cut-off voltages for the same charging cut-off voltage, cycling to lower voltages progressively increases resistance over 528 cycles. For example, with a charging voltage of 4.2 V, lowering the discharging cut-off voltage from 3.4 V to 3.1 V to 2.5 V increases the resistance by ~5% and 15%, respectively. This would support the mechanism of increased SEI formation when repeatedly discharging to lower voltages, which would produce a thicker, more restrictive passivation layer due to pulverisation. It is therefore advised to avoid the steep voltage profile regions when discharging to 2.5 V, but instead choose 3.1 V to minimise battery ageing, but maximising capacity utilisation.
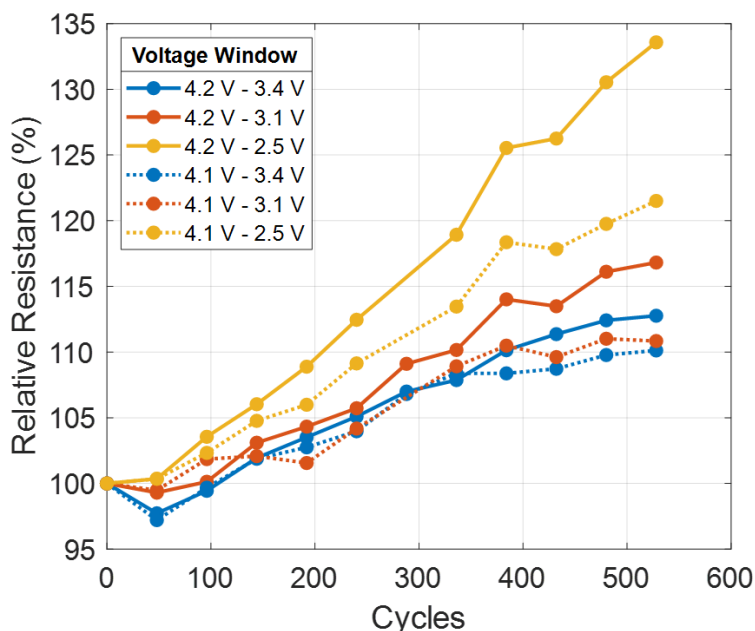
Figure 44. Relative DC resistance vs. cycles for all 6 different cycling voltage windows. Cycles are given as duty cycles and represent one charge and discharge sequence in a given voltage window.

5.3.1.3 Smoothing of Differential Voltage Analysis Features Poses a Challenge for Marker Tracking

The differential voltage analysis (DVA) profiles for all 6 test conditions over 528 cycles are shown aligned to the left in Figure 45 and to the right in Figure 46. Aligning to the left aids comparison of the Q1 and Q_{cell} regions, whilst aligning to the right highlights changes associated with the Q3 region. This, along with definitions of the three Q regions and DVA calculation, can be found in section 3.8.2 (page 42). In it has been suggested that Q2 provides no further information than Q_{cell} and that Q_{cell} is a more robust indicator for the cyclable lithium inventory.

Starting with Figure 45, significant smearing of the DVA curve is observed in the Q1 region, which makes the identification and quantification of peak shifts challenging, especially when comparing all test conditions. The central graphite peak located at around 1.9 Ah shows a substantial flattening and broadening with cycling for all cells, to the point at which it merges with a cathode peak and is no longer visible in some cases after less than 250 cycles (e.g. 4.1 V to 3.4 V).

An inhomogeneous distribution of lithium in the graphite, described as a lower homogeneity of lithium distribution (HLD), is the probable cause of what is observed here[18,95,128,129]. A broad state-of-charge (SoC) range across the anode means the configurational transitions occur at different points in time during a charge or discharge. A given transition would then not be displayed as a sharp peak, but as an average over different points in time to produce a gradient that is shallower. The differential of this shallower gradient is then demonstrated as a flatter peak (see section 3.8.2, page 43). This flattening of the central graphite peak occurs with a shift to lower capacities (left), indicating a reduction in the Q1 region and thus a reduction of the storage capabilities of the anode. Due to the substantial smearing of the Q1 region in all cells, specific differences in the magnitude of degradation modes between the test conditions could not be quantified.

With all curves aligned to the right in Figure 46, the Q3 region can be closely examined. All cells show exceptional alignment of the cathode peak at approximately -0.7 Ah,

indicating very little change to the storage capabilities of the cathode over 528 cycles. These cycling parameters present conditions that have very little effect on the cathode over 528, which shows almost no apparent degradation related to the cathode.
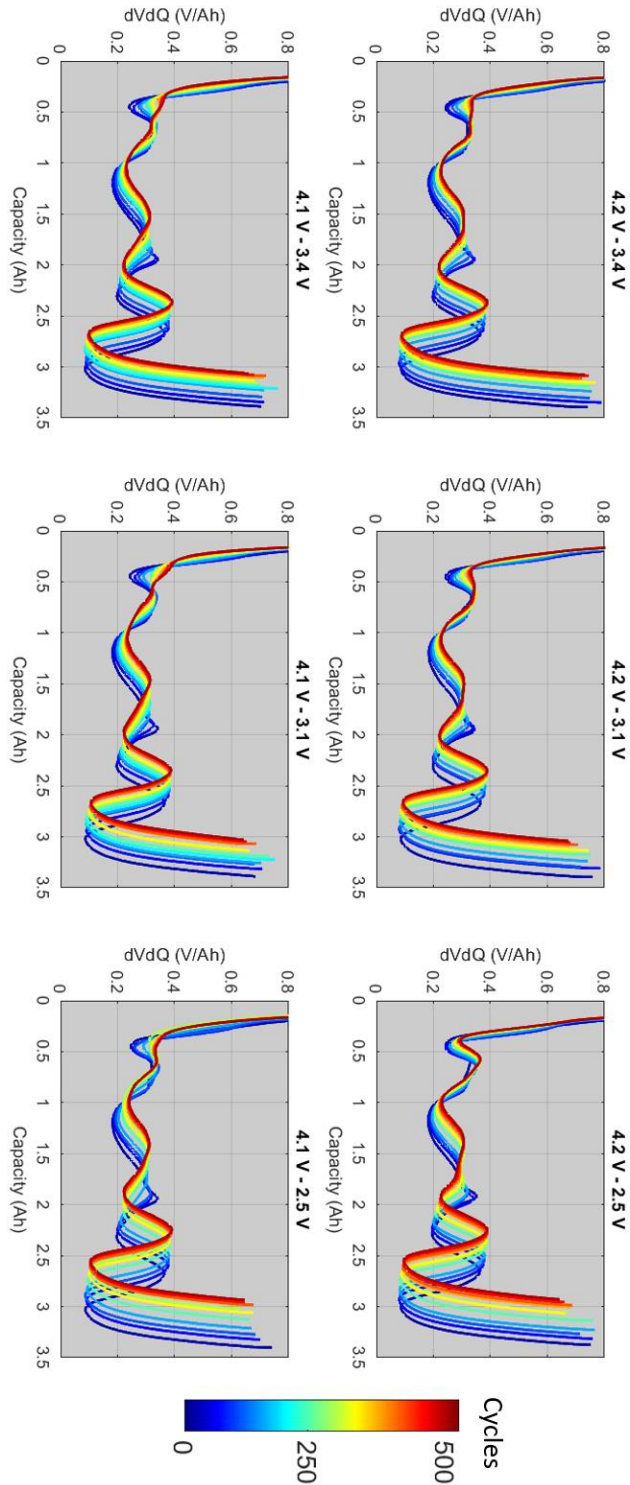
Figure 45. Left-aligned DVA profiles obtained during each check-up over 528 cycles for all six test conditions. DVAs were calculated from a 0.25 A charging sequence.
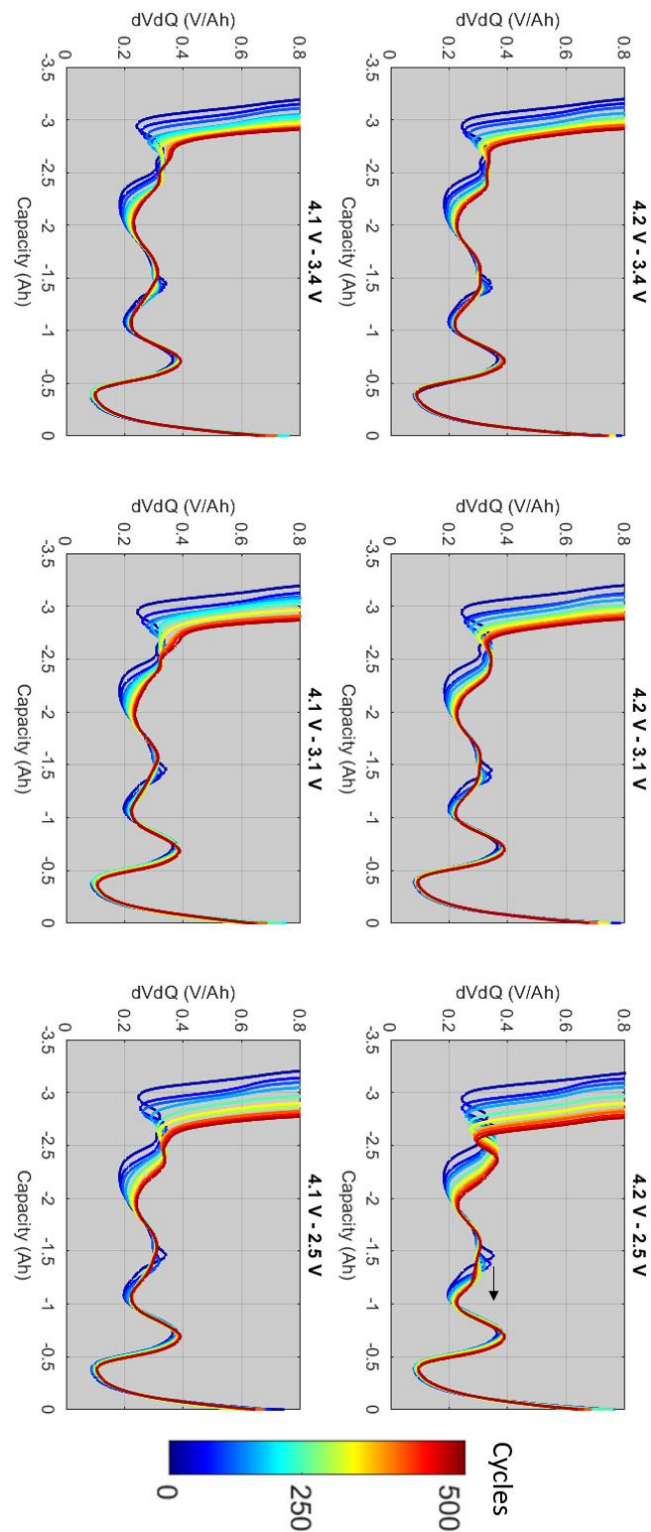
Figure 46. Right-aligned DVA profiles obtained during each check-up over 528 cycles for all six test conditions. DVAs were calculated from a 0.25 A charging sequence.

5.3.2 Impact of Storage Periods

After the initial cycling period, all cells were stored at defined SoCs to observe their response with respect to capacity/resistance recovery and the redistribution of Li within the active materials. It has been previously demonstrated that storage periods can yield important information about reversible capacity effects, such as recovery of lithium from the anode overhang areas and a redistribution of Li[18]. Therefore, storage for 12 weeks at 50% SoC followed by an additional 12 weeks at 0% SoC was used to probe such effects and to elucidate a potential mechanism for the technically capped capacity loss process seen in Figure 43.

5.3.2.1 The Recovery in Capacity After Storage

Figure 47 displays the relative capacities for all 6 cells during the storage periods immediately after cycling. Therefore, at t=0, the relative capacities shown in Figure 47 are the same capacities as the last data points exhibited in Figure 43. When storing the cells at 50% SoC, there is little change in the relative capacity for cells previously charged to 4.2 V during cycling, however, small gains in capacity are observed for cells previously charged to 4.1 V during cycling. As the average SoC during cycling is higher than 50% due to CV phases at the end of charge, storage at 50% SoC brings the system to an SoC lower than what it was previously, enabling lithium from the anode overhang regions to be recovered. In addition, the capacity for cells with the same discharging cut-off voltage but a different charging cut-off voltage appears to converge to the same point after 12 weeks of storage.

After just 3 weeks of storage at 0% SoC, all cells show substantial increases in capacity of up to 2%. From week 3 to week 12, further gains can be observed in most cases, although slight reductions in capacity are visible in week 12 for some, indicating the maximum recoverable capacity occurred at around week 9 under these conditions. Interestingly, the cells previously cycled to 4.1 V showed greater recoveries of capacity over their 4.2 V counterparts, with a maximum recovery of 2.5% during the 0% SoC

storage period. This means a significant portion of the capacity loss for cells charged to 4.1 V during cycling is reversible, and now the ageing trend observed at the end of cycling has been reversed; the irreversible ageing for the cells charged to 4.2 V is greater.

The origin of the capacity recovery when storing the cells at 0% SoC likely lies with the anode overhang. Concentration gradients between the overhang and the active regions will drive Li diffusion into and out of the overhang regions throughout the life of a cell[19,93]. A quantity of Li will thus be stored in the overhang regions during cycling. When stored at 0% SoC, the concentration of Li in the overhang regions will be higher than the concentration of Li in the active anode regions, which have now largely been depleted. This creates a concentration gradient that drives Li diffusion back into the active region and is observable as a boost in capacity output, as seen in Figure 47. Because more capacity has been recovered during low SoC storage for those cells previously cycled to 4.1 V, it is fair to assume that more Li has been lost to the overhang regions during cycling for these cells. This phenomenon could also explain the technically capped capacity loss mechanism; the more Li lost to the overhang during cycling, the shallower the (average) concentration gradient becomes, to a point where there is no net concentration gradient. At this point, there would be no further net Li diffusion to the overhang regions, thus no further capacity is lost.
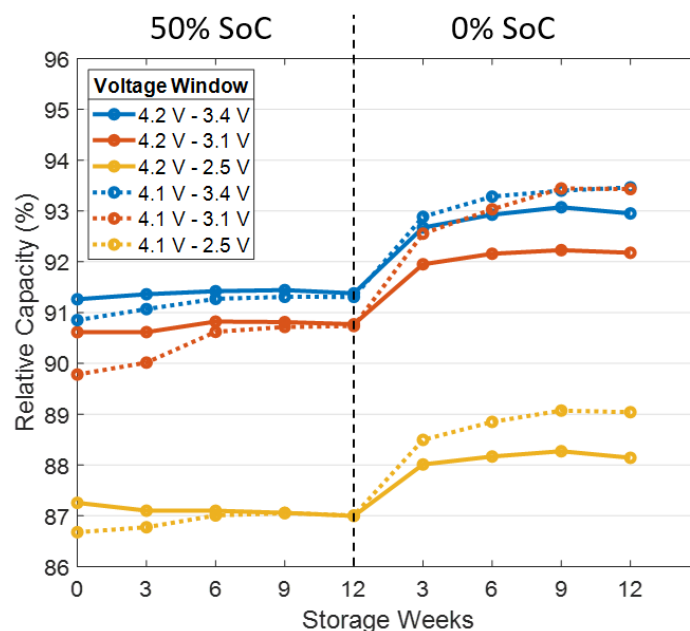
Figure 47. Relative capacity vs. storage weeks at 50% and 0% SoC with a temperature of 25ºC. The figure is a continuation of the relative capacity values in Figure 43.

5.3.2.2 Resistance does not Correlate with Capacity During Storage

The relative resistances during the storage periods at 50% and 0% SoC are displayed in Figure 48 and are a continuation of the resistance values given in Figure 44. All cells show an almost identical trend; a sizeable decrease in resistance (up to 6%) over the first 3 weeks of storage at 50% SoC, a flattening of the curve between week 3 and 6, a moderate increase in resistance (up to 4%) between week 6 and week 9, and finally a steady but slight increase in resistance through to the end of the 0% SoC storage period. Reducing the storage SoC from 50% to 0% appears to induce no noticeable change in relative resistance at all.
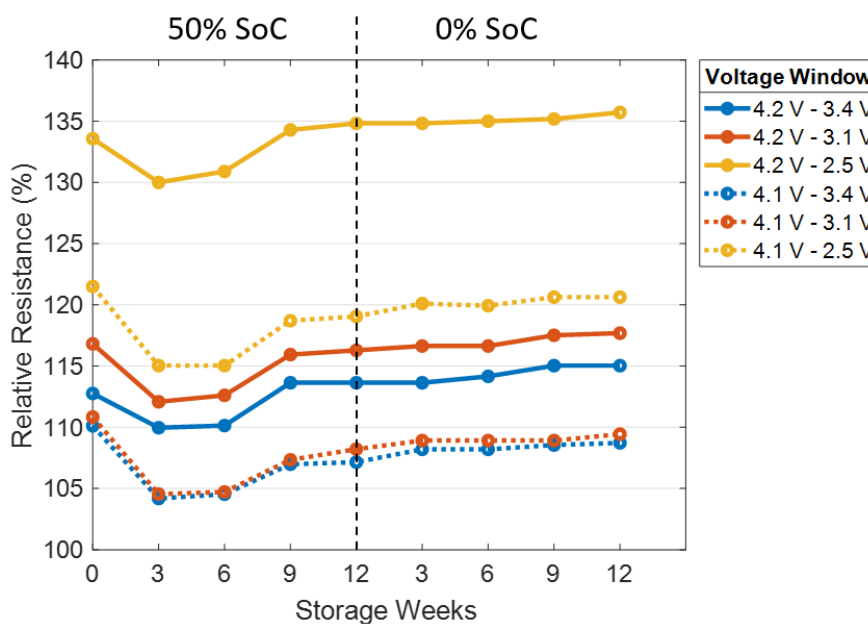
Figure 48. Relative resistance vs. storage weeks at 50% and 0% SoC with a temperature of 25ºC. This figure is a continuation of the relative resistance values in Figure 44.

The fact that these different storage periods do not alter the ageing trend with respect to resistance suggests that the initial drop in resistance is associated with a process that affects all cells equally and that the process causing the initial decrease in resistance is independent of the storage SoC. To summarise, the effect that the storage periods have on the capacity are very dependent on both the voltage window and storage SoC,

however, the effect the storage periods have on the relative resistance is independent of both the voltage window and the storage SoC. The majority of relative resistance change arises immediately after the cells ceased cycling.

5.3.2.3 Recovery of DVA Features During Storage

To observe the effect that storage periods have on the Q1-3 and Q_{cell} regions and the HLD, DVA curves are plotted for the full 24 weeks of storage. These are compared against the fresh cell and at the end of cycling and can be found (aligned left) in Figure 49. After storage at 50% SoC for 12 weeks, almost no change in the shape of the DVA curve can be identified in all cases. The size of Q1-3 and Q_{cell} regions and individual peak heights remain constant, indicating the storage capabilities of both electrodes, the cyclable lithium content and the HLD remain constant throughout this period. This lack of change in the DVA curves occurs concurrently with small changes in the relative capacity and large changes in the relative resistance values during this period, hinting that the process(es) responsible for the capacity gain and resistance decrease do not significantly contribute to a change in the Q regions or in the redistribution of Li that affects the homogeneity.

When reducing the storage SoC from 50% to 0%, significant regains in peak shapes are observed in the Q1 region to an extent that bears similarity to that of a fresh cell. For the remainder of storage at 0%, the features of the DVA curve in the Q1 region continue to sharpen, which is particularly apparent for the central graphite peak, indicating increases in the HLD associated with the graphite and the reversible nature of the lithium distribution within the anode[95]. Furthermore, a substantial amount of the anode storage capabilities has been regained in all cells, since the size of the Q1 region has increased to a size that is comparable with that of a fresh cell.

The reason for the increased HLD when storing at 0% SoC but not 50% SoC could be explained by the corresponding electrochemical potential gradients of the anode. In steeper regions, such as when the anode is nearly completely delithiated (0% SoC), inhomogeneity, and thus a spatial variation in electrochemical potential, will provide a stronger driving force for diffusion than an inhomogeneous lithium distribution in comparably flatter electrochemical potential regions (50%)[152]. Therefore, the distribution of Li^+ would become more homogeneous in a shorter space of time. This would provide

a much narrower SoC distribution across the graphite anode active material which represents itself as a sharper peak in the DVA profiles.

Although all cells show largely similar responses, the sharpening of features after storage at 0% SoC can potentially reveal effects that would otherwise go unseen. For example, the central graphite peak for cells discharged to 2.5 V appears marginally sharper, but smaller in height than cells discharged to 3.1 V or 3.4 V with the same charging voltage. This may also be due to greater changes in the electrode balancing due to a loss of cyclable lithium for those cells discharged to 2.5 V, which represents itself as a sliding of the two internal electrode half-cell curves towards each other[126]. This is evident when observing the relative positions of the central graphite peak and central cathode peak on the capacity axis, which are side-by-side in the DVA curve of a fresh cell. In the aged cell, and evident after storage at 0% SoC, they appear to have moved further away from each other in opposite directions. Because the full-cell DVA curve is calculated from the summation of the DVA curves of the respective half-cells, the central graphite peak appears smaller in height as there is now less overlap between the anode and cathode peak as well as a reduction in HLD.

Due to significant smearing of the DVA curves in all cases, it remains difficult to identify any further differences between cells previously cycling in different voltage windows. Nevertheless, the strong impact of storage periods on the DVA has been identified and has provided insight into the locations of changes occurring during these periods.
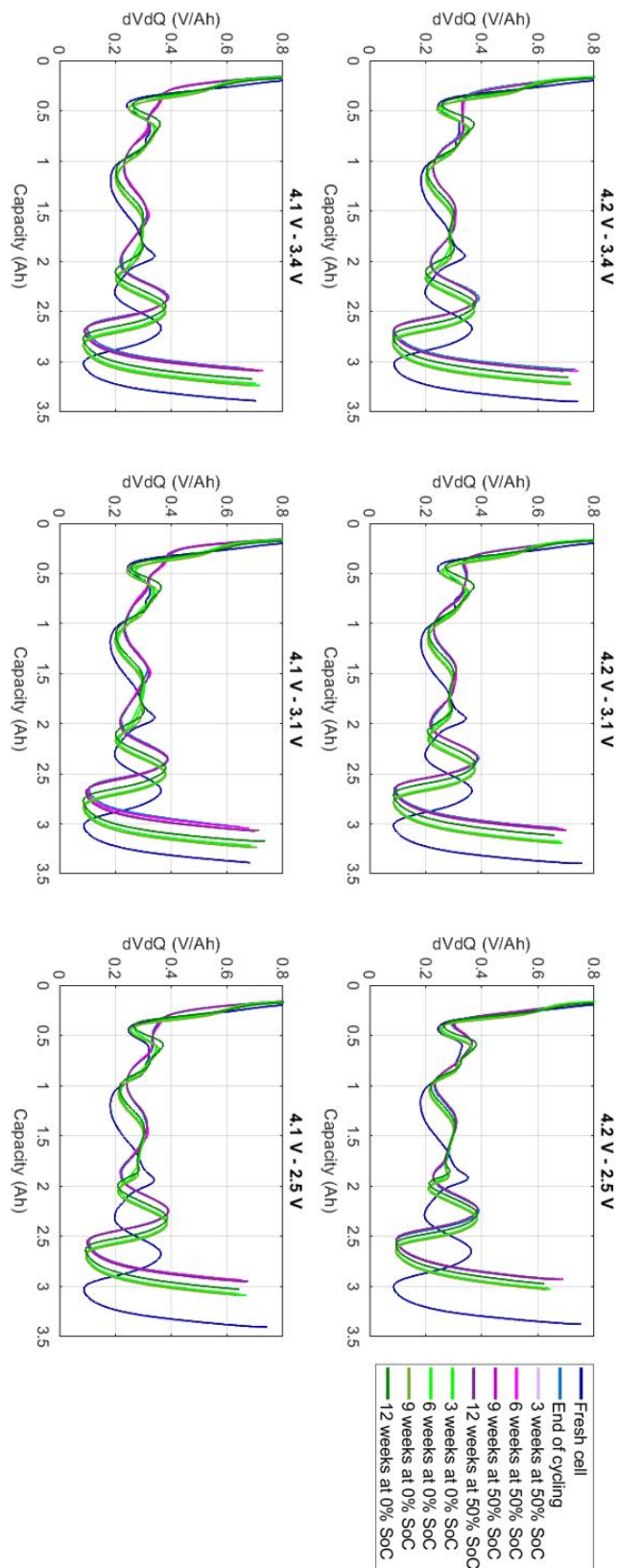
Figure 49. Left-aligned DVA profiles during relaxation storage for all test conditions. Graph titles represent the previous cycling voltage window. End of cycling DVA profile represents the beginning of storage and each fresh cell profile is included for reference.

5.3.3 Charging Times to 4.1 V and 4.2 V

Calendar storage periods demonstrated that charging to 4.1 V during cycling induces greater reversible capacity losses than charging to 4.2 V. This has been linked to the loss of lithium to the anode overhang regions, as determined by the greater recovery of capacity during storage at 0% SoC for those cells previously charged to 4.1 V. However, distinct explanations for how this may arise have yet been identified. The following section explores further differences between the two conditions by providing an insight into the charging times to 4.1 V and 4.2 V.

5.3.3.1 CC vs. CCCV – an Extended CV Phase at 4.1 V

Figure 50 displays the breakdown of a CCCV charging sequence to both 4.1 V and 4.2 V from 2.5 V at four different charging currents. For each current value, the plotted timescales are a representation of an average of 5 consecutive cycles of a fresh cell. The tests started with the lowest charging current and progressed to higher charging currents, with significant rest periods in between each set of charges.
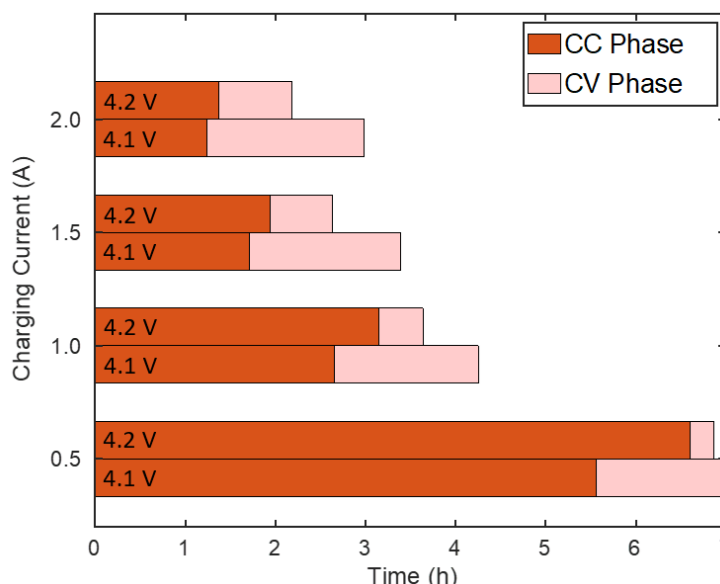
Figure 50. Total CCCV charging times and a breakdown of CC and CV phase times to 4.1 V and 4.2 V with different charging currents[19]**.**

Robert Burrell - January 2022

Firstly, it takes less time for a CC charge to 4.1 V than 4.2 V at all four charging currents. This is expected as less intercalated Li is required to reach 4.1 V. On the other hand, a CCCV charge to 4.1 V takes longer than a CCCV charge to 4.2 V; a trend that increases with charging current. A closer look at the two phases reveals significantly longer CV phases when charging to 4.1 V, which extends the overall charging time to beyond that of 4.2 V, particularly when using higher charging currents.

One would expect the length of the CV phase to shorten when lower charging currents are used in the preceding CC phase. This is demonstrated for 4.2 V, where the CV phase for a charging current of 2.0 A is 3 to 4 times longer than when the charging current is 0.5 A. As the (de)intercalation and migration processes have more time during a low current charge, the concentration gradients of Li within the cell are far shallower. The open circuit voltage (OCV) of the cell is then closer to the voltage of the subsequent CV phase and is considerably shortened. This does not appear to be the case when charging to 4.1 V, as the length of the CV phase varies little with a substantial variation in charging current. Certain cell parameters at 4.1 V must therefore be hindering the transport of Li and extending the CV phase. The potential origins of this sluggish transport are explored in the following sections.

5.3.3.2 Introduction of the 2D Timesheet Tool

Displayed in Figure 51 is a 2D histogram created to highlight the time spent in certain voltage and current regions. Termed the 2D timesheet tool, this heat map graphic provides a visual history of the cell that captures time-domain effects. Figure 51a and Figure 51b show the heat maps for the cells cycling in the voltage window 4.2 V to 2.5 V and 4.1 V to 2.5 V, respectively. For both, the two charging currents and a single discharging current are observed as the horizontal lines at 1.0 A, 1.7 A and -1.0 A, respectively. The points observed at 0.0 A represent time spent during an OCV pause after a charge/discharge, where the voltage relaxation in the absence of current is displayed. The vertical lines at 4.1 V and 4.2 V show the time spent in the current vs. voltage regions during the CV phase of the charging sequence and how the current falls to a predetermined cut-off value during this period.
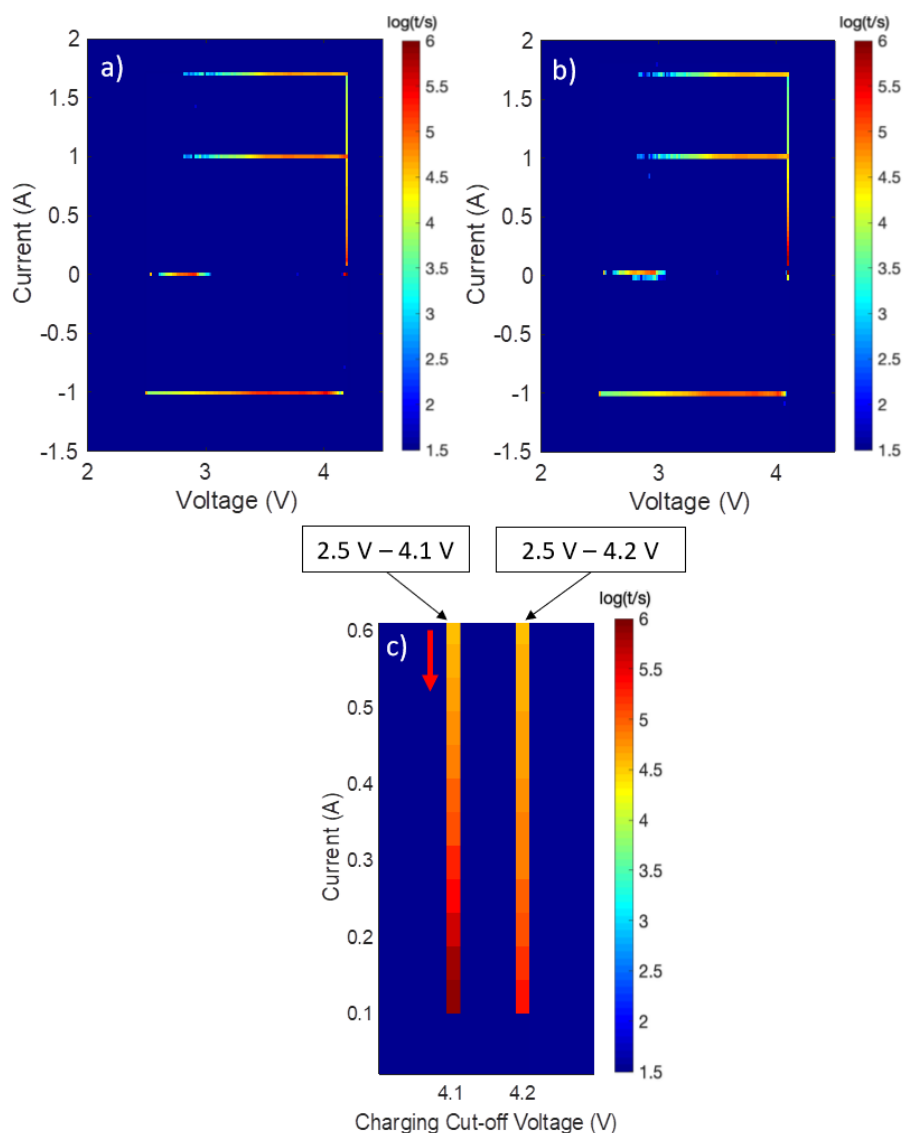
Figure 51. 2D timesheet tool: 2D histogram displaying the time spent in different current vs. voltage regions during cycling over 528 cycles (see Figure 43). (a) entire cycling dataset for the cell cycled 4.2 V to 2.5V, (b) entire dataset for the cell cycled 4.1 V.

As the two cells were cycled under largely similar protocols, the history of the cells in Figure 51a and Figure 51b look qualitatively similar. However, zooming into the CV phase reveals significant differences between the two cells. Figure 51c shows a zoom of the CV regions at both 4.1 V and 4.2 V where the red arrow indicates the direction of the current change during the CV phase. It is apparent that the time spent in the CV phase is largely similar up until the current reaches approximately 0.4 A, at which point the cell charged to 4.1 V spends orders of magnitude increased time in the low current region.

This confirms that the extended CV phase identified in Figure 50 translates into a quantifiable, negative outcome during cycling. This would otherwise go unnoticed when simply observing ageing as a function of cycles, despite the protocols allowing the voltage and current to vary. The 2D timesheet tool has helped to identify the location of the time extension, which could largely be reduced by raising the current cut-off to something higher than 0.4 A. This would inevitably result in a slight undershoot of the target SoC after the CCCV charge, but the charging time would be considerably shorter.

5.3.4 Lithium Mobility

It has been demonstrated that the cells charged to 4.1 V during cycling have an extended CV phase and suffer from greater reversible capacity loss compared to those charged to 4.2 V. It was stated that the reversible capacity losses may arise from an influx of Li from the anode overhang areas, as more capacity was recovered during low SoC storage. This section explores potential sources for the extended CV phase and describes a reversible capacity loss mechanism to support the idea of Li loss to the overhang regions.

5.3.4.1 Relative Diffusion Coefficients at 4.1 V and 4.2 V

The diffusion coefficients for both the anode and cathode during lithiation and delithiation, respectively, are plotted in Figure 52. These values were calculated using Sand's approach from GITT measurements of the respective half-cells[108]. For more information on this approach, please see section 3.4.

Figure 52a shows the diffusion coefficient of the anode during lithiation with highlighted regions indicating the relative lithiation degrees of the anode when the full cell is at 4.1 V and 4.2 V. The location of central graphite peak at $Li_{0.5}C_6$ in the DVA curve of a fresh cell was found to occur at ~57% SoC of the full cell, meaning a full-cell SoC of 114% would be required to fully lithiate the anode. Thus, the anode is oversized by 14% by mass loading and at a full cell voltage of 4.1 V and 4.2 V, the anode is approximately 75% and 87% lithiated, respectively.
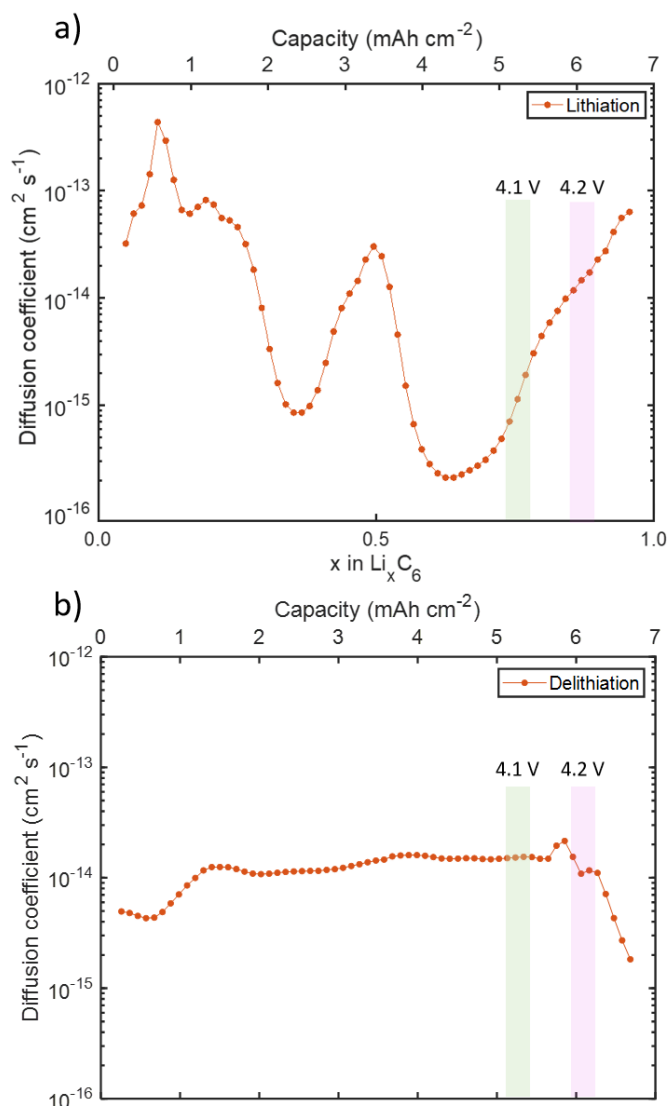
Figure 52. GITT-based diffusion coefficients for (a) the anode during lithiation vs. areal capacity and vs. degree of lithiation of a half-cell, and (b) the cathode during delithiation vs. areal capacity. The shaded regions in (a) highlight the approximate regions of the lithiation degree of the anode when the full-cell is at 4.1 V and 4.2 V.

Qualitatively similar plots have been previously reported in the literature, albeit with different absolute values[165]. That is an expected discrepancy as the effective diffusivities measured by GITT will highly depend on the active material volume, particle sizes, tortuosity and experimental differences with the fabrication of coin cells (e.g., coin cell pressure) and GITT protocols. Nevertheless, the shape of the plot in Figure 52a can still provide a valuable insight into the relative diffusion coefficients as a function of the lithiation of the anode.

The longer CV phase at 4.1 V observed in Figure 50 is the result of an apparent slower Li transport in the anode, which hampers the relaxation processes during the final stages of the CV phase[19]. This is confirmed by the diffusion coefficients in Figure 52a; the anode's effective diffusion coefficient is approximately an order of magnitude lower at 4.1 V than 4.2 V. This retards the approach of the user-defined cut-off current that terminates the CV phase[19].

Observing the diffusion coefficients of Li in the cathode in Figure 52b, it is evident that that the values are comparatively higher by up to an order of magnitude than in the anode when the full cell is at 4.1 V. In addition, the diffusion coefficients of Li in the cathode are relatively flat throughout the entire delithiation process and only collapses when the cell voltage is >4.2 V. Therefore, diffusion processes at 4.1 V seem to be limited by the hampered Li mobility in the anode rather than the cathode. At >4.2 V, the hampered delithiation of the cathode becomes limiting. However, this would not alter the proposed explanation of the extended CV phase; if the cathode were more limiting at 4.2 V, the CV phase would still likely be extended due to the reduced mobility of Li, therefore *reducing* the observed differences between the CV phases at 4.1 V and 4.2 V.

5.3.4.2 Anode Equilibrium Potential at 4.1 V and 4.2 V

The reduced mobility of Li^+ within the anode can also be verified by observing the phase transitions displayed in the anode equilibrium voltage curve in Figure 53. Previous studies have proposed that the flat regions of the anode equilibrium potential provide an insufficient driving force for the re-homogenisation of lithium distribution across the electrode on the occasion that it has become non-uniform[19,152,163]. This is because the existence of a concentration gradient in these regions would produce a smaller spatial variation of the chemical potential, thus reducing the driving force for diffusion. With the data presented in Figure 53, it is clear that when the full cell is at 4.1 V, the local equilibrium potential of the anode is towards the end of a plateau: a region indicating the existence of a two-phase equilibria[151]. However, when the full cell is at 4.2 V, the local equilibrium potential of the anode is in a far steeper region. This means that a variation of the full cell cut-off voltage of just 100 mV can result in substantially different thermodynamic states in the anode active material, which drastically varies the driving force for Li^+ mobility.
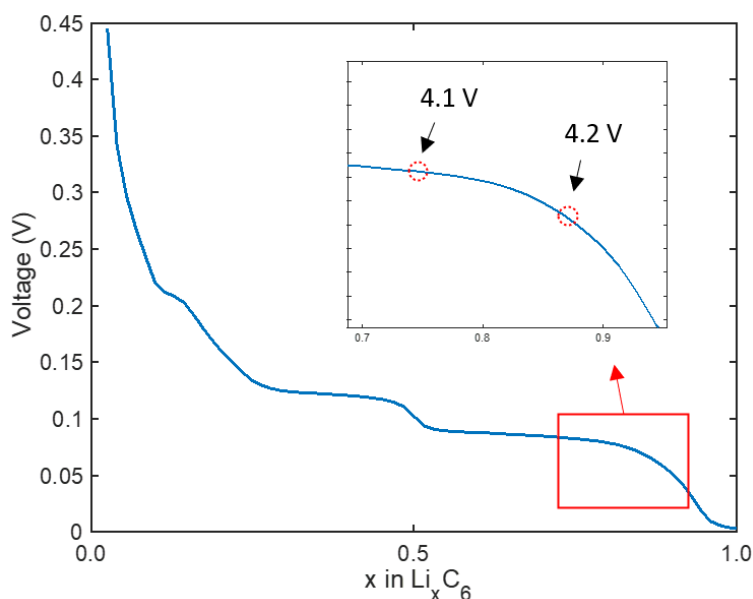
Figure 53. Anode equilibrium potential vs degree of lithiation of the anode during lithiation. The red square displays a zoom of the curve, highlighting the approximate relative lithiation degrees when the full cell is at 4.1 V and 4.2[19].

5.3.4.3 Loss of Lithium to anode Overhang Regions During Cycling

The key difference when charging to 4.1 V and 4.2 V during cycle ageing has been identified as sluggish Li^+ transport in the anode which significantly extends the CV phase at 4.1 V. Lower diffusion coefficients and flat equilibrium potential regions were identified as the key hinderance factors for this effect. These factors will increase the time spent at high SoC for cells charged to 4.1 V and raise the time-averaged SoC for the cell throughout cycling.

A higher time-averaged SoC will affect the concentration gradient between the active anode and the anode overhang. Simple representations of these regions are presented in Figure 54a and Figure 54b. Also known as the passive anode, these regions can act as a lithium sink or source, depending on the concentration gradient between them, which is inherently affected by the time averaged SoC[162]. A cell at a higher SoC will initially have a greater concentration of lithium in the active region than the less-lithiated overhang regions and will produce a stronger concentration gradient between the two. This drives lithium into the overhang regions, as demonstrated in Figure 54a. This process can occur on the timescale of weeks, as shown in the contrary scenario by the recovery in Figure 47 when storing at a low SoC and is demonstrated in Figure 54b.

In the case of the data presented in this chapter, the extended CV phase during cycling at 4.1 V vs. 4.2 V creates a higher time-averaged SoC which draws a slow net movement of Li from the now (on average) more lithiated active anode into the anode overhang[19]. Lithium that diffuses into these regions becomes inactive, reduces the cyclable lithium content and increases capacity fade. When observing Figure 54a it is evident that this concentration gradient becomes shallower with time and continues to reduce to the point that the average concentration at the edge of the active anode resembles that of the anode overhang. It is anticipated that this phenomenon is behind the technically capped capacity difference that is observed in Figure 43 as only a certain quantity of lithium can diffuse to the overhang regions before there is no further net movement.
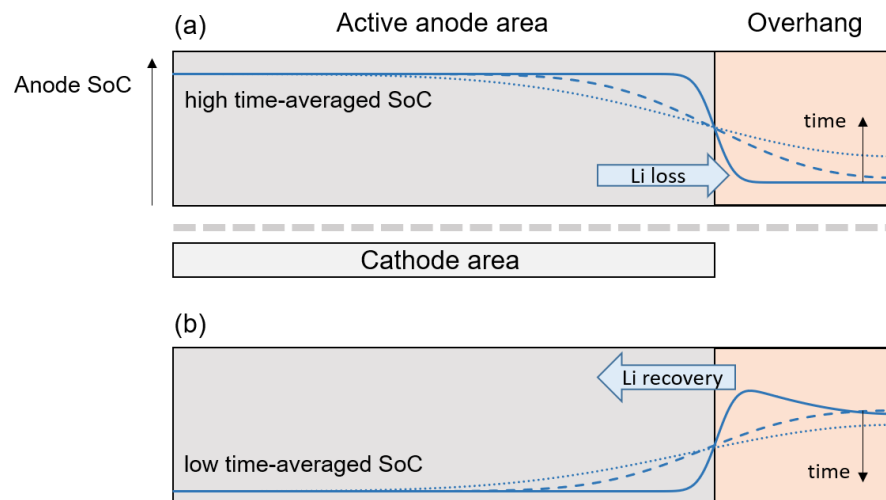
Figure 54. Representation of Li+ movement to and from the anode overhang at (a) high time-averaged SoC and (b) low time-averaged SoC. The solid line represents the Li concentration after reaching a new SoC; concentration gradients drive Li+ diffusion. The dashed lines represent Li+ concentration after some weeks[19].

5.4 Conclusions

To ensure correct interpretation of laboratory-based cycle ageing results, it is vital to consider both irreversible and reversible capacity losses. This experimental ageing study explored the impact of cycling in varying voltage windows on the degradation of LIBs and accounted for both the irreversible and reversible losses.

CV Phase Duration is Dependent on Lithium Mobility in the Anode

The duration of the CV at the end of charging is highly dependent on Li mobility at the respective SoC of the anode. Changes of just 100 mV in the charging cut-off voltage of the full cell can lead to vastly different transport properties in the anode at the respective equilibrium potential. Lowering the charging cut-off voltage from 4.2 V to 4.1 V reduced the effective diffusion coefficient of Li within the anode by orders of magnitude and produced a significantly shallower anode equilibrium potential. The combined effect of this was an increase of the average CV phase time from 0.6 h to 1.6 h at 4.2 V and 4.1 V, respectively.

Increased CV phase Durations Promote Reversible Capacity Losses

Spending increased lengths of time in the CV phase for cells charged to 4.1 V raised the time-averaged SoC, which produced a stronger concentration gradient between the active anode and anode overhang areas. A larger net movement of Li^+ into the overhang regions ensued during cycling, resulting in a reduced cyclable lithium content that exhibited itself as capacity fade. This inverted the ageing outcome to the extent that the cell charged to 4.1 V showed greater capacity fade than its 4.2 V counterpart. The appropriate identification and management of CV time lengths to avoid incorrect ageing determination was demonstrated.

The Importance of Rest Periods in Cycle Ageing Studies

Rest periods at low SoC allowed the quantification of the reversible capacity losses and identified potential sources of such losses. Storage at 0% SoC recovered up to 2% capacity in just three weeks and up to 3% in the entire 12-week period. Cells previously cycled to 4.1 V recovered more capacity than their 4.2 V counterparts in all cases, inverting the ageing outcome in the process. Because cells stored at 0% SoC primarily recover lithium from the overhang regions, it was suggested that the cells cycled to 4.1 V temporarily lost greater quantities of lithium to the overhang regions during cycling. Rest periods were paramount for identification and quantification of such losses. Storage at

0% SoC prompted no noticeable variation in resistance after the first 3 weeks, but steady increments were observed thereafter.

Rest periods at 50% SoC produced very little recovery in capacity due to the similarity between storage SoC and previous average cycling SoC. This was met with large declines in resistance after just 3 weeks of storage.

The variation in resistance during both storage periods were found to be independent of both previous history and storage SoC. All cells showed an initial decline in resistance of up to 7% after 3 weeks of storage at 50% SoC, but increases were observed thereafter.

The Importance of Considering Time Spent in Current and Voltage Regions

To avoid the misinterpretation of experimental artefacts, the time spent in current and voltage regions during cycling should be routinely examined. The confirmation of increased time spent at higher voltages for cells charged to 4.1 V was crucial in understanding the origin of increased capacity fade for these cells. The low current region at the end of the CV phase was found to be the most detrimental to the overall charging time and the 2D timesheet tool enabled this identification. Raising the current cut-off to >0.4 A for cells charged to 4.1 V would significantly reduce the overall charging time of the cell and reduce reversible capacity losses.

For future applications, this tool can provide an instant visual diary of the current and voltage regions in which the cell spends time in and can flag cost saving opportunities by avoiding time-damaging regions. Furthermore, it was demonstrated that both cycles and time spent in operational regions should be considered in accelerated ageing studies to ensure correct interpretation of results.

6 Methodological Development of a Test Rig for the Homogeneous Compression of Lithium-ion Pouch Cells

6.1 Introduction

Lithium-ion batteries (LIBs) have achieved widespread success for portable electronics and electric vehicles (EVs) due to their high output and fall in production costs[44]. This increasing demand, particularly in EVs, calls for LIBs with higher energy densities in increasingly compact systems and spaces[166].

Throughout their stationary and operational life, LIB pouch cells may experience varying stack pressures, particularly if they are confined to small spaces. Unlike in cylindrical and prismatic cells that possess hard externals, lithium-ion pouch cells are encased in a flexible aluminium-polymer pouch that is vulnerable to external loads and pressures. Previous studies have explored and quantified the effects of non-destructive compressive loads on LIB performance in an attempt to disentangle the complex nature of mechanical and electrochemical interactions, however strong contradictory and ambiguous conclusions exist[2,21,76,96–98].

Low levels of externally applied pressure were often found to reduce capacity fade through the redistribution of gas by-products and by minimising electrode layer delamination that can otherwise cause a separation of the active material from the current collectors. In addition, externally applied pressure has been reported to increase the capacity of an aged LIB by up to 15%, but with no significant effect on a fresh cell[98].

Similarly, a study applying a range of pressures to single-layer pouch cells (0.66 – 1.98 MPa) found that an optimum pressure of 1.32 MPa extended cycle life by reducing the loss of cyclable lithium[21]. Furthermore, electrochemical impedance spectroscopy (EIS) was tested as a means of probing coupled electrochemical and mechanical effects by revealing impeded kinetic and mass transport rates of electrochemical reactions in compressed pouch cells due to pore deformation in the separator[76]. In cases of high temperatures (>80⁰C), the external pressures were shown to reduce capacity loss by up to 13%[167]. The primary route of degradation prevention was found to be reduced electrode layer delamination from gas evolution at higher temperatures. By contrast, low stack pressures in a prismatic cell have also been shown to increase capacity fade when compared to a cylindrical cell of identical chemistry and materials[99]. The lower pressure resulted in an increased swelling of the anode active material that reduced ion access and limited electrochemical kinetics during cycling. Another study explored the effects of both tensile and compressive stresses and found that tensile stresses improved electrochemical performance whereas compressive forces repressed electrochemical performance[168]. Tensile stresses gave a higher specific capacity, capacity retention, improved ion migration (by diffusion coefficient) and reduced polarisation resistances, whereas compressive stresses had the opposite effect.

Because cells of different form-factors might not experience uniform pressure distributions throughout their life, studies have probed the effect of pressure non-uniformity in lithium-ion cells. The existence of non-uniform pressures has been shown to produce a non-uniform ageing response in cylindrical cells, where the centre of the jelly roll is said to experience higher pressures than the outer regions. Klett et al[160] reported a thicker solid electrolyte interphase (SEI) layer in the central jelly roll regions, whereas Bach et al[86] observed a thinner SEI layer. Moreover, bach et al[86] found increased lithium plating in areas of higher pressure, whereas Petzl et al[48] reported lower levels of lithium plating in the central region of the jelly roll. It is therefore evident that multiple studies exist with contrasting but overlapping findings that tend to convolute the effect of pressure and pressure inhomogeneities on LIBs.

Electrochemical ageing studies typically contain a vast array of experimental variables with these types of studies. For cycling studies, voltage windows and charge/discharge currents are often varied[19], whilst calendar ageing experiments typically play with storage SoCs and temperatures[13]. These parameters are crucial in the design of the investigation

and practices are often standardised and well documented. However, there appears to be no standardised procedure for the application of pressure to LIBs. Multiple test rig designs and set-ups are presented in studies, largely without the reporting of the pressure distribution experienced by the cell under compression. Based on the previous reports about the non-uniform effect of inhomogeneous pressure distribution on the ageing of lithium-ion cells, it is important to consider pressure rig design and its effectiveness at applying even pressure.

In laboratory settings, pressure test rigs are often designed with size, weight and ease of manufacture at the forefront. Limited space in space in thermal chambers and bench tops means rigs must comply to size and weight maxima, which can reduce the complexity of design and components. One of the most common test rig designs uses bolts and nuts at each corner of two flat plates to sandwich and compress the cell[2,40,96,97]. The ease and customisability with which this design can be constructed makes it a popular choice for the compression of pouch cells. To measure the applied pressure, load cells or calibrated springs of known spring constant (stiffness) are used. From the measured displacement of the spring, the applied force can then be calculated using Hooke's Law

$$F = kx \tag{19}$$

where F is the applied force in Newtons, k is the spring constant and x is the displacement of the spring in metres. The pressure can then be calculated using equation (20)

$$P = A/F \tag{20}$$

where P is the pressure in Pascals, A is the area of applied force in m^2 and F is the force in Newtons. The accuracy of using this method, particularly with flat plate designs, to achieve an even pressure distribution across LIBs remains unclear. For accurate comparison of results between different studies and to minimise variations arising from experimental inconsistencies, standardised practices and procedures should be adopted.

This work explores the effect of applied pressure on single-layer LIB pouch cells, which are commonly used by manufacturers for the parameterisation and prototyping of new materials. An example set of three test rig designs from the literature are evaluated and compared for their effectiveness at applying homogeneous pressure across a model pouch cell. The findings and insights from this are implemented in an additional design of a proposed test rig, whose pressure distributions are evaluated. Finite element analysis

(FEA) simulations are used to examine the pressure distributions for each of the test rigs and pressure-sensitive films are employed to experimentally validate the results. Moreover, an evaluation of different cell structures and compositions provides an accurate basis for the FEA simulations presented here and for future studies. These results provide a foundation for the future testing of LIBs under compressive loads and for how to achieve homogeneous pressure distributions.

6.2 Experimental

The principal aim of this study was to perform FEA simulations to evaluate the pressure distributions across single-layer pouch cells when using test rig designs from the literature. This section entails the experimental procedure for this study.

6.2.1 Simulation Details and Boundary Conditions

FEA simulations were performed in conjunction with Dr. Kenneth Nwanoro using ANSYS Mechanical (ANSYS Workbench version 2019 R3) and with Solid Elements (Solid 186) description. Mesh refinement was performed until no further pressure magnitude variation was observed in each mesh iteration.

For designs containing bolts that supply a clamping force at each corner, loads were applied using ANSYS Mechanical's bolt pretention algorithm. This distributes loads throughout each bolt by dissecting the bolt in two and adding nodes to each half. The nodes are then brought together until the desired pretention force is achieved. For designs containing a central piston (and piston screw), the force was applied directly to the top of the piston. As no bolt clamping force was present in these designs, the bolt pretension algorithm was not required. Modelling of spring behaviour was not included in simulations as their use in application is solely to measure and maintain a specific load, and hence not fundamental in the distribution of pressure.

Contacts between the pouch cell and compression plates and the bolt threads and compression plates were defined as frictional with as friction coefficient of 0.2. Normal

Lagrange contact formulation was applied for frictional behaviour, which prevents the penetration of two bodies through one another during simulation and maintains rigid contacting surfaces.

6.2.2 Dummy Single-Layered Pouch Cell Structure

Throughout this investigation, a single-layered dummy pouch cell comprised of a graphite anode, $LiNi_{0.6}Mn_{0.2}Co_{0.2}O_2$ (NMC622) cathode and Celgard-2325 separator was used. As a test specimen, the cell was not filled with electrolyte. The total dimensions and features of the cell are presented in Figure 55. The through thickness of the cell ranged from 0.46 mm to 0.67 mm at given points across the pouch. A more comprehensive list of cell component dimensions can be found in Table 7, where the representative Young's modulus and Poisson's ratio values for each cell component were obtained from a previous study[169].
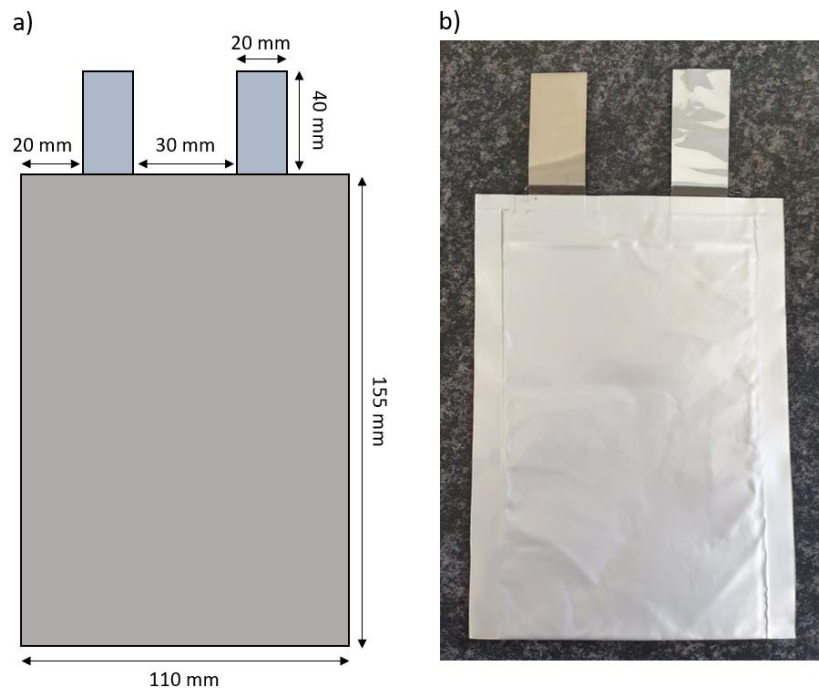
Figure 55. Sketch of single-layer cell with dimension and features. (b) Photograph of single-layer cell specimen.

Table 7. Dimensions and properties[169] for the single-layered dummy pouch cell.

Layers	Description	Thickness (μm)	Young's Modulus (MPa)	Poisson's Ratio
1	Aluminium-polymer pouch	155	575	0.25
2	Anode – graphite-coated copper foil	90	83	0.21
3	Celgard separator	20	90	0.4
4	Cathode – NMC-coated aluminium foil	80	275	0.21
5	Aluminium-polymer pouch	155	575	0.25

LIBs are comprised of multiple porous media which have substantially different mechanical properties (see Table 7). When modelled as a multi-layered representation for a pouch cell, each layer is frequently described by its individual material properties, often with specific porosity values, as depicted in Figure 56a. These values are typically obtained from tensile tests of each cell component[26,170]. Simulating the effect of pressure on each individual particle or unit cell is computationally expensive, thus the components of LIBs are often simplified into homogeneous materials, as depicted in Figure 56. Such tests are simulated using a pouch cell represented as a single component with isotropic and homogeneous properties[171,172]. This is because the active materials and binders typically dominate the total thickness of a multi-layered cell, rather than the foil current collectors or aluminium-polymer pouch.
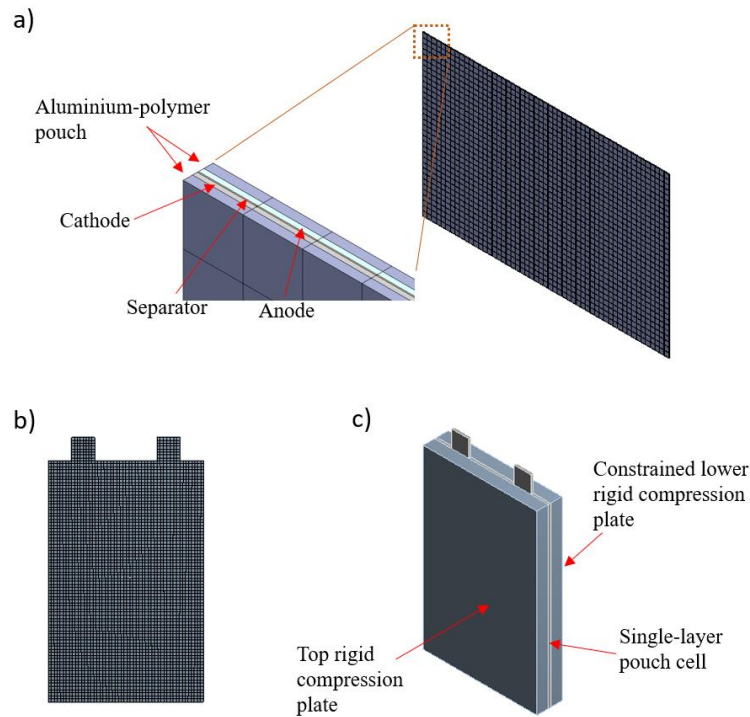
Figure 56. Different set-up routes for modelling a LIB. (a) Multi-component set-up with individual material properties, (b) single, homogeneous component and (c) simplistic model set-up demonstrating a LIB sandwiched between two rigid compression plates.

In the single-layer dummy pouch cell used in this study, the aluminium-polymer pouch dominates the total thickness over the active materials by approximately 2:1 (see Table 7). It was therefore necessary to compare the differences when simulating the compression of a single, homogeneous foam material representing the active materials, and of aluminium, which represents the aluminium-polymer pouch. This was to observe if any significant changes occur if the composition of the single homogeneous component were altered. Previous work[171] has modelled LIBs as a single crushable foam material with a Young's Modulus of 500 MPa and a Poisson's ratio 0.01, which was adopted in this test. The aluminium was simulated with a Young's modulus of 575 MPa and a Poisson's ratio of 0.25 according to Table 7.

For this ideal, static compression test, cell specimens were placed between two rigid compression plates where one compression plate was displaced by 0.001 mm, whilst the other was set to rigid constraint, as seen in Figure 56. Figure 57a and Figure 57b presents the pressure distributions across a single-component dummy cell for a crushable foam and aluminium material, respectively. Linear elastic material behaviour was assumed for

both. A homogeneous pressure distribution can be observed for both compression tests, with little difference between the two materials. It is noted that the aluminium cell experienced higher pressures than the crushable foam for a fixed displacement. This difference likely arises due to the difference in Young's Modulus values for both materials. Higher pressures are expected for aluminium which has the larger modulus of 575 MPa, when compared to the crushable foam's 500 MPa.
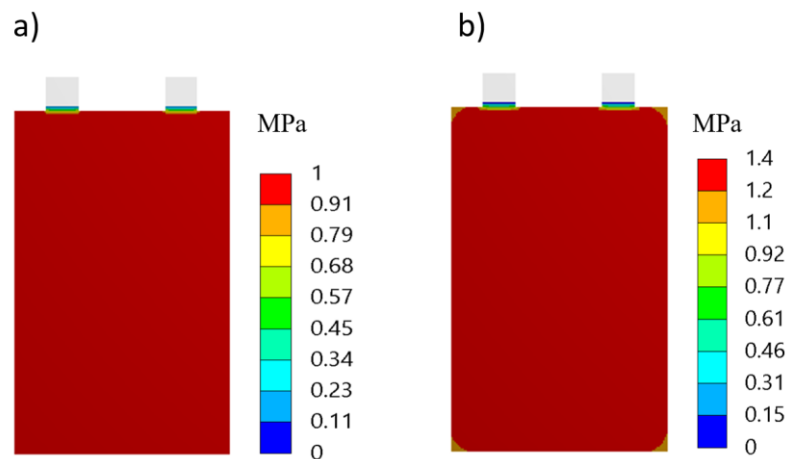
Figure 57. Pressure distributions for the static compression test of (a) a crushable foam and (b) aluminium. Test was performed with a compression plate displacement of 0.001 mm.

Based on these results, it is evident that the pressure distribution is not significantly altered when using aluminium over a crushable foam. Therefore, to resemble the material type presented in previous studies, a crushable foam material with a Young's modulus of 500 MPa and a Poisson's ratio 0.01 was used for the FEA simulations presented in subsequent sections. Furthermore, a single-component test specimen was used to reduce computational cost.

6.2.3 Key Features of Existing and Proposed Test Rig Designs

Multiple test rig designs are reported in the literature for studies on the compression of lithium-ion pouch cells. Three fundamental designs on which most test rigs are based

were identified and considered in this investigation. A custom-built test rig capable of applying homogeneous pressure is proposed and presented as design 4. The following section details the key features for each design and the method behind the pressure application.

6.2.3.1 Design 1 from the Literature

The first, and simplest, of the compression test rigs uses two compression plates and bolts at each corner, as displayed in Figure 58. This design is based on previous designs from the literature[2,40,96]. The benefit of such a design is the ease with which the rig can be constructed and implemented into battery ageing tests. Simple fabrication of the plates means the test rig can be easily tailored for a particular cell shape and size without specialist equipment. The bolts at each corner create a clamping force on the cell to apply pressure and the force is typically measured by using calibrated springs at each corner or with load cells/pressure sensors integrated into the design[53,96]. As the bolts require clearance holes in the compression plates, the clamping force is applied at locations outside the circumference of the cell.
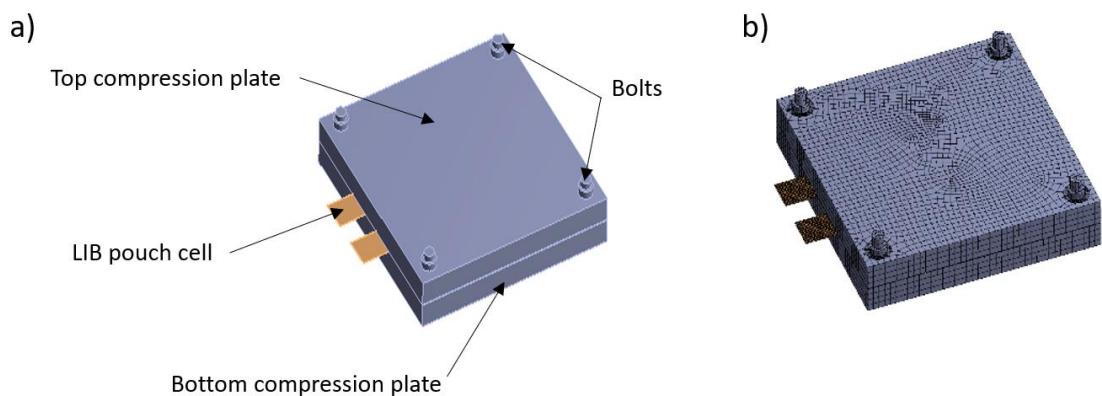
Figure 58. Test rig design 1: two compression plates with bolts. (a) labelled sketch of design and (b) FEA model of design. Design based on previous designs presented in the literature[2,40,96].

6.2.3.2 Design 2 from the Literature

Design 2 bears strong similarity with design 1 and is presented in Figure 59. This design uses two compression plates, but with the addition of two semi-rigid plates that are in direct contact with the cell[97]. These are used to help evenly distribute pressure across the cell, however, studies that implemented this design did not report the pressure distribution experienced by the cell during testing[97,98]. Like design 1, this rig possesses the advantage that it is easy to construct and to adapt to specific needs of the cell. For the FEA simulations of design 2 presented in this investigation, nylon plates with a Young's modulus of 3.3 GPa and a Poisson's ratio of 0.41 were used. Semi-rigid plate thickness was 10 mm.
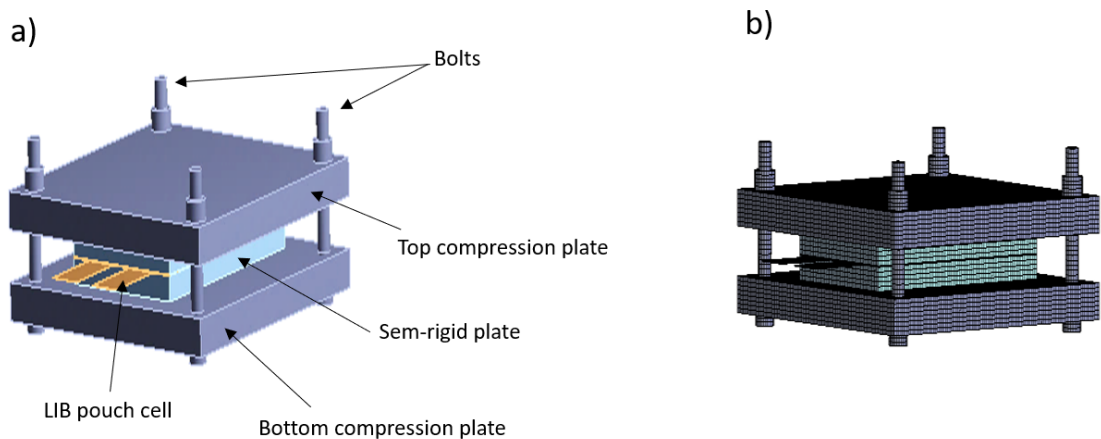
Figure 59. Test rig design 2: two compression plates with bolts and semi-rigid plates. (a) labelled sketch of design and (b) FEA model of design. Design based on previous design presented in the literature[97].

6.2.3.3 Design 3 from the Literature

Design 3 makes use of compression plates and bolts like in design 1 and 2, however, additional central pistons directly apply pressure to the cell. This design is based on a previous investigation into the effects of compression on small single-layer pouch cells and is presented in Figure 60[21,173]. Here, the pouch cell is sandwiched between two pistons that are clamped by compression plates at either end. Calibrated springs are used to both measure the applied force through the piston and to maintain constant pressure. Cartridge

heaters are inserted into polyether ether ketone (PEEK) blocks that surround the cell to provide stable thermal management. It important to note that this design was operated on single-layer pouch cells whose electrodes were circular and possessed a diameter smaller than that of the pistons[21,173]. This meant that the entire area of the electrodes were compressed during operation.
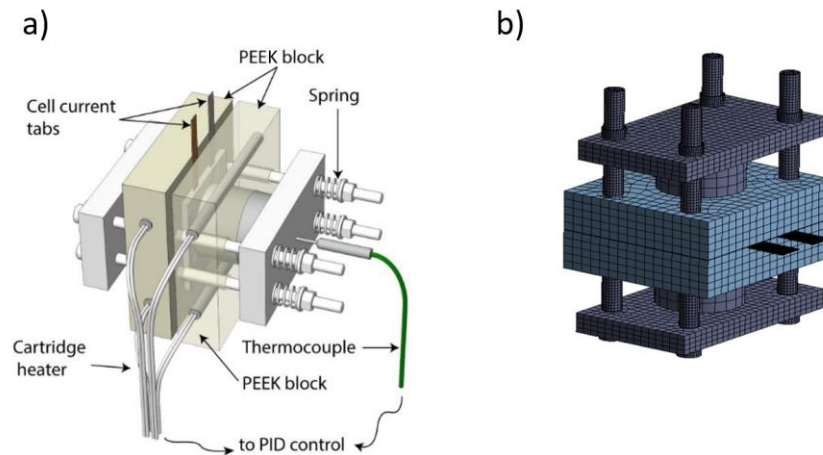
Figure 60. Test rig design 3: compression plates with central pistons. (a) labelled sketch of design and (b) FEA model of design. Design based on previous design from the literature[21,173].

6.2.3.4 Design 4 – Proposed Rig Design

To achieve a homogeneous pressure distribution across lithium-ion cells, a custom-built test rig design is presented in Figure 61. Force is applied through a central piston screw and is distributed onto the cell by a piston block. To increase the force applied to the cell, the central piston screw is screwed down to increase displacement. The entire structure's rigidity is maintained by two stabilisation plates separated by cylindrical supports. The stabilisation plates are clamped together by bolts and nuts (not displayed in Figure 61), however these apply no pressure to the cell and are purely for structural support. A recessed guide hole (depth of 2 mm) in the piston block ensures correct alignment of the piston screw and piston block. In practice, thermal gap fillers are placed either side of the cell to ensure greater thermal stability whilst improving pressure distribution by conforming to the cell. The applied force is measured using Tekscan FlexiForce A502 sensors that are placed directly on top of the cell.
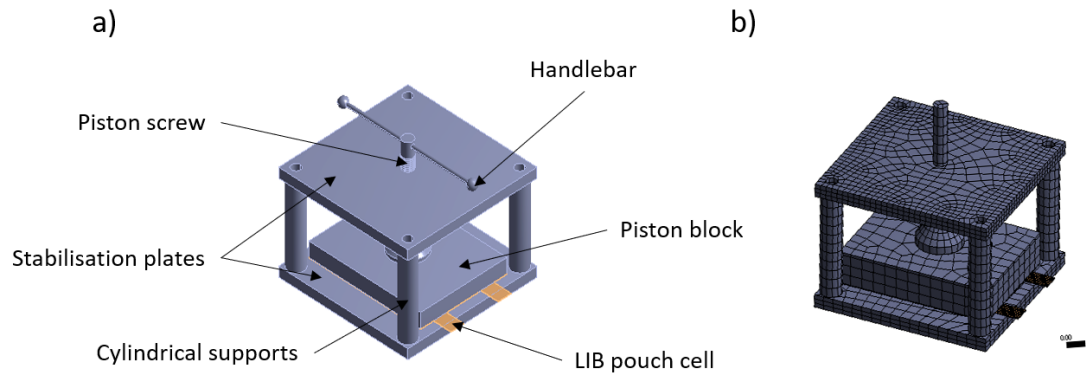
Figure 61. Test rig design 4: custom-built test rig. (a) labelled sketch of proposed design and (b) FEA model of design.

6.2.4 Experimental Validation

Experimental validation tests were paired with the FEA simulations of each test rig design. To emulate designs 1-4 for experimental validation, rigs were constructed in-house with design features that matched those presented in the literature. To represent the cell test specimen, the dry dummy single-layer cell was placed in each test rig and a prescribed force was applied to the cell. To resemble real-world practices, two thermal gap fillers with a thickness of 2 mm were placed either side of the cell in each test rig before experimental validation.

Calibrated springs (Lesjöfors 6154) with a known spring constant were used for the application of force in test rigs designs 1-3. During compression, the displacement of the spring provided a specific force when input into equation (19) and pressure was then calculated using equation (20). For design 4, Tekscan FlexiForce A502 force sensors were placed directly on top of the cell and the resistance response of the sensor was measured using a multimeter. Calibration of the sensor was carried out on an Instron UTM that applied known force values to the sensor, as seen in Figure 62. The force-resistance values were then fitted using equation (21), where F is the applied force in kN, a is a coefficient with a value of 3717, R is the measured resistance in Ohms (Ω) and b is the exponent with a value of -1.034. This allowed the applied force to be directly calculated from the resistance measured by the multimeter.
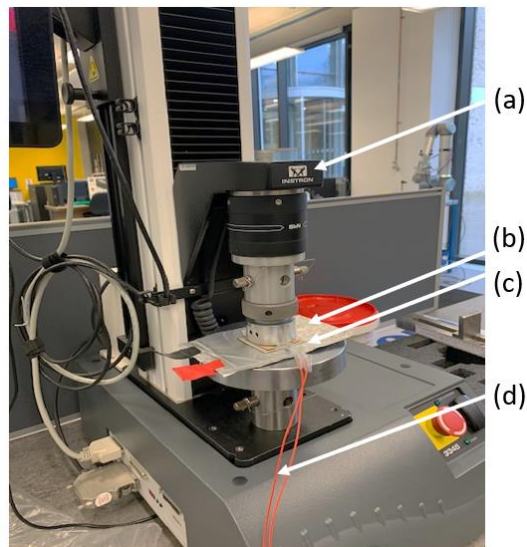
Figure 62. Sensor calibration set-up. (a) Instron UTM, (b) dummy single-layer cell, (c) Tekscan FlexiForce A502 sensor and (d) wired connection to mutimeter.

$$F = aR^b \tag{21}$$

For experimental validation and to map pressure distributions across the cell surface, pressure sensitive films were placed on top of the cell before compression. Fujifilm Prescale type LLW and LLLW provided a visual map of uniformity through the production of red colour, whose intensity is dependent on contact pressure (higher pressure, stronger colour). A representation of the colour difference observed between high and low contact pressure can be observed in Figure 63 below.
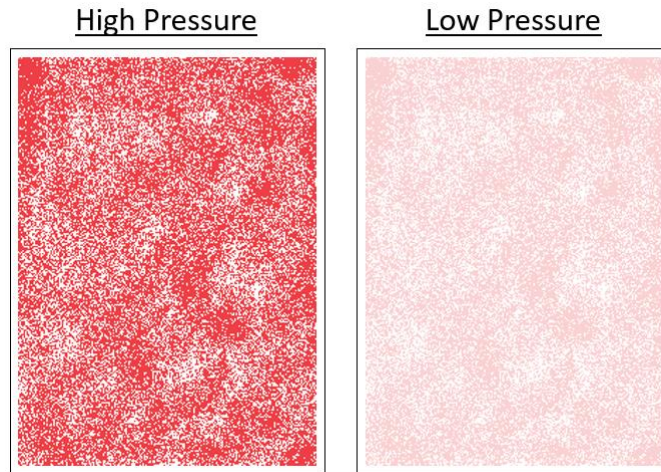
Figure 63. An example sketch of the colour production after the application of high and low pressure. Higher pressures produce stronger red colours.

6.2.5 Cycling with Homogeneous and Inhomogeneous Compression

To observe the differences between homogeneous and inhomogeneous compression on the ageing of lithium-ion pouch cells, an experimental cycling study was performed. The experimental procedure and parameters are described as follows.

6.2.5.1 Equipment Used

All cells were cycled using Basytec CTS battery cyclers at 25ºC in a Binder MK 240 thermal chamber to ensure identical environmental conditions.

6.2.5.2 Pressure Set-Up

Applying homogeneous pressure was achieved using the proposed custom rig (design 4) presented in this chapter. To improve thermal management and pressure distribution, thermal gap fillers (RS-Components 707-4663) were used either side of the cell. For force measurement, Tekscan FlexiForce A502 force sensors were placed on top of the cell and the resulting resistance measurement was recorded. The applied force was calculated from the resistance according to equation (21). The total force applied to the cell was 1.6 kN.

Presented in Figure 64 is the configuration for the inhomogeneous pressure application and bears similarity to the flat plate design presented as design 1 in this chapter. The cell was placed on a flat plate with semi-rigid pads placed overlapping at each corner. The semi-rigid pads placed in this configuration provided the pressure inhomogeneities. A top plate was placed on top of the cell and the semi-rigid plates, and the force was applied at each corner through calibrated springs (Lesjöfors 6154). A force of 400 N was applied at each corner to give a total applied force of 1.6 kN.
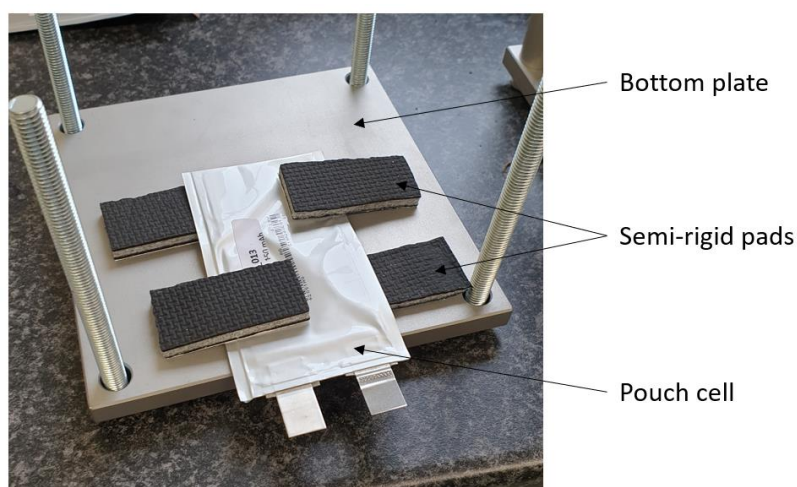
Figure 64. Photo of the configuration used to apply inhomogeneous pressure. Semi-rigid plates at the four corners created pressure 'hot spots'.

6.2.5.3 Cycling

Initially, cells were compressed, and a check-up was performed (see Figure 9, page27). Cells were then cycled under compression for 200 cycles and then uncompressed, followed by a check-up. After this, the cells were recompressed and a check-up was performed, followed by cycling in blocks of 50 cycles through to the end of testing. A flow diagram of the overall procedure is displayed in Figure 65.

During cycling, a +0.1 A (0.75C) charging current and a -0.1 A (0.75C) discharging current was used in conjunction with voltage limits of 4.2 V to 3.0 V. Constant current constant voltage (CCCV) charging with a 0.01 A current cut-off and constant current (CC) discharging was used throughout. All check-ups and cycles were performed at 25ºC.
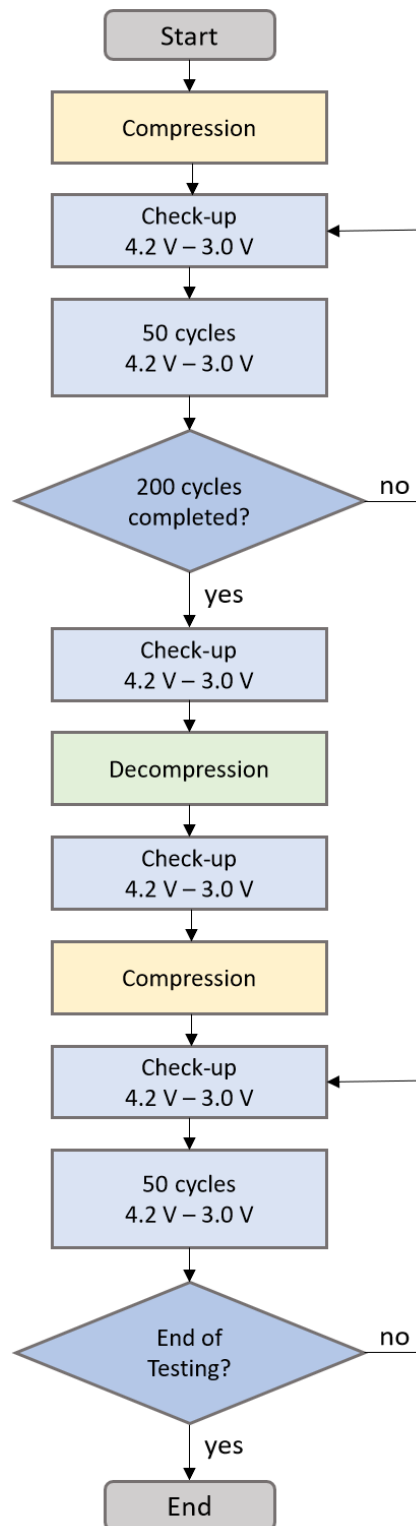
Figure 65. Flow diagram of experimental procedure.

6.3 Results and Discussion

The results obtained from the FEA simulation and experimental validation of each test rig design are presented in this chapter. The uniformity of pressure distributions from the compression of LIB pouch cells in test rigs from the literature are compared against one another and against a proposed custom-built design.

Throughout this results section, the pressures experienced by the cell may differ in value depending on the test rig used. It is important to note that the primary criteria for a given test rig is the ability to apply even pressure to a cell, regardless of the applied force or desired contact pressure. It is therefore stressed that the results of each design are comparable against one another, despite this difference in pressure magnitude.

6.3.1 Evaluation of Design 1

Displayed in Figure 66 are the FEA simulation and experimental validation results for the compression testing of a LIB pouch cell using design 1. A bolt pretension force of 0.5 kN was applied to each bolt at the four corners for the FEA simulations in Figure 66a and Figure 66b and a force of 0.4 kN was applied at each corner for the validation in Figure 66. Calibrated springs were used for the calculation of applied force in the experimental validation. The extreme corner regions of Figure 66a can be neglected due to the 'singularity effect'. Observing Figure 66a, it can be seen that there is significant non-uniformity in the pressure distribution across the single-layer cell. The cell experiences higher pressures of up to 0.7 MPa towards the corners (location of bolts), whilst the central regions show 0 MPa. Moreover, Figure 66b reveals a poor contact between the cell surface and the compression plates during simulation. This effect is likely a result of the location of the bolts, which apply a clamping force outside the circumference of the cell. This can cause an out-of-plane bending of the cell in the central regions that reduces the contact and pressure away from the edges of the cell. In addition, this effect is aggravated due to the thin form-factor of the single-layer cell.

Figure 66c presents the experimental validation of the FEA simulation results for design 1. A strong appearance of red colour is observed at the corners of the cell area, with a production of colour also present along the edge regions, which indicates higher contact pressure in these areas. This confirms the existence of high non-uniformity of pressure distribution when compressing the single-layer pouch cell with design 1 and demonstrates the good agreement between FEA simulation and experimental validation. The concentration of pressure at the cell corners and edge regions appears to be the product of an inherent flaw of test rig designs that implement bolt clamping force at locations that lie outside the footprint of the cell.

Figure 66. Pressure distribution for the compression of a 0.5 mm thick single-layer pouch cell in design 1. (a) FEA simulation result, (b) FEA contact result, (c) experimental validation with pressure sensitive film (LLLW) and (d) FEA model.

Figure 67 displays the pressure distributions for the comparison of cell thickness. A 1.5 kN force was applied to the bolts at the four corners of design 1 for a single-component crushable foam material. It can be seen that increasing the thickness of the cell by a factor

of 10 does not significantly improve pressure distribution. Although pressure is experienced by more (central) regions of the cells, a vastly non-uniform distribution remains. Design 1 is therefore not recommended for applying homogeneous pressure to LIB pouch cells for cells up to 5.6 cm in thickness. Moreover, the negative effects of this design are particularly apparent for thin LIB pouch cells.
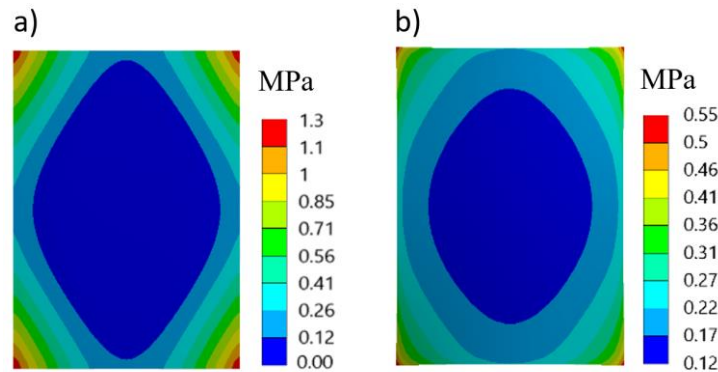
Figure 67. Pressure distribution during compression of a single-component crushable foam for (a) 0.56 cm thick cell and (b) 5.6 cm thick cell. A 1.5 kN force was applied to every bolt at each corner.

6.3.2 Evaluation of Design 2

The pressure distribution results for design 2 are presented in Figure 68 for both a 0.5 mm thick pouch cell and a 5.0 mm pouch cell. A 1.0 kN bolt pretension load was applied to each bolt at each corner for the FEA simulations and a 0.4 kN force was applied to each bolt for the experimental validation. Nylon plates with a thickness of 10 mm were used for both FEA simulations and experimental validation.

Figure 68a and Figure 68b display the contact pressure and contact status of the simulation results, respectively. It is confirmed that the addition of semi-rigid plates improves the pressure distribution across the single-layer cell surface when compared to their absence in design 1. A greater area of the cell experiences contact pressure above 0 MPa in Figure 68a, however the pressure is still largely concentrated towards the corners. Figure 68b demonstrates that a non-sticking contact still remains due to cell bending under compression, which is exacerbated due to the thin form-factor. Despite the

improvements over design 1, it is still not recommended to use bolts to apply force to a single-layer cell when their locations lie outside the circumference of the cell.
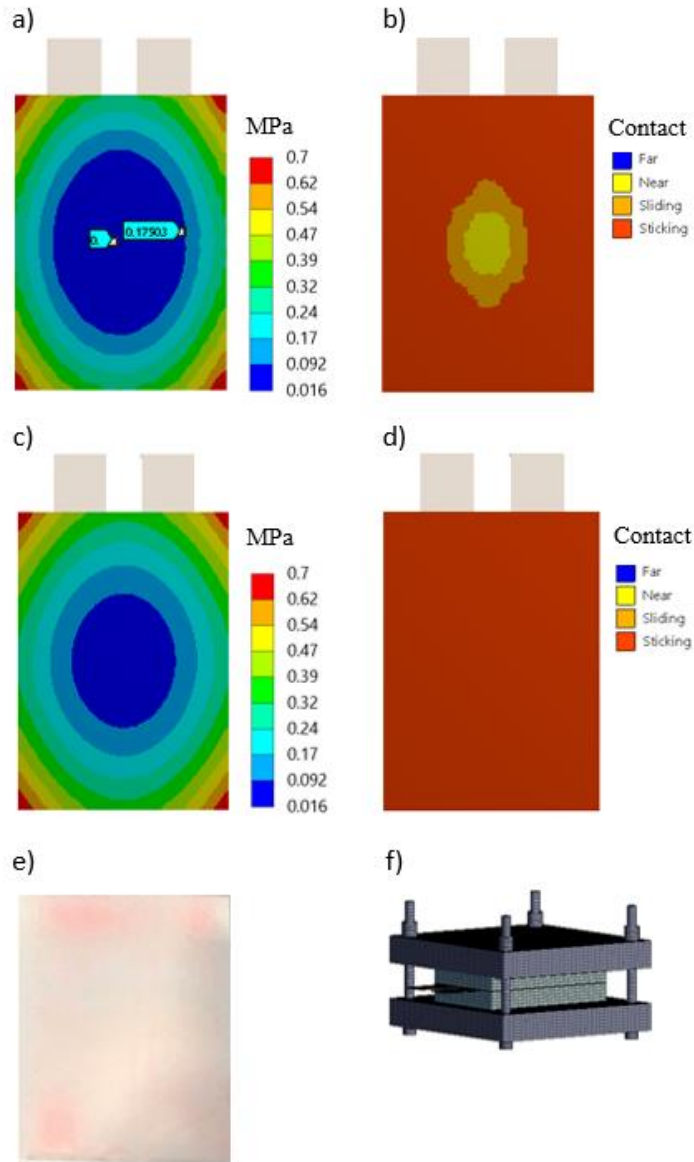
Figure 68. Pressure distribution for the compression of a single-layer pouch cell using design 2 with 10 mm nylon semi-rigid plates. (a) FEA simulation result for a 0.5 mm thick pouch cell, (b) FEA contact result for a 0.5 mm pouch cell, (c) FEA simulation result for a 5.0 mm thick pouch cell, (d) contact result for a 5.0 mm pouch cell, (e) experimental validation of 0.5 mm thick pouch cell with pressure sensitive film (LLW) and (f) FEA model.

Figure 68c and Figure 68d display the pressure distribution and contact status during the compression of a 5.0 mm thick cell, respectively. For a thicker cell, the contact has improved, and the entirety of the cell is in contact with the nylon plates, which demonstrates that cell bending is drastically reduced with a thicker pouch cell. However, the pressure distribution remains significantly non-uniform as higher pressures are exhibited towards the corners.

The experimental validation in Figure 68e confirms the existence of higher pressures located at the corners of a single-layer pouch cell (0.5 mm) when using design 2. Red regions at the corners of the cell remain, which suggests the contact pressure are higher at these locations. It is therefore concluded that designs using bolt clamping force at the corners of compression plates are ineffective for achieving a uniform pressure distribution across single-layer pouch cells. Introducing semi-rigid plates improves the pressure distribution, but distinct regions of the pouch cell still experience no pressure.

6.3.3 Evaluation of Design 3

The pressure distribution results for design 3 using a 1.0 kN bolt pretension at each corner of the compression plates is displayed in Figure 69. Here the compression plates apply force to the pistons which apply the force directly the cell. The PEEK blocks surrounding the cell do not take part in the compression. The pressure distribution presented in the FEA simulation in Figure 69a shows a uniform pressure distribution in the area that the piston is in contact with the cell. A higher level of pressure is observed around the circumference of the piston due to shear forces. Outside this circumference, the cell experiences no pressure, which is to be expected. However, the experimental validation of the FEA results in Figure 69b indicates a non-uniform pressure distribution. Here the pressure is concentrated in roughly four peripheral regions at the edge of the piston area. This finding points to an inherent error with manually applying force using bolts at the four corners, which have to be tightened sequentially. Despite tightening slowly and in a specific order, it is likely that in this case the compression plate applied force directly to the edge of the piston near the location of the bolt being tightened. When tightening the next bolt, the force was applied to a different edge of the piston. This method of sequential tightening concentrated the force applied to the cell around the circumference of the piston at the locations of the four bolts. For the FEA simulation, the bolt pretension was

applied at the same time to each of the four bolts, and hence the pressure distribution was uniform.

These results highlight that in order to achieve a homogeneous pressure distribution using design 3, the bolts must be tightened at the same time to prevent pressure concentration at the edge of the piston. If this can be ensured, then design 3 can provide a uniform pressure distribution to a cell whose size is no larger than the circumference of the piston. Because the single-layer pouch cell used in this investigation possesses a larger area compared to the cell that is used in previous studies[21,173], this test rig design would not be suitable. Increasing the piston diameter to a size larger than the area of the cell would ensure coverage, however the resulting rig would be bulky and heavy and thus not suitable for use in thermal chambers.

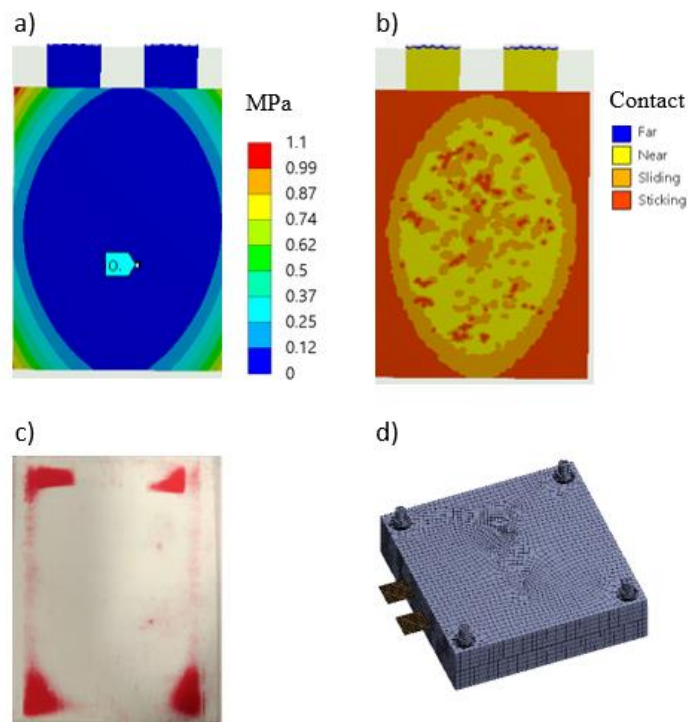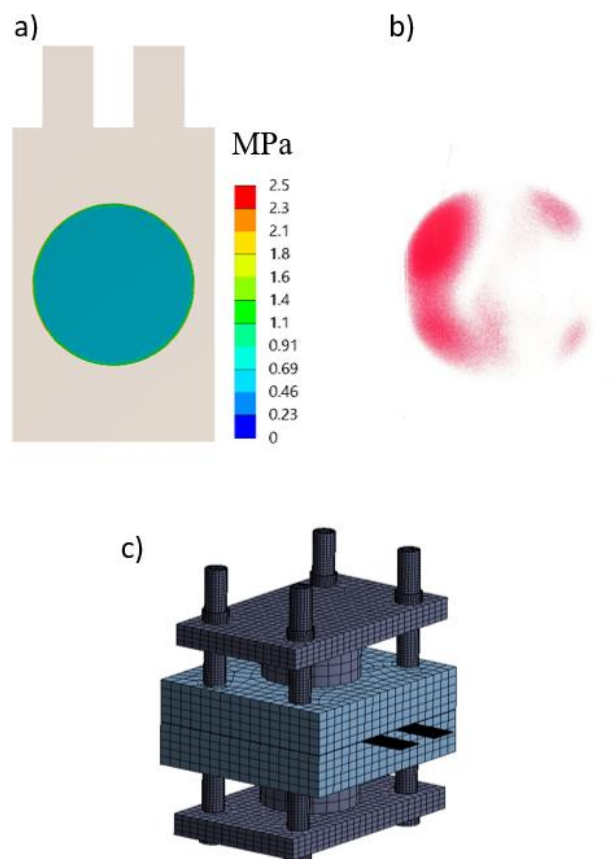**Figure 69. Pressure distribution for the compression of a 0.5 mm thick single-layer pouch cell in design 3. (a) FEA simulation result, (b) experimental validation with pressure sensitive film (LLW) and (c) FEA model.**

6.3.4 Evaluation of Design 4

It has been demonstrated that the use of bolt clamping force at the corners of compression plates are inadequate for the homogenous compression of the single-layer LIB pouch cell. Furthermore, a centrally applied load can produce a uniform pressure distribution, but only if applied evenly in time. These findings provided the basis for the development of a custom test rig design that is capable of applying uniform pressure whilst maintaining a moderately compact form-factor.

Exhibited in Figure 70 are the pressure distribution results for design 4 using a 1.5 kN centrally applied load through the piston screw. The insertion depth of the piston screw is a measure of the depth of the guide hole cut out of the piston block. Increasing/decreasing the insertion depth simulates a thinner/thicker piston block. For example, Figure 70a presents the pressure distribution for an insertion depth of 2 mm into a 25 mm piston block. The effective distance between the piston screw and single-layer cell is therefore 23 mm. Here, a homogeneous pressure distribution is achieved for the entire cell. When increasing the insertion depth to 10 mm and 24 mm for Figure 70b and Figure 70c, respectively, a progressive reduction in the uniformity of pressure distribution is observed.

The experimental validation presented in Figure 70d agrees with the FEA simulations; significantly greater uniformity is achieved when using design 4 with a 2 mm insertion depth into a 25 mm piston block. The entire surface area of the cell shows a similar intensity of red colour, which suggests all areas of the cell are being compressed evenly. At the very edge regions, a slight fade in colour is observed, however this can be explained by the relative areas of the electrodes to the aluminium-polymer pouch. The aluminium-polymer pouch encasing the electrodes has a distinct overlap at the edges where no electrode foils exist. This creates perimeter regions that are significantly thinner than the central parts of the cell and thus are compressed to a lesser degree.

These results demonstrate that design 4 is very capable of achieving a uniform pressure distribution, which is dependent on the thickness of the piston block. To distribute pressure evenly across a LIB pouch cell during electrochemical testing, a centrally applied load is recommended.
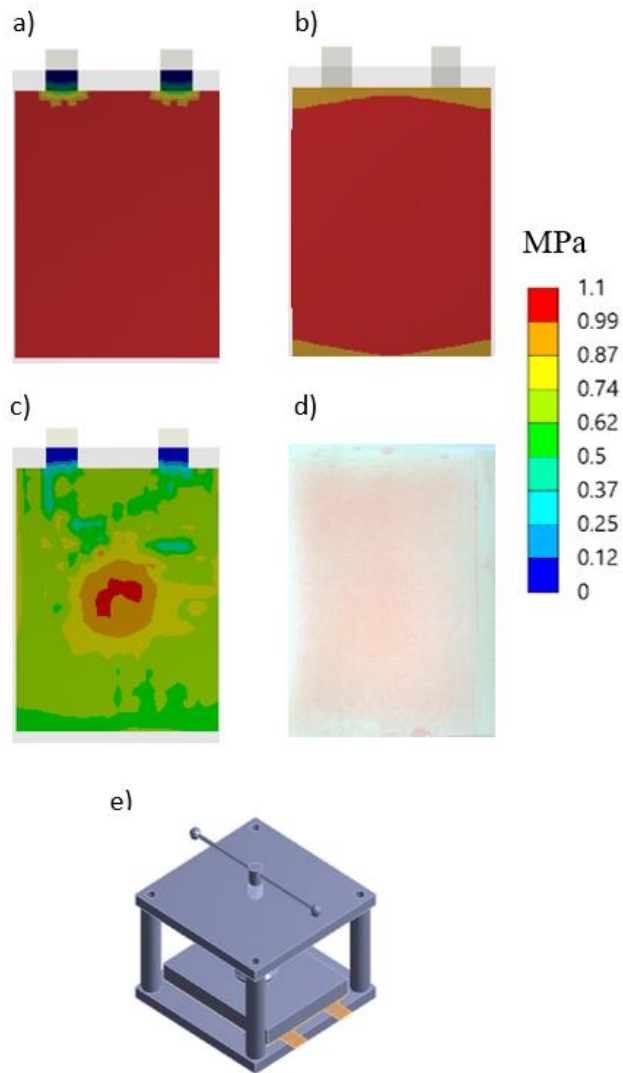
Figure 70. Pressure distribution for the compression of a 0.5 mm thick single-layer pouch cell in design 4 for different insertion depths. (a) A 2 mm insertion depth into a 25 mm piston block, (b) 10 mm insertion depth into a 25 mm piston block, (c) 24 mm insertion depth into a 25 mm piston block, (d) experimental validation of 2 mm insertion depth into a 25 mm piston block with pressure film (LLLW) and (e) FEA model.

6.3.5 The Effect of Cycling Under Inhomogeneous Compression

After the development of a rig capable of applying uniform pressure, it was important to observe the differences between cycling under homogeneous and inhomogeneous compression. For this study, the experimental testing consisted of three sections that were performed sequentially: an initial cycling period, the decompression of the cells and finally the re-compression and the resumption of cycling. Experimental details of the

study can be found in the experimental procedure section of this chapter. For the reasons mentioned in Appendix 1 interpretation of the data was not possible.

6.3.5.1 Initial Cycling Followed by Uncompressing

Displayed in Figure 71 are the relative capacity and resistance values for cells inhomogeneously or homogeneously compressed over 200 cycles, along with the values after decompression. The check-up after uncompressing the cell was performed immediately after releasing the pressure.

For the relative capacity values in Figure 71a, it is evident that inhomogeneously compressing the cell results in capacity fade over the first 200 cycles by up to 4% vs. 1% for the homogeneously compressed cell. The capacity progressively decreases at each check-up from cycle 0 for the inhomogeneously compressed cell, whereas the capacity for the homogeneously compressed cell increases from cycle 0 to cycle 50 and then progressively decreases. Decompressing results in a moderate recovery in capacity for the homogeneously compressed cell and a slight decline in capacity for the inhomogeneosly compressed cell.

The relative resistance values in Figure 71b show a decline in capacity over 200 cycles for both cells, however this decrease is <0.3% of the total resistance. Homogeneously compressing the cell decreases the resistance further than the inhomogeneously compressed cell, however the difference between the two is <0.2%. After decompression, both cells show a substantial increase in resistance, relative to the overall changes exhibited over 200 cycles. It is apparent that switching from a compressed state to an uncompressed state induces rapid changes that alter cell capacity and resistance.

A cautious approach must be adopted when examining the resistance change displayed in Figure 71b due to errors in the measurement. The voltage resolution of the Basytec Test System is 0.3 mV. The approximate voltage change during a -0.15 A 10 s discharge pulse at 50% SoC for a fresh LiFun cell is 0.065 V, meaning one might expect an error of ±0.46% associated with the voltage measurement in these tests. This error is substantially higher than the observed changes in Figure 71b. In particular, the increase in resistance observed in the uncompressed state in Figure 71b is within the error of the measurement and therefore cannot be deemed a significant change.
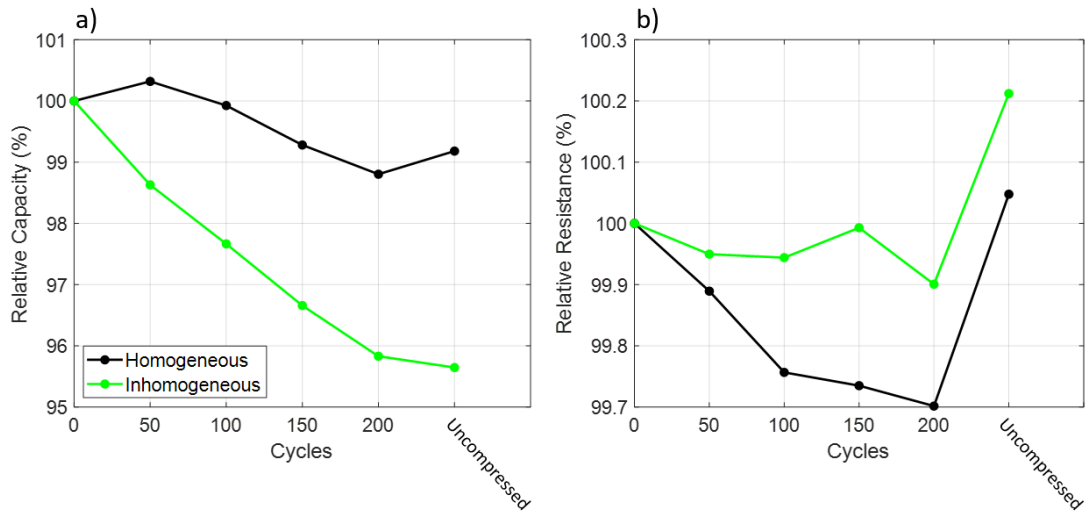
Figure 71. (a) relative capacity vs. cycles and (b) relative resistance vs. cycles for homogeneously and inhomogeneously compressed cells over 200 cycles, including values immediately after uncompressing.

6.3.5.2 Extended Cycling

Figure 72 displays the relative capacity and resistance during the extended cycling period. Figure 72 is a continuation of Figure 71, where the uncompressed datapoints in Figure 72 are the same points presented in Figure 71.

Re-compressing the cells promotes a capacity recovery for homogeneously compressed, and a capacity decline for inhomogeneously compressed cells, which is demonstrated in Figure 72a. The capacity of the homogeneously compressed cell then continues to increase over the subsequent 50 cycles to a value 1% higher than for the fresh cell, followed by a progressive decline to 98% relative capacity after 400 cycles. The capacity of the inhomogeneously compressed cell decreases from cycle 250 to 450 to 88% relative capacity. This is not expected to be an effect caused by the anode overhang area, as check-ups performed when changing between compressed and uncompressed states were performed in short succession, whereas overhang effects are expected to occur on the timescale of weeks. In addition, both cells were kept under identical conditions during this period, with an SoC of 50% SoC and a temperature of 25⁰C between check-ups. This means any anode overhang effects would be expected to be identical across both cells. Lastly, storage at 50% SoC in between check-ups is an SoC very similar to the average

cycling SoC, thus any anode overhang effects in this time period are expected to be minimal.

In Figure 72b, recompressing the homogeneous cell promotes only a minimal increase in resistance, whilst a substantially larger increase in resistance is observed after recompressing the inhomogeneous cell. Both cells only show a minor change in resistance in response to subsequent cycling to 450 cycles: a slight decrease for the homogeneous cell and a slight increase for the inhomogeneous cell. It is evident that cycling under homogeneous or inhomogeneous compression does not induce large changes in resistance, as the maximum observed change is just 0.55%.

These results show a measurable, negative impact of inhomogeneous compression on LIB pouch cell performance. Inhomogeneous compression appears to induce a greater rate of capacity fade and resistance increase over homogeneously compressed cells during cycling by 9% and 0.6%, respectively. Furthermore, these cells display strong, instantaneous responses to the application/removal of pressure, regardless of whether the pressure is homogeneous.

Because of the cell design features described in Appendix 1, interpretation of the data was not provided, thus further examination with single-layered cells is required in the future.
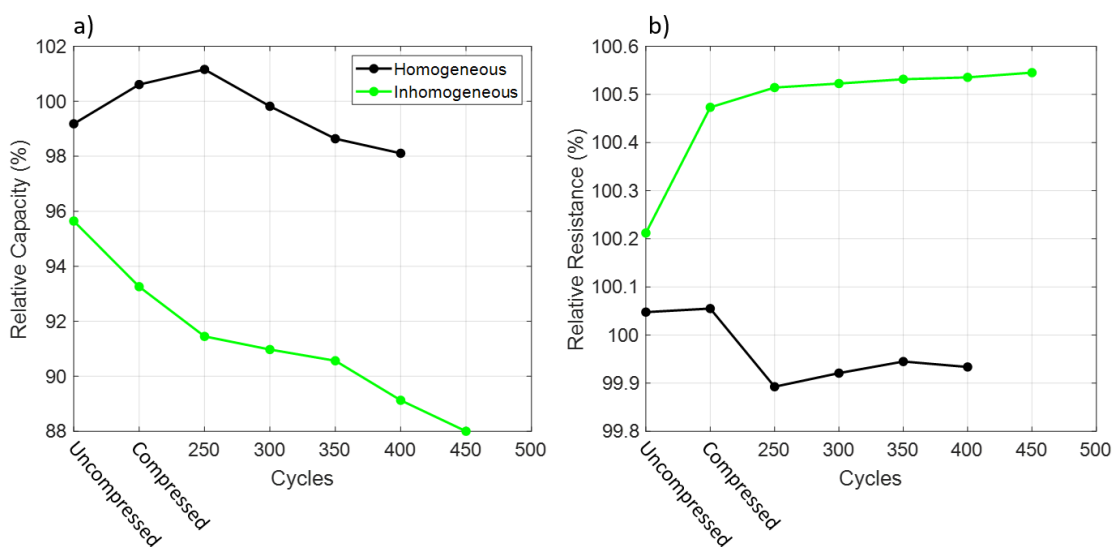
Figure 72. (a) relative capacity Vs. cycles and (b) relative resistance Vs. cycles for homogeneously and inhomogeneously compressed cells during the extended cycling period. Datapoints are a continuation of those seen in Figure 71.

6.4 Conclusions

Using Bolts at the corners of Compression Plates Creates Non-Uniform Pressure

Flat compression plates that apply force using bolts at the four corners could not provide an even pressure distribution in FEA simulations and experimental validations. Using semi-rigid plates in contact with the cell improved distribution, but a large variation persisted. Applying a clamping force outside the cell's circumference likely produced out of plane bending of the cell that reduced contact with compression plates and reduced pressure in the central regions. For the compression of a thicker cell with the same design, large inhomogeneities still existed, but to a lesser extent than for a thin cell.

A Central Piston Can Apply Even Pressure, but only in a Single Tightening Motion

FEA simulations demonstrated that a central piston design can achieve a uniform pressure distribution in the area within the piston's circumference, however, experimental validation revealed large non-uniformity. The origin of the non-uniformity was found to be the sequential tightening of the bolts at the four corners of the compression plates. By tightening one bolt at a time (no matter the order), the force is concentrated through the edge of the piston nearest the bolt, which translates into increased cell pressures in these regions. If all bolts were tightened at the same time like in the FEA simulation, a uniform pressure distribution can be achieved. The sequential tightening of multiple bolts is expected to create pressure inhomogeneities in all test rigs that use compression plates, such as in design 1 and 2.

A Successful Candidate for an Even Pressure Distribution

Key successful elements from design 3 were implemented in the proposed rig, which applied the load centrally through a piston to a block using a single, continuous motion. This mitigated the negative effects that arise with the sequential tightening of bolts at the corners and produced a uniform pressure distribution in both FEA simulations and

experimental validation. A minimum required thickness of the piston block was also established; blocks thinner than 15 mm between the piston screw and the cell produced significant inhomogeneities and an effective block thickness of 23 mm produced an entirely uniform distribution.

By design, the proposed rig is easy to manufacture, simple to adapt to different form factors and compact to maximise the limited space inside thermal chambers. From these findings, it is recommended to use a rig comparable to design 4 to ensure an even pressure distribution during the electrochemical testing of LIB pouch cells.

Inhomogeneous Compression During Cycling Promotes Cell Ageing

Cycling with inhomogeneous compression showed greater capacity fade by 8% and resistance increase by 0.6% than cycling with homogeneous compression over 450 cycles. Although small, this resistance difference was large in comparison to the maximum resistance change over 450 cycles (0.55%). Uncompressing/re-compressing resulted in large, immediate changes in capacity and resistance. Restrictions related to cell design inhibited the determination of degradation pathways, thus further testing on different LIB pouch cells is required. From future testing, the direct effect of inhomogeneous compression on LIB performance will be determined.

7 Static and Cycle Testing of Lithium-Ion Cells Under Compression

7.1 Introduction

During their manufacture and operation, LIBs are subjected to a multitude of stack pressures to improve contacts between components, improve thermal exchange and to prevent electrode layer delamination[2,167]. In addition, LIBs are often packed for volumetric efficiency and constrained within tight spaces, which further increases the external pressures[174,175]. For pouch cells, the lack of mechanical integrity makes them more susceptible to external compression[171,176], the effects of which are not currently well understood.

During the manufacturing process, numerous pressures exist in order to maximise cell performance. LIBs are typically produced by winding, folding or stacking metal foils that are coated with active material and separated by a porous polymer membrane[171]. Prior to assembly, the coated electrode foils undergo a calendaring process where they are subjected to compressive pressures (0.1-1 MPa) applied in the normal plane[96]. This produces more volumetrically constrained active materials with improved thermal and electrical properties, but also smaller pores and greater tortuosities, which presents a crucial challenge in the manufacturing process[171].

Internal mechanical stresses within cells have been previously studied from the perspective of the stresses that arise from the cyclical intercalation/deintercalation of lithium in the active materials. Volume fluctuations leading to particle exfoliation and SEI growth and repair have been routinely identified as dominant factors in the capacity fade and resistance increase during ageing. In volumetrically constrained cells, these

volume fluctuations lead to increased cyclical pressure swings during cycling that contribute to fatigue of the active materials and cell components[1,14,57,110,177].

The early work by Canarella et al.[76] and Peabody et al.[178] first identified the relationship between external compressive loads and LIB performance. Since then, only a handful of studies have explored the effects of external pressures on LIB pouch cell performance, often with somewhat contradictory outcomes[2,20,21,53,86,96,97]. Barai et al. applied compressive loads of up to 15 psi (0.1 MPa) and found that pressure reduced capacity fade during cycling and increased direct current (DC) pulse resistance and ionic transport resistance due to separator pore closure[2]. On the contrary, Canarella et al. found that compressive loads increased capacity fade during cycling as a result of increased surface film formation[96]. Moreover, Muller et al. found that external pressure increased capacity fade during cycling and reduced discharge capacity in C-rate testing above 0.8C[20]. The field remains ambiguous, with many experimental factors influencing the specific outcomes of each study.

Static compression testing, defined here by testing in the absence of cycling, is a promising route for identifying the more fundamental effects of pressure on LIB performance. Although cycling is an important and necessary part of battery testing, its multitude of factors that can play a role in the outcome of experiments can potentially cloud the underlying effects of pressure that are to be reported. Many of the aforementioned studies include both cycle and static testing, but their similarities and differences are often blurred. It is thus important to clearly separate out these two routes and the effects that arise for each.

Static measurements, which inherently probe the more instantaneous response to pressure, have revealed strong effects on battery behaviour. In addition to the above-mentioned studies, Sutter et al. found that the application of pressure increased discharge capacity by 19% and decreased DC pulse resistance by 50% in silicon-graphite cells that displayed no variation during cycling[53]. Similarly, Zhou et al. observed an irreversible increase in discharge capacity of up to 2.3% and a decrease in DC pulse resistance by up to 13.28%[97]. Although briefly mentioned in the latter study, the reversibility of pressure effects has not been explored in detail in the literature. Reversibility is defined here as the propensity for any measured electrochemical changes induced in a cell during the application of external pressure to be reversed upon the decompression of the cell. Because LIBs are often in environments where the pressure change is dynamic and not

constant, it is important to consider whether the positive/negative effects of applying pressure are reversible upon its release. By looking deeper into its reversibility, a new insight into pressure effects may be gained.

To further investigate the effect of pressure on LIB pouch cells, experimental ageing studies with separate static testing and cycling are performed in this chapter. Cells are initially examined with static measurements, which explores the more instantaneous effects of pressure and the reversibility of such effects. Experimental cycling tests are then performed to observe the long-term cycling performance of the LIB pouch cells under compression.

7.2 Experimental Strategy

A two-part experimental study was performed to observe the behaviour of lithium-ion pouch cells under compression. Initially, testing was performed in the absence of cycles to explore the impact of pressure on cell performance under static conditions. Next, cells were cycled under different pressure levels to establish their response during cycle ageing. All compression testing was carried out in the rig developed in chapter 6 (design 4, section 6.2.3.4, page 128)

7.2.1 Lithium-ion Cells Studied and Equipment Used

The lithium-ion cells used throughout this study were commercial LiFun 2051A0 pouch cells with a graphite anode chemistry and a nickel-manganese-cobalt ($LiNi_{0.8}Mn_{0.1}Co_{0.1}O_2$) cathode chemistry, as described in section 3.1.1.2 (page 24). All electrochemical cycling and static measurements were performed on Basytec CTS battery cyclers. For identical environmental conditions, all testing presented in this study was performed at 25⁰C in a Binder MK 240 thermal chamber. Additional galvanostatic intermittent titration technique (GITT) measurements were performed on a Biologic BCS 815 system in a Binder MK 240 thermal chamber. For the application of pressure, a custom rig design (design 4, section 6.2.3.4, page 128) and Tekscan FlexiForce A502 force sensors were placed on top of the cells, where the resulting resistance value was

measured by a multimeter. To convert the resistance values to force, equation (21) was used, where F is the applied force in kN, a is a coefficient with the value of 3717, R is the measured resistance in Ohms (Ω) and b is the exponent with a value of -1.034. The equation was obtained from a polynomial fit of values created during the measurement of resistance from the application of known mass.

$$F = aR^b \tag{21}$$

7.2.2 Experimental Ageing Procedure

7.2.2.1 Static Compression Testing

The first part of this investigation explored static compression testing, in which cells were tested in the absence of cycles. Numerous experimental techniques were used throughout this study and will be outlined in the following. Headings are displayed as they appear in this chapter.

The Instant Effect of Pressure on Capacity and Resistance During a Check-Up

To establish a baseline for capacity and resistance under compression at three levels, check-ups were performed using the procedure found in Figure 9b (page 27). Firstly, a check-up was performed on three cells in an uncompressed state. Then 0.03 MPa, 0.15 MPa and 0.30 MPa of pressure was applied to each cell separately, followed by a check-up immediately after compression. Capacity was calculated from a 0.1 A discharge, whilst resistance was calculated from a -0.15 A 20 second DC discharge pulse at 50% SoC.

A Marginally Improved Rate Capability at Very Low Pressure

A discharge C-rate test was performed to assess the cell's response to varying currents in uncompressed and compressed states. Five discharge currents were tested: -0.03 A (0.2C), -0.05 A (0.4C), -0.1 A (0.75C), -0.13 A (0.95C) and -0.15 A (1.1C). Each cell was charged to 4.2 V with 0.05 A and with constant current constant voltage (CCCV) with a current cut-off of 0.005 A, followed by a constant current (CC) discharge with

each discharge current. Discharges started with the lowest current and progressed to the highest. 10 minute OCV rests were enforced between each charge/discharge.

The Immediate and Reversible Effects of Pressure on Resistance

To observe the more immediate effects of pressure on resistance, cells were subjected to a series of compression-decompressions. In each state (compressed or uncompressed), a discharge pulse test was performed. The test consisted of two 20 second discharge pulses with a discharge current of -0.12 A and at 50% SoC. After each discharge pulse, the cells were rested under OCV conditions and then charged back to 50% SoC to minimise OCV drifts. Charging was followed by another 10 second rest. Each test was performed sequentially, with <2 minutes in between each test. The two-minute break in between each test allowed for compression/decompression of the cells.

The Relaxation of Resistance after the Release of Pressure

To study the reversibility and the relaxation of resistance after releasing pressure, short discharge pulses were performed sequentially at 50% SoC. Firstly, a 2 second discharge pulse with -0.12 A was performed, followed by a 10 second rest under OCV conditions, followed by a charge back to 50% SoC, and finally a 10 second rest. This was repeated 34 times to achieve 34 sequential and continuous discharge pulses. Pulse number 1 and 2 were performed in an uncompressed state, pulse number 3 and 4 were performed under compression with either 0.0013 MPa or 0.56 MPa, and pulses 5-34 were performed in an uncompressed state.

The Limited Effect of Pressure on the Diffusion Coefficients

GITT was performed on full-cells in both uncompressed and compressed states in order to obtain the diffusion coefficients. Cells were discharged to 3.0 V and then subjected to 1-minute charge pulses of +0.13 A to 4.2 V with a OCV relaxation of 4 hours in between each pulse. After charging, cells were subsequently discharged with 1-minute discharge

pulses of -0.13 A to 3.0 V and 4-hour OCV relaxation in between each pulse. Diffusion coefficients were calculated using Sand's approach (see section 3.4, page 33)[108,109].

7.2.2.2 Cycle Ageing

The second part of this study involved the cycling of the lithium-ion pouch cells under three compression levels: 0.00 MPa, 0.03 MPa and 0.30 MPa. Cells were cycled under compression (initial pressure) for 600 cycles, at which point the pressure values were changed to new values (pressure after change) and cycling was resumed. A flow diagram of this procedure is presented in Figure 73. During cycling, all cells were charged and discharged using 0.1 A (0.74C) and -0.1 A (0.74C) with 10-minute open circuit voltage (OCV) rests in between each charge/discharge. Constant-current constant-voltage (CCCV) charging, and constant-current (CC) discharging procedures were used. The full voltage limits of 4.2 V and 3.0 V were employed throughout cycling. The full details of cycling parameters and pressures can be found in Table 8. Every 50 cycles, a check-up according to Figure 9b (page 27) was performed to provide a performance reference for all cells under identical conditions.
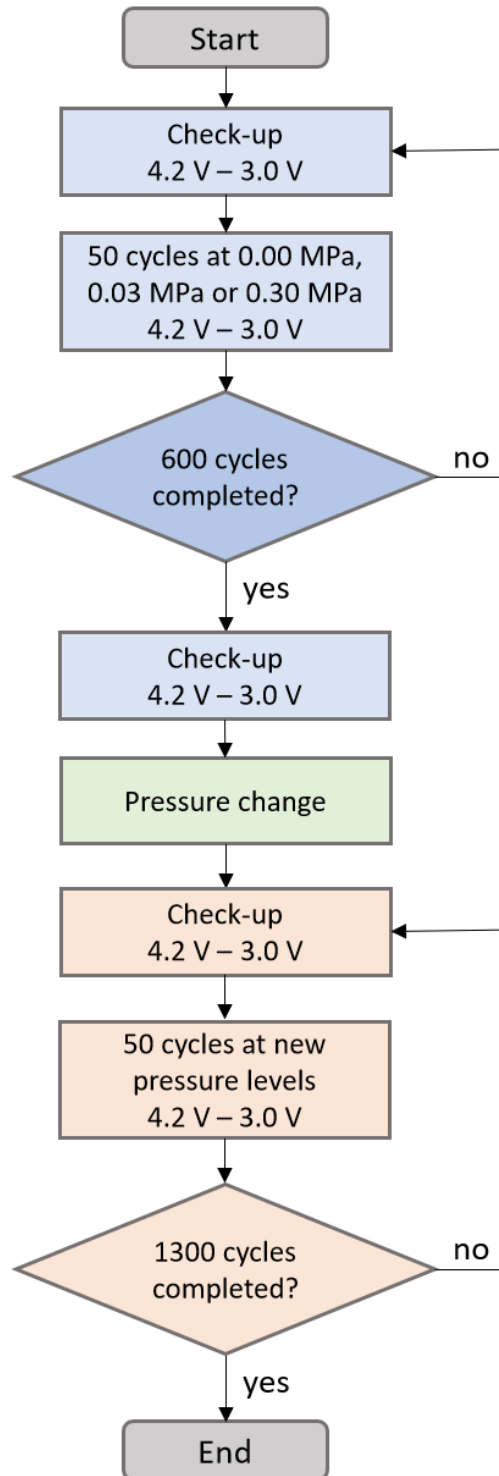
Figure 73. Flow diagram of the experimental procedure.

Table 8. Cycling protocol parameters with applied pressure.

Cell	Charge cut-off voltage/V	Discharge cut-off voltage/V	Charge current/A	Discharge current/A	Initial pressure/MPa	Pressure after change/MPa
1	4.2	3.0	+0.1	-0.1	0.00	0.30
2	4.2	3.0	+0.1	-0.1	0.03	0.00
3	4.2	3.0	+0.1	-0.1	0.30	0.03

7.3 Results and Discussion

7.3.1 Static Compression Testing

To explore the direct effect of pressure on LIB performance, static electrochemical measurements were conducted in which no cycling was completed. In this section, capacity, resistance, diffusion and rate capability are evaluated in the compressed and uncompressed state in order to gain a deeper insight into the processes that occur.

7.3.1.1 The Instant Effect of Pressure on Capacity and Resistance during a Check-Up

To obtain baseline static performance measurements of the cells, check-ups (see Figure 9b, page 27) were performed in an uncompressed state, then in a compressed state at three different pressure levels on fresh cells. The absolute capacity and DC resistance values from these are presented in Figure 74a and Figure 74b, respectively. The percentages given in the compressed state are calculated relative to the values in the uncompressed state.

Because the different processes that occur within a LIB possess various time constants (10^{-3} Hz to 10^8 Hz), a DC discharge pulse will contain multiple contributions to the total resistance (see section 3.7.1, page 38). For pulse durations above ~1 second, the

calculated resistance will likely contain charge transfer, SEI transport, partial diffusion and ohmic resistance contributions[114,117]. Increasing the pulse duration above ~1 second will increase the diffusional contribution, thus the calculated resistance will rise. The following sections display the resistance calculated from either 2, 10 or 20 second pulses. Therefore, all resistance values hereon presented are comparable, but with varying levels of diffusional contribution, which likely explains the slight initial magnitude variations.

For the capacity values in Figure 74a, 0.03 MPa and 0.30 MPa reduced capacity by 3% and 0.5%, respectively, whereas a median value of 0.15 MPa increased capacity by 3% when compared to no pressure. In Figure 74b, applying 0.03 MPa and 0.30 MPa of pressure increased resistance by 9%, whereas a median value of 0.15 MPa reduced resistance by 0.5%.

From these data, capacity is reduced by both lower and higher pressure, whilst it is increased by a medium pressure level. However, the influence of pressure on discharge capacity is small in comparison to resistance. Lower and higher pressure levels measurably increase the resistance, whilst a medium pressure only slightly reduces resistance.

Two things are evident from this: firstly, an apparent pressure sweet spot is observed where the median pressure level positively impacts cell performance and high/lower pressure negatively impacts performance during a check-up. Secondly, resistance is more strongly impacted by pressure than capacity, particularly at the extremes of the pressure range presented here. This finding is in line with a previous report that found little change in discharge capacity, but larger changes in both impedance and DC resistance upon compression[2]. Moreover, the increase in resistance upon the application of pressure has also been observed in previous studies and has been ascribed to increases in the ohmic resistance resulting from a rise in the separator ionic pore resistance and the reduction of active material surface area[2,76,179]. However, the origins of resistance rise were not determined in this study.

These results were obtained from a single check-up in each condition. No repeats were performed for this test, thus for the results to be significant and for the conclusions to be more robust, additional testing is required in each condition.
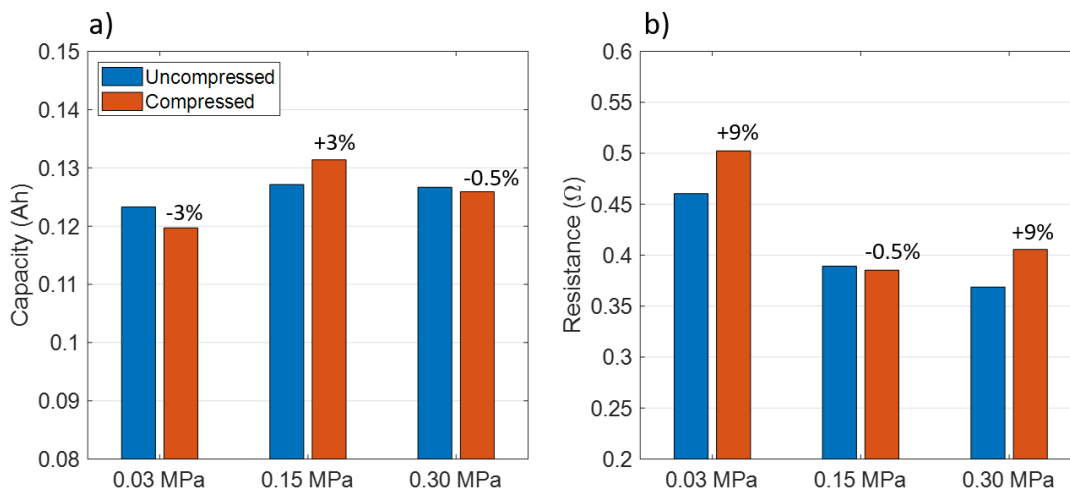
Figure 74. (a) Relative capacity and (b) relative resistance for LiFun 2051A0 cells compressed at three pressure levels, relative to their uncompressed state. Capacity was calculated from a 0.05 A discharge and resistance values were calculated from 10 s discharge pulses at 50% SoC.

7.3.1.2 A Marginally Improved Rate Capability at Very Low Pressure

Presented in Figure 75a and Figure 75b are the rate capability results for cells in uncompressed and compressed state for very low and high pressure, respectively. Initially, the rate capability test is performed on each uncompressed cell. Then, each cell is compressed at either very low or high pressure according to the values detailed in Table 9.

Table 9. Force and pressure values at each pressure level.

Pressure Level	Force	Pressure
Very low	7.55 N	0.0013 MPa
Low	354.66 N	0.059 MPa
Medium	1.72 kN	0.29 MPa
High	3.35 kN	0.56 MPa

At low C-rates of 0.2C, the application of pressure increases the discharge capacity at both pressure levels by up to 1%. Increasing the C-rate produces progressive decreases in

discharge capacity, which is to be expected in LIBs[32]. With C-rates higher than 0.2C, differences are observed between very low and high pressure: very low pressure increases discharge capacity, whereas high pressure decreases discharge capacity. All slopes from 0.4C through to 1.1C exhibit a linear decrease of discharge capacity with increasing resistance, the gradient of which is not significantly altered by the application of pressure.

The maximum change in discharge capacity after the application of pressure is just 1% of the total capacity, which is seen in Figure 75a at 0.2C. Such a small variation in capacity cannot be seen as a significant impact of pressure on the rate capability of the LiFun cells, particularly as the majority of changes are far smaller than this. Because resistance shows a stronger response to compression than capacity, the results discussed in the following sections will focus on the DC discharge pulse resistance.
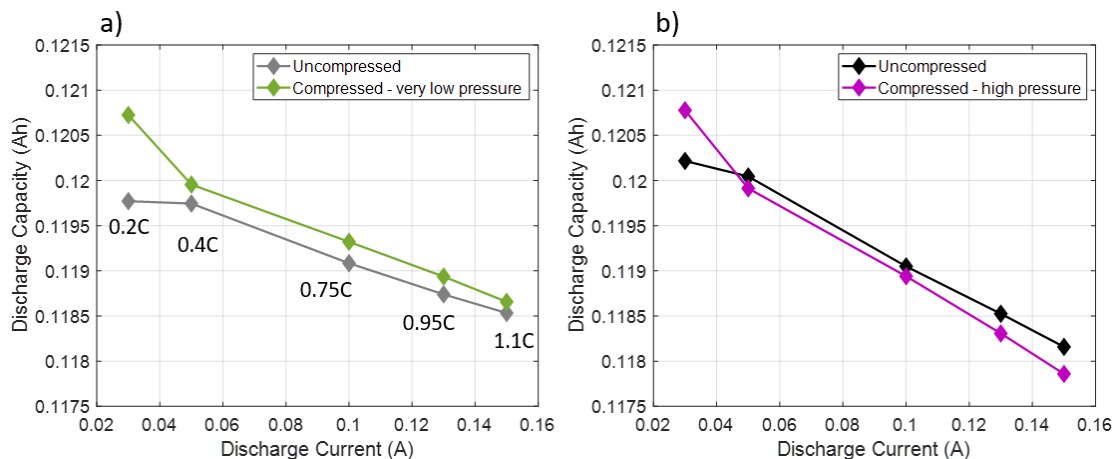
Figure 75. Rate capability of uncompressed cells against (a) compressed at very low pressure 0.0013 MPa and (b) high pressure 0.56 MPa.

7.3.1.3 The Immediate and Reversible Effects of Pressure on Resistance

It has been established that the effects of pressure can be observed in a check-up performed immediately after compression. Because the DC pulse resistance appears to produce a stronger response than the discharge capacity, and the DC pulse test can be performed in a short space of time, the following focuses on the resistance values obtained under compression/decompression. The duration of a single check-up is approximately two days, so to further explore the timescales involved, and the potentially reversible nature of the changes, 20 second discharge pulses were performed immediately after

compressing/uncompressing. Table 9 lists the force and pressure values corresponding to each pressure level and is presented in Figure 76, which displays the absolute resistance values in the compressed and uncompressed states. Two minutes in between each DC discharge pulse allowed for the compression/decompression of the cells.

Applying a very low pressure sharply increases cell resistance by 16%, as observed in Figure 76. After the initially applied (very low) pressure, subsequent applications of pressure result in sharp increases in resistance. Uncompressing the cell after each compression prompts a reduction in cell resistance. Apart from after applying very low pressure, uncompressing results in a complete reversibility of the resistance increase. Resting the cell in the uncompressed state for 1 week results in a further decline in resistance to a point that is similar to the starting value.
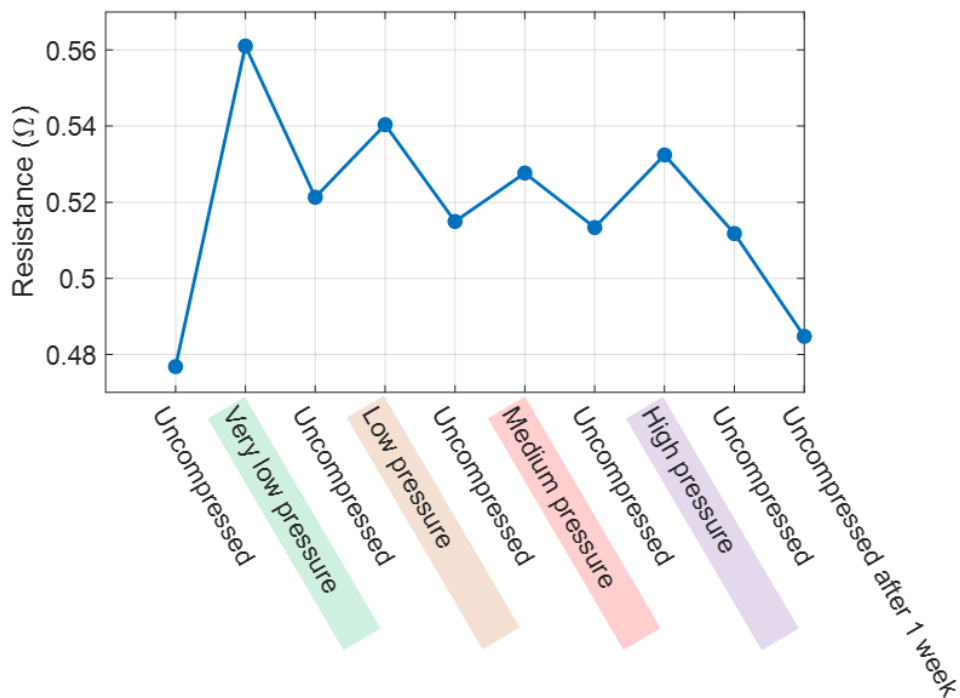
Figure 76. DC resistance values for a 20 s discharge pulse at 50% SoC during sequential compression/decompression tests.

The first instance of pressure induces the strongest response on resistance, even with a very low pressure value, and that subsequent applications increase resistance but to a lesser extent. It is apparent that in terms of resistance, these cells are highly responsive to

just slight increases in pressure and show the strongest response with respect to very low pressure. In addition, the highly reversible nature of this resistance increase is highlighted in the moment after cells are uncompressed. The resistance relaxes further when the cell is left in an uncompressed state for extended periods of time and that, in this case, the total resistance increase was almost entirely reversible.

The test presented in Figure 76 was repeated for another cell and the relationship between absolute resistance and pressure is plotted in Figure 77 to evaluate the repeatability of this finding. Although the absolute resistance values between the two cells differ, the approximate trends remain very similar. Very low pressure produces high resistance values that sharply decline with the application of higher pressures. This larger resistance increase for lower pressure than high pressure has also been reported previously, which found that the DC discharge pulse resistance of the cell was higher at 5 psi (0.034 MPa) than at 15 psi (0.10 MPa) in compressed pouch cells[2].
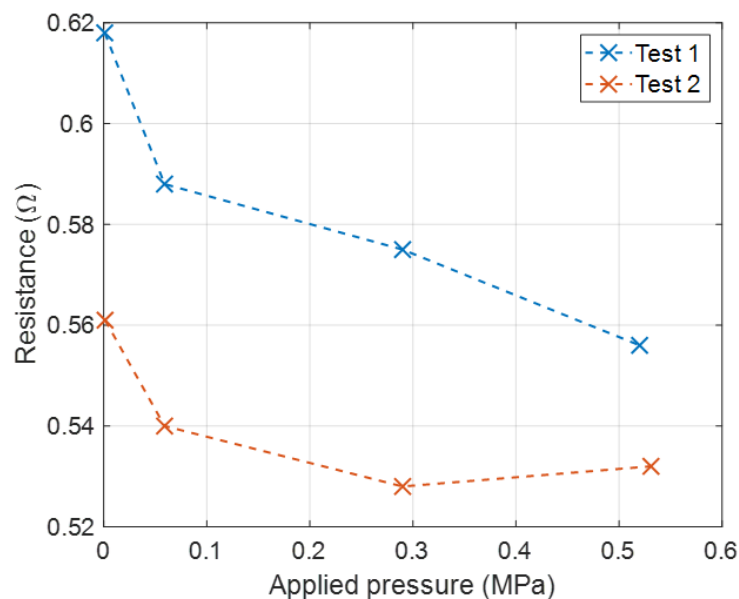
Figure 77. Resistance Vs. applied pressure at four pressure levels. Test 2 represents a repeat of test 1.

7.3.1.4 The Relaxation of Resistance after the Release of Pressure

To further explore the observed reversibility and relaxation effect of resistance after the release of pressure, a series of 2 s discharge pulses were performed in short succession at

50% SoC, as exhibited in Figure 78. After each discharge pulse, cells were rested under OCV conditions for 10 s before being charged back to 50% SoC. For the 'test with compression' curve, discharge pulse 1 and 2 are in an uncompressed state, pulse 3 and 4 (red circles) are in a compressed state, and pulse 5-34 are in an uncompressed state. For the baseline curve, all discharge pulses are in an uncompressed state.
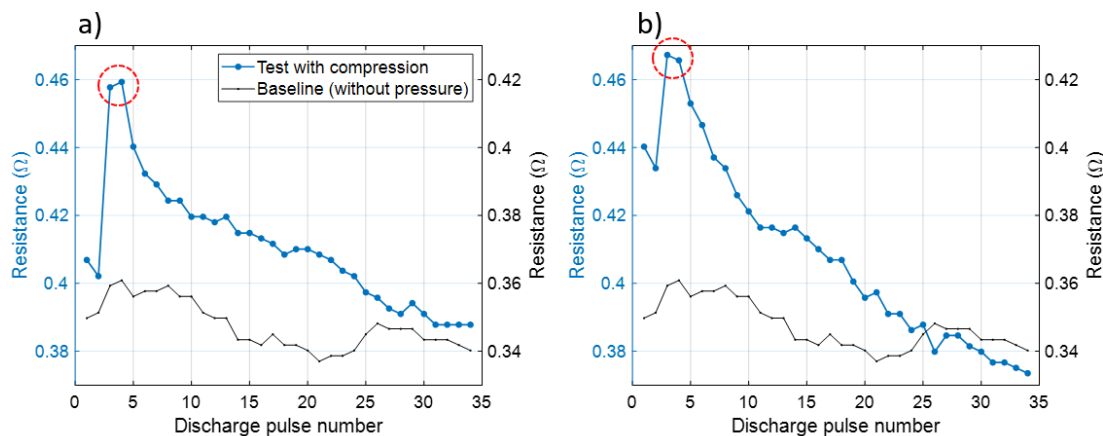
Figure 78. DC resistance values during a series of discharge pulses at 50% SoC. Each pulse sequence lasted approximately 25 seconds, giving a total test time of approximately 14 minutes. Red circles indicate pulses where (a) very low pressure 0.0013 MPa and (b) high pressure 0.56 MPa is applied. All other discharge pulses were performed in an uncompressed state.

For both very low and high pressure in Figure 78a and Figure 78b, respectively, the application of pressure causes a sudden increase in cell resistance. Very low pressure increases resistance by 0.06 Ω (15%), whilst applying a high pressure increases resistance by approximately 0.03 Ω (7%). After uncompressing, cell resistance falls sharply, initially in a non-linear fashion, followed by a period of linear decrease. Cell resistance continues to decrease to values below the resistance at the beginning of the test, which is particularly apparent for the cell that experienced high pressure in Figure 78b. The final resistance value for this cell is nearly 0.07 Ω (16%) lower than the initial value.

The timescales involved with both resistance increase and subsequent relaxation can be identified by observing the length of each pulse segment, which is approximately 25 seconds including the OCV rest and the charge back to 50%. The application of pressure between pulse 2 and 3 in Figure 78a and Figure 78b prompts the sharp increase in resistance within 25 seconds. The subsequent 25 seconds (pulse 3-4) under compression prompts no significant change in the resistance, which indicates that the entire resistance

increase as a result of compression is likely induced in well under 25 seconds. After decompressing between pulse 4 and 5, 30% of the resistance increase is reduced for 0.0013 MPa in Figure 78a and 40% for 0.56 MPa in Figure 78b. Between pulse 5 and 34, which lasts approximately 12 minutes, the resistance continues to fall to below the initial value at the start of the test.

This finding flags the highly reversible nature of resistance increase when these compressed LiFun cells are decompressed. Furthermore, a significant portion of the resistance changes occur within 25 seconds of compression/decompression and are more pronounced in the instance after compression. From this, it is recommended that the reversibility of resistance change is accounted for in the static pressure testing of LIB pouch cells.

In a search for the origins of the observed resistance relaxation/reversibility effect, the elastic nature of the separator membrane is perhaps the culprit, which has been identified as a dominant factor for the resistance increase, even at low pressures[2,76,179]. In the moment pressure is applied to the cell, the separator pores may become compressed, thus reducing the ionic conductivity from electrode to electrode and increasing the resistance. When the pressure is released, the polymer separator may relax to its previous shape and the compressed pores reopen to reduce the ionic conductivity resistance. Moreover, the reopening of pores may then promote a greater uptake of the electrolyte in a similar manner to that of a sponge, thus improving the wetting of the separator and further reducing the resistance, which may explain the lower final resistance values.

Higher pressures increasing the resistance less than lower pressures may be speculated as changes in the charge transfer resistance. At lower pressures, only the separator may be compressed, whereas at higher pressures, both the separator *and* the electrodes may become compressed. In the latter, an improved contact between the electrode particles could arise, which would effectively reduce the charge transfer (CT) resistance[2]. Higher pressure levels might thus promote a greater contact between electrode particles - an effect that is not observed at low pressures due to the less compressible nature of the electrodes compared to the separator. Overall, the reduced CT resistance may then offset the negative effect that pressure may have on separator pores. This could result in a smaller resistance increase when higher pressure is applied than when lower pressure is applied. Electrochemical impedance spectroscopy (EIS) may help to observe this effect

with greater depth by uncovering resistance contributions in more detail and is suggested for future study.

7.3.1.5 The Limited Effect of Pressure on Diffusion Coefficients

To identify whether the application of pressure affects the diffusional response of a cell, GITT measurements we conducted on cells in an uncompressed and compressed state. Displayed in Figure 79 are the effective diffusion coefficients in the compressed and uncompressed states for full-cells, calculated from a charging sequence during a GITT procedure. Firstly, the two uncompressed cells in Figure 79a and Figure 79c show remarkably similar diffusion coefficients during the charging procedure, which highlights the repeatable nature of these cells with respect to the diffusion coefficients during charging. Comparing the uncompressed state against the compressed state in Figure 79a with b and c with d, it is evident that applying pressure induces no substantial changes in the magnitude of the diffusion coefficients. This stands true at both very low and high pressure levels and indicates that it is unlikely that the diffusion coefficients, local concentration gradients, and electrode morphology changes within the cell influence the resistance and capacity values[2]. One further observation is the apparent smoothing of the curve after pressure is applied and that, in the absence of pressure, the curve exhibits a somewhat noisier trend.

The lack of change in LIBs associated with diffusion when under compression has also been reported previously: Barai et al. found that there were no morphology changes (no particle cracking) as a result of pressure, thus the solid-state diffusion remained the same[2]. On the other hand, diffusion coefficients have been found to increase upon compression due to enhanced electron and ion transport abilities[168].
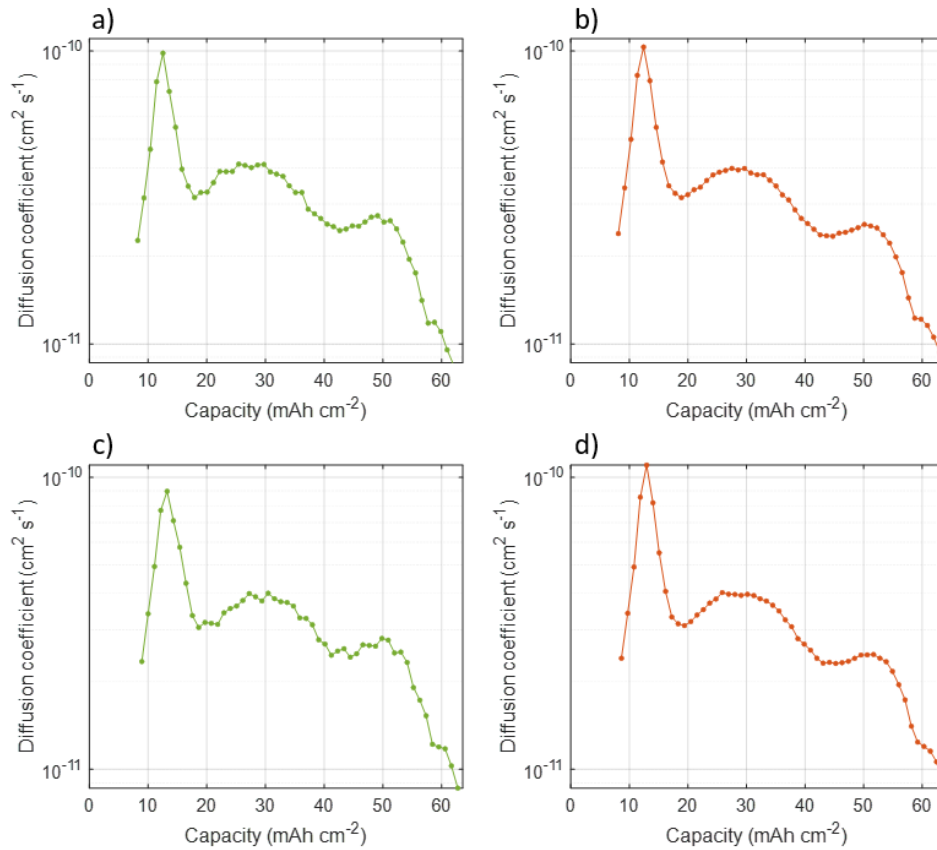
Figure 79. Effective diffusion coefficients calculated from GITT during a charging sequence for the full-cell for (a) uncompressed, (b) very low pressure 0.0013 MPa, (c) uncompressed and (d) high pressure 0.5 MPa.

7.3.2 Cycling Under Compression

The cycling of LIBs under compression has shown to produce varying results in the literature. It is therefore important to benchmark the LiFun pouch cells and to observe their response to varying levels of pressure during cycling. This section presents the results acquired from the extended cycling tests under three pressure levels.

7.3.2.1 Initial Cycling Under Three Pressure Levels

Depicted in Figure 80 are the relative capacity and relative resistance values for cells compressed under three pressure levels over 600 cycles (see section 7.2, page 149). The start point reference (100%) is the resistance measured before any cycles. In Figure 80a, cycling to 600 cycles under the initial pressure values reveals a maximum capacity loss of 10% for an applied pressure of 0.03 MPa, whilst 0.00 MPa (no pressure) and 0.30 MPa both display an 8% capacity loss. This indicates that a low pressure value (0.03 MPa) is

more detrimental to battery capacity than either no (0.00 MPa) or high (0.30 MPa) pressure.

Figure 80b presents the relative resistance values during cycling. Over the three pressure values, only a ~0.4% variation in resistance is observed over the first 600 cycles, which is a substantially low figure. At 0.03 MPa, the relative resistance increases to around 100.5% after 400 cycles, then shows a steady decline in resistance through to 100.2% at 600 cycles. At 0.0 MPa, an initial rise to 100.2% is observed over the first 100 cycles, followed by a steady decrease to 100% after 600 cycles. For the highest pressure level of 0.30 MPa, a steady decrease in resistance to 99.8% is observed over the first 600 cycles. Although the differences are small, a low applied pressure value of 0.03 MPa appears to have the most negative impact on both the relative resistance and relative capacity.
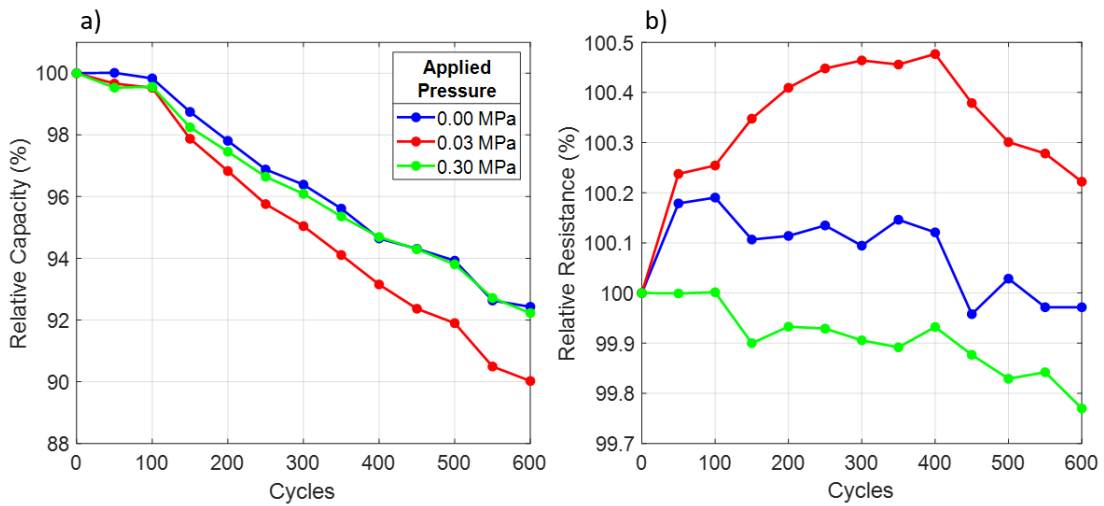
Figure 80. (a) Relative capacity Vs. cycles and (b) relative resistance Vs. cycles for cells under compression at three different pressure levels over initial cycling period.

7.3.2.2 The Instant Effect of a Pressure Change

After 600 cycles, the cells' pressure values were changed to observe the effect of releasing compression, followed by recompression at a new value. Immediately after the pressure change, a check-up was performed to assess the cells' response to these changes (see Figure 9b, page 27). Table 10 indicates the pressure values before and after the change.

Table 10. Pressure values for each cell before and after change.

Cell	Initial Pressure	Pressure After Change
1	0.0 MPa	0.30 MPa
2	0.03 MPa	0.00 MPa
3	0.30 MPa	0.03 MPa

Figure 81 depicts the percentage change in relative capacity and relative resistance after compression at each new pressure value. In Figure 81a, all cells show a decrease in relative capacity, with the greatest reduction seen for cell 1 at -1.6%. Cell 3 shows a moderate reduction in relative capacity, whilst cell 2 shows very little change in relative capacity. This decrease in capacity is directly reflected in Figure 81b with increases in relative resistance. Cell 1 showed the largest increase in resistance, then cell 3 and then cell 2. Interestingly, cell 1 was in an uncompressed state before the change (and throughout initial cycling), and then was compressed at the highest pressure level after the change. This highlights that these cells are most responsive to a change going from an uncompressed state to a compressed state than from just a change in pressure value after compression.

When comparing the relative changes between capacity and resistance, two differences are evident. Firstly, all capacity values decrease, and all resistance values increase accordingly, which could indicate an increase in ageing after the change in pressure. Secondly, the magnitudes of changes are larger for capacity than resistance. However, the changes in resistance relative to the changes during initial cycling (Figure 80) are much larger than for capacity. For example, cell 1 showed an 8% change in capacity during initial cycling and a 1.6% change after the pressure change, whereas the same cell showed a 0.02% change in resistance during initial cycling and a 0.4% change after the pressure change. This highlights that these cells may be more responsive to changes in pressure with respect to resistance than to capacity, but both are clearly affected.
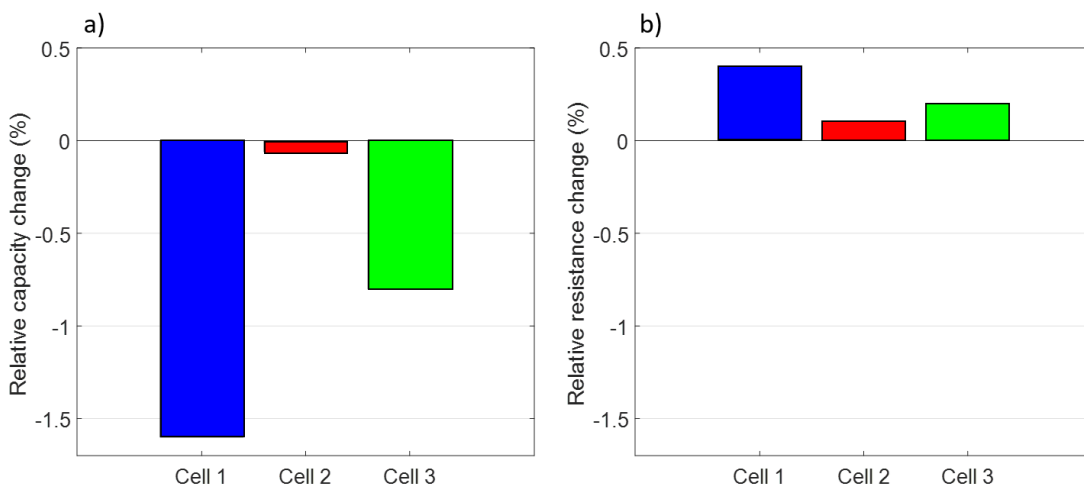
Figure 81. (a) Relative capacity and (b) relative resistance change after compression at new pressure level according to Table 10. Values were calculated from the check-up after compression.

7.3.2.3 Extended Cycling at New Pressure Levels

After the pressure change, the cycling of all cells was resumed at new pressure values. Figure 82a and Figure 82b display the relative capacity and resistance during the extended cycling period, respectively. Each graph is a continuation of those presented in Figure 80 with the values at 600 cycles representing the values after the pressure change and not the values after the initial cycling period. The pressure values during this cycling period are those displayed in the 'After Change' legend.

The relative capacity in Figure 82a presents a similar rate of capacity fade for all cells through to 1300 cycles. A somewhat turbulent period is observed after the pressure change between cycle 600 and 800, however, the cells appear to stabilise after cycle 800 and converge to within 1% of one another. The cell that previously suffered greater capacity fade during initial cycling (initial pressure of 0.03 MPa) does not appear to continue to decline at a faster rate as changing its pressure from 0.03 MPa to 0.00 MPa reduces its ageing rate during extended cycling.

The relative resistance values displayed in Figure 82b reveal a similar ageing rate for all cells: an initial turbulent period followed by a progressive decrease in resistance through to 1300 cycles. An initial drop is observed for cells cycling with pressures of 0.30 MPa and 0.03 MPa (after change) between cycle 600 to 800. This fall appears to diminish the

increases in resistance observed immediately after the pressure change observed in Figure 80b and highlights a potentially reversible nature of the previous resistance increase.

The progressive decrease in resistance with extended cycling is counter to the expected result that resistance would increase in a manner that reflects the capacity fade. Moreover, the maximum decrease in resistance over 1300 cycles is just 0.6%, which can be considered negligible over the lifetime of a cell.

From this, no clear effect of pressure on capacity or resistance can be established during extended cycling. Although a pressure of 0.03 MPa marginally increased capacity fade during initial cycling, it did not negatively influence the extended cycling for the cell subjected to this level after the change. After 1300 cycles, the three cells displayed a difference of <1% for capacity and <0.5% for resistance, indicating a relatively benign effect of pressure on ageing. Cells displayed a stronger and more immediate effect of pressure on capacity and resistance when pressure values were changed than after cycling. This was particularly apparent when changing from no pressure (0.00 MPa) to high pressure (0.30 MPa). With resistance, a certain reversibility of resistance increase was observed, where resistance gains were reduced over the first 200 cycles after the pressure change.
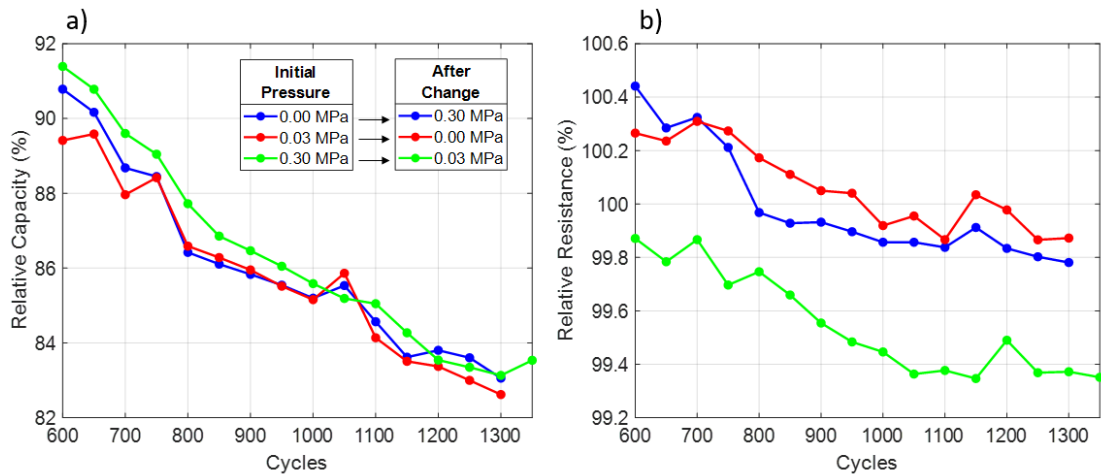
Figure 82. (a) Relative capacity Vs. cycles and (b) relative resistance Vs. cycles during extended cycling period at new pressure levels (after change). Graphs are a continuation of those in Figure 80.

7.3.2.4 The Variation in Coulombic Efficiencies as a Function of Applied Pressure

The coulombic efficiencies (CEs) during the entire testing period were calculated for each cell according to equation (10) (see section 3.6, page 37) and are plotted in Figure 83. Qualitatively, the plots presented in Figure 83a show that a high pressure of 0.30 MPa produces the highest CEs that are closest to 1, and that a low pressure of 0.03 MPa produces the lowest CEs, however this is similar to the values for no pressure (0.00 MPa). This trend approximately continues over both the initial cycling period and the period after the pressure change. This suggests that higher pressures reduce lithium consumption during cycling[44].

Interestingly, the variation of points appears to differ depending on the applied pressure, which is more clearly demonstrated in Figure 83b, c and d. It is apparent that reducing the pressure towards 0.00 MPa increases the variation of CE points. For example, in Figure 83b a moderately large variation of points is observed when cycling in the period before the pressure change (0.00 MPa), which seems to narrow immediately after increasing the pressure to 0.30 MPa. Moreover, going from 0.03 MPa to 0.00 MPa at 600 cycles in Figure 83c results in a substantial increase in the variation of data points. Although the pressure for the cell in Figure 83d switches from a higher (0.30 MPa) to a lower (0.03 MPa), it remains under pressure throughout testing and qualitatively shows the smallest variation.
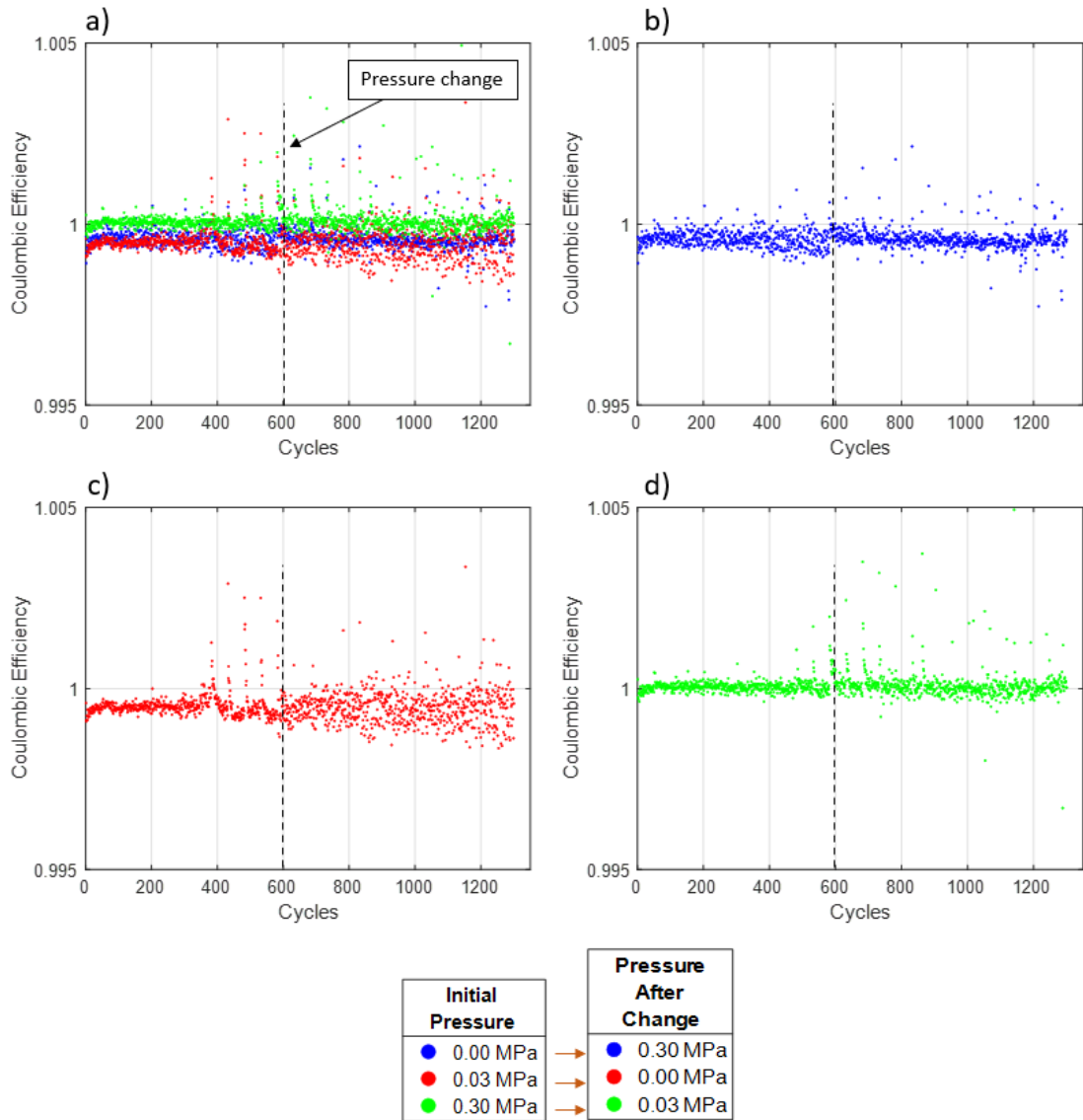
Figure 83. Coulombic efficiencies over entire testing period, where dashed line represents the point at which the pressures were changed from 'initial pressure' to 'pressure after change'. (a) All three cells, (b) cell cycling initially with 0.00 MPa then 0.30 MPa after change, (c) cell cycling initially with 0.03 MPa then 0.00 MPa after change, (d) cell cycling with 0.30 MPa then 0.03 MPa after change.

Figure 84 displays the histograms for the CEs displayed in Figure 83, but to only 1200 cycles, where the 'initial pressure' and 'pressure after change' represent the data before and after the dashed lines in Figure 83, respectively. The total number of cycles was shortened to 1200 to ensure an even number of cycles before and after the change, which gives 600 cycles for each histogram plot. In Figure 84, increasing the pressure from 0.00 MPa to 0.30 MPa results in a slight narrowing of the distribution of CE values. For Figure 84b, decreasing the pressure from an initial value of 0.03 MPa to a value of 0.00 MPa

prompts a substantial increase in the variation of CE data points during cycling. Decreasing the pressure from 0.30 MPa to 0.03 MPa in Figure 84c results in a marginally increased variation of CE values. These data show that increasing the applied pressure reduces the variation in CE during cycling and that reducing the applied pressure increases the variation.

The modal CE values largely remain similar before and after the pressure change, which suggests that the change in the variation of values does not occur concurrently with a consistent change to the charge and discharge capacities. If lowering the pressure was to more strongly influence a decrease of the discharge capacity for example, then one might expect the modal CE values to increase. Instead, it appears that changing the pressure has no preference over increasing or decreasing the modal CE values.
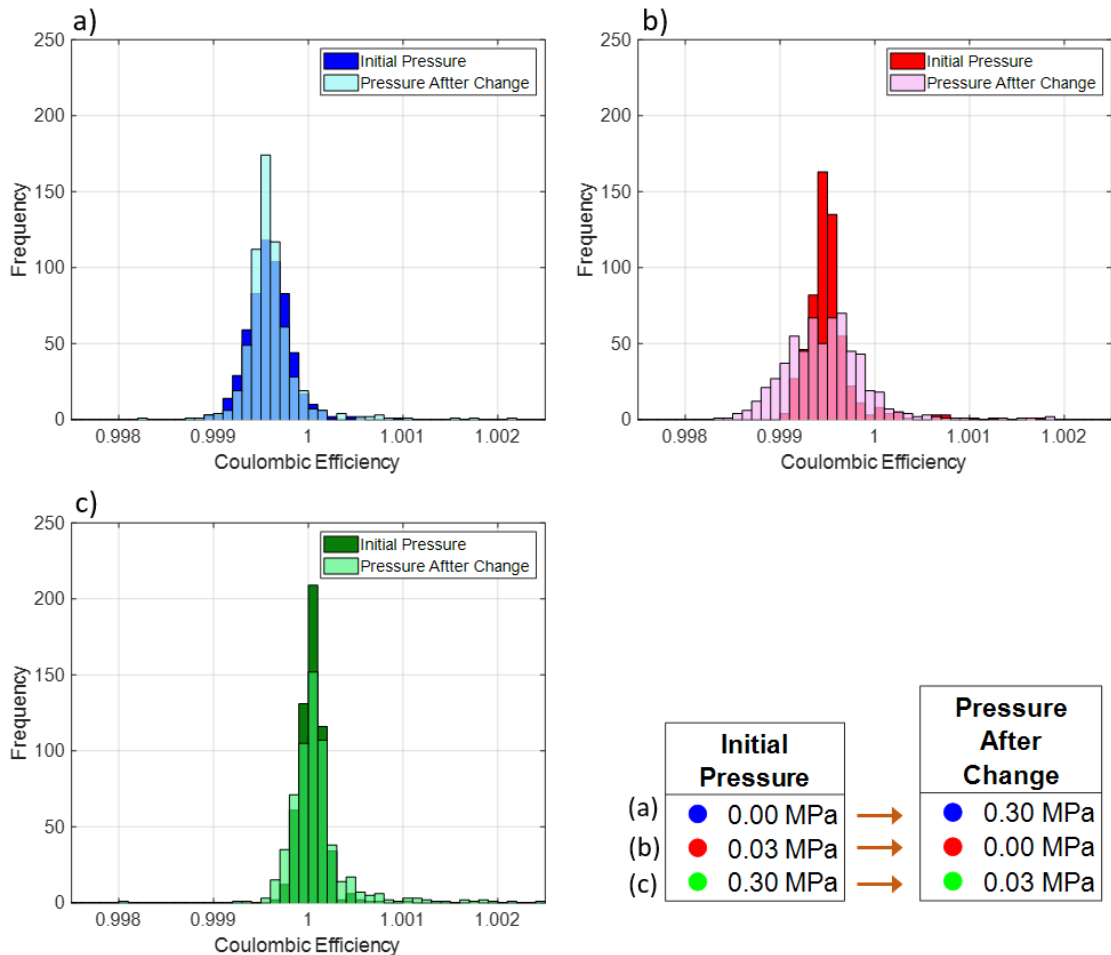
Figure 84. Histograms for the coulombic efficiencies during cycling to 1200 cycles under three pressure levels. Each plot on each axes represents the frequency of coulombic efficiency values over 600 cycles. (a) Cell cycling initially with 0.00 MPa then 0.30 MPa after change, (b) cell cycling initially with 0.03 MPa then 0.00 MPa after change, (c) cell cycling initially with 0.30 MPa then 0.03 MPa after change.

7.4 Conclusions

Pressure Produces an Instant Response on Battery Performance

During static compression testing, capacity and resistance were found to change during check-ups: low and high pressure produced a negative response on capacity and resistance, whilst a median pressure level improved performance. During DC pulse resistance measurements, resistance was found to increase significantly upon compression of the cells in the timescale of less than 2 minutes. Further DC pulse testing revealed an almost instantaneous response of resistance, which increased by as much as 15% in less than 25 seconds. Moreover, almost the entire increase in resistance occurred within this 25 second time frame. Instantaneous effects were also observed in the cycling study when the pressure values were changed after 600 cycles for each cell: discharge capacity was reduced and resistance increased.

The Reversible Nature of Resistance Increase

Further examination of resistance with pressure revealed a reversible response for cell resistance. During sequential DC discharge pulse measurements, the application of pressure produced an instant increase in resistance that subsequently reduced upon decompression by up to 30% within 25 seconds. Increasing the resolution of the resistance relaxation exposed a sharp, non-linear decline followed by a steady linear decrease. After the total relaxation time of approximately 12 minutes, the resistance values were comparable to the absolute values before applying pressure for very low pressure, but lower than initial values for high pressure. Based on the fact that the pressure-induced changes relax that slowly, one may speculate that pressure-induced changes of physical structures (particles positions, separator pores), rather than pressure itself, are behind the measurable responses.

Very Low Pressure (0.0013 MPa) Produced the Strongest Response on Resistance

Of all pressure levels, very low pressure (0.0013 MPa) appeared to produce the strongest, instant increase in resistance over any other pressure value tested. Very low pressure was found to increase resistance by 15%, compared with a 7% increase at high pressure (0.56 MPa). In discharge capacity C-rate testing, very low pressure increased discharge capacity at all rates, whereas high pressure decreased discharge capacity at almost all rates. This finding highlighted the cell's heightened response to even slight changes in stack pressures.

Effects of Pressure on Capacity, Resistance and Coulombic Efficiency During Cycling

A limited effect of pressure on capacity and resistance was observed over 1300 cycles. Over the first 600 cycles, cycling at a pressure of 0.03 MPa resulted in increased capacity fade of 2% when compared to 0.30 MPa and 0.00 MPa. From cycle 600 to 1300 (after the pressure change), a pressure of 0.03 MPa did not induce a faster rate of capacity decline over the other pressure values, however. At the end of the cycling period after 1300 cycles, the difference in capacity and resistance between the test conditions was <1% and <0.5%, respectively.

A strong influence of applied pressure on the variation of coulombic efficiency was observed during cycling. Cycling with higher pressure levels resulted in a narrower variation of coulombic efficiency values, whereas cycling with lower pressure levels resulted in a greater variation. Cycling in the absence of pressure induced the largest variation during cycling. The modal coulombic efficiency values were largely unaffected by changes to higher/lower pressures.

Acknowledgement of the Small Sample Size

It is acknowledged that the results presented in this chapter are the product of the testing of a small sample size. The variation in capacity and resistance over all 25 cells was found to be 2% and 5%, respectively. For the results to be truly statistically significant, repeats of measurements is required. To maintain clarity with the results, absolute resistances

have also been presented in many figures to provide the reader with an idea of the variation within each test.

The Vast Complexities of the Effects of Pressure on Cell Performance

As demonstrated by the conflicting statements in the literature, the effects of pressure on lithium-ion batteries' performance is vastly complex and with many contributing factors. Trends have emerged within this study that present an insight into such effects, however the compression experiments turned out to produce more complex and less straightforward results than initially anticipated. It is therefore recommended that further work is required to disentangle the electrochemical and mechanical influences on cell performance, and that static compression could provide a simpler approach to help achieve this.

8 Summary, Conclusion and Outlook

To successfully reduce global emissions and to achieve a true electrification of vehicle fleets, a deployment of lithium-ion batteries (LIBs) with higher energy densities and longer cycle lifetimes is required. Breakthroughs in the materials sector must be accompanied by the precise analysis of degradation mechanisms that occur during battery operation and storage. In practice, non-destructive analysis methods provide a crucial insight into battery state-of-health (SoH), as the option for destructively opening a cell does not exist in application. Moreover, because the usage patterns of LIBs are often highly varied, it is important to observe the degradation of cells under different operating conditions.

The critical aims of this thesis were to examine the effect of different operating conditions on battery degradation by experimental ageing studies. Cells were aged by means of cycle and calendar procedures, as well as under compression at defined pressure levels. By obtaining a greater understanding of the mechanisms that occur for each, battery performance can be improved and the utilisation can be maximised.

8.1 Conclusions

8.1.1 Cycle and Calendar Ageing

High-energy cylindrical cells were subjected to cycle and calendar ageing conditions over varying operational timeframes. The effects of calendar and cycle ageing were first evaluated individually, followed by examining the combination of both. The key aims of the first experimental study were to analyse the degradation mechanisms arising during calendar and cycle ageing, and to identify if any ageing path dependencies prevail. The

Robert Burrell - January 2022

aims of the second experimental study were to examine and separate the reversible and irreversible capacity losses during cycling by means of short-term calendar storage periods.

Extended calendar ageing periods promoted a progressive decline in capacity for all cells over 19 months, with an approximate square root of time dependence on capacity fade. Analysing the capacity fade as a function of storage state-of-charge (SoC) revealed a spoon-shaped trend, where storage at 70% SoC promoted the greatest capacity fade and increasing the storage SoC to 100% progressively reduced the capacity fade. The dominant driving mechanism for the spoon-shaped trend was proposed as an increased rate of side reactions due to higher cathode and lower anode electrochemical potentials towards higher storage SoCs. These side reactions then promoted an increased frequency of shuttle mechanisms that transported electrons from anode to cathode and induced a reversible self-discharge. The increased rate of shuttle mechanisms consumed a greater proportion of the Li^+ current that is also shared with irreversible SEI, reducing the amount of Li^+ current available for SEI formation. In turn, this reduced the rate of SEI formation and reduced the irreversible capacity loss when storing the cells at higher SoCs towards 100% and led to the observed spoon-shaped dependency across the SoC range.

A potential ageing path dependence was observed in the cycling periods after extended calendar storage. Differences in the differential voltage analysis (DVA) profiles between each storage condition during initial calendar ageing persisted throughout extended cycle ageing for both aggressive (high C-rate) and soft (low C-rate) cycling. In other words, the DVA ageing profiles that were established for each individual condition during calendar ageing did not converge to a similar/common shape when the cells were subjected to identical cycling conditions. Moreover, the cells that exhibited greater capacity fade during calendar ageing (70% SoC) were first to reach end-of-life (EoL) during cycling.

A separation of reversible and irreversible capacity losses was achieved through the use of short-term calendar storage periods after cycling periods. Storage at 0% SoC recovered lithium from the anode overhang regions by forcing a disparity in the lithiation degree between the (delithiated) active anode and the (lithiated) anode overhang regions. This difference in lithium concentration was the key driving factor for lithium diffusion from the overhang region to the active region, which increased the observed discharge capacity. The capacity lost to the anode overhang regions could thus be quantified. Importantly, this effect inverted the ageing outcome previously established during cycling: cells

charged to a lower cut-off voltage of 4.1 V showed greater capacity fade than those charged to 4.2 V, however these 4.1 V cells then recovered more capacity during storage at 0% SoC. This indicated that larger quantities of lithium were lost to the overhang regions when charging to 4.1 V during cycling. It was found that lower diffusion coefficients and shallower anode potential gradients promoted sluggish lithium mobility at 4.1 V, which extended the constant voltage (CV) phase and resulted in orders of magnitude increased time spent at high voltage. It was proposed that this higher time-averaged SoC for cells cycled to 4.1 V drew a larger net diffusion of lithium from the active anode to the anode overhang, which was represented as capacity fade in the cycling data.

8.1.2 The Effects of Pressure on Cell Performance

To ensure that the pressure applied to the cell was homogeneous in distribution, a pressure test rig was developed using the successful elements of test rig designs found in the literature. Once rig development was completed, electrochemical testing of LIB pouch cells commenced. The key aim of the electrochemical testing was to examine the direct effects of pressure on the performance of LIBs, with a clear separation of static testing (in the absence of cycles) and cycle ageing.

No standardised test rig design or approach for the application of pressure to LIBs was identified in the literature. Multiple methods existed, which raised concerns about the homogeneity of the pressure distribution on the cell surface. Finite element analysis (FEA) simulations on three key design approaches from the literature were examined, which were supported by experimental validation with pressure-sensitive films. Flat plate designs with bolts applying the force at each corner produced vastly non-uniform pressure distributions, which was likely caused by an out-of-plane bending of the cell due to clamping forces located outside the circumference of the cell. The addition of semi-rigid plates in contact with the cell improved the distribution, but a significantly non-uniform distribution persisted. Using a central piston to directly apply the force to the cell resulted in a uniform pressure distribution in FEA simulations, but a non-uniform distribution in the pressure film validation. It was suggested that the sequential tightening of the bolts that apply force through a top plate and then the piston concentrate the force through the edge of the piston at each bolt location. In the FEA simulations, the force was applied to

the piston in a single tightening motion, and thus the distribution was homogeneous. These findings provided the foundations for a proposed custom rig design that utilised the successful elements from previous designs. The proposed design consisted of a central piston screw that applied the force in a single tightening motion. The force was then directed onto a piston (flat plate) block and then onto the cell. This design achieved a uniform pressure distribution in both FEA simulations and experimental validations, whilst maintaining a small form factor necessary for use in thermal chambers.

The compression testing of small form-factor LIB pouch cells was divided into two, clear sections: static measurements (absence of cycles) and cycle ageing. Static testing revealed that pressure produces an instant response on battery performance, with low (0.03 MPa) and high (0.30 MPa) pressure inducing a negative effect on capacity and resistance, whilst a median pressure (0.15 MPa) induced a positive effect on capacity and resistance during check-up measurements. In more instantaneous testing, direct current (DC) pulse resistance measurements demonstrated a 15% increase in cell resistance in response to pressure, which occurred in less than 25 seconds. This increase was also found to be highly reversible upon decompression of the cells, as the gains in resistance produced in response to pressure were shown to reduce by up to 30% upon decompression. After a total relaxation (decompression) time of 12 minutes, the resistance values were comparable to those measured at the start of testing, indicating that the resistance changes were entirely reversible. Perhaps most interestingly, a very low pressure value of 0.0013 MPa produced the strongest response on cell resistance. Very low pressure was found to increase cell resistance by 15% when compared with 7% for high pressure (0.56 MPa). It was hypothesised that only higher pressures compressed the electrode active material, which improved electrode particle contact and thus reduced the charge transfer (CT) resistance and offset the increased ionic pore resistance.

A limited effect of pressure on the capacity and resistance was observed during extended cycling (1300 cycles), with <1% variation between each pressure condition. Interestingly, cycling under higher pressure levels produced a narrower variation in coulombic efficiency values, whereas lower pressure levels resulted in a greater variation. Cycling in the absence of pressure induced the largest variation during cycling. The modal coulombic efficiency values were mostly unaffected by changes to higher/lower pressures.

At the bottom line, my work demonstrated that even once a homogeneous application of pressure becomes experimentally possible, the observable effects are rather subtle, creating high demands on quality, stability and reproducibility of the tested pouch cells.

8.2 Outlook

The extension of the work presented in this thesis is possible through multiple avenues. The following section identifies interesting topics for further research.

Identifying a Strong Ageing Path Dependence

A potential ageing path dependence was identified for cells during the experimental ageing studies presented in this thesis, which was observed during cycling after extended calendar ageing periods. However, it remains a question whether a specific ageing route during cycling at the initial stages of cell life can influence the ageing trends in subsequent cycling. If such an ageing path dependence could be identified in further study, it would also be interesting to identify in which stage of life this influence is most prominent. For example, is the non-linear capacity decline region at the BoL, when the solid electrolyte interphase (SEI) is still maturing, a more sensitive period to different ageing routes?

Periodic and Regular Rest Periods

Calendar rest periods, particularly at 0% SOC, were identified as a useful tool for identifying and managing irreversible and reversible capacity losses. These were performed at a single moment in time after a considerable number of cycles, however intermittent storage periods at more regular intervals throughout cycling have not been studied in detail. With more regular quantification of the irreversible and reversible losses, can cycle life be extended and more accurate lifetime estimations be achieved? LIBs often spend significant periods of time in storage in between use (e.g., parked EVs), thus it is important to study what influence intermittent storage periods may have on cell ageing, and whether they can be effectively used as a tool to further understand cell behaviour.

Separating Resistance Contributions at Each Pressure Level

The results from this work showed that the change in DC internal resistance of LIB pouch cells varied depending on the magnitude of applied pressure. Because the DC resistance pulses presented in this thesis are comprised of contributions from many resistance origins, the separation of each contribution could not be determined. For a deeper understanding of the direct effect of different pressure levels on resistance, these contributions must be separated. Further research using electrochemical impedance spectroscopy (EIS) can help in identifying the root causes of resistance increase, in particular, the differences that occur between very low pressure (0.0013 MPa) and high pressure (0.56 MPa). Further, distribution of relaxation times (DRT) may provide a useful technique for the separation of resistance contributions and the magnitudes of the associated changes.

Perform many static measurements on many cell configurations to identify similarities and differences?

Because cell design varies substantially, from active material porosities and binder properties to electrode layers and size, it is important to observe the similarities and differences that may exist between different cells as a result of static measurements.

A Closer Examination of the Effects of Pressure on Cycling Performance

This work found that different pressure levels had only a minor impact on the cycling performance of LIB pouch cells, therefore, to identify if pressure can produce more clear trends in degradation, further research is required. To elucidate such changes, cells could be cycled in identical uncompressed states to establish a base ageing rate for each cell. Then, the application of different pressure levels and a resumption of cycling may induce more noticeable changes in the observed ageing rate. The effect of pressure on the measured coulombic efficiency (CE) is also an area to be examined further.

9 References

1. J. Asenbauer, T. Eisenmann, M. Kuenzel, A. Kazzazi, Z. Chen, and D. Bresser, *Sustain. Energy Fuels* (2020).

2. A. Barai, R. Tangirala, K. Uddin, J. Chevalier, Y. Guo, A. McGordon, and P. Jennings, *J. Energy Storage*, **13**, 211–219 (2017).

3. J. B. Goodenough and K. S. Park, *J. Am. Chem. Soc.*, **135**, 1167–1176 (2013).

4. H. S. Das, M. M. Rahman, S. Li, and C. W. Tan, *Renew. Sustain. Energy Rev.*, **120** (2020).

5. D. W. Murphy and J. N. Carides, *J. Electrochem. Soc.*, **126**, 349–351 (1979).

6. B. Scrosati, *J. Solid State Electrochem.*, **15**, 1623–1630 (2011).

7. K. Mizushima, P. C. Jones, P. J. Wiseman, and J. B. Goodenough, *Solid State Ionics* (1981).

8. European Commission, *Com(2018) 773*, 114 (2018).

9. D. J. Teece, *Manag. Organ. Rev.*, **14**, 501–512 (2018).

10. H. Jung, R. Silva, and M. Han, *World Electr. Veh. J.*, **9**, 1–14 (2018).

11. L. Nicoletti, A. Romano, A. König, P. Köhler, M. Heinrich, and M. Lienkamp, *Energies*, **14**, 1–29 (2021).

12. M. Wetjen, D. Pritzl, R. Jung, S. Solchenbach, R. Ghadimi, and H. A. Gasteiger, *J. Electrochem. Soc.*, **164**, A2840–A2852 (2017).

13. A. Zülke, Y. Li, P. Keil, R. Burrell, and S. Belaisch, *Batter. Supercaps*, **4**, 934–947 (2021).

14. V. A. Sethuraman, L. J. Hardwick, V. Srinivasan, and R. Kostecki, *J. Power Sources*, **195**, 3655–3660 (2010).

15. I. Zilberman, J. Sturm, and A. Jossen, *J. Power Sources*, **425**, 217–226 (2019).

16. M. Ecker, N. Nieto, S. Käbitz, J. Schmalstieg, H. Blanke, A. Warnecke, and D. U. Sauer, *J. Power Sources*, **248**, 839–851 (2014).

17. M. Dubarry, G. Baure, and A. Devie, *J. Electrochem. Soc.*, **165**, A773–A783 (2018).

18. M. Lewerenz, P. Dechent, and D. U. Sauer, *J. Energy Storage*, **21**, 680–690 (2019).

19. R. Burrell, A. Zulke, P. Keil, and H. Hoster, *J. Electrochem. Soc.*, **167**, 130544 (2020).

20. V. Müller, R. Scurtu, M. Memm, M. A. Danzer, and M. Wohlfahrt-mehrens, *J. Power Sources*, **440**, 227148 (2019).

21. A. S. Mussa, M. Klett, G. Lindbergh, and R. W. Lindström, *J. Power Sources*, **385**, 18–26 (2018).

22. J. R. Dahn, T. Zheng, Y. Liu, and J. S. Xue, *Science (80-.).*, **270**, 590–593 (1995).

23. W. M. Dose, M. J. Piernas-Muñoz, V. A. Maroni, S. E. Trask, I. Bloom, and C. S. Johnson, *Chem. Commun.*, **54**, 3586–3589 (2018).

24. S. T. Myung, F. Maglia, K. J. Park, C. S. Yoon, P. Lamp, S. J. Kim, and Y. K. Sun, *ACS Energy Lett.*, **2**, 196–223 (2017).

25. D. Andre, S. J. Kim, P. Lamp, S. F. Lux, F. Maglia, O. Paschos, and B. Stiaszny, *J. Mater. Chem. A*, **3**, 6709–6732 (2015).

26. A. Sheidaei, X. Xiao, X. Huang, and J. Hitt, *J. Power Sources*, **196**, 8728–8734 (2011).

27. T. R. Jow, K. Xu, O. Borodin, and M. Ue, *Electrolytes for Lithium and Lithium-Ion Batteries*, p. 1277–1283, (2014).

28. C. M. Lewandowski, N. Co-investigator, and C. M. Lewandowski, *Lindens Handbook of Batteries 4th Edition*, p. 1689–1699, (2015).

29. T. Waldmann, B. I. Hogg, and M. Wohlfahrt-Mehrens, *J. Power Sources*, **384**, 107–124 (2018).

30. Z. Liu, Q. Yu, Y. Zhao, R. He, M. Xu, S. Feng, S. Li, L. Zhou, and L. Mai, *Chem. Soc. Rev.*, **48**, 285–309 (2019).

31. M. B. Pinson and M. Z. Bazant, *J. Electrochem. Soc.*, **160**, A243–A250 (2012).

32. P. Keil, thesis, Technische Universität München (2017).

33. H. J. Ploehn, P. Ramadass, and R. E. White, *J. Electrochem. Soc.*, **151**, A456 (2004).

34. P. Verma, P. Maire, and P. Novák, *Electrochim. Acta*, **55**, 6332–6341 (2010).

35. A. J. Smith, J. C. Burns, X. Zhao, D. Xiong, and J. R. Dahn, *J. Electrochem. Soc.*, **158**, A447 (2011).

36. V. A. Agubra and J. W. Fergus, *J. Power Sources*, **268**, 153–162 (2014).

37. S. J. An, J. Li, C. Daniel, D. Mohanty, S. Nagpure, and D. L. Wood, *Carbon N. Y.*, **105**, 52–76 (2016).

38. J. Kasnatscheew, M. Börner, B. Streipert, P. Meister, R. Wagner, I. Cekic Laskovic, and M. Winter, *J. Power Sources*, **362**, 278–282 (2017).

39. C. E. Hendricks, A. N. Mansour, D. A. Fuentevilla, H. Waller, J. K. Ko, and M. G. Pecht, *J. Electrochem. Soc.*, **167** (2020).

40. L. De Sutter, G. Berckmans, M. Marinaro, M. Wohlfahrt-Mehrens, M. Berecibar, and J. Van Mierlo, *J. Power Sources*, **451**, 227774 (2020).

41. N. Lin, Z. Jia, Z. Wang, H. Zhao, G. Ai, X. Song, and Y. Bai, *J. Power Sources*, **365**, 235–239 (2017).

42. J. Vetter, P. Novák, M. R. Wagner, C. Veit, K. C. Möller, J. O. Besenhard, M. Winter, M. Wohlfahrt-Mehrens, C. Vogler, and A. Hammouche, *J. Power Sources*, **147**, 269–281 (2005).

43. P. Arora, *J. Electrochem. Soc.*, **145**, 3647 (1998).

44. A. J. Smith, J. C. Burns, D. Xiong, and J. R. Dahn, *J. Electrochem. Soc.*, **158**, A1136 (2011).

45. X. G. Yang, Y. Leng, G. Zhang, S. Ge, and C. Y. Wang, *J. Power Sources*, **360**, 28–40 (2017).

46. J. C. Burns, D. A. Stevens, and J. R. Dahn, *J. Electrochem. Soc.*, **160** (2015).

47. Q. Liu, C. Du, B. Shen, P. Zuo, X. Cheng, Y. Ma, G. Yin, and Y. Gao, *RSC Adv.*, **6** (2016).

48. M. Petzl, M. Kasper, and M. A. Danzer, *J. Power Sources*, **275**, 799–807 (2015).

49. I. D. Campbell, M. Marzook, M. Marinescu, and G. J. Offer, *J. Electrochem. Soc.*, **166**, A725–A739 (2019).

50. J. Wandt, P. Jakes, J. Granwehr, R. A. Eichel, and H. A. Gasteiger, *Mater. Today*, **21**, 231–240 (2018).

51. B. Epding, B. Rumberg, H. Jahnke, I. Stradtmann, and A. Kwade, *J. Energy Storage*, **22**, 249–256 (2019).

52. M. Klett, J. A. Gilbert, K. Z. Pupek, S. E. Trask, and D. P. Abraham, *J. Electrochem. Soc.*, **164**, A6095–A6102 (2017).

53. G. Berckmans, L. De Sutter, M. Marinaro, J. Smekens, J. Jaguemont, M. Wohlfahrt-Mehrens, J. van Mierlo, and N. Omar, *Electrochim. Acta*, **306**, 387–395 (2019).

54. Y. Li, B. Lu, B. Guo, Y. Song, and J. Zhang, *Electrochim. Acta*, **295**, 778–786 (2019).

55. B. Fuchsbichler, C. Stangl, H. Kren, F. Uhlig, and S. Koller, *J. Power Sources*, **196**, 2889–2892 (2011).

56. A. V. Plakhotnyk, L. Ernst, and R. Schmutzler, *J. Fluor. Chem.*, **126**, 27–31 (2005).

57. J. Bareño, I. A. Shkrob, J. A. Gilbert, M. Klett, and D. P. Abraham, *J. Phys. Chem. C*, **121**, 20640–20649 (2017).

58. J. A. Gilbert, I. A. Shkrob, and D. P. Abraham, *J. Electrochem. Soc.*, **164**, A389–A399 (2017).

59. C. Delacourt, A. Kwong, X. Liu, R. Qiao, W. L. Yang, P. Lu, S. J. Harris, and V.

Srinivasan, *J. Electrochem. Soc.*, **160**, A1099–A1107 (2013).

60. B. Wang, F. Zhang, X. Zhou, P. Wang, J. Wang, H. Ding, H. Dong, W. Liang, N. Zhang, and S. Li, *J. Mater. Chem. A*, **7**, 13540–13551 (2021).

61. W. Liu, P. Oh, X. Liu, M. J. Lee, W. Cho, S. Chae, Y. Kim, and J. Cho, *Angew. Chemie - Int. Ed.*, **54**, 4440–4457 (2015).

62. D. Mohanty, J. Li, S. C. Nagpure, D. L. Wood, and C. Daniel, *MRS Energy Sustain.*, **2**, 1–24 (2015).

63. S. K. Jung, H. Gwon, J. Hong, K. Y. Park, D. H. Seo, H. Kim, J. Hyun, W. Yang, and K. Kang, *Adv. Energy Mater.*, **4**, 1–7 (2014).

64. S. Albrecht, J. Kümpers, M. Kruft, S. Malcus, C. Vogler, M. Wahl, and M. Wohlfahrt-Mehrens, *J. Power Sources*, **119–121**, 178–183 (2003).

65. S. Watanabe, M. Kinoshita, T. Hosokawa, K. Morigaki, and K. Nakura, *J. Power Sources*, **258**, 210–217 (2014).

66. S. Watanabe, M. Kinoshita, and K. Nakura, *J. Power Sources*, **196**, 6906–6910 (2011).

67. S. Brown, N. Mellgren, M. Vynnycky, and G. Lindbergh, *J. Electrochem. Soc.*, **155**, A320 (2008).

68. J. Wandt, A. T. S. Freiberg, A. Ogrodnik, and H. A. Gasteiger, *Mater. Today*, **21**, 825–833 (2018).

69. D. J. Xiong, R. Petibon, M. Nie, L. Ma, J. Xia, and J. R. Dahn, *J. Electrochem. Soc.*, **163**, A546–A551 (2016).

70. S. S. Zhang, *J. Power Sources*, **162**, 1379–1394 (2006).

71. J. Henschel, F. Horsthemke, Y. P. Stenzel, M. Evertz, S. Girod, C. Lürenbaum, K. Kösters, S. Wiemers-Meyer, M. Winter, and S. Nowak, *J. Power Sources*, **447** (2020).

72. C. Schultz, S. Vedder, B. Streipert, M. Winter, and S. Nowak, *RSC Adv.*, **7**, 27853–27862 (2017).

73. M. Winter, *Zeitschrift fur Phys. Chemie*, **223**, 1395–1406 (2009).

74. M. Broussely, P. Biensan, F. Bonhomme, P. Blanchard, S. Herreyre, K. Nechev, and R. J. Staniewicz, *J. Power Sources*, **146**, 90–96 (2005).

75. T. Waldmann, A. Iturrondobeitia, M. Kasper, N. Ghanbari, E. Bekaert, L. Daniel, S. Genies, I. Jim, E. De Vito, and M. Wohlfahrt-mehrens, *J. Electrochem. Soc.*, **163**, 50–52 (2016).

76. J. Cannarella and C. B. Arnold, *J. Power Sources*, **226**, 149–155 (2013).

77. C. T. Love, *J. Power Sources*, **196**, 2905–2912 (2011).

78. R. Kostecki, L. Norin, X. Song, and F. McLarnon, *J. Electrochem. Soc.*, **151**, A522

(2004).

79. M. M. K. and D. E. Demirocak, *Arch. Thermodyn.*, **33**, 23–40 (2012).

80. P. Keil and A. Jossen, *J. Energy Storage*, **6**, 125–141 (2016).

81. P. Keil and A. Jossen, *J. Electrochem. Soc.*, **164**, A6066–A6074 (2017).

82. A. Maheshwari, M. Heck, and M. Santarelli, *Electrochim. Acta*, **273**, 335–348 (2018).

83. J. Xia, M. Nie, L. Ma, and J. R. Dahn, *J. Power Sources*, **306**, 233–240 (2016).

84. P. Keil and A. Jossen, *J. Energy Storage*, **6**, 125–141 (2016).

85. F. Benavente-Araoz, M. Varini, A. Lundblad, S. Cabrera, and G. Lindbergh, *J. Electrochem. Soc.*, **167**, 040529 (2020).

86. T. C. Bach, S. F. Schuster, E. Fleder, J. Müller, M. J. Brand, H. Lorrmann, A. Jossen, and G. Sextl, *J. Energy Storage*, **5**, 212–223 (2016).

87. J. B. Gerschler, S. Käbitz, Y. Yurdagel, D. U. Sauer, M. Ecker, B. Emmermacher, T. Mitsch, and D. André, *J. Power Sources*, **239**, 572–583 (2013).

88. W. M. Seong, K. Y. Park, M. H. Lee, S. Moon, K. Oh, H. Park, S. Lee, and K. Kang, *Energy Environ. Sci.*, **11**, 970–978 (2018).

89. M. Kassem, J. Bernard, R. Revel, S. Pélissier, F. Duclaud, and C. Delacourt, *J. Power Sources*, **208**, 296–305 (2012).

90. J. Schmalstieg, S. Käbitz, M. Ecker, and D. U. Sauer, *J. Power Sources*, **257**, 325–334 (2014).

91. T. Raj, A. A. Wang, C. W. Monroe, and D. A. Howey, *Batter. Supercaps*, **3**, 1–10 (2020).

92. M. Lewerenz, G. Fuchs, L. Becker, and D. U. Sauer, *J. Energy Storage*, **18**, 149–159 (2018).

93. B. Gyenes, D. A. Stevens, V. L. Chevrier, and J. R. Dahn, *J. Electrochem. Soc.*, **162**, A278–A283 (2014).

94. M. Naumann, M. Schimpe, P. Keil, H. C. Hesse, and A. Jossen, *J. Energy Storage*, **17**, 153–169 (2018).

95. M. Lewerenz, A. Marongiu, A. Warnecke, and D. U. Sauer, *J. Power Sources*, **368**, 57–67 (2017).

96. J. Cannarella and C. B. Arnold, *J. Power Sources*, **245**, 745–751 (2014).

97. L. Zhou, L. Xing, Y. Zheng, X. Lai, J. Su, C. Deng, and T. Sun, *Int. J. Energy Res.*, 1–14 (2020).

98. Z. Mao, M. Farkhondeh, M. Pritzker, M. Fowler, and Z. Chen, *J. Electrochem. Soc.*, **164**, A3469–A3483 (2017).

99. R. S. Rubino, H. Gan, and E. S. Takeuchi, *J. Electrochem. Soc.*, **148**, A1029 (2001).

100. Y. Itou and Y. Ukyo, *J. Power Sources*, **146**, 39–44 (2005).

101. H. He, Y. Liu, Q. Liu, Z. Li, F. Xu, C. Dun, Y. Ren, M. Wang, and J. Xie, *J. Electrochem. Soc.*, **160**, A793–A804 (2013).

102. G. Plett, *Battery Management Systems, Volume I: Battery Modeling*, Artech House, Boston, (2015).

103. A. Jossen, *J. Power Sources*, **154**, 530–538 (2006).

104. G. Pi, A. Marongiu, J. Drillkens, P. Sinhuber, and D. Uwe, *J. Power Sources*, **296** (2015).

105. M. Ecker, N. Nieto, S. Käbitz, J. Schmalstieg, H. Blanke, A. Warnecke, and D. U. Sauer, *J. Power Sources*, **248**, 839–851 (2014).

106. P. Keil, S. F. Schuster, J. Wilhelm, J. Travi, A. Hauser, R. C. Karl, and A. Jossen, *J. Electrochem. Soc.*, **163**, A1872–A1880 (2016).

107. Y. Wu and A. Jossen, *Electrochim. Acta*, **276**, e5–e8 (2018).

108. P. Bai, J. Li, F. R. Brushett, and M. Z. Bazant, *Energy Environ. Sci.*, **9**, 3221–3229 (2016).

109. C.-H. Chen, F. Brosa Planella, K. O'Regan, D. Gastol, W. D. Widanage, and E. Kendrick, *J. Electrochem. Soc.*, **167**, 080534 (2020).

110. J. Xu, R. D. Deshpande, J. Pan, and Y. Cheng, *J. Electrochem. Soc.*, **162**, 2026–2035 (2015).

111. A. J. Smith, J. C. Burns, S. Trussler, and J. R. Dahn, *J. Electrochem. Soc.*, **157**, A196 (2009).

112. J. R. Macdonald, *Ann. Biomed. Eng.*, **20**, 289–305 (1992).

113. L. A. Middlemiss, A. J. R. Rennie, R. Sayers, and A. R. West, *Energy Reports*, **6**, 232–241 (2020).

114. M. Orazem and B. Tribollet, *Electrochemical Impedance Spectroscopy*, 2nd ed., John Wiley & Sons, (2017).

115. M. C. H. Mckubre, D. D. Macdonald, B. Sayers, and J. R. Macdonald, *Measuring Techniques and Data Analysis*, p. 129–204, (2005).

116. J. P. Schmidt, T. Chrobak, M. Ender, J. Illig, D. Klotz, and E. Ivers-Tiffée, *J. Power Sources*, **196**, 5342–5348 (2011).

117. J. Illig, J. P. Schmidt, M. Weiss, A. Weber, and E. Ivers-Tiffée, *J. Power Sources*, **239**, 670–679 (2013).

118. S. Schindler and M. A. Danzer, *J. Energy Storage*, **12**, 157–166 (2017).

119. J. R. Macdonald and E. Tuncer, *J. Electroanal. Chem.*, **602**, 255–262 (2007).

120. T. H. Wan, M. Saccoccio, C. Chen, and F. Ciucci, *Electrochim. Acta*, **184**, 483–499 (2015).

121. I. Bloom, A. N. Jansen, D. P. Abraham, J. Knuth, S. A. Jones, V. S. Battaglia, and G. L. Henriksen, *J. Power Sources*, **139**, 295–303 (2004).

122. M. Dubarry, V. Svoboda, R. Hwu, and B. Y. Liaw, *Electrochem. Solid-State Lett.*, **9** (2006).

123. Y. Gao, J. Jiang, C. Zhang, W. Zhang, Z. Ma, and Y. Jiang, *J. Power Sources* (2017).

124. T. Ohzuku, Y. Iwakoshi, and K. Sawai, *J. Electrochem. Soc.*, **140**, 2490–2498 (1993).

125. C. R. Birkl, M. R. Roberts, E. McTurk, P. G. Bruce, and D. A. Howey, *J. Power Sources*, **341** (2017).

126. W. M. Dose, C. Xu, C. P. Grey, and M. F. L. De Volder, *Cell Reports Phys. Sci.*, **1**, 100253 (2020).

127. M. Dubarry, C. Truchot, and B. Y. Liaw, *J. Power Sources*, **219**, 204–216 (2012).

128. M. Lewerenz and D. U. Sauer, *J. Energy Storage*, **18**, 421–434 (2018).

129. J. P. Fath, D. Dragicevic, L. Bittel, A. Nuhic, J. Sieg, S. Hahn, L. Alsheimer, B. Spier, and T. Wetzel, *J. Energy Storage*, **25**, 100813 (2019).

130. G. Pasaoglu, D. Fiorello, A. Martino, G. Scarcella, A. Alemanno, A. Zubaryeva, and C. Thiel, *Driving and parking patterns of European car drivers - a mobility survey*, p. 112, (2012).

131. P. Keil, S. F. Schuster, J. Wilhelm, J. Travi, A. Hauser, R. C. Karl, and A. Jossen, *J. Electrochem. Soc.*, **163**, A1872–A1880 (2016).

132. N. N. Sinha, A. J. Smith, J. C. Burns, G. Jain, K. W. Eberman, E. Scott, J. P. Gardner, and J. R. Dahn, *J. Electrochem. Soc.*, **158**, A1194 (2011).

133. D. Li, D. L. Danilov, J. Xie, L. Raijmakers, L. Gao, Y. Yang, and P. H. L. Notten, *Electrochim. Acta*, **190**, 1124–1133 (2016).

134. B. Stiaszny, J. C. Ziegler, E. E. Krauß, M. Zhang, J. P. Schmidt, and E. Ivers-Tiffée, *J. Power Sources*, **258**, 61–75 (2014).

135. R. V. Bugga and M. C. Smart, *J. Electrochem. Soc.*, **25**, 241–252 (2010).

136. S. F. Schuster, T. Bach, E. Fleder, J. Müller, M. Brand, G. Sextl, and A. Jossen, *J. Energy Storage*, **1**, 44–53 (2015).

137. S. Grolleau, I. Baghdadi, P. Gyan, M. Ben Marzouk, S. Grolleau, I. Baghdadi, P. Gyan, and M. Ben Marzouk, *Evs29*, **8**, 339–349 (2016).

138. T. Hüfner, M. Oldenburger, B. Bedürftig, and A. Gruhle, *J. Energy Storage*, **24**,

100790 (2019).

139. M. Dubarry, N. Qin, and P. Brooker, *Curr. Opin. Electrochem.*, **9**, 106–113 (2018).

140. R. Hausbrand, G. Cherkashinin, H. Ehrenberg, M. Gröting, K. Albe, C. Hess, and W. Jaegermann, *Mater. Sci. Eng. B Solid-State Mater. Adv. Technol.*, **192**, 3–25 (2015).

141. K. Kalaga, M. T. F. Rodrigues, S. E. Trask, I. A. Shkrob, and D. P. Abraham, *Electrochim. Acta*, **280**, 221–228 (2018).

142. F. Grimsmann, F. Brauchle, T. Gerbert, A. Gruhle, M. Knipper, and J. Parisi, *J. Energy Storage*, **12**, 132–137 (2017).

143. S. S. Zhang, K. Xu, and T. R. Jow, *J. Power Sources*, **115**, 137–140 (2003).

144. M. S. Ding, K. Xu, S. S. Zhang, K. Amine, G. L. Henriksen, and T. R. Jow, *J. Electrochem. Soc.*, **148**, A1196 (2001).

145. K. Xu, *Chem. Rev.*, **114**, 11503–11618 (2014).

146. X. Zhou, J. Huang, Z. Pan, and M. Ouyang, *J. Power Sources*, **426**, 216–222 (2019).

147. P. Shafiei Sabet and D. U. Sauer, *J. Power Sources*, **425**, 121–129 (2019).

148. E. Goldammer and J. Kowal, *2020 IEEE Veh. Power Propuls. Conf.*, 0–7 (2020).

149. P. Shafiei Sabet, A. J. Warnecke, F. Meier, H. Witzenhausen, E. Martinez-Laserna, and D. U. Sauer, *J. Power Sources*, **449**, 227369 (2020).

150. C. H. Chen, J. Liu, and K. Amine, *J. Power Sources*, **96**, 321–328 (2001).

151. M. P. Mercer, M. Otero, M. Ferrer-Huerta, A. Sigal, D. E. Barraco, H. E. Hoster, and E. P. M. Leiva, *Electrochim. Acta*, **324**, 134774 (2019).

152. F. B. Spingler, M. Naumann, and A. Jossen, *J. Electrochem. Soc.*, **167**, 040526 (2020).

153. M. A. Danzer, *Batteries*, **5**, 1–16 (2019).

154. W. Choi, H. C. Shin, J. M. Kim, J. Y. Choi, and W. S. Yoon, *J. Electrochem. Sci. Technol.*, **11**, 1–13 (2020).

155. M. Lewerenz, A. Warnecke, and D. U. Sauer, *J. Power Sources*, **354**, 157–166 (2017).

156. S. Gantenbein, M. Schönleber, M. Weiss, and E. Ivers-Tiffée, *Sustain.*, **11**, 1–15 (2019).

157. M. Lewerenz, thesis, RWTH Aachen University (2018).

158. F. Grimsmann, T. Gerbert, F. Brauchle, A. Gruhle, J. Parisi, and M. Knipper, *J. Energy Storage*, **15**, 17–22 (2018).

159. M. Lewerenz, A. Warnecke, and D. U. Sauer, *J. Power Sources*, **369**, 122–132

(2017).

160. M. Klett, R. Eriksson, J. Groot, P. Svens, K. Ciosek Högström, R. W. Lindström, H. Berg, T. Gustafson, G. Lindbergh, and K. Edström, *J. Power Sources*, **257**, 126–137 (2014).

161. J. Wilhelm, S. Seidlmayer, P. Keil, J. Schuster, A. Kriele, R. Gilles, and A. Jossen, *J. Power Sources*, **365**, 327–338 (2017).

162. M. Lewerenz, J. Münnix, J. Schmalstieg, S. Käbitz, M. Knips, and D. U. Sauer, *J. Power Sources*, **345**, 254–263 (2017).

163. M. Naumann, F. Spingler, and A. Jossen, *J. Power Sources*, **451**, 227666 (2020).

164. W. M. Dose, M. J. Piernas-Muñoz, V. A. Maroni, S. E. Trask, I. Bloom, and C. S. Johnson, *Chem. Commun.*, **54**, 3586–3589 (2018).

165. M. Ecker, T. K. D. Tran, P. Dechent, S. Käbitz, A. Warnecke, and D. U. Sauer, *J. Electrochem. Soc.*, **162**, A1836–A1848 (2015).

166. A. Eftekhari, *ACS Sustain. Chem. Eng.*, **7**, 5602–5613 (2019).

167. Y. Zhao, Y. Patel, I. A. Hunt, K. M. Kareh, A. A. Holland, C. Korte, J. P. Dear, Y. Yue, and G. J. Offer, *J. Energy Storage*, **13**, 296–303 (2017).

168. Z. H. Liu, Y. L. Kang, H. Bin Song, Q. Zhang, and H. M. Xie, *Chinese Phys. B*, **30** (2021).

169. M. Y. Ali, W. J. Lai, and J. Pan, *J. Power Sources*, **242**, 325–340 (2013).

170. I. C. Halalay, M. J. Lukitsch, M. P. Balogh, and C. A. Wong, *J. Power Sources*, **238**, 469–477 (2013).

171. E. Sahraei, R. Hill, and T. Wierzbicki, *J. Power Sources*, **201**, 307–321 (2012).

172. E. Sahraei, J. Meier, and T. Wierzbicki, *J. Power Sources*, **247**, 503–516 (2014).

173. A. S. Mussa, thesis, KTH Royal Institute of Technology (2018).

174. H. Löbberding, S. Wessel, C. Offermanns, M. Kehrer, J. Rother, H. Heimes, and A. Kampker, *World Electr. Veh. J.*, **11**, 1–15 (2020).

175. Y. H. Choi, H. K. Lim, J. H. Seo, W. J. Shin, J. H. Choi, and J. H. Park, *SAE Int. J. Altern. Powertrains*, **7** (2018).

176. W. J. Lai, M. Y. Ali, and J. Pan, *J. Power Sources*, **245**, 609–623 (2014).

177. K. J. Park, J. Y. Hwang, H. H. Ryu, F. Maglia, S. J. Kim, P. Lamp, C. S. Yoon, and Y. K. Sun, *ACS Energy Lett.*, **4**, 1394–1400 (2019).

178. C. Peabody and C. B. Arnold, *J. Power Sources*, **196**, 8147–8153 (2011).

179. V. Müller, R. G. Scurtu, M. Memm, M. A. Danzer, and M. Wohlfahrt-Mehrens, *J. Power Sources*, **440**, 227148 (2019).

180. C. Uhlmann, J. Illig, M. Ender, R. Schuster, and E. Ivers-Tiffée, *J. Power Sources*, **279**, 428–438 (2015).

10 Appendices

The Inclusion of All Data Points for Figure 25 - Capacity Plots During Calendar Ageing

To aid viewing of Figure 25, certain outliers were removed due to brief issues with the thermal chambers, which altered the test measurement values during the check-ups. Figure 85 displays the same plots, but with the inclusion of all data points for transparency on the data set. It can be clearly seen that large changes in relative capacity are observed, particularly at around 7 months in Figure 85b, which complicates the plot and obscures the trends, thus they were removed in Figure 25. It should also be noted that the general trends remain unaffected by this momentary change in temperature and that it appears to have no lasting effect on these cells.
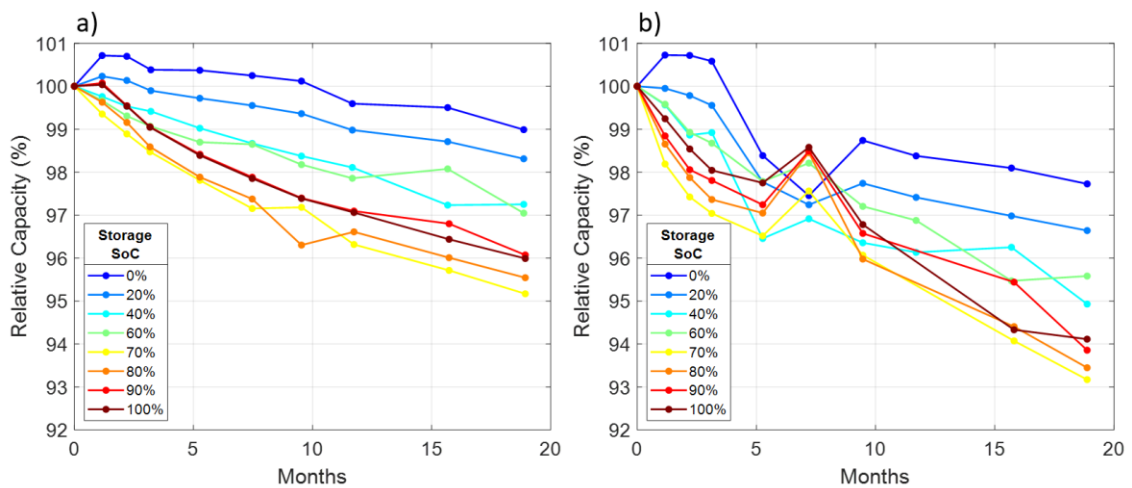

Figure 85. Relative capacity for cells stored at (a) 25oC, and (b) 40oC. All data points remain for transparency on the data set.

The Design Configuration of the Tested LiFun Cell

The design configuration of the LiFun cells visually highlighted an interesting phenomenon that occurs within lithium-ion cells that have passive anode regions (see section 2.3.3, page 19) Lithium can diffuse between active and passive anode regions to alter both the cyclable lithium content and the homogeneity of lithium distribution within the cell. In the extreme case of this process, difficulties can arise with the interpretation of data, which will be discussed in the following section.

Presented in Figure 86 are the photos taken after the disassembly of a LiFun cell charged to 100% SoC (4.2 V), with a charging current of 0.01 A and a constant current constant voltage (CCCV) charging procedure with a current cut-off of 0.001 A. Two anode sheets, one cathode sheet and the separator were contained within the cell, which is presented in Figure 86a. Figure 86b displays a close-up of the right-hand anode sheet observed in Figure 86a. The anode faces displayed in Figure 86a and Figure 86b are directly opposed the cathode when in the full-cell configuration.

A central golden region and reddish-brown surrounding regions that become darker towards the edges are all clearly observed on the anode faces depicted in Figure 86. Golden colours are indicative of more highly lithiated graphite that becomes reddish-brown and then black with increasing delithiation[158,180]. Since the colour of the graphite is an indication of the lithiation degree of the active material, where gold colour is stage I graphite with lithium filling fraction x>0.95[180], it can be inferred that the anode displays a vastly inhomogeneous lithium distribution.
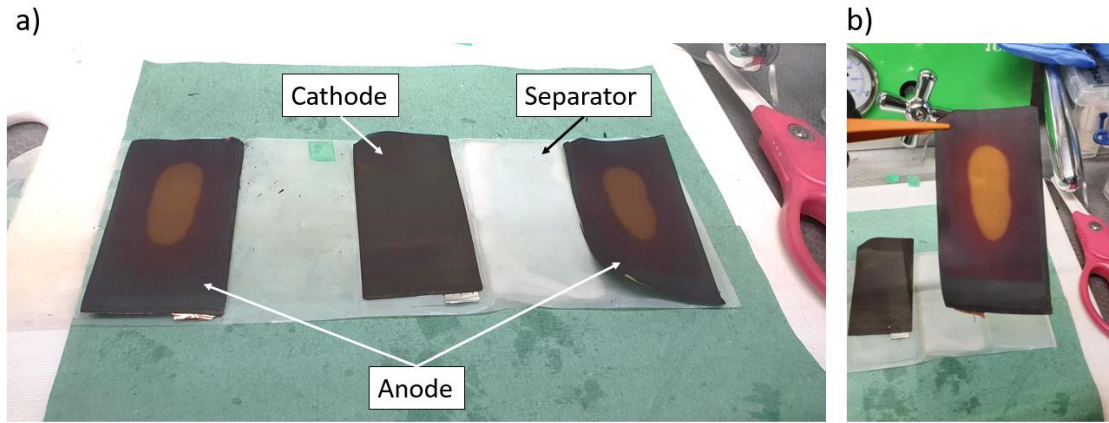
a)

b)

Figure 86. (a) Disassembled LiFun cell showing the anodes, cathode, and separator material. (b) Close-up of the anode containing highly lithiated golden region. Images kindly provided by Dr Mangayarkarasi Nagarathinam.

The electrode configuration of the LiFun cell is displayed in Figure 87, which highlights two double-sided anode sheets sandwiching one double-sided cathode sheet. This configuration produces two (outer facing) anode active material surfaces that are not opposite the cathode and therefore cannot take part in charge/discharge cycling. However, these far sides of the anode can act as vast passive anode regions that accept lithium only by diffusion within the electrolyte from the active region, thus removing lithium from the edges of the active region facing the cathode. This is akin to lithium lost to the overhang regions[19,93]. However, instead of having only a perimeter passive region, the entire outer surface opposite the active region behaves as a lithium sink. This movement of lithium from the active region to the passive region on the outer surface occurs via the electrode edges and is indicated by the yellow arrows in Figure 87. The resulting effect of extended cell storage is the diffusion of large quantities of lithium from the edges of the active regions to the edges of the passive regions, as seen in Figure 86b. Because the cells were shipped at 45% SoC and stored before use, it is possible that this inhomogeneity was formed before any electrochemical testing.
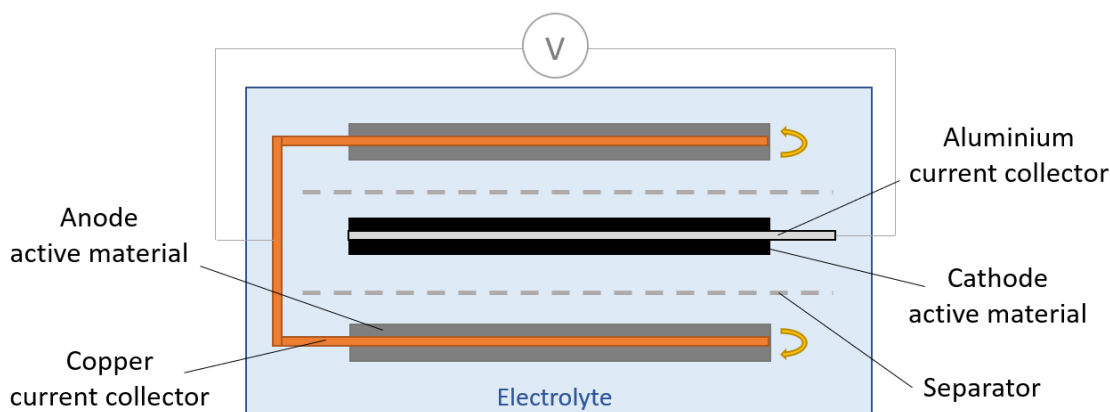
Figure 87. Diagram of the LiFun internal configuration of the anode, cathode and separator.

This process, that occurs over the timescales of days/weeks, can have ramifications on data interpretation and cell performance[138]. Firstly, the inhomogeneity of lithium distribution can strongly influence the calculated DVA curve of the full-cells, as described in section 3.8.2, page 43). Local differences in the lithiation degree of the anode mean that, during a charge/discharge, the phase transitions occur at different points in time across the electrode. In turn, broader, flatter peaks are produced in the resulting DVA curve during a low current charge and the features become smoothed[18,95]. With the LiFun cells, this effect is so strong that the more subtle features of the anode (and cathode) are lost and that no DVA markers can be identified. The relative capacity regions can thus not be tracked reliably, and interpretation and the identification of degradation modes becomes increasingly challenging using this non-destructive method.

Secondly, the large inhomogeneity in lithiation degree across the anode can mean the discharging cut-off voltage is reached sooner[95,155]. The extracted discharge capacity is thus reduced, which may explain the reason for the lower measured capacity of 0.135 Ah compared to rated capacity by the manufacturer of >0.150 Ah.

Because all cells had identical storage conditions before experimental testing, and all cells were consistent in electrode configuration, this process is likely to affect all cells equally. It is thus proposed that the results presented in this chapter are the product of the differences in ageing condition and not a cell-to-cell variation.